Chemomechanical regulation of integrin activation and cellular processes in acidic extracellular pH

by

Ranjani Krishnan Paradise

B.S.E., Princeton University (2006)

Submitted to the Department of Biological Engineering
in Partial Fulfillment of the Requirements for the Degree of
Doctor of Philosophy
at the
Massachusetts Institute of Technology

June 2012

Signature of Author ____

Ranjani Krishnan Paradise
Department of Biological Engineering

Certified by ____

Krystyn J. Van Vliet
Paul M. Cook Career Development Associate Professor of Materials Science and
Engineering and Biological Engineering
Thesis Supervisor

Certified by ____

Douglas A. Lauffenburger
Ford Professor of Biological Engineering, Chemical Engineering, and Biology
Thesis Supervisor

Accepted by ____

Forest M. White
Associate Professor of Biological Engineering
Chair, Departmental Committee on Graduate Students

Chemomechanical regulation of integrin activation and cellular processes in acidic extracellular pH

by

Ranjani Krishnan Paradise

Submitted to the Department of Biological Engineering
on March 15, 2012 in Partial Fulfillment of the
Requirements for the Degree of Doctor of Philosophy

ABSTRACT

It is well established that extracellular pH (pH_e) becomes acidic in several important physiological and pathological contexts, including the tumor and wound microenvironments. Although it is known that acidic pH_e can have profound effects on cell adhesion and migration processes integral to tumor progression and wound healing, the molecular mechanisms underlying the cellular responses to acidic pH_e are largely unknown. Transmembrane integrin receptors form a physical linkage between cells and the extracellular matrix, and are thus capable of modulating cell adhesion and migration in response to extracellular conditions. In this thesis, computational and experimental approaches are used to investigate the role of acidic extracellular pH in regulating activation and binding of integrin $\alpha_v\beta_3$, and to characterize the consequences for downstream subcellular- and cellular-scale processes.

Molecular dynamics simulations demonstrate that opening of the integrin $\alpha_v\beta_3$ headpiece occurs more frequently in acidic pH_e than in normal pH_e, and that this increased headpiece opening can be partially attributed to protonation of ASPβ127 in acidic pH_e. These computational data indicate that acidic pH_e can promote activation of integrin $\alpha_v\beta_3$. This is consistent with flow cytometry and atomic force microscope-enabled molecular force spectroscopy experiments, which demonstrate that there are more activated $\alpha_v\beta_3$ receptors on live $\alpha_v\beta_3$ CHO-B2 cell surfaces at acidic pH_e than at normal pH_e 7.4. Put together, these atomistic- and molecular-level data suggest a novel mechanism of outside-in integrin activation regulation by acidic extracellular pH.

Next, the consequences of acid-induced integrin activation for subcellular- and cellular-scale processes are investigated. Kymography experiments show that $\alpha_v\beta_3$ CHO-B2 cell membrane protrusion lifetime is increased and protrusion velocity is decreased for cells in pH_e 6.5, compared to cells in pH_e 7.4. Furthermore, $\alpha_v\beta_3$ CHO-B2 cells in pH_e 6.5 form more actin-integrin adhesion complexes than cells in pH_e 7.4, and acidic extracellular pH results in increased cell area and decreased cell circularity. Cell migration measurements demonstrate that $\alpha_v\beta_3$ CHO-B2 cells in pH_e 6.5 migrate slower than cells in pH_e 7.4, and that the fibronectin ligand density required for peak migration speed is lower for cells in pH_e 6.5. Together, these data show that acidic pH_e affects subcellular- and cellular-scale processes in a manner that is consistent with increased integrin activation in this condition.

Finally, the migration behavior of $\alpha_v\beta_3$ CHO-B2 cells, bovine retinal microvascular endothelial cells, and NIH-3T3 fibroblasts in an extracellular pH gradient is investigated. Results demonstrate that NIH-3T3 fibroblasts do not exhibit directional preferences in the $\mathrm{pH_e}$ gradient, but that $\alpha_v\beta_3$ CHO-B2 cells and bovine retinal microvascular endothelial cells migrate preferentially toward the acidic end of the gradient. These data suggest that acidic extracellular pH may serve as a cue that directs migration of angiogenic endothelial cells to poorly vascularized regions of tumors and wounds. Overall, this thesis research results in multiscale, in-depth understanding of extracellular pH as a critical regulator of cell function, with associated implications for tumor growth, wound healing, and the role of proton pumps in cell migration.

Thesis Committee Chair: Roger D. Kamm
Title: Singapore Research Professor of Biological Engineering and Mechanical Engineering

Thesis Supervisor: Krystyn J. Van Vliet
Title: Paul M. Cook Career Development Associate Professor of Materials Science and Engineering and Biological Engineering

Thesis Supervisor: Douglas A. Lauffenburger
Title: Ford Professor of Biological Engineering, Chemical Engineering, and Biology

Thesis Committee Member: Bruce Tidor
Title: Professor of Biological Engineering and Computer Science

Acknowledgments

I am deeply grateful to many people for their advice, support, and friendship throughout my graduate school experience. I especially thank:

My advisor Krystyn Van Vliet, for her constant energy, enthusiasm, and support. Krystyn has devoted countless hours to me and my research over the years, and her dedicated guidance has been invaluable in my development as a researcher. Her passion, intensity, and enthusiasm will always be an inspiration to me in my future endeavors.

My co-advisor Doug Lauffenburger, for his encouragement, guidance, and wisdom. His comments and advice been instrumental in shaping this thesis, and it has been a pleasure being part of the Biological Engineering community under his leadership. I will always look up to him as a model of a great leader.

My thesis committee members Bruce Tidor and Roger Kamm, for their thoughtful questions and comments that have helped focus and improve my work.

My labmates in the Van Vliet group, for making my work environment pleasant and fun, as well as productive. I thank them for many good memories of group lunches, potlucks, and outings, and I couldn't have asked for a more intelligent or supportive group of colleagues. I especially thank Emily Walton Vinocur, Sunyoung Lee, Irene Chen, John Maloney, Anna Jagielska, Adam Zeiger, and Matt Whitfield for many insightful discussions about research and graduate student life.

My friends Pam Brownstein, Melody Morris, Michelle Sukup-Jackon, John Maloney, Katie Maloney, Emily Florine, Kristin Bernick, Lorenna Buck, and Scott Carlson, for many memories of shared laughter and good conversation. Over the last few years, their friendship has helped me enjoy the good moments that life has given me and recover from the bad. My time at MIT would not have been nearly so happy without all of them.

My parents, Krishnan Raghavachari and Akola Krishnan, for their everlasting love, support, and encouragement. Their example has shown me what it means to have a happy, successful, and fulfilling life, and they are a constant inspiration to me.

My sister Meera Krishnan, for always being there for me through all the ups and downs of the last several years. She has unfailingly offered exactly what I needed, whether it was a listening ear, a shoulder to cry on, or a companion to celebrate with. I am so grateful to have a sister that I can call my best friend.

My husband Andrew Paradise, for making my life so very happy. From thesis proposal to thesis defense, he has patiently listened to all my research-related woes, encouraged and reassured me when I doubted myself, and given me the confidence to take on new challenges. His love, companionship, and support have been more valuable to me than I can say.

Table of Contents

Chapter 1: Background and motivation ... 23

1.1. Introduction ... 23
1.2. Acidic extracellular pH (pH_e) ... 23

1.2.1. Tumor environment ... 23
1.2.2. Wound environment ... 25
1.2.3. NHE1 and local acidification of the cell microenvironment ... 25

1.3. Cell adhesion and migration in acidic extracellular pH ... 26
1.4. Integrins ... 28

1.4.1. General background ... 28
1.4.2. Integrin structure ... 29
1.4.3. Integrin activation ... 30
1.4.4. Integrin signaling ... 33
1.4.5. Tools and techniques for studying integrins ... 33

1.5. Thesis motivation and objective ... 34

1.5.1. Motivating question: What is the role of integrins in mediating cellular responses to acidic pH_e? ... 34
1.5.2. Overall thesis objective ... 35

1.6. Thesis strategy and organization ... 35

1.6.1. $\alpha_v\beta_3$ as a model integrin ... 35
1.6.2. Thesis aims and organization ... 36

Chapter 2: Atomistic-scale simulations ... 39

2.1. Overview ... 39
2.2. Molecular dynamics methodology ... 39

2.2.1. Basic principles ... 39
2.2.2. Steered molecular dynamics ... 40

2.3. Using replicate MD simulations to characterize rare-event property distributions ... 41

2.3.1. The problem: characterizing rare events in molecular simulations ... 41
2.3.2. Using clustering analysis to test for a configuration-property relationship. 43
2.3.3. Necessary number of replicate simulations ... 44
2.3.4. Discussion ... 45
2.3.5. Conclusions and suggestions for design of computational experiments ... 47

2.4. MD simulations of integrin $\alpha_v\beta_3$: Does acidic pH_e affect the conformational changes involved in integrin activation? ... 48

2.4.1. Changing pH_e in MD simulations: MCCE ... 48
2.4.2. Simulation system and MCCE results ... 49
2.4.3. MD results ... 51
2.4.4. Discussion of MD results ... 54

2.5. SMD simulations of $\alpha_v\beta_3$-RGD: Within a single activation state, does acidic pH_e change $\alpha_v\beta_3$-RGD affinity via local changes to the binding pocket? 56

2.5.1. Simulation system and pulling methods 56
2.5.2. SMD results: rupture forces and unbinding rates 56
2.5.3. Discussion of SMD results 60

2.6. Conclusions and transition to molecular-scale experiments 62

2.6.1. Conclusions 62
2.6.2. Next question: Can these predictions be experimentally validated? 62

2.7. Acknowledgments 62

Chapter 3: Molecular-scale experiments 63

3.1. Overview 63
3.2. Flow cytometry 63

3.2.1. Results 63
3.2.2. Discussion of flow cytometry results 65

3.3. AFM-enabled molecular force spectroscopy 65

3.3.1. Introduction to AFM methodology 65
3.3.2. Results 66
3.3.3. Discussion of AFM-MFS results 70

3.4. Conclusions and transition to subcellular-scale experiments 72

3.4.1. Conclusions 72
3.4.2. Next question: How does increased integrin activation in acidic pH_e impact subcellular processes critical to cell adhesion and migration? 73

Chapter 4: Subcellular-scale experiments 74

4.1. Overview 74
4.2. Kymography 74

4.2.1. Background 74
4.2.2. Results for normal and acidic pH_e 76
4.2.3. Intracellular pH manipulation and kymography measurements 77
4.2.4. Discussion of kymography results 80

4.3. Imaging of actin-integrin adhesion complexes 81

4.3.1. Background 81
4.3.2. Results for normal and acidic pH_e 82
4.3.3. Discussion of AIAC imaging results 83

4.4. Conclusions and transition to cellular-scale experiments 84

4.4.1. Conclusions 84
4.4.2. Next question: how does acidic extracellular pH impact cell spreading and migration? 85

4.5. Acknowledgments 85

Chapter 5: Cellular-scale experiments and modeling 86

5.1. Overview 86
5.2. Introduction 86
5.3. Cell spreading and morphology 87

5.3.1. Background 87
5.3.2. Results: cell spreading over short timescales 87
5.3.3. Discussion of short timescale cell spreading results 89
5.3.4. Results: cell spreading and morphology over long timescales 89
5.3.5. Discussion of long timescale cell spreading and morphology results 92

5.4. Cell migration 94

5.4.1. Background 94
5.4.2. Experimental results 95
5.4.3. Cell migration model 96
5.4.4. Discussion of cell migration results 104

5.5. Role of intracellular pH in long-timescale experiments 105
5.6. Conclusions and transition to pH_e gradient experiments 106

5.6.1. Conclusions 106
5.6.2. Next question: How do cells migrate in pH_e gradients? 106

5.7. Acknowledgments 107

Chapter 6: Cell migration in an extracellular pH gradient 108

6.1. Overview 108
6.2. Background 108
6.3. Results 109

6.3.1. Gradient stability 109
6.3.2. $\alpha_v\beta_3$ CHO-B2 cells 112
6.3.3. Bovine retinal microvascular endothelial cells (BRECs) 113
6.3.4. NIH-3T3 fibroblasts 115

6.4. Discussion 120

6.4.1. Mechanism for migration toward acid 120
6.4.2. Extent of response in the cell population 124
6.4.3. Lack of response for NIH-3T3 cells 127
6.4.4. Implications for tumor growth and wound healing 129

6.5. Conclusions 130
6.6. Acknowledgments 131

Chapter 7: Overarching discussion 132

7.1. Major findings 132

7.1.1. Summary of previous chapters 132
7.1.2. Role of intracellular acidification 135
7.1.3. Extension to other integrins 137

7.2. Previous work in the context of our results 137
7.3. Implications 139
  7.3.1. Regulation of integrin activation and binding in varied environments 139
  7.3.2. Tumor growth and wound healing 139
  7.3.3. The role of NHE1 in cell migration 139
7.4. Suggestions for future study 141
  7.4.1. Exploration of other integrins 141
  7.4.2. Fibroblast migration in pH_e gradients 141
  7.4.3. 3-D cell migration 142
  7.4.4. ECM stiffness 142
7.5. Contributions 143
Chapter 8: Materials and methods 144
8.1. Antibodies and reagents 144
8.2. MD simulations 145
  8.2.1. Biotin-streptavidin simulations 145
  8.2.2. Integrin simulations 146
8.3. Cell culture 148
8.4. Flow cytometry 149
8.5. AFM-enabled molecular force spectroscopy 150
8.6. Kymography 151
8.7. Measurement and manipulation of pH_i 151
8.8. GFP-vinculin transfection and AIAC imaging 153
8.9. Cell spreading, morphology, and migration measurements 154
  8.9.1. Cell spreading with cyclic pH_e changes 154
  8.9.2. Cell spreading from the detached state 154
  8.9.3. Cell spreading and morphology over long timescales 155
  8.9.4. Cell migration 155
8.10. Cell migration in an extracellular pH gradient 156
  8.10.1. Dunn chamber setup and gradient imaging 156
  8.10.2. Cell migration measurements and image analysis 156
  8.10.3. Statistical analysis 157
8.11. Migration model 158
8.12. Statistical analysis 161
References 162
Appendix A: Run files for MD simulations 177
Appendix B: Integrin beta subunit sequence alignment 180

List of figures

Figure 1.1 Mean extracellular pH values measured in tumors and normal tissue. Midrange pH_e is used in cases where mean is not given. Individual pH_e measurements are not plotted here. Data from the review by Wike-Hooley et al. 1984 [1] include measurements from many investigators. In general, average extracellular pH in tumors is lower than that in normal tissue. 24

Figure 1.2 (A) Schematic of a spread cell with adhesion sites represented by grey dots. Magnification illustrates an integrin receptor within the adhesion site with its extracellular domain bound to an ECM protein. On the cytoplasmic side, talin (green) links the integrin β tail to actin, and vinculin (yellow) cross-links talin and actin. (B) Integrin structure and subunit domains, adapted from Ref. [76]. β sheets are depicted in blue, α helices are in red, and metal ions in yellow........ 29

Figure 1.3 Integrins exhibit three distinct conformations with varying binding affinities. Headpiece domains are depicted in black. These headpiece domains were analyzed computationally in the atomistic simulations that will be discussed in Chapter 2. In the low-affinity conformation, the integrin leg domains are bent and the headpiece is closed. In the intermediate-affinity conformation, the leg domains are extended and the headpiece is closed. In the high-affinity conformation, the leg domains are extended, and the headpiece is open. Figure from Ref. [85]........ 31

Figure 1.4 Model of how large scale conformational changes in the integrin headpiece alter binding affinity. (A) For integrins without the I domain, hybrid domain movement during headpiece opening pulls down the α7 helix of the I-like domain, which changes the position of the MIDAS site, making the MIDAS ion more accessible for coordination by ligand. (B) For integrins with an I domain, the same conformational changes occur (Step 1), but the I-like domain MIDAS ion binds a linker which pulls down the I domain α7 helix and makes the I domain MIDAS ion more available for ligand binding (Step 2). Figure adapted from Ref. [72]........ 32

Figure 1.5 Schematic of the multiple lengthscales explored in this thesis. Computational and experimental approaches are used to connect molecular binding to cellular responses. 37

Figure 2.1 (A) Hypothetical clustering results in the case that a correlation exists between initial bound configuration and output rupture force F_R. Filled circles denote cluster centroid rupture forces and dashes denote rupture forces for configurations within each cluster, with individual clusters indicated with brackets. (B) Clustering results with centroids from three different groups used for similarity calculation: Group 1: streptavidin tetramer plus four bound biotin molecules (filled circles); Group 2: streptavidin binding pocket plus one bound biotin molecule (squares); Group 3: streptavidin binding pocket (triangles). Dashes denote F_R values for configurations within a single cluster. This same set of configurations comprised one full cluster for each of the three clustering metrics used. Open circles denote F_R values for a single initial configuration with varied initial atomic velocities. Even considering three different similarity metrics, we find no evidence to support a correlation between initial configuration and rupture force. Figure is from Ref. [128].. 44

Figure 2.2 The full set of 53 rupture forces was split into randomly generated subsets of size ranging from $N = 4$ to $N = 40$. The rupture force distribution of each subset was compared to the distribution of the full set of 53 rupture forces. The percentage of subsets that were statistically different ($p < 0.05$) than the full set of rupture forces is plotted here for each N. Consistent with many other fields, a set of 30 samples seems to consistently reproduce features of the original property distribution. Figure is from Ref. [128].............. 45

Figure 2.3 Protein energy landscapes are rough and multi-dimensional (A), but are often represented as smooth and one-dimensional (B, red). In rough, one-dimensional landscapes (B, blue), similar configurations may have very different initial energies (pathway *a* and *b* in C), causing a difference in the energy barrier and therefore in values of protein properties. Multi-dimensional landscapes introduce additional mechanisms of property variation: the transition state roughness (pathways *b* and *c* in C) and the initial sampling direction (pathways *c* and *d* in C). Many protein interactions are described by rough, multi-dimensional energy landscapes that result in a natural variation in energy-dependent properties. Figure from Ref. [128].. 46

Figure 2.4 A suggested method of testing for the presence of configuration-property correlation in rare event MD simulations and implications on selecting an ensemble of initial configurations for replicate production-run simulations. Figure from Ref. [128]. 47

Figure 2.5 Rendering of the simulation system used in this study: the $\alpha_v\beta_3$ headpiece in complex with an RGD peptide. Spheres depict MG^{2+} ions (blue), RGD ligand (red), residues with elevated pK_a that were protonated at both normal and acidic pH_e (green), and residues with elevated pK_a that were protonated at acidic pH_e only (orange). Figure from Ref. [85].. 50

Figure 2.6 (A) Rendering of the $\alpha_v\beta_3$ headpiece in a closed conformation displayed as in Figure 2.5. Arrow indicates headpiece opening distance. (B) Rendering of the $\alpha_v\beta_3$ headpiece in a partially open conformation. (C) Histograms of headpiece opening distances from all recorded frames of every simulation trajectory. Frequencies are displayed as the average of the eight simulations at each pH_e condition. Error bars are SEM. Figure from Ref. [85]. 51

Figure 2.7 (A) Histogram of headpiece opening distances displayed as in Figure 2.7. (B) Snapshot of the $\alpha_v\beta_3$ I-like domain in the normal pH_e system demonstrating ASPβ127-ADMIDAS ion coordination. The ADMIDAS ion is displayed as a blue sphere, ASPβ127 is displayed in orange spheres, and the α1-β1 loop and α1 helix are displayed in black. (C) Snapshot of the $\alpha_v\beta_3$ I-like domain in the acidic pH_e system demonstrating the lack of ASPβ127-ADMIDAS ion coordination. (D) Average distances between the centers-of-mass of the ADMIDAS ion and ASPβ127 in each simulation trajectory. Error bars (SEM) are within data points. Figure from Ref. [85]. 52

Figure 2.8 Headpiece opening distance over time for a single simulation that was extended to a longer timescale of 56 ns. Headpiece distance did not increase appreciably between 8 – 56 ns. Data between 15.5 – 36 ns was lost due to a computer failure. 53

Figure 2.9 (A) SMD force vs. extension trace at loading rate F' = 8.28 N/s published by Craig et al [46]. (B) SMD force vs. extension trace obtained with our simulation protocol. 57

Figure 2.10 $\alpha_v\beta_3$-RGD rupture forces obtained from SMD simulations. Filled circles are rupture forces for the entire group of cluster centroids for normal pH_e. Open circles are subgroups of cluster centroid rupture forces, based on initial ASP_{RGD} ion coordination state. Ball-and-stick diagrams illustrate the RGD ligand (black sticks) and MIDAS (bottom red ball) and LIMBS (top red ball) ions. The distribution of rupture forces for the MIDAS subgroup and LIMBS subgroup is narrower than that for the full set of rupture forces. 58

Figure 2.11 Comparison of rupture force distributions from cluster centroids with different atomic configurations (open circles) and a single configuration with different initial atomic velocities (gray filled circles) for each initial ion coordination state................. 59

Figure 2.12 Average rupture forces as a function of ln(F') for normal and acidic pH_e simulations, with best fit lines. There was no significant difference between average rupture force at normal vs. acidic pH_e for any of the three loading rates tested. Error bars are SEM. 60

Figure 3.1 Control experiments confirming WOW-1 specificity. (A) WOW-1 Fab binding in the presence of various divalent cations. CHO-B2 pCDNA cells (negative control) do not express $\alpha_v\beta_3$, Ca^{2+} (negative control) stabilizes inactivate $\alpha_v\beta_3$, and Mn^{2+} (positive control) promotes $\alpha_v\beta_3$ activation. Data are displayed as the average geometric mean fluorescence intensity (MFI) of triplicate samples from a single representative experiment (primary axis), as well as the normalized geometric MFI expressed relative to the average value measured in the presence of Mg^{2+} ions (secondary axis), to enable direct comparison to Figure 3.2. (B) Representative flow cytometry fluorescence intensity histograms illustrating WOW-1 Fab binding for CHO-B2 pCDNA cells, which do not express the integrin β_3 subunit, and $\alpha_v\beta_3$ CHO-B2 cells exposed to Mn^{2+}, which activates integrin $\alpha_v\beta_3$. Error bars are SEM. Figure from Ref. [85]. 64

Figure 3.2 (A) WOW-1 Fab binding after exposure to pH_e 6.0 – 8.0. WOW-1 Fab binds preferentially to the activated conformation of $\alpha_v\beta_3$. Data are normalized geometric MFI at each pH_e expressed relative to the average value measured at pH_e 7.4. Average data were calculated from at least two independent experiments at each pH_e. Asterisk indicates $p < 0.01$ with respect to all other pH_e conditions. Red bars indicate acidic conditions, and blue bar outlined with dashed line indicates physiological pH_e 7.4. (B) LM609 binding after exposure to pH_e 6.0 or 7.4. LM609 is an antibody that binds all conformations of $\alpha_v\beta_3$. Data are expressed as in (A). Error bars are SEM. Figure from Ref. [85]. 64

Figure 3.3 (A) Schematic depiction of a typical AFM molecular force spectroscopy setup with receptors expressed on the cell surface. (B) Optical image of an AFM cantilever positioned over an $\alpha_v\beta_3$ CHO-B2 cell. (C) A sample force-displacement trace during which a ligand-receptor binding interaction occurred. 1. Cantilever is above the cell surface; 2. Cantilever contacts the cell; 3. After indenting the cell briefly, cantilever begins to retract; 4. Immediately before rupture, the linker-ligand-receptor system is stretched; 5. The ligand-receptor complex has ruptured, and the cantilever is free of the cell. The offset in approach and retraction traces is due to fluid drag. Portions of figure are from Ref. [85]. 66

Figure 3.4 (A) Schematic of a RGD-functionalized cantilever illustrating the linkers used for functionalization chemistry. (B) Fully functionalized non-gold-coated cantilevers (left) compared with fully functionalized gold-coated cantilevers (right). (C) Gold-coated cantilevers functionalized without the PEG linker (left) compared with fully functionalized gold-coated cantilevers (right). (D) Gold-coated cantilevers functionalized without the cross-linker (left) compared with fully functionalized gold-coated cantilevers (right). Images within each pair (horizontal rows) were imaged on the same day and are displayed with the same contrast settings. However, different pairs were imaged on different days, and the three images of fully functionalized gold-coated cantilevers are not identical for this reason. 67

Figure 3.5 Heat maps illustrating the frequencies of binding events with F_R and k_{eff} within the indicated ranges. (A) Adhesion events before blocking the RGD binding site on $\alpha_v\beta_3$ with antibody LM609. (B) Adhesion events after blocking the RGD binding site on $\alpha_v\beta_3$ with antibody LM609. White lines outline region with $F_R > 50$ pN and $k_{eff} > 400$ pN/μm. 69

Figure 3.6 (A) Rupture forces at pH$_e$ 7.4 grouped by effective loading rate F'_{eff}. Data are consistent with the Bell-Evans model [137-139], even with the small range of F'_{eff} that we observed. (B) Mean rupture forces measured at pH$_e$ 7.4, pH$_e$ 7.4 after $\alpha_v\beta_3$ activation by antibody LIBS-6, and pH$_e$ 6.0. (C) Mean specific binding frequencies at pH$_e$ 7.4 before and after $\alpha_v\beta_3$ activation by antibody LIBS-6 or $\alpha_v\beta_3$ blocking by antibody LM609. (D) Mean specific binding frequencies at pH$_e$ 6.0 and pH$_e$ 7.4. Figure includes data from three independent experiments. For each experiment, the single-cell specific binding frequencies were normalized to the average value at pH$_e$ 7.4. These relative specific binding frequencies were then pooled and averaged. (F) Single cell specific binding frequencies used to calculate the average in (E). All error bars are SEM. Portions of figure are from Ref. [85]. 70

Figure 3.7 Model of pH$_e$-regulated integrin activation. Inside-out activation mechanisms can cause the bent-closed conformation to convert to the extended-closed conformation. Acidic extracellular pH can then promote headpiece opening to the extended-open conformation. In addition, acidic pH$_e$ can stimulate headpiece opening on the bent-closed integrin, which is expected to lead to extension of the integrin legs. Through these dual mechanisms, acidic extracellular pH can shift the integrin conformational equilibrium to the high affinity extended-open state. Figure from Ref. [85]. 72

Figure 4.1 Images illustrating kymography experimental methods. (A) Images of $\alpha_v\beta_3$ CHO-B2 cells on fibronectin-coated glass (30 μg/ml) were taken at 40x magnification every 5 s for a duration of 25 min. A one-pixel-wide line was drawn perpendicular to the cell membrane at every location that exhibits activity. (B) This line was sequentially compiled for all image frames to produce a kymograph displaying individual protrusion events. (C) For each protrusion event (P), a straight line was drawn from the base to the peak. The slope of this line represents the protrusion velocity and the x-axis projection represents the lifetime. 75

Figure 4.2 $\alpha_v\beta_3$ CHO-B2 cell membrane protrusion lifetime and velocity measured by kymography. Kymography measurements demonstrated that mean protrusion lifetime was significantly increased and mean protrusion velocity was significantly decreased at acidic extracellular pH (asterisks represent $p < 0.0001$). 501 individual protrusion events were measured for pH_e 7.4 and 204 events were measured for pH_e 6.5. Error bars are SEM........ 76

Figure 4.3 BCECF dye loading and calibration. (A) Fluorescent image (~495 nm excitation) illustrating BCECF loading into $\alpha_v\beta_3$ CHO-B2 cells. (B) Calibration of BCECF fluorescence intensity ratio in the pH_i range of interest. Fluorescence intensity ratio was calculated as the mean intensity of a cell imaged with ~495 nm excitation divided by the mean intensity of a cell imaged with ~440 nm excitation. Emission is at ~535 nm for both excitation wavelengths. The fluorescence intensity ratio was linear with pH_i. At least 28 cells were imaged for each calibration pH condition. Error bars are SEM. 77

Figure 4.4 Intracellular pH measurements for cells exposed to acidic pH_e and for cells incubated with the NHE1 inhibitor EIPA. (A) Intracellular pH measurements for $\alpha_v\beta_3$ CHO-B2 cells exposed to pH_e 6.0 for 0 – 30 min. 3 – 14 cells were imaged at each timepoint. (B) Intracellular pH measurements for $\alpha_v\beta_3$ CHO-B2 cells exposed to pH_e 6.0 or pH_e 6.5 for 30 – 90 min. At least 36 cells were imaged at each timepoint. (C) Incubation with 50 μM EIPA (NHE1 inhibitor) for 120 – 240 min caused intracellular pH to reach the same range as that shown in (B) for cells exposed to pH_e 6.5 for 30 – 90 min. All errors are SEM........ 78

Figure 4.5 Average membrane protrusion lifetime and velocity measurements for cells in various extra- and intracellular pH conditions. As measurements were taken on different days, all data are normalized to the average value for control cells tested on the same day. (A) Left two bars: average membrane protrusion lifetime for cells in $pH_e = 6.5$ and $pH_i \leq 6.7$ compared to that for control cells ($pH_e = 7.4$, $pH_i \sim 7.4$). Data is the same as that shown in Figure 4.2. Center two bars: average membrane protrusion lifetime for cells in $pH_e = 7.4$ and $pH_i \leq 6.7$ with NHE1 blocked compared to that for control cells. Right two bars: average membrane protrusion lifetime for cells in $pH_e = 6.5$ and $pH_i \leq 6.7$ with NHE1 blocked compared to that for control cells. (B) Average protrusion velocity for the same conditions shown in (A). At least 100 protrusion events were measured for each experimental condition. All error bars are SEM. $^{**}p \leq 0.0001$, $^{*}p < 0.05$ 79

Figure 4.6 Characterization of actin-integrin adhesion complexes (AIACs) for cells in pH_e 7.4 and pH_e 6.5. (A) Representative fluorescent images of $\alpha_v\beta_3$ CHO-B2 cells transfected with GFP-vinculin. Some cells had AIACs mainly at the cell periphery (left), while others had AIACs throughout the cell body (right). (B) Mean number of AIACs per cell and mean AIAC area for cells exposed to pH_e 7.4 or 6.5 for 20 – 40 min. $N = 61$ cells for pH_e 7.4 and $N = 56$ cells for pH_e 6.5. (C) Mean number of AIACs per cell and mean AIAC area for cells exposed to pH_e 7.4 or 6.5 for 2 – 3 hr. $N = 48$ cells for pH_e 7.4 and $N = 63$ cells for pH_e 6.5. Error bars are SEM. $*p < 0.01$, $**p < 0.001$. 83

Figure 5.1 (A) Projected cell area for a representative cell over 8 hr, during which media pH_e was changed to pH 6.0 every hour. After each pH_e change, media pH_e drifted up to ~7.2 due to presence of bicarbonate buffer, as evidenced by the color change of the pH_e indicator in the media (shown for 1 hr). Images are snapshots of the cell at area minima and maxima. Arrowheads indicate points immediately before media pH_e was changed to pH_e 6.0. Each hour, cell area increased within minutes after pH_e was dropped to 6.0, and decreased as pH_e drifted up. Figure from Ref. [85]. (B) Cell area for a representative cell over 8 hr in conditions where the extracellular pH_e was maintained at a steady level of $pH_e = 7.4$. To maintain steady pH_e, cells were plated in polystyrene dishes with tight-fitting lids, which eliminated CO_2-dependent media buffering. 88

Figure 5.2 Mean spread area of $\alpha_v\beta_3$ CHO-B2 cells 30 min after plating from the suspended state onto fibronectin-coated glass in media at pH 6.0 or pH 7.4. Media initially set to pH 6.0 remained below pH 7.0 for the duration of the experiment. Mean cell area was significantly higher at pH_e 6.0 than at pH_e 7.4 ($p = 0.025$). $N = 44$ cells for pH_e 7.4 and $N = 42$ cells for pH_e 6.0. Error bars are SEM. Figure from Ref. [85]. 88

Figure 5.3 (A) Mean $\alpha_v\beta_3$ CHO-B2 cell projected area as a function of fibronectin surface coating concentration measured 8 hr after setting media pH_e to 7.4 or 6.5. Cell area increased as fibronectin concentration increased for both pH_e values. Cells at pH_e 6.5 had larger cell area than cells at pH_e 7.4 for all conditions, with the exception of 0.1 μg/ml fibronectin. (B) Mean $\alpha_v\beta_3$ CHO-B2 cell area at 10 μg/ml fibronectin measured 8 hr after setting media pH to 7.4 or 6.5. Soluble RGD peptide or Mn^{2+} was added in some cases, and one set of experiments was conducted with CHO-B2 pCDNA cells, as indicated. The difference in mean area at pH_e 7.4 vs. pH_e 6.5 for cells observed under basal conditions was eliminated for CHO-B2 pCDNA cells and for $\alpha_v\beta_3$ CHO-B2 cells incubated with 1 mM Mn^{2+}. At least 50 cells were measured for each condition, and all error bars are SEM. $***p \leq 0.0001$, $**p < 0.01$, $*p < 0.05$. 91

Figure 5.4 (A) Mean $\alpha_v\beta_3$ CHO-B2 cell circularity as a function of fibronectin surface coating concentration measured 8 hr after setting media pH to 7.4 or 6.5. Cell circularity decreased as fibronectin concentration increased for both pH_e values. Cells at pH_e 6.5 had lower cell circularity than cells at pH_e 7.4 for all conditions, with the exception of 0.1 μg/ml fibronectin. Images show representative snapshots of $\alpha_v\beta_3$ CHO-B2 cells at pH_e 7.4 or 6.5. (B) Mean $\alpha_v\beta_3$ CHO-B2 cell circularity at 10 μg/ml fibronectin measured 8 hr after setting media pH to 7.4 or 6.5. Soluble RGD peptide or Mn^{2+} was added in some cases, and one set of experiments was conducted with CHO-B2 pCDNA cells, as indicated. The difference in mean circularity at pH_e 7.4 vs. pH_e 6.5 for cells observed under basal conditions was eliminated for CHO-B2 pCDNA cells and for $\alpha_v\beta_3$ CHO-B2 cells incubated with 200 μg/ml RGD or 1 mM Mn^{2+}. At least 50 cells were measured for each condition, and all error bars are SEM. $***p \leq 0.0001$, $**p < 0.01$. 92

Figure 5.5 Mean speeds and persistence times for cells migrating on fibronectin-coated polystyrene (A,B) or fibronectin-coated glass (C,D). (A) Mean cell migration speed as a function of fibronectin coating concentration for cells migrating on fibronectin-coated polystyrene. Maximum migration speed occurred at a lower fibronectin concentration when cells were in acidic pH$_e$. Asterisks indicate peak migration speeds. Statistical significance of maximum migration speed value at pH$_e$ 7.4: 0.1 vs. 1 μg/ml, $p < 0.05$; 1 vs. 20 μg/ml, $p < 0.001$; 1 vs. 30 μg/ml, $p < 0.001$. For pH$_e$ 6.5: 0.1 vs. 1 μg/ml, $p < 0.1$; 0.1 vs. 10 μg/ml, $p < 0.05$; 0.1 vs. 20 μg/ml, $p < 0.001$; 0.1 vs. 30 μg/ml, $p < 0.001$. (B) Mean cell persistence time as a function of fibronectin coating concentration for cells migrating on fibronectin-coated polystyrene. Maximum persistence time occurred at a lower fibronectin concentration when cells were in acidic pH$_e$. Asterisks indicate peak persistence times. Statistical significance of maximum persistence times at pH$_e$ 7.4: 0.1 vs. 30 μg/ml, $p<0.05$; 1 vs. 30 μg/ml, $p<0.05$. For pH$_e$ 6.5: 0.01 vs. 1 μg/ml, $p<0.001$; 0.1 vs. 1 μg/ml, $p<0.01$; 1 vs. 10 μg/ml, $p<0.05$; 1 vs. 30 μg/ml, $p<0.01$. (C) Mean cell migration speed as a function of fibronectin coating concentration for cells migrating on fibronectin-coated glass in pH$_e$ 7.4. Asterisk indicates peak migration speed. Statistical significance of maximum migration speed: 10 vs. 30 μg/ml, $p<0.01$; 30 vs. 50 μg/ml, $p<0.001$; 30 vs. 60 μg/ml, $p< 0.001$. (D) Mean cell persistence time as a function of fibronectin coating concentration for cells migrating on fibronectin-coated glass in pH$_e$ 7.4. None of the values for persistence time are statistically significantly different than any other values. For (A) and (B), at least 40 cells were analyzed for each condition. For (C) and (D), at least 50 cells were analyzed for each condition. All error bars represent SEM. 96

Figure 5.6 (A) Schematic of receptor adhesion and trafficking events that take place in our model formulation. For clarity, the cell is represented here with a separation between the top and bottom membranes; however, in the model, the cell is flat with no space between the top and bottom. Integrin receptors can diffuse within the cell membrane (a), undergo endocytosis (b), and be reinserted into the membrane (c). These events can occur for both activated and inactivated integrins, and reinsertion occurs preferentially at the leading edge of the cell. Receptors can switch between inactivated and activated conformations (e) and activated integrins can bind reversibly to ligand molecules (d) which are immobilized on an underlying substratum. (B) Schematic of the cell mechanics model used for calculation of cell displacement. The cell is divided into six compartments. Compartments #2 - #4 represent the cell body, compartment #1 is the trailing edge uropod, and compartment #6 is the leading edge lamellipod. All six compartments contain a spring and dashpot describing the intrinsic mechanical properties of the cell. The internal four cell body compartments also contain a contractile element, and the uropod and lamellipod compartments contain springs describing the adhesion bonds between the cell and substratum. Figure adapted from Ref. [95]. 97

Figure 5.7 Reproduction of results from DiMilla et al. (Ref. [95]) produced with our updated code compared to original figures. (A) Dimensionless cell velocity ν as a function of dimensionless cell-substratum adhesiveness κ from our implementation of the DiMilla et al. model. Results are shown for several values of ψ, the ratio of uropodal to lamellipodial adhesiveness. (B) Original figure adapted from Ref. [95], illustrating ν as a function of κ for several values of ψ. (C) Dimensionless cell velocity ν as a function of dimensionless cell-substratum adhesiveness κ from our implementation of the DiMilla et al. model. Results are shown for several values of R_T, the total receptor number. (D) Original figure adapted from Ref. [95], illustrating ν as a function of κ for several values of R_T. 99

Figure 5.8 Cell migration model predictions for the effect of acidic extracellular pH on cell migration velocity. Decreasing extracellular pH is modeled as increasing the integrin activation rate k_a. This corresponds to an increasing percentage of total receptors becoming activated. pH_e 7.4 is assumed to correspond to 20% activation. As pH_e decreases, the biphasic curve of cell migration speed as a function of dimensionless adhesiveness shifts to the left. The adhesiveness values corresponding to peak migration speeds for 20% and 50% activation are indicated with dashed lines. 101

Figure 5.9 Parameters in the migration model that can cause peak cell migration speed to decrease. Cell migration speed is displayed as a function of dimensionless adhesiveness κ over a range of each parameter. The direction of parameter change (increase or decrease) that causes migration speed to decrease is indicated within each plot....................................102

Figure 6.1 Extracellular pH and pO_2 gradients that have been measured in tumors and wounds. (A) Extracellular pH (open squares) and pO_2 (closed triangles) gradients measured in human tumor xenografts. Distance was measured moving away from the nearest blood vessel, with 0 μm taken as the center of the nearest vessel. Figure adapted from Ref. [8]. (B) pO_2 gradients measured in 4-day-old wounds in rats. Measurements were taken at the wound center, wound edge, and surrounding normal tissue. Shaded area represents the average pO_2 for unwounded control tissues (25 ± 5.4 mmHg, mean ± SD). Figure adapted from Ref. [23]. 109

Figure 6.2 Experimental system used to establish pH_e gradients. (A) Illustration of the Dunn chamber used to establish pH_e gradients. When the inner and outer wells are filled with solutions of different concentrations, a linear concentration gradient forms across the bridge. Figure is adapted from www.hawksley.co.uk (B) Schematic of orientation used for analysis of cell tracks. Based on the cell position at time 0, images were rotated such that the gradient was oriented vertically, with the acidic end at the top of the image, and with the initial cell position at the origin. 110

Figure 6.3 Imaging pH_e gradients using the pH-sensitive fluorophore BCECF. (A) Calibration of BCECF light intensity ratio over a pH_e range of 6.0 – 7.5. Light intensity ratio was linear with respect to pH_e in this range. (B) Linescan of BCECF light intensity ratio over the center of the Dunn chamber bridge, when both wells of the chamber were filled with solution of pH_e 7.0. The pH_e profile over the center of the bridge was flat. (C) Linescan of BCECF light intensity ratio over the center of the Dunn chamber bridge, when the inner well was filled with pH_e 7.5 solution and the outer well was filled with pH_e 6.0 solution. The pH_e gradient that formed over the center of the bridge was approximately linear and was in good agreement with the theoretical logarithmic gradient from pH_e 7.5 to pH_e 6.0 (red line). (D) Stability of the pH_e gradient at room temperature. The gradient slope at each timepoint was normalized to the slope at time 0. The slope decreased to 77% of the original value after 8 hr. Data are average values from two independent experiments. (E) Stability of the pH$_e$ gradient at 37°C. The gradient slope at each timepoint was normalized to the slope at time 0. The slope decreased to 81% of the initial original value after 8 hr. Data are average values from two independent experiments. Error bars are SEM. 111

Figure 6.4 Results for $\alpha_v\beta_3$ CHO-B2 cells migrating in a pH$_e$ gradient. For cells in the pH$_e$ gradient, the y-axis is parallel to the gradient direction and the x-axis is perpendicular to the gradient direction. Cells in the control region are not exposed to a gradient. (A) Mean y-coordinate (red line) with 95% confidence intervals (gray shaded regions) over time for $\alpha_v\beta_3$ CHO-B2 cells in the pH$_e$ gradient. The mean y-coordinate is significantly different than zero for all timepoints at which the error bars do not encompass the x-axis. Box illustrates the coordinate system used for data analysis. (B) Mean x-coordinate over time for $\alpha_v\beta_3$ CHO-B2 cells in the pH$_e$ gradient. The mean x-coordinate is not significantly different than zero at any of the timepoints. (C) Angular histogram for $\alpha_v\beta_3$ CHO-B2 cells in the pH$_e$ gradient. The distribution of angles is significantly different than a uniform distribution (Rayleigh test $p = 2.4 \times 10^{-6}$). Box illustrates calculation of angles from cell trajectories. For each 1-hr displacement, angles were calculated with respect to the horizontal. (D) Mean y-coordinate over time for $\alpha_v\beta_3$ CHO-B2 cells over the center control post. The mean y-coordinate is not significantly different than zero at any of the timepoints. (E) Mean x-coordinate over time for $\alpha_v\beta_3$ CHO-B2 cells over the center control post. The mean x-coordinate is not significantly different than zero at any of the timepoints. (F) Angular histogram for $\alpha_v\beta_3$ CHO-B2 cells over the center control post. The distribution of angles is not significantly different than a uniform distribution. (G) Percentage of $\alpha_v\beta_3$ CHO-B2 cells that attained a position with positive x- or y-coordinate at the 8-hr timepoint. After 8 hr of migration, significantly more than 50% of the cells over the bridge had a positive y-coordinate ($p < 0.0004$), but the percentage of cells with a positive x-coordinate is not significantly different than 50%. For cells over the center control post, the percentage of cells with a positive y-coordinate is not significantly different than 50%. Asterisk indicates $p < 0.0004$ with respect to 50%. (H) Percentage of $\alpha_v\beta_3$ CHO-B2 cells in the pH$_e$ gradient that attained a position with positive y-coordinate at the 8-hr timepoint as a function of cell location within the gradient. No significant dependence on position was observed. (I) Mean $\alpha_v\beta_3$ CHO-B2 cell velocity as a function of cell location within the gradient. Cells closer to the inner well (pH$_e$ 7.5) moved significantly faster than those closer to the outer well (pH$_e$ 6.0). Asterisk at location 1 indicates $p < 0.05$ with respect to locations 4 and 5. Asterisk at position 2 indicates $p < 0.05$ with respect to location 4. Gradient data are for 133 cells, and control data are for 88 cells, each pooled from 3 independent experiments. All error bars are 95% CI. 114

Figure 6.5 Results for BRECs migrating in pH$_e$ gradient. For cells in the pH$_e$ gradient, the y-axis is parallel to the gradient direction and the x-axis is perpendicular to the gradient direction. Cells in the control region are not exposed to a gradient. (A) Mean y-coordinate (red line) with 95% confidence intervals (gray shaded regions) over time for BRECs in the pH$_e$ gradient. The mean y-coordinate is significantly different than zero for all timepoints at which the error bars do not encompass the x-axis. (B) Mean x-coordinate over time for BRECs in the pH$_e$ gradient. The mean x-coordinate is not significantly different than zero at any of the timepoints. (C) Angular histogram for BRECs in the pH$_e$ gradient. The distribution of angles is significantly different than a uniform distribution (Rayleigh test p = 0.0011). (D) Mean y-coordinate over time for BRECs over the center control post. The mean y-coordinate is not significantly different than zero at any of the timepoints. (E) Mean x-coordinate over time for BRECs over the center control post. The mean x-coordinate is not significantly different than zero at any of the timepoints. (F) Angular histogram for BRECs over the center control post. The distribution of angles is not significantly different than a uniform distribution. (G) Percentage of BRECs that attained a position with positive x- or y-coordinate at the 8-hr timepoint. After 8 hr of migration, significantly more than 50% of the cells over the bridge had a positive y-coordinate, but the percentage of cells with a positive x-coordinate is not significantly different than 50%. For cells over the center control post, the percentage of cells with a positive y-coordinate is not significantly different than 50%. Asterisk indicates $p < 0.02$ with respect to 50%. (H) Percentage of BRECs in the pH$_e$ gradient that attained a position with positive y-coordinate at the 8-hr timepoint as a function of cell location within the gradient. No significant dependence on position was observed. (I) Mean BREC velocity as a function of cell location within the gradient. Cells closer to the inner well (pH$_e$ 7.5) moved significantly faster than those closer to the outer well (pH$_e$ 6.0). Asterisk at location 1 indicates $p < 0.05$ with respect to locations 2, 3, 4, and 5. Asterisk at position 2 indicates $p < 0.05$ with respect to locations 4 and 5. Gradient data are for 120 cells, and control data are for 32 cells, each pooled from 2 independent experiments. Error bars are 95% CI. 116

Figure 6.6 Results for NIH-3T3 fibroblasts migrating in a pH$_e$ gradient. For cells in the pH$_e$ gradient, the y-axis is parallel to the gradient direction and the x-axis is perpendicular to the gradient direction. Cells in the control region are not exposed to a gradient. (A) Mean y-coordinate (red line) with 95% confidence intervals (gray shaded regions) over time for NIH-3T3 fibroblasts in the pH$_e$ gradient. The mean y-coordinate is not significantly different than zero for any of the timepoints. (B) Mean x-coordinate over time for NIH-3T3 fibroblasts in the pH$_e$ gradient. The mean x-coordinate is not significantly different than zero at any of the timepoints. (C) Angular histogram for NIH-3T3 fibroblasts in the pH$_e$ gradient. The distribution of angles is not significantly different than a uniform distribution. (D) Mean y-coordinate over time for NIH-3T3 fibroblasts over the center control post. The mean y-coordinate is not significantly different than zero at any of the timepoints. (E) Mean x-coordinate over time for NIH-3T3 fibroblasts over the center control post. The mean x-coordinate is not significantly different than zero at any of the timepoints. (F) Angular histogram for NIH-3T3 fibroblasts over the center control post. The distribution of angles is not significantly different than a uniform distribution. (G) Percentage of NIH-3T3 fibroblasts that attained a position with positive x- or y-coordinate at the 8-hr timepoint. After 8 hr of migration, the percentage of cells in the gradient that had a positive y-coordinate is not significantly different from 50%. The percentage of cells with a positive x-coordinate is also not significantly different than 50%. For cells over the center control post, the percentage of cells with a positive y-coordinate is not significantly different than 50%. (H) Percentage of NIH-3T3 fibroblasts in the pH$_e$ gradient that attained a position with positive y-coordinate at the 8-hr timepoint as a function of cell location within the gradient. No significant dependence on position was observed. (I) Mean NIH-3T3 velocity as a function of cell location within the gradient. Cells closer to the inner well

(pH_e 7.5) moved significantly faster than those closer to the outer well (pH_e 6.0). Asterisk at location 1 indicates $p < 0.05$ with respect to location 3. Asterisk at position 2 indicates $p < 0.05$ with respect to location 3. Gradient data are for 147 cells, and control data are for 52 cells, each pooled from 3 independent experiments. All error bars are 95% CI....................117

Figure 6.7 Results for NIH-3T3 fibroblasts migrating in a pH_e gradient in the presence of $\alpha_5\beta_1$-blocking antibody. For cells in the pH_e gradient, the y-axis is parallel to the gradient direction and the x-axis is perpendicular to the gradient direction. (A) Phase contrast image of NIH-3T3 fibroblasts taken after ~20 hr of incubation with $\alpha_5\beta_1$-blocking antibody. Cells are predominantly adhered and spread out. (B) Phase contrast image of NIH-3T3 fibroblasts that were not exposed to $\alpha_5\beta_1$-blocking antibody. Many cells are detached, and attached cells appear to be less well spread than those in (A). (C) Mean y-coordinate (red line) with 95% confidence intervals (gray shaded regions) over time for NIH-3T3 fibroblasts with $\alpha_5\beta_1$ blocked in the pH_e gradient. The mean y-coordinate is significantly lower than zero for all timepoints after ~2.5 hr. (D) Mean x-coordinate over time for NIH-3T3 fibroblasts with $\alpha_5\beta_1$ blocked in the pH_e gradient. The mean x-coordinate is not significantly different than zero at any of the timepoints. (E) Percentage of NIH-3T3 fibroblasts with $\alpha_5\beta_1$ blocked in the pH_e gradient that attained a position with positive y-coordinate at the 8-hr timepoint as a function of cell location within the gradient. A significant dependence on position was observed, with percentage increasing for cells that are located in more acidic portions of the gradient. Asterisk at location 4 indicates $p < 0.005$ with respect to locations 1 and 2. Asterisk at location 5 indications $p < 0.005$ with respect to location 3 and $p < 0.0001$ with respect to locations 1 and 2. (E) Mean NIH-3T3 velocity as a function of cell location within the gradient. Cells closer to the inner well (pH_e 7.5) moved significantly faster than those closer to the outer well (pH_e 6.0). Asterisk at location 1 indicates $p < 0.001$ with respect to locations 4 and 5. Asterisk at position 2 indicates $p < 0.01$ with respect to location 4 and $p < 0.05$ with respect to location 5. Asterisk as location 3 indicates $p < 0.05$ with respect to location 4. Gradient data are for 125 cells pooled from 2 independent experiments. All error bars are 95% CI....................119

Figure 6.8 Schematic depiction of the three possible mechanisms underlying the shift in mean cell position toward acid over time. The blue end of the gradient is pH_e 7.5 and the red end is pH_e 6.0. Arrows indicate the magnitude of cell velocity, with larger arrows indicating higher speed. The direction of the arrows indicates the direction of the leading edge (i.e., the direction of polarization). Cell movement is restricted to one dimension for simplicity. (A) Cells polarize preferentially toward acid, but cell velocity does not depend on polarization direction or position within gradient. (B) Cell velocity is higher for cells polarized toward acid, but velocity is independent of the position within the gradient. In this scenario, cells polarize equally in both directions. (C) Cell velocity depends on the position within the gradient, decreasing for cells in more acidic positions. However, cell velocity does not depend on polarization direction, and cells polarize equally in both directions. 122

Figure 6.9 Mean cell displacements (over a 1-hr period) for cells polarized away from acid compared to cells polarized toward acid. Data are normalized to the values for cells polarized away from acid. Our cell migration model predicts that mean displacement toward acid will be greater than that away from acid (left bars), assuming that cells are equally positioned throughout the gradient. Our experimental data for $\alpha_v\beta_3$ CHO-B2 cells show that the mean displacement toward acid is greater than the mean displacement away from acid, but this difference is not statistically significant (middle bars). Measurements for BRECs show that the mean displacement toward acid is significantly greater than the mean displacement away from acid (right bars). Asterisk indicates p = 0.0084. Error bars are SEM. 123

Figure 6.10 (A) Percentage of cells orienting toward acid as a function of position within the gradient, for various values of k_f, with T = 5 min and N^* = 30. (B) Percentage of cells orienting toward acid as a function of position within the gradient, for various values of N^*, with T = 5 min and $k_f = 3 \times 10^{10}$ M^{-1}min^{-1}. (C) Percentage of cells orienting toward acid as a function of position within the gradient, for various values of T, with $k_f = 3 \times 10^{10}$ M^{-1}min^{-1} and N^* = 30. (D) Top: reproduction of Figure 6.4H. Percentage of $\alpha_v\beta_3$ CHO-B2 cells in the pH_e gradient that attained a position with positive y-coordinate at the 8-hr timepoint as a function of cell location within the gradient. Bottom: reproduction of Figure 6.5H. Percentage of BRECs in the pH_e gradient that attained a position with positive y-coordinate at the 8-hr timepoint as a function of cell location within the gradient. 126

Figure 6.11 Schematic of how an extracellular pH gradient could direct cell migration toward regions of insufficient or damaged vasculature. 129

Figure 6.12 Percentage of cells orienting toward acid as a function of position within the indicated gradients, with $k_f = 3 \times 10^{10}$ M^{-1}min^{-1}, T = 5 min, and N^* = 30. All gradients are over 1 mm distance. 130

Figure 7.1 Schematic diagram illustrating major thesis results in a cue-signal-response framework. Acidic extracellular pH is a chemical cue found in several physiological contexts. The major effect of acidic pH_e uncovered in this thesis is activation of integrin $\alpha_v\beta_3$, which acts as a signal mediating several subcellular- and cellular-scale responses. For some responses, we have shown that activation of $\alpha_v\beta_3$ is sufficient to cause the observed effects, and these connections are indicated with black solid arrows. Gray solid arrows indicate subcellular- and cellular-scale responses that we speculate are direct downstream effects of increased integrin activation in acidic pH_e. Gray dashed arrows indicate places where subcellular-scale responses may possibly contribute to the observed cellular-scale responses. Dashed black arrows indicate responses to acidic pH_e that we cannot directly attribute to increased integrin activation at this time 135

Figure 7.2 Schematic illustration of pH_e gradients in tumors and wounds, and the effect such gradients have on endothelial cell migration. (A) In the tumor context, pH_e gradients form at the interfaces between tumor cells (gray) and normal tissue (peach), as well as at insufficiently vascularized regions within tumors. Red represents the more acidic part of the gradient, while blue represents extracellular pH close to 7.4. (B) It is likely that pH_e gradients exist at wound sites, due to anaerobic cellular metabolism in the hypoxic environment resulting from damaged vasculature. (C) Our data show that endothelial cells preferentially migrate toward the acidic part of a pH_e gradient, likely due to increased integrin activation and membrane protrusion stabilization in acid. 140

Figure 7.3 Schematic depiction of the possible role of NHE1 in integrin activation during cell migration. NHE1 localizes to the leading edge of migrating cells and extrudes hydrogen ions proximal to integrin receptors. The locally acidified environment caused by NHE1 activity may activate integrins preferentially at the leading edge, thus creating an asymmetry in cell-surface adhesiveness. 141

List of tables

Table 1.1 Summary of previous work investigating the effects of acidic extracellular pH on cell adhesion and migration. 27

Table 2.1 Residues with elevated pK_a values as predicted by MCCE. GLUα123, ASPβ217, and HISβ244 were protonated in both the normal and acidic pH_e systems. HISα91, ASPα186, ASPβ127, and HISβ274 were protonated in the acidic system only. Table from Ref. [85] 50

Table 2.2 Parameters from best fit lines and application of a modified Bell-Evans model [139]. Errors are SEM and were obtained by a bootstrapping sampling method (slope and intercept) and error propagation (x_b and k_{off}). 60

Table 4.1 Average protrusion lifetime and velocity data for all experimental conditions shown in Figure 4.5. Asterisks indicate statistically significant differences compared to the pH_e 7.4 condition with that experimental pair. $^{**}p \leq 0.0001$, $^{*}p < 0.05$ 80

Table 5.1 Summary of parameter changes that cause peak migration speed to decrease in the cell migration model. Most of these parameters can be measured experimentally, and results indicate that none of these parameters were altered in acidic pH_e in a manner that is consistent with a decrease in peak migration speed. 103

Table 6.1 Parameter values used for calculation of cell orientation percentages in a pH_e gradient. 125

Table 8.1 Manufacturers and catalog numbers for the reagents used in this thesis work. 144

Table 8.2 Modified equations for the first part of the cell migration model. 159

Table 8.3 Modified equations for the second part of the cell migration model. 160

Table 8.4 Parameters used for data generation with the modified DiMilla et al. cell migration model. 160

Chapter 1: Background and motivation

1.1. Introduction

Tissue cells are extraordinarily dynamic and have the ability to detect and respond to myriad chemical and mechanical cues in the extracellular environment. How are diverse extracellular signals sensed and translated into changes in cellular behaviors? This is a broad question that requires understanding at multiple length scales, as complex cellular processes such as cell migration or proliferation require the integration of several subcellular systems and can be critically influenced by molecular parameters. Furthermore, this question involves the coupling between chemistry and mechanics, which are intricately linked in the cellular systems context. Chemical and mechanical cues in the extracellular environment may regulate the processes of cell-matrix adhesion, cellular force transmission, chemical signaling, and more.

In this thesis, this complex chemomechanical problem is reduced to focus on a single chemical cue – extracellular pH – and its effect on the fundamental interaction event at the cell-matrix interface: the binding between integrin receptors and matrix ligands. This binding creates a physical connection between cells and the extracellular environment that is capable of transmitting both mechanical forces and chemical signals. Thus, integrins serve as a hub to convert chemomechanical cues into cellular responses. Utilizing a range of experimental and computational approaches, this thesis lends insight into how pH-induced structural changes at the atomistic and molecular level translate into functional responses at the cellular scale. This chapter summarizes the current state of knowledge regarding acidic extracellular pH in physiological and pathological contexts, effects of acidic extracellular pH on cell responses in vitro, and the molecular receptors and ligands at the cell-matrix interface.

1.2. Acidic extracellular pH (pH_e)

Acidic pH is a characteristic of the extracellular environment that can be found in multiple physiological contexts relevant to disease states as well as normal cell functions. In this section, we will discuss the acidic extracellular pH (pH_e) conditions that are characteristic of tumor and wound sites, as well as the role of the Na^+/H^+ ion exchanger NHE1 in creating locally acidified extracellular environments around healthy cells. We will also review several studies that have examined the effects of acidic pH_e on cell adhesion and migration.

1.2.1. Tumor environment

It is well documented that the average extracellular pH in the tumor environment is often significantly more acidic than in normal tissue environments [1-7] (Figure 1.1). There are two main causes of this acidosis. First, tumors characteristically contain regions of damaged or irregular vasculature, resulting in a hypoxic microenvironment. For example, measurements of the partial pressure of oxygen (pO_2) for human colon adenocarcinoma tumors grown in mice showed that pO_2 in tumors was less than 15 mmHg, compared to

~30 mmHg for normal tissue [1]. Cells in such regions tend to undergo anaerobic metabolism of glucose to pyruvate, which is converted to lactic acid via fermentation [2]. Second, alterations in gene expression cause cancer cells to increase reliance on anaerobic metabolism even in regions with sufficient oxygen, a phenomenon known as the Warburg effect [2-5]. As glycolysis is an inefficient means of ATP production, cancer cells must increase the rate of glucose consumption and metabolism in order to maintain sufficient energy levels, which accelerates acid production [6]. This intracellularly generated acid is pumped into the extracellular space by ion exchangers such as the Na^+/H^+ exchanger NHE1. NHE1 extrudes an intracellular H^+ ion in exchange for an extracellular Na^+ ion, and displays upregulated activity in cancer cells and oncogenically transformed cells [7-10]. Thus, intracellular pH (pH_i) is maintained at ~7.1 – 7.3 [2, 11-14], comparable to pH_i in normal cells, while extracellular pH becomes acidic.

Many studies have measured extracellular pH for both human and animal tumors, with a variety of methods including pH electrode measurements [12, 15-17], magnetic resonance spectroscopy [14], and fluorescence ratio imaging [6, 18]. From these reports, mean measurements of pH_e in the tumor environment varied between 6.25 – 7.29, and mean measurements for pH_e for normal tissue varied between 7.0 – 7.65 (Figure 1.1) [6, 12, 14-18]. Three studies also published the range of individual pH_e measurements in addition to the mean values. For tumors, individual pH_e measurements ranged as low as 5.44, while individual measurements for normal tissues did not range below 6.95 [15-17]. The locations of these individual measurements in relation to cells or blood vessels are not known. Although there is large variation in measured pH_e values, it is clear that on average, tumor extracellular pH is lowered compared to normal tissue.

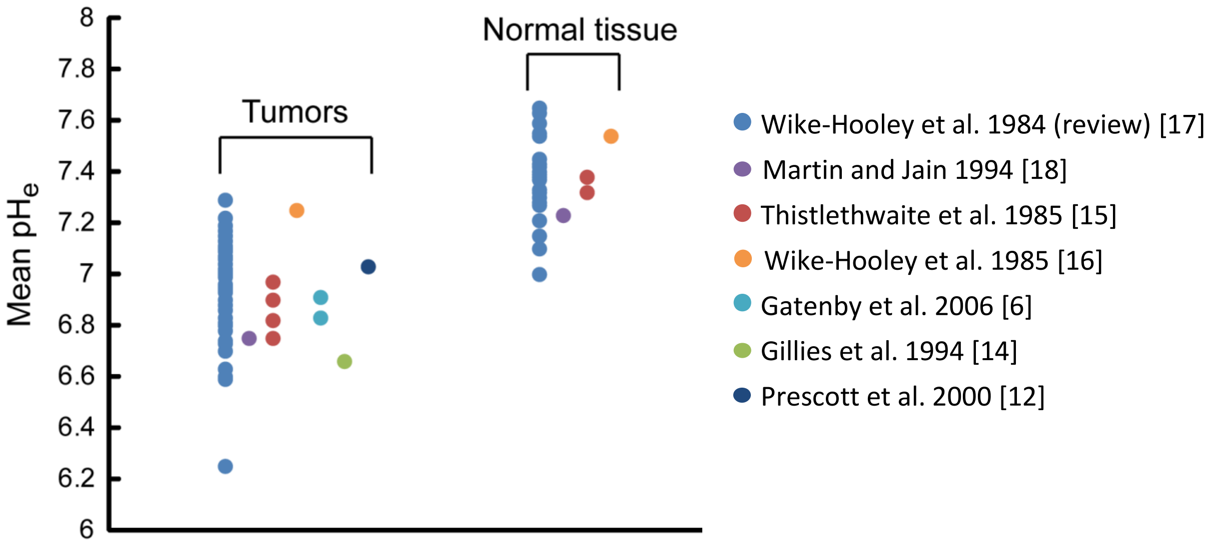

Figure 1.1 Mean extracellular pH values measured in tumors and normal tissue. Midrange pH_e is used in cases where mean is not given. Individual pH_e measurements are not plotted here. Data from the review by Wike-Hooley et al. 1984 [17] include measurements from many investigators. In general, average extracellular pH in tumors is lower than that in normal tissue.

High resolution methods for measuring pH have shown significant spatial variations in pH profiles in tumors [1, 6, 18]. In particular, pH gradients exist within tumors, with pH decreasing about 0.6 units (~4-fold increase in H^+ concentration) over a distance of about 350 μm from blood vessels in the case of human colon adenocarcinoma xenografts grown in mice [1]. In another study, pH decreased about 0.15 units (~1.4-fold increase in H^+ concentration) over a distance of 50 μm from microvessels in human VX2 carcinoma tumors grown in rabbit ear chambers [18]. Furthermore, for tumors grown from PC3N human prostate cancer cells implanted into mice, clear pH gradients have been measured at the interfaces between tumors and normal tissue, with pH increasing toward the normal tissue. Gradients in pH that were measured for several radial directions from the center of a given tumor were found to be quite uniform for newer, more avascular tumors. However, after tumor growth and vascularization, gradients in different radial directions exhibited more spatial heterogeneity [6].

1.2.2. Wound environment

Wound healing is a complex process that involves many different cell types. The first stage of wound healing is hemostasis, which begins immediately after injury. Tissue injury causes damage to vasculature, and resulting exposure of collagen and other ECM components to blood causes platelet activation and initiates the coagulation cascade. This leads to the formation of a fibrin clot, which provides a provisional ECM for cell migration that includes proteins such as fibronectin. The next stage is inflammation (1 – 7 days post-injury), during which chemotactic factors attract neutrophils and then macrophages to the wound site to clean the area of bacteria and debris. This is followed by the proliferative phase (4 – 14 days post-injury) in which fibroblasts migrate into the wound site and begin to create a new matrix consisting largely of collagen. Angiogenesis also begins during this stage as vascular endothelial cells migrate on the provisional matrix into the wound site and begin formation of new blood vessels. Finally, during the maturation and remodeling phase (1 week – several months post-injury), more collagen is synthesized and remodeled by myofibroblast contraction [19-22].

Due to the disruption in vasculature and tissue oxygenation, wound environments become hypoxic. For example, one study showed that pO_2 in wound centers was less than 10 mmHg, compared to ~25 mmHg for uninjured tissue [23]. Extracellular pH becomes acidic in this environment by the same mechanism as in tumors: cells undergo anaerobic metabolism, leading to lactic acid production [24]. In acute wound healing, pH_e begins to drop at 2-10 days post-injury [25-27], and average values for extracellular pH in these early stage wounds range from 5.7 – 6.9 [24, 25]. This coincides with the period in which macrophages, fibroblasts, and endothelial cells enter wound sites [19, 20]. Furthermore, the presence of oxygen gradients at wound sites implies that pH_e gradients occur in these environments as well, although pH_e gradients have not been directly measured [23, 26, 28].

1.2.3. NHE1 and local acidification of the cell microenvironment

The relevance of acidic extracellular pH is not limited to the cancerous and wounded tissue environments discussed above. Cells in healthy tissues can also experience locally acidified extracellular environments due to the action of the NHE1 ion exchanger. As mentioned previously, NHE1 extrudes a hydrogen ion in exchange for a sodium ion, and this proton pump activity is important in regulating intracellular pH, especially for cells undergoing glycolysis at high rates. NHE1 is ubiquitously expressed, and its ion exchange activity is critically involved in cell migration [29-31]. It is important to note that NHE1 can also affect cell migration by mechanisms distinct from its ion exchange activity. For example, NHE1 is linked to the actin cytoskeleton via association with actin binding proteins and can regulate cytoskeletal assembly and cell shape [32].

Interestingly, it has been shown that NHE1 localizes to adhesion sites [30, 33], indicating that it can selectively acidify the extracellular environment proximal to transmembrane integrin receptors. This could explain the observation that pH_e at the adhered surface of MCF7 breast cancer cells was lower than that at the free surface, reaching a value of ~5.5 [34]. Furthermore, in motile cells, NHE1 localizes to leading edge membrane protrusions such as lamellipodia [31, 35] and pseudopodia [36]. This leading edge localization can create a pH_e gradient at the single cell level; for human melanoma cells, extracellular pH at the leading edge was approximately 0.2 units lower than the pH_e at the trailing edge, and it has been demonstrated that localized cell-surface pH_e gradients can exist even when the bulk pH_e is acidic [37, 38]. Although similar studies have not been conducted for other cell types, it is possible that extracellular pH gradients caused by NHE1 polarization could be present at the surfaces of noncancerous cells as well. However, the gradient slope may differ depending on the amount of NHE1 activity for each cell type.

1.3. Cell adhesion and migration in acidic extracellular pH

It has been well established in the literature that acidic extracellular pH can strongly affect a wide range of molecular and cellular processes. This section will focus on several studies that directly investigated the effects of pH_e on cellular-scale adhesion and migration (Table 1.1). These cellular processes are of particular interest due to their critical roles in cancer progression, metastasis and wound healing.

Serrano et al. demonstrated that adhesion between neutrophils and endothelial cells increased when the extracellular environment was acidified to pH 6.52. Although neutrophil β_2 integrin receptor expression increased in acidic conditions, expression of the endothelial cell ligand ICAM-1 concurrently decreased. Therefore, the strengthened neutrophil-endothelial cell adhesion that was observed in this study is unlikely to be due to changes in receptor expression alone. The authors also note that intracellular pH may have decreased slightly in their experiments, but do not address the role that this might be mediating the observed responses [39].

Stock et al. showed that human melanoma cells had more lamellipodia and exhibited a more spread morphology as extracellular pH was lowered to 6.6. In addition, the number of adherent cells on collagen-coated surfaces increased, and cells embedded in collagen matrices induced greater matrix deformations at acidic pH_e, indicating that cell adhesion was generally enhanced in this condition. Furthermore, melanoma cell migration speed on two-dimensional substrata or in three-dimensional collagen gels showed a biphasic dependence on pH_e, with a maximum at pH_e 7.0 and pH_e 7.18 for 2-D and 3-D migration, respectively [29]. In this case, changing extracellular pH did not affect the level of integrin expression. Although intracellular pH did decrease in these experiments, the authors argue that this cannot fully account for the observed effects.

In a study by Rofstad et al., human melanoma cells cultured in a media bath at pH_e 6.8 displayed enhanced invasiveness in a Matrigel invasion assay, compared to cells cultured at pH_e 7.4. Secretion of pro-angiogenic factors and proteinases was also increased in response to acidic extracellular pH [40]. Similarly, Kato et al. showed that mouse metastatic melanoma cells displayed increased migration through collagen-coated filters and increased gelatinase secretion at pH_e 6.1, compared to cells at pH_e 7.3. Cells cultured at pH_e 4.7 or pH_e 5.9 also became longer and more spread than cells cultured at pH_e 7.3. [41]. In these two studies, it is unclear if acidic extracellular pH had other effects beyond promoting protease secretion that contributed to the observed enhancement of invasiveness and migration.

Study	**Cell types**	**pH_e**	**Effects of acidic pH_e**
Serrano et al. 1996 [39]	Human aortic endothelial cells (HAECs); human neutrophils	6.52 vs. 7.4	Increased HAEC-neutrophil adhesion; increased β2 integrin expression; decreased ICAM-1 expression
Stock et al. 2005 [29]	Human melanoma cells (MV3 line)	6.6 – 7.5	More lamellipodia, enhanced spreading and adhesion, biphasic migration speed vs. pH_e
Rofstad et al. 2006 [40]	Human melanoma cells (A-07, D-12, T-22 lines)	6.8 vs. 7.4	Increased invasiveness, increased secretion of proteinases and pro-angiogenic factors
Kato et al. 1992 [41]	Mouse metastatic melanoma cells (B16-F10 line)	4.7 – 7.3	Increased migration, increased gelatinase secretion, larger and longer cells
Glunde et al. 2003 [42]	Human breast cancer cells (MDA-MB-231 and MDA-MB-435 lines)	6.4 – 7.4	More filopodia, increased filopodial length
Faff and Nolte 2000 [43]	Mouse microglial cells	6.0 vs. 7.4	Stress fiber formation, reduction in motility

Table 1.1 Summary of previous work investigating the effects of acidic extracellular pH on cell adhesion and migration.

Glunde et al. demonstrated that for human breast cancer cells, the number and length of filopodia increased at pH_e 6.4 and pH_e 6.8 relative to pH_e 7.4. The authors did not propose a mechanism for this effect and did not explore the consequences of these filopodial changes for cell migration [42]. Finally, Faff and Nolte showed that for mouse microglial cells, exposure to pH 6.0 led to cytoskeletal rearrangement and stress fiber formation, as well as a reduction in cell motility. Intracellular pH decreased in these experiments, and this intracellular acidification was at least partially responsible for these effects. It is unclear if acidic extracellular pH had a direct regulatory role in addition to leading to decreased pH_i [43].

These studies clearly demonstrate that acidic extracellular pH can have profound effects on adhesion and migration for several different cell types. However, the molecular mechanisms that transmit information about pH_e and cause the reported changes to physiologically relevant cellular parameters have not been adequately characterized, and remain open for investigation. To begin to form hypotheses about possible underlying mechanisms, we will now turn our focus toward fundamental molecular binding events at the cell-matrix interface that are critical for cell adhesion and migration processes.

1.4. Integrins

The complex cellular-scale adhesion and migration processes that were the focus of the studies described above depend on molecular-scale binding events between cell surface integrin receptors and extracellular matrix (ECM) ligand molecules (Figure 1.2A). In this section, we will review current knowledge pertaining to the structure and function of the important integrin family of proteins.

1.4.1. General background

Integrins are heterodimeric transmembrane receptors, each consisting of an α and β subunit. Currently, there are 18 known α subunits and 8 β subunits which can combine to form 24 known integrin dimers. Integrins can bind to a variety of ligands in the ECM, with each integrin having particular ligand specificities [44]. ECM ligands include collagen, fibronectin, laminin, vitronectin, fibrinogen, osteopontin, and more. Several ECM ligands, including fibronectin and vitronectin, contain the common ARG-GLY-ASP (RGD) sequence, and the acidic ASP residue is especially important for integrin binding [44-47]. In general, integrin-ligand binding is critical for stabilization of membrane protrusions [48, 49], cell spreading [50, 51], and cell migration [52, 53]. Integrins can also undergo internalization, recycling into the plasma membrane, lateral diffusion within the membrane, and clustering at specific adhesion sites to the adjacent ECM [54-60].

Integrin-ligand binding initiates the intracellular formation of large multi-protein assemblies that are believed to contain >50 different molecular components [61]. The macromolecular complexes made up of integrin clusters and associated cytoplasmic proteins can be subdivided into different classes, depending on their size, stability, and molecular constituents [62, 63]. These molecular assemblies at adhesion sites include proteins that play structural roles in linking integrins to the actin cytoskeleton and stabilizing the physical connection at the cell-matrix interface, such as vinculin and talin. Talin can bind the integrin β tail and actin, as well as other molecules, and vinculin has binding sites for several proteins, including talin and actin (Figure 1.2A) [64-67]. As a result of their physical engagement of the cytoskeleton, integrins can transmit actomyosin-generated forces against the ECM. In addition to their structural and mechanical role in connecting the ECM to the cytoskeleton, integrins interact with many signaling proteins that regulate a variety of cellular processes [68, 69]. Because of their position connecting the cell to the ECM, integrins are capable of transmitting chemical and mechanical information about the extracellular environment into the cell, and vice versa.

1.4.2. Integrin structure

Integrin α subunits are 150 – 180 kDa (>950 amino acids) and β subunits are ~90 kDa (>690 amino acids). Each subunit consists of a transmembrane domain and short cytoplasmic domain, in addition to several extracellular domains (Figure 1.2B). Extracellular domains in integrin α subunits include the β-propeller, thigh domain, and two calf domains. The β-propeller domain is part of the integrin headpiece and consists of seven repeats of a four-stranded β sheet. This domain contains four metal ion binding sites [70]. Nine integrin α subunits also contain a ~200 amino acid von Willebrand factor type A domain, also called the inserted (I) domain, which is located within the β-propeller domain and contains a metal ion binding site called the Metal Ion Dependent Adhesion Site (MIDAS). This divalent cation at this site is a critical part of the ligand-binding site for integrins containing this domain and coordinates an acidic amino acid residue in ligands, such as the aspartate residue in the RGD binding sequence. Integrin subunits that contain the I domain are α1, α2, α10, α11, αL, αM, αX, αD, and αE [70-75]. The remaining α subunit domains are the thigh and calf domains, which all have β sheet structures, and one more metal ion binding site is located at the interface between the thigh domain and the first calf domain [70].

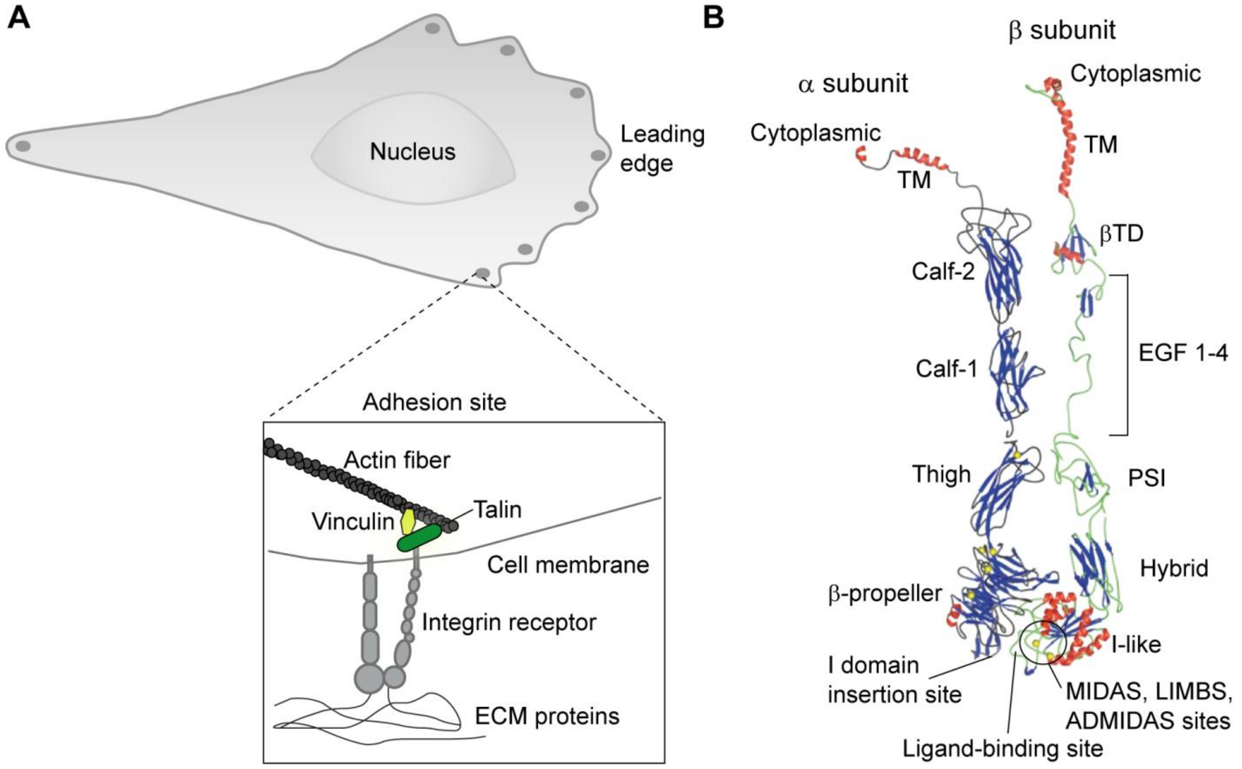

Figure 1.2 (A) Schematic of a spread cell with adhesion sites represented by grey dots. Magnification illustrates an integrin receptor within the adhesion site with its extracellular domain bound to an ECM protein. On the cytoplasmic side, talin (green) links the integrin β tail to actin, and vinculin (yellow) cross-links talin and actin. (B) Integrin structure and subunit domains, adapted from Ref. [76]. β sheets are depicted in blue, α helices are in red, and metal ions in yellow.

The headpiece domains of the integrin β subunit include the hybrid and I-like domains. The hybrid domain has a β sheet structure, and the I-like domain (also called the βA domain) is inserted into the hybrid domain and consists of six β strands surrounded by seven α helices. The I-like domain is very similar in structure to the I domain found in some integrin α subunits and also contains the MIDAS site. This domain includes two additional metal ion binding sites, the Ligand-Associated Metal Binding Site (LIMBS), and the Adjacent to MIDAS (ADMIDAS) [45, 70, 77]. These sites can be occupied by various divalent cations, such as Ca^{2+}, Mg^{2+}, and Mn^{2+}, and each of these sites has a distinct and important role in regulating of integrin-ligand binding [73, 78, 79]. For integrins lacking the I domain, the ligand binding site is located at the interface between the β-propeller and I-like domains in the integrin headpiece, and the divalent cation at the MIDAS site coordinates an acidic amino acid in the ligand. The other extracellular β subunit domains include a PSI (plexins, semaphorins, and integrins) domain, four cysteine-rich epidermal growth factor (EGF)-like domains, and a β sheet tail domain [70].

1.4.3. Integrin activation

Integrins undergo large-scale conformational changes in order to attain a high-affinity conformation during the process of integrin activation. Integrin activation before ligand binding is referred to as “priming” [72]. Integrins are currently understood to exist in equilibrium between three main conformational states (Figure 1.3). In the low-affinity, inactivated conformation, the integrin extracellular leg domains are bent with the headpiece positioned close to the leg domains near the cell membrane. The headpiece is closed, with an acute angle between the I-like and hybrid domains. In this conformation, the ligand binding site is directed toward the cell membrane, which reduces accessibility to ECM ligands. This conformation generally exhibits little to no binding to biological ligands [80-83], but is capable of binding small RGD peptides in solution [45]. In the high-affinity, activated conformation, the leg domains are extended and the α and β tails are separated. Extension of the leg domains increases the integrin length by about ~130 Å [70]. In addition, the headpiece is open, with an obtuse angle between the I-like and hybrid domains. The headpiece angle in this conformation is increased by ~80° compared to the low-affinity conformation [72, 80], which corresponds to an increase in distance between the β-propeller and hybrid domains of ~1.8 nm. The third conformation, with extended legs and a closed headpiece, is expected to be of intermediate affinity [80]. These three conformational states are predicted to occur in all integrins, including those that contain the I domain [71, 76]. The fourth possible conformation, with bent leg domains and an open headpiece, is neglected here, as headpiece opening destabilizes the headpiece-tailpiece interface, which results in extension and separation of the leg domains and adoption of the high-affinity extended-open conformation [80, 82].

It has been suggested that these structural rearrangements result in increased binding affinity by changing the position of the MIDAS site in the binding cleft such that the divalent cation at this site becomes more accessible for coordination by an acidic residue in the ECM ligand. For integrins without the I domain, it is predicted that hybrid domain movement during headpiece opening pulls down the carboxy-terminal α7 helix of the I-like domain and shifts the position of the loop connecting the α7 helix and β6 strand, which is tightly coupled to rearrangement of the MIDAS site [72, 74, 80, 82, 84] (Figure 1.4A). In this manner, global conformational changes are linked to local rearrangements of the binding pocket and consequent changes in binding affinity. For integrins with the I domain, these conformational changes result in binding of the I-like MIDAS ion to a linker at the bottom of the α7 helix of the I domain. This pulls down the I domain α7 helix and alters the position of the I domain MIDAS site, making it more favorable for ligand binding [72] (Figure 1.4B).

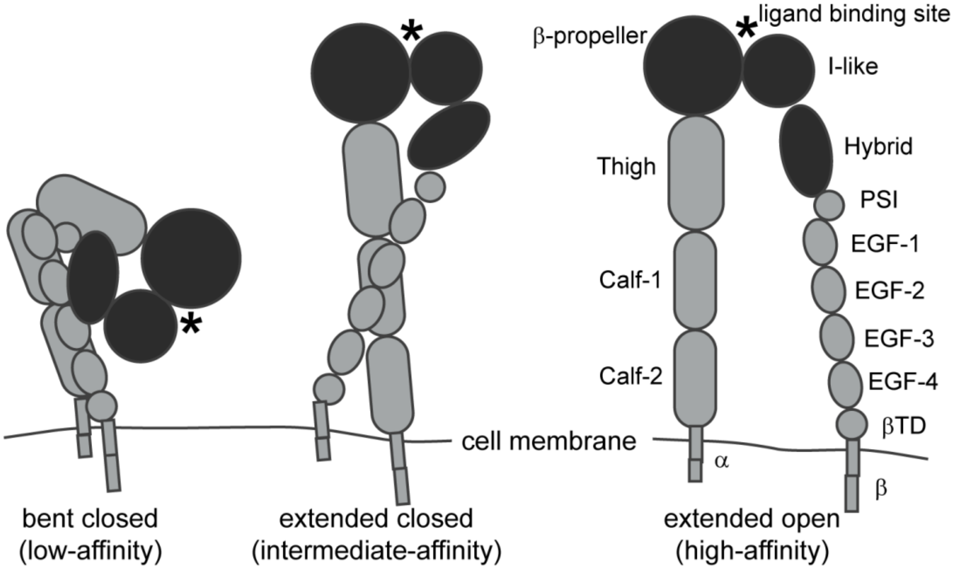

Figure 1.3 Integrins exhibit three distinct conformations with varying binding affinities. Headpiece domains are depicted in black. These headpiece domains were analyzed computationally in the atomistic simulations that will be discussed in Chapter 2. In the low-affinity conformation, the integrin leg domains are bent and the headpiece is closed. In the intermediate-affinity conformation, the leg domains are extended and the headpiece is closed. In the high-affinity conformation, the leg domains are extended, and the headpiece is open. Figure from Ref. [85].

Integrin activation can be regulated by signals from the extracellular ("outside-in activation") or intracellular ("inside-out activation") environments. In the process of outside-in activation, the headpiece-tailpiece interface is destabilized by the opening of the headpiece hinge. This is followed by extension of the leg domains and separation of the intracellular tail domains, resulting in adoption of the extended open conformation [80, 82]. Outside-in activation can be regulated by different divalent cations; for example, Mn^{2+} promotes activation while Ca^{2+} stabilizes the low affinity conformation [73, 78, 80, 86-88]. In addition, integrins can be activated by ligand binding [80], binding of certain antibodies [89], and fluid shear stress [90]. During inside-out activation, the intracellular α and β tails separate first, followed by extension of the leg domains. Once in the extended state, the integrin headpiece can remain in the closed form, or the headpiece can open to the fully activated state [80]. Inside-out activation is regulated by signals from within the cell, such as talin binding to the integrin cytoplasmic domain [81, 83]. Furthermore, molecular simulations suggest that both extracellular and intracellular mechanical force can regulate integrin activation [91].

Proper regulation of integrin affinity is essential for a variety of cell behaviors. For example, platelet adhesion to fibrinogen, von Willebrand factor, and fibronectin during the initial stages of wound healing depends on activation of integrin $\alpha_{IIb}\beta_3$. Correct regulation of integrin activation ensures that platelets in circulation can adhere to wounded vessels but do not adhere in areas where they are not needed [44, 92, 93]. Integrin activation regulation is also critical to adhesion and recruitment of leukocytes to sites of inflammation, especially to controlling the transition from rolling to firm adhesion [78, 94]. For migrating cells, integrin affinity regulation can enable cells to adjust their migration speed in response to diverse chemical and mechanical cues [52, 95, 96], and can thus impact complex processes such as tissue development, angiogenesis, tumor metastasis, and wound healing. For example, integrin activation is required for tumor cell arrest in the circulation during metastasis [97]. The impact that dysregulated integrin activation can have on disease progression has been clearly demonstrated in the cancer context, as human breast carcinoma cells expressing a constitutively active mutant of integrin $\alpha_v\beta_3$ display enhanced metastatic activity in a mouse model [98].

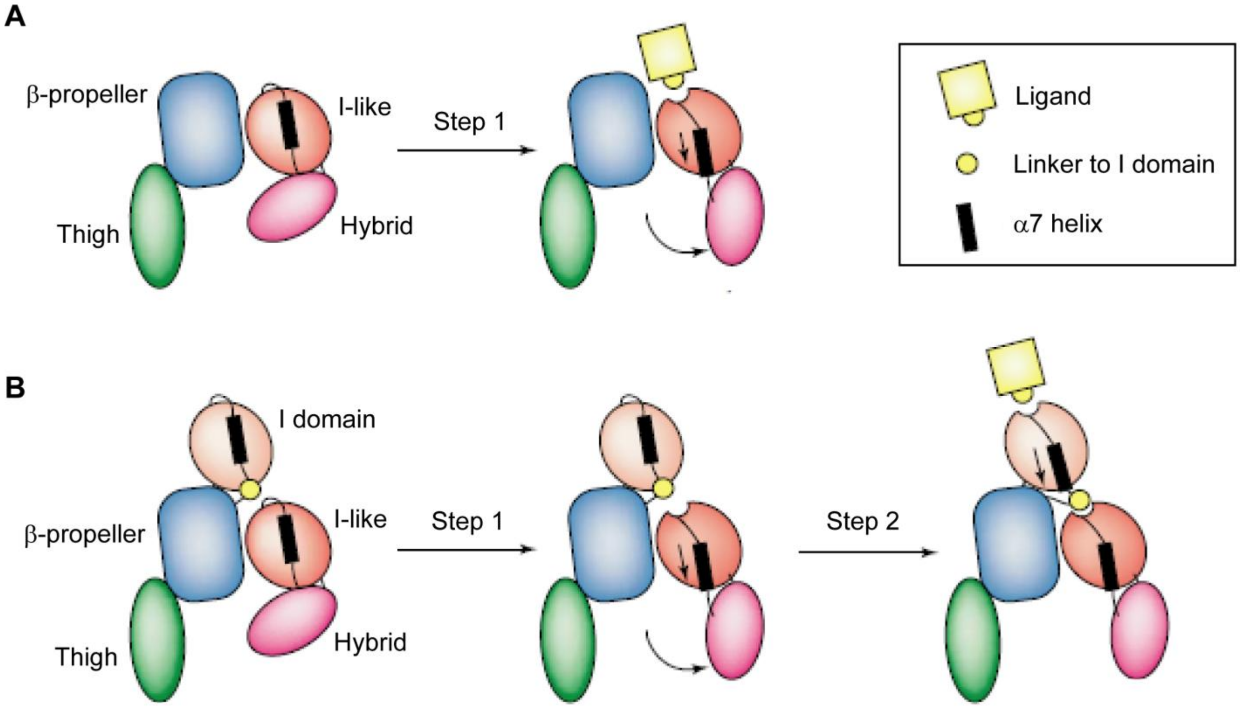

Figure 1.4 Model of how large scale conformational changes in the integrin headpiece alter binding affinity. (A) For integrins without the I domain, hybrid domain movement during headpiece opening pulls down the α7 helix of the I-like domain, which changes the position of the MIDAS site, making the MIDAS ion more accessible for coordination by ligand. (B) For integrins with an I domain, the same conformational changes occur (Step 1), but the I-like domain MIDAS ion binds a linker which pulls down the I domain α7 helix and makes the I domain MIDAS ion more available for ligand binding (Step 2). Figure adapted from Ref. [72].

1.4.4. Integrin signaling

The multi-protein assemblies that form at sites of integrin-ligand asssociation can interact with a wide array of signaling molecules. Thus, integrin-ligand binding can trigger and modulate a diverse array of chemical signaling pathways that affect cell processes such as gene expression, proliferation, cell cycle progression, cytoskeletal remodeling, and cell migration. One of the key signaling proteins that co-localizes with integrins is focal adhesion kinase (FAK), which becomes phosphorylated upon integrin ligation and clustering [99, 100]. Via association with other signaling molecules, phosphorylated FAK regulates a variety of downstream pathways, including the mitogen-activated protein kinase (MAPK) cascade and the Rho GTPase pathway [69, 99-101].

Some integrins also associate with transmembrane growth factor receptors, such as platelet-derived growth factor receptor (PDGFR), vascular endothelial growth factor receptor (VEGFR), and epidermal growth factor receptor (EGFR) [69, 101-103]. Integrin clustering can regulate growth factor signaling by bringing growth factor receptors into closer proximity and enabling their activation, and crosstalk between integrins and growth factor receptors can regulate several downstream processes such as cell survival and proliferation [69, 101-103]. Furthermore, dysregulated signaling between integrins and growth factor receptors has been postulated to contribute to tumor progression and metastasis via perturbations in pathways regulating migration and cell survival [68].

This discussion highlights a small fraction of the many important signaling proteins that co-localize with integrins at adhesion sites. Although this thesis will primarily focus on the biophysical aspects of cell-matrix binding, it is important to recognize the important role that integrins play in modulating chemical signaling pathways to regulate downstream cell fate decisions, particularly in localizing signals to areas of cell-matrix contact, and transferring chemomechanical information from the ECM into the intracellular space.

1.4.5. Tools and techniques for studying integrins

A wide variety of experimental and computational methods have been used in the literature to study integrin expression, ligand binding affinities, and conformations. Cell surface integrin expression can be assessed with approaches such as fluorescent labeling and imaging of receptors on adhered cells, flow cytometry analysis of detached cells, or immunoprecipitation and Western blotting of integrin receptors [104]. Quantification of the number of receptors per cell can be achieved with saturation radioligand binding experiments, which also enable measurement of the equilibrium receptor-ligand dissociation constant K_D [104, 105]. Binding of radiolabeled ligands to cell surface integrins can be monitored at different timepoints to measure the kinetic binding and unbinding rates k_{on} and k_{off} [105], and surface plasmon resonance can be used to measure these parameters for purified integrins [80, 81]. In addition to these population-average approaches, atomic force microscope-enabled molecular force spectroscopy is a technique that can be used to measure integrin-ligand rupture forces on the single molecule level, and such rupture force data can be used to calculate k_{off} [106, 107].

Solved crystal structures of integrin domains have allowed detailed characterization of integrin conformational states and intramolecular interactions [45, 70, 74, 91, 108]. The first structure of a complete integrin extracellular region was solved in 2001 for integrin

$\alpha_v\beta_3$ and was followed in 2002 by a structure for this integrin in the ligand-bound state [45, 70]. These two crystal structures provided a great deal of insight into the configurational details of integrin domains and the role of metal ions in ligand binding. Integrin conformations can be also directly imaged with electron microscopy of purified receptors. This technique was essential to the groundbreaking study by Takagi et al. in 2002 that characterized the large-scale conformational changes involved in integrin $\alpha_v\beta_3$ activation [80, 81]. Integrin activation states can be further assessed with conformation-specific antibodies that bind to epitopes that are only exposed on activated integrins [82, 87, 109].

In addition to these experimental methods, computational molecular dynamics (MD) simulation techniques have been used to study integrin conformations and integrin-ligand interactions with atomistic resolution [46, 91, 110-113]. For example, Jin et al. used MD simulations to study the transitions between different conformation of integrin I domains [113], and Puklin-Faucher et al. employed MD simulations to investigate how conformational changes are propagated during $\alpha_v\beta_3$ headpiece opening [110, 111]. Furthermore, MD simulations have been utilized to study how mechanical force alters conformation equilibrium for integrin $\alpha_{IIb}\beta_3$ [91] and to examine pathways of leg extension for $\alpha_v\beta_3$ [112]. Finally, Craig et al. used forced unbinding simulations to study the interactions involved in $\alpha_v\beta_3$-RGD binding [46]. The use of MD simulations in these studies enabled direct assessment of integrin conformational dynamics and precise manipulation of integrin receptors (e.g., alteration of particular amino acids or application of mechanical force at specific points), both of which are very difficult to achieve, if not impossible, with most experimental approaches.

1.5. Thesis motivation and objective

1.5.1. Motivating question: What is the role of integrins in mediating cellular responses to acidic pH_e?

It is clear that acidic extracellular pH is a characteristic property of the cellular microenvironment in several pathological and physiological contexts, and that extracellular acidification can profoundly influence cell adhesion and migration. This raises the question: what are the molecular mechanisms underlying the cellular responses to acidic pH_e? While some of the observed effects of acidic extracellular pH on cell adhesion and migration have been attributed to intracellular acidification or changes in protein expression or secretion, the primary molecular mechanisms of pH_e sensing and information transfer remain largely unknown. In particular, although integrin receptors physically connect the cell to the extracellular environment and can regulate cell adhesion and migration, their role in mediating the observed cellular responses to acidic pH_e has not been explored in depth. As transmembrane adhesion receptors, integrins may be capable of directly regulating cellular processes in response to extracellular pH changes even when intracellular pH is maintained at normal levels, such as in the tumor environment. For example, it is plausible that acidic pH_e could alter the total number of integrin receptors on the cell surface, the activation/inactivation rates of integrin receptors, or the binding affinities between integrins and their ligands. In cases where the intracellular environment becomes acidified, this could modify the conformations of the integrin cytoplasmic domains or change the binding affinities between these cytoplasmic domains and intracellular binding proteins.

Currently, only two studies have addressed the question of whether integrin-ligand binding is altered in acidic pH_e. Stock et al. speculated that an acid-induced strengthening of the integrin-ligand bond could explain the effects of acidic extracellular pH on melanoma cell adhesion and migration, but did not directly investigate this hypothesis [29]. Lehenkari and Horton observed that the rupture force between integrin $\alpha_v\beta_3$ and a GRGDSP peptide was maximum at pH 6.5, but did not assess the possible reasons that this occurred [114]. In addition, this result has not been repeated or supported by other molecular-level experiments. Thus, the role of integrins in acting as pH sensors and regulating cellular responses to acidic pH remains unclear and open to investigation.

1.5.2. Overall thesis objective

This thesis will investigate the hypothesis that acidic extracellular pH can directly alter integrin-ligand binding interactions, and that this plays a role in regulating cell adhesion and migration in acidic environments. The overall objective of this work is to use complementary computational and experimental approaches to explore and characterize the effect of extracellular pH on integrin-ligand interactions, and to predict and measure the consequences for cell adhesion and migration. The methods utilized in this research span length scales ranging from single atoms to whole cells in order to gain in-depth understanding of the role of extracellular pH as a critical regulator of cell function. This will provide insight into how the altered chemical environments of tumor and wound sites affect cell processes critical to cancer progression and wound healing, as well as how healthy cells may use proton pumps to modulate migration.

1.6. Thesis strategy and organization

1.6.1. $\alpha_v\beta_3$ as a model integrin

This thesis will focus on integrin $\alpha_v\beta_3$, which binds the RGD sequence in matrix proteins such as fibronectin, vitronectin, fibrinogen, and osteopontin [47]. The crystal structure of the extracellular portion of $\alpha_v\beta_3$ has been solved [45, 70], and it is therefore an appropriate candidate for atomistic-level studies. Integrin $\alpha_v\beta_3$ was used for some of the seminal studies that characterized the large-scale conformational changes involved in integrin activation [80, 82], and activation-specific as well as activation-promoting antibodies exist for this integrin [89, 109]. Although integrin $\alpha_v\beta_3$ does not have the I domain in the α subunit, the conformational changes that have been described for this integrin are expected to occur generally for all integrins [72] (Figure 1.4).

Integrin $\alpha_v\beta_3$ is highly relevant in the cancer context and is expressed on tumor cells from several different tissue origins [115]. For example, $\alpha_v\beta_3$ is expressed in breast cancer cells, and the activated form of this integrin promoted breast cancer metastasis in a mouse model [98, 115-117]. $\alpha_v\beta_3$ expression is also upregulated in metastatic melanoma cells [118, 119] and activation of this integrin enables melanoma cell arrest in the presence of flow [97]. Furthermore, $\alpha_v\beta_3$ enables melanoma cells to adhere to extracellular matrix proteins in the lymph nodes [119]. In addition, $\alpha_v\beta_3$ is expressed in prostate carcinoma cells [115, 120] and was shown to be required for the growth of bone metastases in mice [121]. It has been suggested that $\alpha_v\beta_3$ expression may also promote metastasis of other tumor types to bone, due to the ability of this integrin to bind the bone matrix protein vitronectin [117, 122].

$\alpha_v\beta_3$ expression is upregulated in angiogenic endothelial cells and antibodies against this integrin can block angiogenesis, which is an essential process for tumor growth and wound healing. Integrin $\alpha_v\beta_3$-mediated signaling is believed to promote survival in these cells [123, 124]. Integrin $\alpha_v\beta_3$ is also expressed on fibroblasts, which are involved in matrix deposition and remodeling during wound healing [125-127]. Thus, due to its expression in the tumor and wound healing contexts and its well-characterized structure, integrin $\alpha_v\beta_3$ is ideal for use as a model integrin in this study.

1.6.2. Thesis aims and organization

This thesis utilizes several computational and experimental approaches spanning multiple length scales (Figure 1.5). Our studies address three broad aims, which are organized by the length scale of the biological processes of interest, and results are described in Chapters 2 – 6. Chapter 7 provides an overarching discussion of the thesis results as a whole, as well as the conclusions, implications, and future directions of this work.

Aim 1 (atomistic- and molecular-scale): Determine how acidic pH_e affects integrin conformational states and integrin-ligand unbinding. Here, we use simulation and experimental approaches to answer two main questions. First, how does acidic pH_e affect the conformational changes involved in integrin activation? Second, within a single activation state, does acidic pH_e affect $\alpha_v\beta_3$-RGD interaction kinetics through local changes at the binding pocket?

Chapter 2: Atomistic-scale molecular dynamics simulations are used to explore the effect of acidic pH_e on integrin headpiece conformations, and steered molecular dynamics simulations are used to assess $\alpha_v\beta_3$-RGD rupture forces at three different loading rates.

Chapter 3: Flow cytometry is used to measure the level of activated $\alpha_v\beta_3$ on live cell surfaces, and atomic-force mediated molecular force spectroscopy is utilized to measure $\alpha_v\beta_3$-RGD binding frequency and rupture forces as a function of pH_e. Results from these molecular-scale experiments are compared to the simulation results in Chapter 2 to draw conclusions about the effects of extracellular acidification on integrin activation and binding.

Aim 2 (subcellular-scale): Determine how acidic pH_e affects cell membrane dynamics and actin-integrin adhesion complex formation. Aim 2 considers the effect of acidic pH_e on cell membrane protrusion and intracellular adhesion complex formation, which are subcellular-scale processes that can be affected by altered integrin-ligand interactions and are critical for cell migration.

Chapter 4: Kymography is used to measure membrane protrusion properties as a function of pH_e. These experiments are also used to examine the role of intracellular acidification in causing the observed effects. In addition, cells transfected with fluorescently labeled vinculin are imaged and focal adhesion number and area are measured as a function of pH_e. The results from Aim 1 are used to inform interpretation of these data.

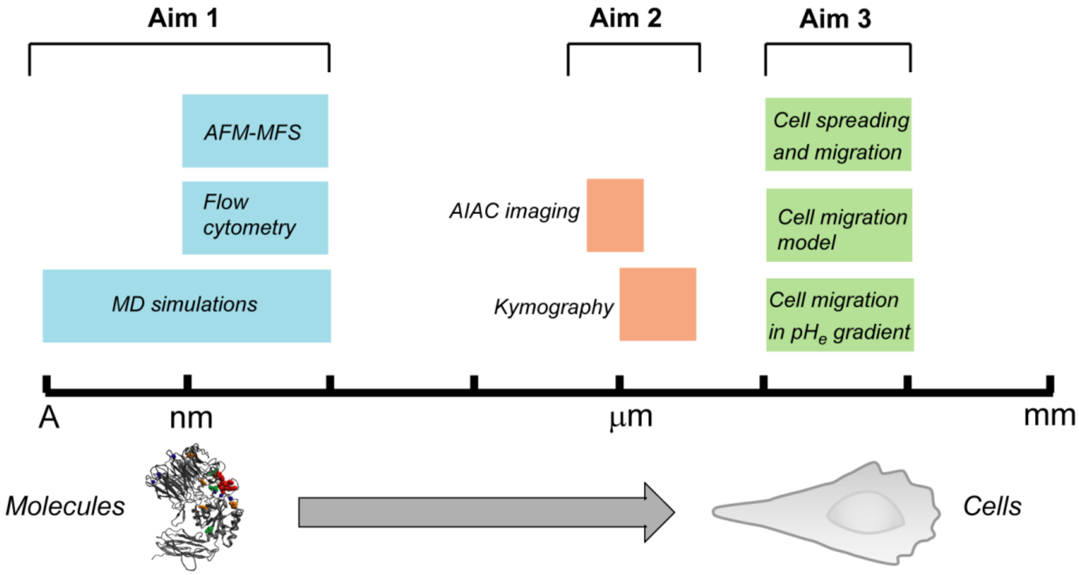

Figure 1.5 Schematic of the multiple lengthscales explored in this thesis. Computational and experimental approaches are used to connect molecular binding to cellular responses.

Aim 3 (cellular-scale): Determine how acidic pH_e affects cell spreading, morphology, and migration. Aims 1 and 2 are focused on molecular and subcellular events that are critical to cellular-scale adhesion and migration. Aim 3 extends these results to cellular-scale processes.

Chapter 5: Cell spreading, morphology, and migration parameters are measured as a function of pH_e. Interpretation of these data is informed by results from Aims 1 and 2. Furthermore, a mathematical model of cell migration is used to connect molecular-scale and cellular-scale results. This model allows assessment of the extent to which changes in integrin activation and binding are responsible for the migration effects measured here.

Chapter 6: All the experiments thus far have used $\alpha_v\beta_3$-CHO cells as a model cell type and have investigated the effects of bulk pH_e changes. In this chapter, we move toward an experimental setup that more closely mimics the tumor and wound sites of interest. The pH_e profiles that cells are likely to experience in vivo are considered and cell migration parameters are measured in pH_e gradients similar to those that occur in tumors. These experiments are conducted for cell types that are relevant to the tumor and wound environments, in addition to the model $\alpha_v\beta_3$-CHO cells. The migration model introduced in Chapter 5 is applied again here to aid interpretation of results.

Overarching discussion

Chapter 7: The results of the thesis are taken as a whole and interpreted to draw conclusions about how acidic extracellular pH can regulate molecular and cellular function. Implications for cancer progression, wound healing, and the role of NHE1 in cell migration are discussed. Finally, several ideas for future work are outlined and the major contributions of this research are summarized.

Chapter 2: Atomistic-scale simulations

Several sections of this chapter include material that has been published in peer-reviewed journals. The content from Section 2.3 has been published in Ref. [128], the material from Section 2.4 was published in Ref. [85], and some data from Section 2.5.2 was published in Ref. [129]. For all of those publications, R.K. Paradise conducted simulations, analyzed and interpreted data, and wrote the manuscripts.

2.1. Overview

In this chapter, two major questions regarding integrin-ligand binding are addressed using molecular dynamics simulations. First, does acidic extracellular pH affect integrin activation? It is conceivable that protonation of specific amino acids on the integrin receptor in acidic pH_e could promote or inhibit the conformational changes involved in the integrin activation process. This could cause a shift in the integrin conformational equilibrium and correspondingly change the overall cell-matrix binding affinity. Second, within a single activation state, does acidic extracellular pH directly alter $\alpha_v\beta_3$-RGD interaction kinetics via local changes to the integrin binding pocket? If so, this could change the overall cell-matrix binding affinity independently of any changes to the number of activated integrins. Here, molecular dynamics simulation techniques are used to investigate these two possible modes of pH_e regulation at the atomistic level and form predictions for integrin-ligand binding in intact cellular systems. Simulation results show that partial opening of the integrin $\alpha_v\beta_3$ headpiece occurs more frequently in acidic extracellular pH_e, indicating that integrin activation is promoted in this condition. We also find that the increased integrin activation in acidic pH_e can be partially attributed to protonation of ASPβ127. Furthermore, steered molecular dynamics simulations demonstrate that the $\alpha_v\beta_3$-RGD rupture force depends on the initial ion coordination state of ASP_{RGD}, but that acidic extracellular pH does not significantly alter the receptor-ligand rupture force or kinetic unbinding rate.

2.2. Molecular dynamics methodology

2.2.1. Basic principles

Molecular dynamics (MD) is a simulation method that enables study of protein conformational motions with atomic resolution. MD simulations are based on force fields that describe the forces acting on the atomic nuclei in the molecule of interest. These force fields include non-bonded terms such as Lennard-Jones and Coulombic interactions, as well as bonded terms describing bond stretching between two atoms, bond angle vibrations among three atoms, and dihedral angle vibrations among four atoms. Using experimentally derived protein structures as input, these force fields are used to solve Newton's equations of motion and create simulations of protein dynamics over time [130].

Molecular dynamics simulations offer a means to explore intra- and intermolecular interactions at the atomistic level. This can provide insight into mechanisms of conformational change and receptor-ligand binding at a resolution that is extremely difficult to achieve experimentally. Simulations also offer an advantage over experimental approaches because molecules of interest can be studied in isolation, and interpretation is not complicated by challenges such as decoupling extracellular and intracellular effects on transmembrane proteins. Furthermore, specific amino acids or atoms can be easily mutated in simulation systems, enabling computational testing of proposed mechanisms. MD is particularly appropriate for studying the role of extracellular pH on proteins, as the effects of different amino acid protonation states can be assessed directly.

Molecular dynamics also has several methodological limitations. First, due to its classical dynamics framework, this method does not incorporate motions of electrons and thus does not allow for covalent bond breakage or formation. In addition, the force fields used for MD include many approximations that improve computational efficiency but can sometimes lead to inaccuracies in simulation results. Furthermore, in spite of improvements in simulation software and computing technology, MD is still computationally expensive, especially when large molecules are simulated with explicit solvent particles. As a result, the simulation timescale is limited, generally to less than 1 μs. This means that it is often not possible to simulate complete large-scale conformational changes, which can require more time [131-134], or to simulate an ensemble of proteins structures to characterize variation in responses. Finally, the behavior of a protein studied in isolation neglects the contributions of membrane or cytoplasmic molecules that could stabilize the protein structure or alter its conformations, and thus may not be a good representation of the protein behavior in the cellular context. Thus, MD is best applied in conjunction with complementary experimental approaches.

2.2.2. Steered molecular dynamics

Steered molecular dynamics (SMD) is a variation of MD that enables computational modeling of events like receptor-ligand unbinding that occur rarely in the restricted timescales currently available to MD. With SMD, an external force is applied in order to displace the ligand from the receptor binding cleft. This makes it possible to observe unbinding events in atomistic detail over short timescales [135, 136].

In a typically SMD simulation, external force is applied to the receptor-ligand complex with a computational spring of known stiffness that is moved at constant velocity. The force applied to the complex can be calculated from the spring extension, and parameters such as receptor-ligand rupture force can be easily measured. In addition, unbinding mechanisms and intermediate states can be characterized with atomic resolution. Compared to forced unbinding experimental methods such as atomic force microscope-enabled molecular force spectroscopy, SMD is often easier to perform and offers much more control over pulling conditions such as spring stiffness and loading rate.

The Bell-Evans model gives a functional relation between measured rupture forces (F_R) and loading rates (F') and can be used to extract the distance from the bound state to the energetic maximum (x_b) and the unbinding rate at zero force (k_{off}) from data taken at multiple loading rates [137, 138]. According to a modified Bell-Evans model proposed by Walton and Van Vliet that takes into account the effect of spring stiffness [139], the rupture force F_R varies linearly with $\ln(F')$:

$$F_R = \frac{k_B}{x_b} \ln\left(\frac{F' x_b}{k_B T k_{off}}\right) + \frac{1}{2} k_{sp} x_b \tag{Eq. 2.1}$$

where F_R is the measured rupture force, k_B is Boltzmann's constant, x_b is the distance between the bound state and the energetic maximum, F' is the loading rate, T is the absolute temperature, k_{off} is the unbinding rate at zero force, and k_{sp} is the spring constant. Thus, the distance between the bound state and energetic maximum can be expressed as:

$$x_b = \frac{k_B T}{m} \tag{Eq. 2.2}$$

and the unbinding rate can be expressed as:

$$k_{off} = \left[m \times exp\left(\frac{b - \frac{k_{sp} k_B T}{2m}}{m} \right) \right]^{-1} \tag{Eq. 2.3}$$

In order to feasibly sample rare events such as receptor-ligand unbinding or protein unfolding with current resources, SMD loading rates must significantly exceed the loading rates used for forced unbinding experiments. For example, SMD loading rates are generally in the range of Newtons per second (N/s), compared to pN/s – μN/s for experiments. Due to these extremely high loading rates, simulated rupture forces cannot be extrapolated to the experimental regime, and the SMD-derived k_{off} and x_{b} will not quantitatively match experimental measurements [138, 140]. However, SMD remains useful for relative comparisons of rupture forces or kinetic parameters at different conditions.

2.3. Using replicate MD simulations to characterize rare-event property distributions

2.3.1. The problem: characterizing rare events in molecular simulations

Our goal is to use (steered) molecular dynamics to investigate integrin activation and integrin-ligand unbinding as a function of extracellular pH. The properties of interest here – large conformational changes and receptor-ligand unbinding – are rare events that are expected to occur infrequently in a single simulation trajectory. Rare event properties can display considerable variation, and thus should be measured as averages over many events such that the property distribution is characterized accurately. Before beginning simulations of integrin $\alpha_v\beta_3$, it is appropriate to consider the general methodological question of how best to generate a set of replicate simulations that will enable proper characterization of rare events property distributions.

One straightforward way to sample a property distribution in molecular simulations is to perform an ensemble of replicate production-run[1] simulations, each with a different initial configuration taken from an equilibration trajectory, and observe the resulting distribution in behavior. Some researchers have begun to use multiple initial configurations for replicate simulations [141, 142]; however, two major methodological questions have not been explicitly addressed. First, how should an ensemble of representative initial configurations be chosen? Second, how many replicate production-run simulations are necessary in order to characterize molecular property distributions reasonably accurately without incurring excessive computational expense?

Selecting an ensemble of representative initial configurations generates a third, more fundamental question: can we expect there to be a discernable relationship between the minute configurational changes accessible in atomistic simulations and the functional biomolecular properties of interest? If configurational differences can be correlated directly with changes in properties, then a method of selecting an ensemble of initial configurations must reflect this correlation. This ensures that that the simulations utilizing these configurations will appropriately sample the property distribution of interest. However, it is unclear what kind of relationship will exist between the subtle, sub-nm configurational differences among a set of configurations selected from an ostensibly equilibrium MD trajectory and the biomolecular properties inferred from production-run MD simulations. Two recent studies highlight this question and suggest that the answer may depend on the particular biomolecular system of interest. MD simulations described by Dastidar et al. showed that multiple configurations of p53 peptides in complex with the protein MDM2 yield similar binding affinities [143]. In contrast, experiments reported by Coureux et al. showed that very small configurational differences (< 0.1 nm root-mean square displacement) separate active and non-active states of a photoreceptor protein [144], indicating that photoreceptor function varies with sub-nm configurational changes.

In this section, these three questions are addressed through a combination of clustering analysis, replicate SMD simulations, and statistical analysis. We focus on a particular rare-event: unbinding of a biotin ligand from a streptavidin receptor. This high-affinity ligand-receptor complex has been widely studied through both experiments and simulations [135, 145-150] and is thus an ideal model system for investigating fundamental methodological questions. In these SMD simulations, the rare-event property of interest is the rupture force F_R, defined as the maximum force observed in each unbinding trajectory. We demonstrate a method for testing for a correlation between configuration and rare-event properties in any biomolecular system, and offer general guidelines for selecting an ensemble of initial configurations for atomistic simulation of rare-event properties.

---

[1] Here, the term "production-run simulation" is taken to mean a simulation that samples the rare event of interest, such as an SMD receptor-ligand unbinding simulation. A production-run simulation is differentiated from an "equilibration" simulation which allows the protein to begin exploring its equilibrium phase space and from which initial configurations may be chosen.

2.3.2. Using clustering analysis to test for a configuration-property relationship

We used clustering analysis as a tool to enable testing for a correlation between initial configuration and output property F_R. Clustering analysis is a well-established tool for identifying distinct configurational groups within an MD trajectory [151-159], but it has not previously been applied to testing for functional differences among configurational subsets.

All initial configurations considered in this study were selected from a single MD equilibration simulation trajectory of 101 ns duration. This equilibration trajectory was only used to generate and identify initial configurations as distinct starting points for production-run SMD simulations. We applied a clustering algorithm to divide the frames of the equilibration trajectory into configurationally similar subsets, termed clusters. Because it is not clear which residues might capture configurational information that correlates with rupture force, we used three different groups of residues for the similarity metric in the clustering algorithm: (i) all atoms of the streptavidin tetramer with four bound biotin molecules; (ii) the streptavidin binding pocket [135, 160, 161] inclusive of the biotin ligand; and (iii) the binding pocket exclusive of the biotin ligand. The centroid (most representative configuration) of each cluster was also identified.

From the clustering results, we selected four groups of configurations to be used as input into SMD simulations: the set of cluster centroids that resulted from each similarity metric (three groups) as well as all of the configurations within a single cluster from each similarity metric (one group). This last criterion resulted in one group instead of three because there happened to be one cluster that coincidentally occurred with all three similarity metrics. The configurations within a single cluster are necessarily more similar than the set of centroids from different clusters.

All SMD simulations of forced biotin unbinding from the streptavidin receptor were conducted under otherwise identical conditions. If the initial bound configuration were correlated with F_R of the complex, the set of all configurations from within a single cluster should result in a narrower distribution of rupture forces than the distribution observed for the set of cluster centroids (Figure 2.1A). However, in our simulations, the distribution of rupture forces for a single cluster had a similar range as that of the cluster centroids, regardless of the group used for the similarity calculation (Figure 2.1B). Therefore, in this system, configurational similarity does not necessarily lead to similar rupture forces.

We also performed a set of SMD simulations using a single initial configuration but varying the randomly assigned initial velocities of the atoms (Figure 2.1B). The distribution of rupture forces in this subset was approximately the same as that obtained for the subsets that differed in initial configuration, underscoring the point that initial configuration does not correlate with F_R.

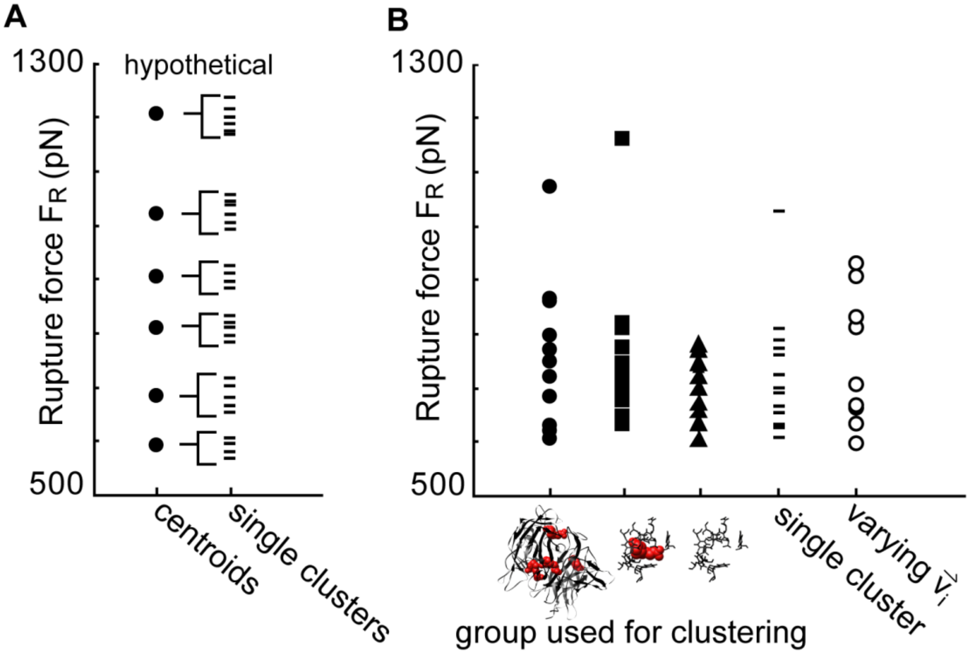

Figure 2.1 (A) Hypothetical clustering results in the case that a correlation exists between initial bound configuration and output rupture force F_R. Filled circles denote cluster centroid rupture forces and dashes denote rupture forces for configurations within each cluster, with individual clusters indicated with brackets. (B) Clustering results with centroids from three different groups used for similarity calculation: Group 1: streptavidin tetramer plus four bound biotin molecules (filled circles); Group 2: streptavidin binding pocket plus one bound biotin molecule (squares); Group 3: streptavidin binding pocket (triangles). Dashes denote F_R values for configurations within a single cluster. This same set of configurations comprised one full cluster for each of the three clustering metrics used. Open circles denote F_R values for a single initial configuration with varied initial atomic velocities. Even considering three different similarity metrics, we find no evidence to support a correlation between initial configuration and rupture force. Figure is from Ref. [128].

2.3.3. Necessary number of replicate simulations

The goal of conducting replicate atomic simulations with multiple initial configurations is to characterize a property distribution of interest. In this study, SMD simulations were conducted on 53 different initial configurations (total number of configurations in the four groups selected after clustering). This is similar to the number of unbinding measurements recommended for forced unbinding experiments [162], and is assumed to be sufficient for reliable characterization of the rupture force distribution. However, it is possible that this characterization could have been done more efficiently with fewer simulations.

To investigate how many replicate simulations are necessary to reliably represent the full rupture force distribution, we generated 200 subsets of N rupture force values randomly selected from the full set of 53, where N ranged from 4 to 40. We then used a two-tailed t-test to identify subsets that had a mean F_R that was statistically significantly different ($p < 0.05$) than the full set of rupture forces and would therefore lead to incorrect characterization of the rupture force distribution. As shown in Figure 2.2, for $N = 4$, 75% of the randomly generated distributions were statistically significantly different from the full distribution, while for $N \geq 30$, none of the randomly generated distributions were statistically significantly different from the full distribution.

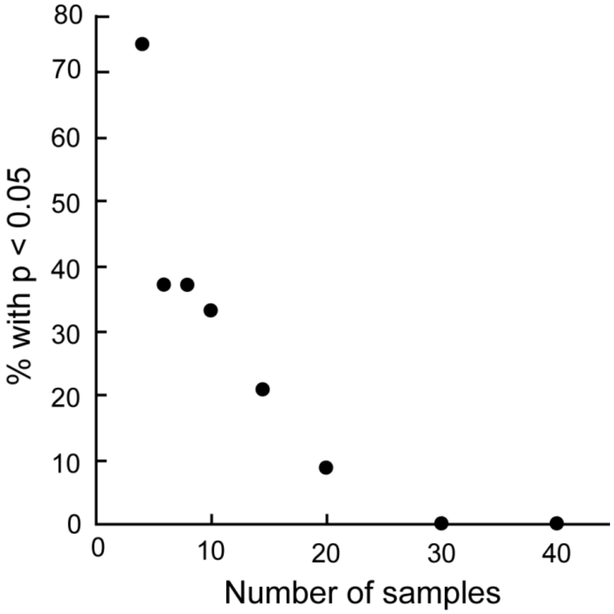

Figure 2.2 The full set of 53 rupture forces was split into randomly generated subsets of size ranging from $N = 4$ to $N = 40$. The rupture force distribution of each subset was compared to the distribution of the full set of 53 rupture forces. The percentage of subsets that were statistically different ($p < 0.05$) than the full set of rupture forces is plotted here for each N. Consistent with many other fields, a set of 30 samples seems to consistently reproduce features of the original property distribution. Figure is from Ref. [128].

2.3.4. Discussion

We found no evidence for correlation between the initial bound configuration and the measured rupture force of the biotin-streptavidin complex. This is consistent with the concept that protein behavior is often governed by rough, multi-dimensional energy landscapes [150, 160, 163, 164] (Figure 2.3A), as opposed to idealized energy landscapes, which are typically depicted as smooth and one-dimensional (Figure 2.3B). With a smooth, one-dimensional energy landscape, a small change in initial configuration would result in a small change in the energy barrier height and corresponding small changes in energy-dependent properties such as F_R. With a rough, one-dimensional energy landscape, although the transition state is fixed at the point of highest energy, complexes with similar initial configurations may have very different initial energies, leading to different energy barrier heights and differences in measured properties [150]. When a rough energy landscape is extended to multiple dimensions, the transition state also becomes variable because there is roughness in the saddle point as well as in the energy wells. Therefore, initial configurations with nearly identical initial energies can have trajectories with different energy barriers (Figure 2.3C). Multiple dimensions also allow for variation in the direction of movement from a single configuration, meaning that identical initial configurations with different sets of initial atomic velocities may follow divergent trajectories (Figure 2.3C). Thus, a rough, multi-dimensional energy landscape is a possible explanation for the lack of configuration-property correlation in our simulations.

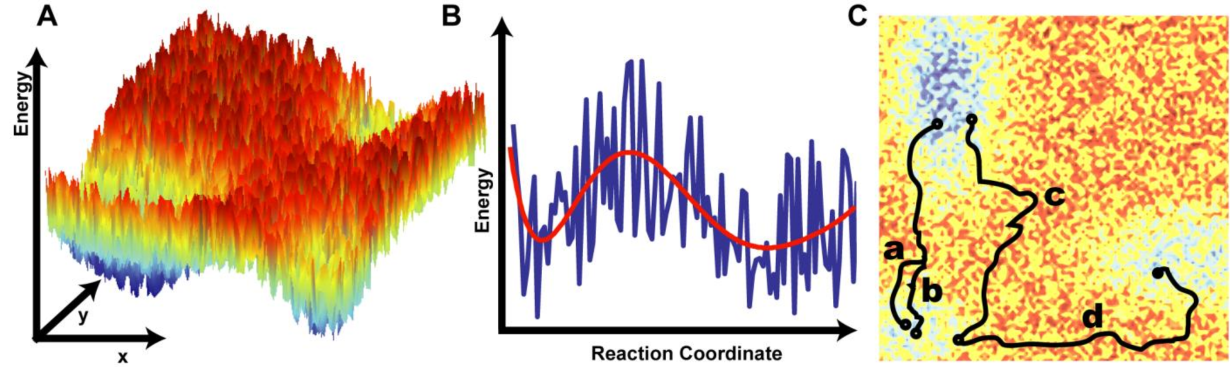

Figure 2.3 Protein energy landscapes are rough and multi-dimensional (A), but are often represented as smooth and one-dimensional (B, red). In rough, one-dimensional landscapes (B, blue), similar configurations may have very different initial energies (pathway *a* and *b* in C), causing a difference in the energy barrier and therefore in values of protein properties. Multi-dimensional landscapes introduce additional mechanisms of property variation: the transition state roughness (pathways *b* and *c* in C) and the initial sampling direction (pathways *c* and *d* in C). Many protein interactions are described by rough, multi-dimensional energy landscapes that result in a natural variation in energy-dependent properties. Figure from Ref. [128].

Given that many protein interactions are reasonably described by a rough, multi-dimensional energy landscape [150, 154, 158, 159], we anticipate that this lack of configuration-property correlation will be observed for other rare event properties and other protein systems. However, if differences among configurations increase as phase space sampling increases (longer simulation timescale), or if energy landscape roughness decreases (system-dependent), it is possible that correlations will exist.

Testing for a correlation between initial configuration and output property informs the selection of a representative set of configurations for production-run simulations. If configuration is not correlated with the observed property, then no particular configuration is more representative than any other; thus, any subset of configurations will randomly sample the underlying distribution of the observed property. For example, configurations generated from equally spaced timepoints would be as valid as those generated randomly.

To efficiently characterize the underlying distribution of a biomolecular rare-event property, one should consider how many replicate samples are required. A statistical rule of thumb, used in fields as diverse as economics and epidemiology, is that approximately 30 samples are needed to adequately characterize the mean of an underlying distribution because with $N \geq 30$, the Central Limit Theorem becomes valid. The Central Limit Theorem states that the distribution of sampled means approaches a normal distribution. This normal distribution will be centered on the mean of the underlying distribution, regardless of the shape of the underlying distribution [165]. Our results from randomly generated subsets of size $N = 4$ to $N = 40$ are consistent with this. It is possible that in our system, $N \geq 30$ led to accurate characterization of the mean F_R simply because this large N sampled more than half of our full set of 53 rupture forces. However, the consistency with the Central Limit Theorem rule of thumb suggests that this result is valid. Given the general applicability of this statistical concept, we predict that at least 30 replicate simulations will be necessary to ensure adequate characterization of an observed property for many biomolecular systems.

2.3.5. Conclusions and suggestions for design of computational experiments

As expanding computational capabilities make it increasingly tractable to perform multiple simulations of rare-events, it becomes important to consider the procedures necessary for performing and analyzing replicate simulations. We suggest the following approach, schematically outlined in Figure 2.4. First, one should assess the relationship between initial configuration and the simulated rare-event property of interest. If information regarding configuration-property correlations (or lack thereof) already exists, this can be taken into account when selecting representative initial configurations for simulations. If such information is not available, once can use clustering analysis to test for a configuration-property relationship, as described in Section 2.3.2. This includes applying a clustering algorithm to an equilibration MD trajectory, conducting production-run simulations on the set of cluster centroids and every member of a single cluster (or a single configuration with different atomic velocities), and comparing the resulting property distributions.

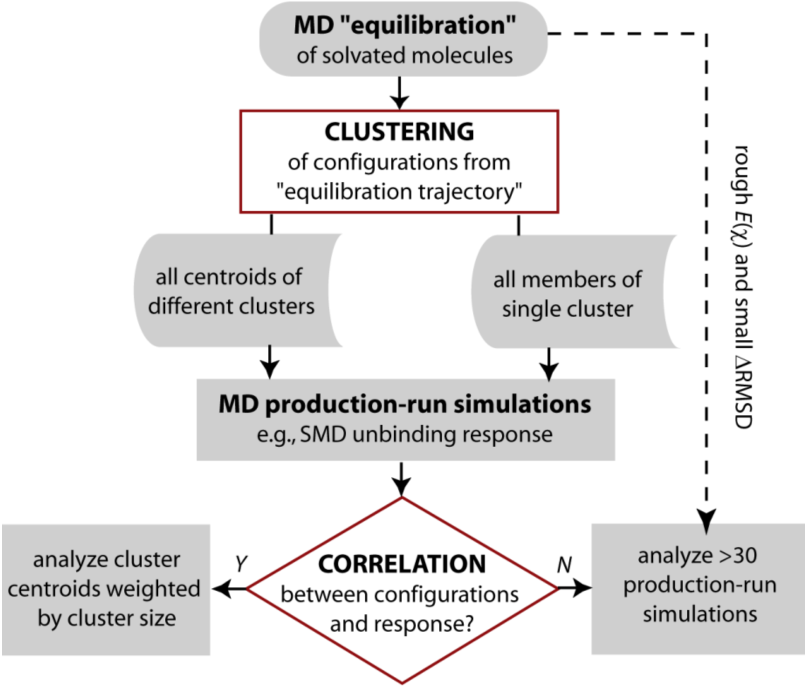

Figure 2.4 A suggested method of testing for the presence of configuration-property correlation in rare event MD simulations and implications on selecting an ensemble of initial configurations for replicate production-run simulations. Figure from Ref. [128].

If there is no correlation between initial configuration and measured property (as we anticipate to be the case for protein systems with rough energy landscapes under current computational limitations), then any set of 30 configurations will randomly sample the property distribution and can be used for characterization. Note that some or all of these 30 configurations could be the same as those employed to test for a configuration-property correlation, improving computational efficiency. If 30 simulations are not computationally feasible, then it is important to consider the fact that there may be errors in calculations of mean parameters due to insufficient sampling.

However, if a configuration-property correlation exists (indicated by the observation that the property distribution exhibited by a single cluster is significantly narrower than that exhibited by the set of cluster centroids), the cluster centroids may be representative initial configurations for characterizing the property distribution of interest and must be weighted appropriately to account for cluster size. These general guidelines for choosing configurations for replicate simulations can be adapted to suit any molecular system of interest, including the integrin $\alpha_v\beta_3$ system that is the focus of this thesis.

In the time since the publication of this study, many researchers have begun to conduct replicate simulations to characterize variation in molecular properties [112, 166-170], although some other investigators continue to conduct only one simulation per condition [171, 172]. In the studies that considered replicate simulations, the number of replicates is generally small ($N < 7$), with the exception of the study by Xu et al., who conducted 40 independent replicate simulations per condition [170]. It is likely that computational resources are currently too limited for most researchers to conduct ~30 independent simulations for all conditions of interest. However, as computational efficiency and simulation methods continue to improve, we hope that conducting 30+ replicate simulations will become an increasingly common practice for studies of rare events.

2.4. MD simulations of integrin $\alpha_v\beta_3$: Does acidic pH_e affect the conformational changes involved in integrin activation?

In this section, we investigate the effect of acidic pH_e on the conformational changes involved in integrin activation, specifically headpiece opening. Molecular dynamics simulations provide a method by which the effects of individual amino acid protonation events resulting from extracellular acidification can be studied at the atomistic level. With MD, it is possible to break down the cell-matrix system to the most fundamental component – an isolated integrin-RGD complex – and thus gain mechanistic understanding of the effect of pH_e on integrin conformations without the added complexity of the cellular environment and intracellular signaling.

2.4.1. Changing pH_e in MD simulations: MCCE

Molecular dynamics does not allow for chemical reactions to occur during simulations. Therefore, extracellular acidification cannot be simulated by simply adding hydrogen ions to the simulation system, as amino acid protonation will not happen naturally in a simulation trajectory. Instead, in this work, protonation states were defined at the start of the simulation based on amino acid pK_a values to create systems that effectively simulated different extracellular pH conditions.

Amino acid pK_a values for residues within the context of a specific protein can differ appreciably from those measured for residues in isolation. To address this, Multi-

Conformation Continuum Electrostatics (MCCE) was used to predict pK_a values for the amino acids within the context of the integrin $\alpha_v\beta_3$ receptor [173, 174]. To incorporate the protein environment into pK_a prediction calculations, MCCE gives flexibility to the protein structure by allowing each residue to exist in multiple positions (within a predefined set) and ionization states. Each combination of amino acid position and ionization state is called a conformer, and a particular set of conformers comprises a protein microstate. For each protein microstate, MCCE calculates electrostatic energies using a Poisson-Boltzmann continuum formulation, as well as nonelectrostatic energy terms. Finally, Monte Carlo sampling is employed to find the distribution of conformer states during a simulated titration. This is used to estimate a pK_a value for each residue [173, 174].

2.4.2. Simulation system and MCCE results

The crystal structure of the extracellular potion of integrin $\alpha_v\beta_3$ in complex with a cyclic RGD pentapeptide [45] (PDB ID 1L5G) was used as the input structure for these MD simulations. Although the integrin is bound to a ligand in this solved structure, the overall conformation of the integrin receptor is in the inactive form, with bent legs and a closed headpiece. It is believed that this is due to the fact that this structure was obtained by soaking pre-existing crystals of unliganded $\alpha_v\beta_3$ with Mn^{2+} ions and RGD peptides, and the crystal lattice impeded long-range conformational changes [80]. However, ligand binding did induce small conformation rearrangements local to the binding site [45, 70]. Because this integrin structure is in the overall inactive conformation, it is suitable for studies of the integrin activation process.

For this study, only the integrin headpiece domains (β-propeller, hybrid, and I-like domains) and RGD ligand were simulated in order to be consistent with the previous work of Puklin-Faucher et al., who used MD simulations to study mechanisms of integrin $\alpha_v\beta_3$ headpiece opening [110, 111] (Figure 2.5). These previous studies offered a framework and protocol for simulating the integrin headpiece that was very helpful in informing our simulation design. Furthermore, limiting the system to the integrin headpiece domains made the simulations much more computationally tractable with the available resources. The headpiece domains used in our simulations contained 818 amino acid residues, compared to 1649 residues for the full integrin extracellular structure. After adding ions and water molecules, the headpiece system contained 97,984 atoms and each ns of simulation required ~48 hr on a 2.66 GHz Intel Xeon X5355 processor.

To simulate normal physiological pH_e, all amino acid residues with p$K_a > 8.2$ were protonated. To simulate effective acidic pH_e, all residues with p$K_a > 6.2$ were protonated. Although this acidic pH_e protonation threshold does not simulate a specific extracellular pH value, it means that for p$H_e < 6.2$, these residues will be protonated for more than 50% of the available integrins. The simulation states in this study are hereafter generally referred to as "normal pH_e" and "acidic pH_e". All metal ion binding sites in the integrin headpiece were filled by Mg^{2+} ions in our simulations.

Amino acid residue	Predicted pK_a value
GLUα123	11.933
ASPβ217	8.53
HISβ244	8.492
HISα91	6.223
ASPα186	7.109
ASPβ127	6.692
HISβ274	7.103

Table 2.1 Residues with elevated pK_a values as predicted by MCCE. GLUα123, ASPβ217, and HISβ244 were protonated in both the normal and acidic pH$_e$ systems. HISα91, ASPα186, ASPβ127, and HISβ274 were protonated in the acidic system only. Table from Ref. [85].

MCCE results indicated seven amino acids with pK_a values that were elevated from their expected solution values and were thus protonated in our simulations (Table 2.1, Figure 2.5). Four of these residues (HISα91, ASPα186, ASPβ127, and HISβ274) were protonated only in the acidic pH$_e$ system and are therefore of special interest in understanding the mechanisms underlying the effects of acidic pH$_e$ on $\alpha_v\beta_3$ conformations and binding. Two additional amino acids (GLUβ400 and GLUβ409) had elevated pK_a values but were not protonated in our simulations. These residues are close to the C-terminus of the simulations system and are thus artificially solvent exposed rather than being in contact with the integrin leg domains, which could lead to errors in MCCE pK_a calculations.

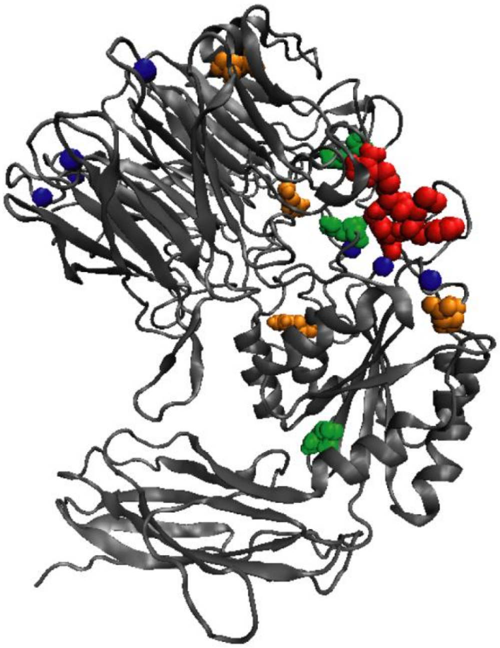

Figure 2.5 Rendering of the simulation system used in this study: the $\alpha_v\beta_3$ headpiece in complex with an RGD peptide. Spheres depict MG^{2+} ions (blue), RGD ligand (red), residues with elevated pK_a that were protonated at both normal and acidic pH$_e$ (green), and residues with elevated pK_a that were protonated at acidic pH$_e$ only (orange). Figure from Ref. [85].

2.4.3. MD results

Eight MD simulations (8 ns each) were run for each pH_e system. This 8 ns simulation timescale was based on the studies of Puklin-Faucher et al., who previously reported that headpiece opening can begin within 8 ns in MD simulations of $\alpha_v\beta_3$ in complex with the fibronectin III_{10} domain [110, 111]. In spite of some differences in simulation setup, the maximum level of headpiece opening observed in our simulations was comparable to that reported by Puklin-Faucher et al. For our simulations, the amount of headpiece opening that occurred was quantified by calculating the y-component of the distance d between a portion of the β-propeller domain at the top of the integrin headpiece (residues α250-438) and a portion of the hybrid domain at the bottom of the headpiece (residues β55-106 and β356-434). The x- and z- components of this distance were excluded because headpiece opening results in negligible movements in these dimensions.

At normal pH, the distribution of headpiece opening distances had one peak centered at $d = 4.2$ nm. At acidic pH, the histogram had two peaks, centered at $d = 4.1$ nm and 4.55 nm (Figure 2.6). The existence of this second peak demonstrates that the integrin headpiece more frequently sampled a partially open state at acidic pH. Although the $\alpha_v\beta_3$ headpiece did not reach the fully open conformation during the 8 ns timescale of these simulations, the partial headpiece opening observed in simulations is expected to be on the pathway to complete opening [110]. Therefore, these results indicate that acidic extracellular pH promotes opening of the $\alpha_v\beta_3$ headpiece.

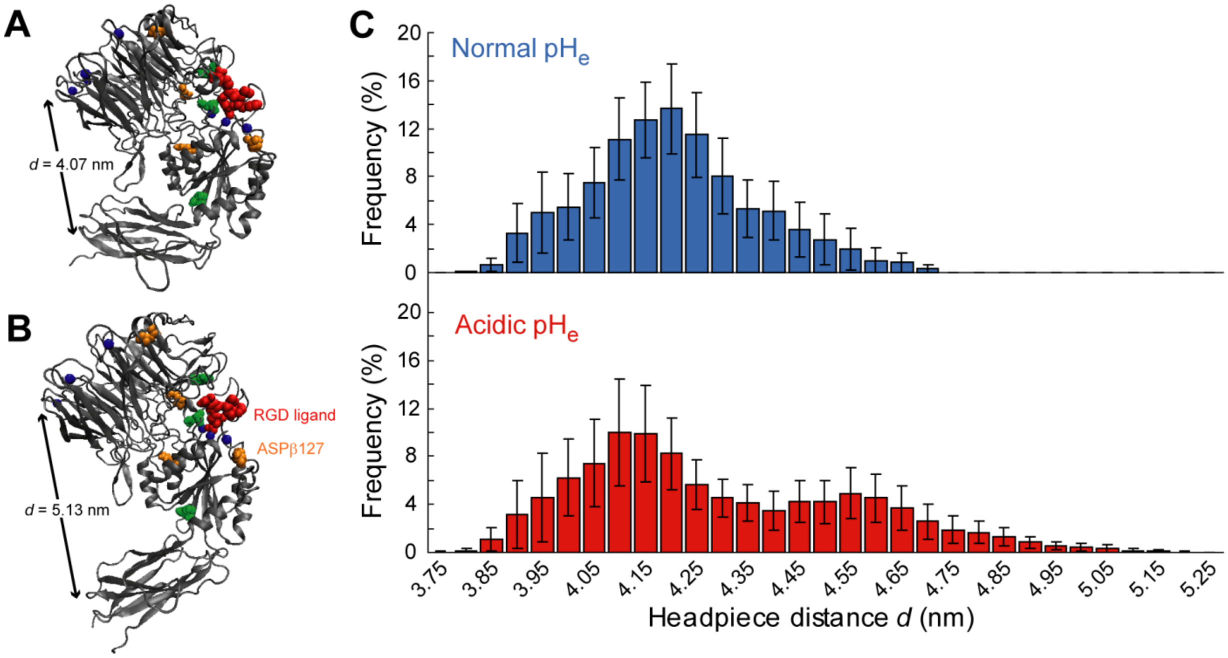

Figure 2.6 (A) Rendering of the $\alpha_v\beta_3$ headpiece in a closed conformation displayed as in Figure 2.5. Arrow indicates headpiece opening distance. (B) Rendering of the $\alpha_v\beta_3$ headpiece in a partially open conformation. (C) Histograms of headpiece opening distances from all recorded frames of every simulation trajectory. Frequencies are displayed as the average of the eight simulations at each pH_e condition. Error bars are SEM. Figure from Ref. [85].

We next investigated the mechanism behind the acid-induced headpiece opening observed in our simulations. ASPβ127, which is protonated in our acidic pH_e system, is located in the α1-β1 loop at the top of the α1 helix in the I-like domain, and coordinates the divalent cation at the ADMIDAS site. As movements of the α1 helix have been implicated in headpiece opening [87, 110], we investigated the role of ASPβ127 protonation in $\alpha_v\beta_3$ headpiece opening. We set up a third simulation system that was identical to the normal pH_e system, with the additional protonation of ASPβ127. The distribution of headpiece opening distances for this system revealed three peaks, two of which were shifted to higher distances than the normal pH_e peak (Figure 2.7A). This indicates that protonation of ASPβ127 could be at least partially responsible for the headpiece opening observed at acidic pH_e.

At normal pH_e, ASPβ127 is negatively charged and coordinates the divalent cation at the ADMIDAS site (Figure 2.7B). When ASPβ127 is protonated at acidic pH_e, it has neutral charge and no longer coordinates the ADMIDAS ion (Figure 2.7C). This is demonstrated by the distance between ASPβ127 and the ADMIDAS ion, which is much lower at normal pH_e (Figure 2.7D). We suggest that the loss of ASPβ127-ADMIDAS ion coordination that occurs at acidic pH_e makes it more likely for the α1-β1 loop and the α1 helix to sample movements that promote opening of the integrin headpiece.

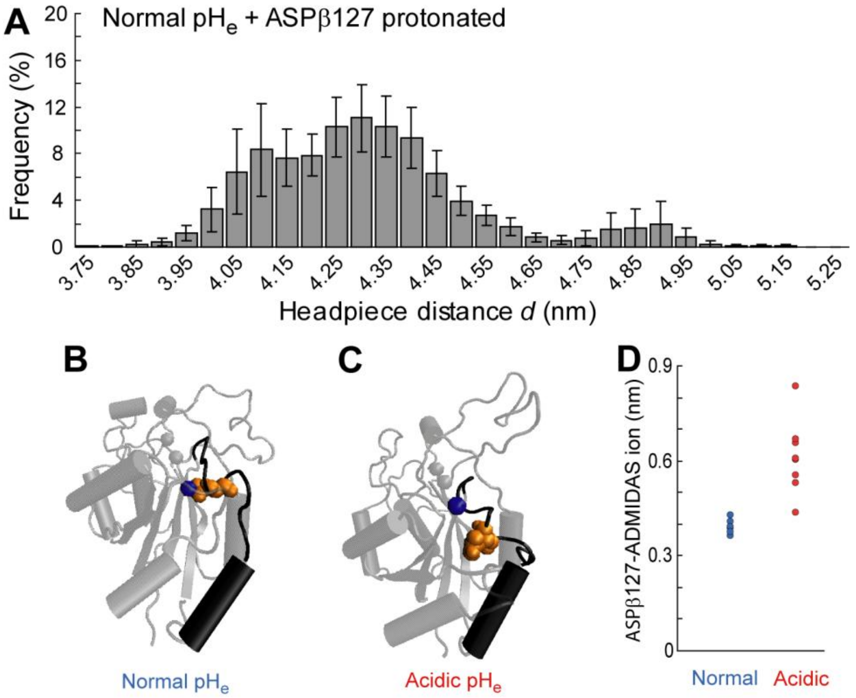

Figure 2.7 (A) Histogram of headpiece opening distances displayed as in Figure 2.7. (B) Snapshot of the $\alpha_v\beta_3$ I-like domain in the normal pH_e system demonstrating ASPβ127-ADMIDAS ion coordination. The ADMIDAS ion is displayed as a blue sphere, ASPβ127 is displayed in orange spheres, and the α1-β1 loop and α1 helix are displayed in black. (C) Snapshot of the $\alpha_v\beta_3$ I-like domain in the acidic pH_e system demonstrating the lack of ASPβ127-ADMIDAS ion coordination. (D) Average distances between the centers-of-mass of the ADMIDAS ion and ASPβ127 in each simulation trajectory. Error bars (SEM) are within data points. Figure from Ref. [85].

The timescale of these simulations was limited to 8 ns to enable us to run multiple replicate simulations at three pH_e conditions and calculate error bars for the headpiece distance distribution. To test whether the integrin headpiece would open to a greater extent with a longer simulation timescale, the simulation that displayed the greatest headpiece opening was extended to a total of 56 ns. Analysis of the headpiece distance *d* for this single simulation demonstrated that the integrin $\alpha_v\beta_3$ headpiece did not open significantly more during the addition 48 ns of simulation, but rather continued to fluctuate around a headpiece distance of about ~4.8 nm (Figure 2.8). Although the data from 15.5 – 46 ns was lost due to a computer failure and is not displayed in Figure 2.8, we had monitored the extent headpiece opening while the simulation was in progress and are confident that greater opening did not occur during this interval. This indicates that the headpiece opening sampled in these simulations may represent an intermediate state on the pathway to complete opening. As large scale conformational changes can take 10 – 100 ms [131-134], full headpiece opening would likely take much longer than 56 ns and using simulation to study the complete large-scale conformational change is impractical within the constraints of current computational resources.

Integrins exist in a conformational equilibrium between the bent, extended-closed, and extended-open states. Our simulations demonstrate that acidic pH_e promotes opening of the integrin $\alpha_v\beta_3$ headpiece, attributable in part to the protonation of ASPβ127 in the I-like domain. In the intact integrin, acid-induced headpiece opening can occur in the extended-closed or the bent-closed conformation. Headpiece opening in the bent-closed conformation destabilizes the bent state and is expected to lead to extension of the integrin [71, 82, 175]. Therefore, our MD data indicate that acidic pH_e will shift the integrin conformational equilibrium toward the fully activated, extended-open state, independently of other possible downstream effects of extracellular acidification.

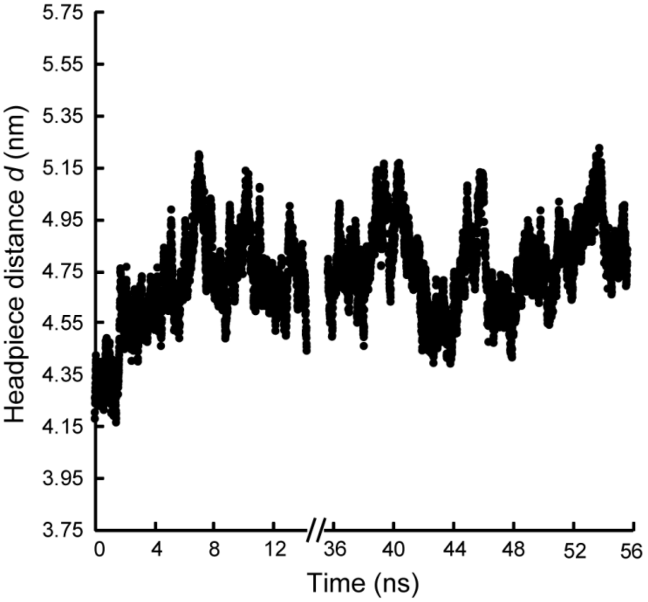

Figure 2.8 Headpiece opening distance over time for a single simulation that was extended to a longer timescale of 56 ns. Headpiece distance did not increase appreciably between 8 – 56 ns. Data between 15.5 – 36 ns was lost due to a computer failure.

2.4.4. Discussion of MD results

Our MD simulation setup was informed largely by the work of Puklin-Faucher et al., who previously used MD simulations to study integrin $\alpha_v\beta_3$ headpiece opening [110, 111]. However, our simulation setup was not identical to that in this previously published work. First, our simulations were based on a GROMOS force field while those of Puklin-Faucher et al. used a CHARMM force field. Furthermore, in our simulations, $\alpha_v\beta_3$ is bound to a cyclic RGD pentapeptide, while in the simulations of Puklin-Faucher et al., the integrin is bound to the 10th type III fibronectin domain ($FnIII_{10}$). We chose to use the RGD ligand because this is the ligand in the crystal structure that was used as input for these simulations. Replacing this ligand with $FnIII_{10}$ requires docking and rotation of the fibronectin domain to remove steric conflicts, as there is no crystal structure available for $\alpha_v\beta_3$ bound to $FnIII_{10}$ [110]. This arbitrary rotation may result in an unphysiological orientation of the ligand which could cause artifacts in simulation results. Puklin-Faucher et al. report that in their simulations headpiece opening requires interactions between $\alpha_v\beta_3$ and $FnIII_{10}$ beyond just the RGD binding interaction [110]. However, it has been shown experimentally that integrin activation and headpiece opening can occur with small RGD peptides rather than full ECM ligand domains [80]. Thus, we feel that it was appropriate to use an RGD peptide for the ligand in this work.

Our molecular dynamics simulations demonstrated that the $\alpha_v\beta_3$ headpiece attained a partially open state more frequently at acidic pH_e than at normal physiological pH_e, possibly due to the protonation of ASPβ127. This protonation results in a loss of coordination of ASPβ127 to the ADMIDAS ion, which may promote movements of the α1 helix that are favorable for headpiece opening. Interestingly, the ADMIDAS position is occupied by a metal ion both in the liganded and unliganded integrin structures [45, 70]; therefore, this ion could play a role in integrin priming before ligand binding occurs.

Experiments with ASPβ127 mutations provide a direct test of the effects of losing ASPβ127-ADMIDAS ion coordination on integrin activation and binding. Several studies have been performed in which ASPβ127 in β_3 or the equivalent residue in other β subunits was mutated to alanine, which results in loss of ADMIDAS ion coordination. Overall, previous results of this mutation with respect to different integrin conformations and binding capacities are inconsistent, varying with the beta subunit. $\alpha_2\beta_1$ and $\alpha_5\beta_1$ integrins with alanine substitution of ASP138 were capable of binding, but mainly had a closed headpiece. However, they could be activated by antibodies [73, 79]. Integrin $\alpha_L\beta_2$ showed constitutive ligand binding when ASPβ120 was mutated to alanine. However, the integrin remained in the bent conformation [176]. In contrast, ASPβ127 mutations in $\alpha_{IIb}\beta_3$did not inhibit normal activation and binding [177]. This indicates that the ASPβ127-equivalent residue may play a different role in different beta subunits, but that coordination of ASPβ127 to the ADMIDAS ion in β_3 is not required for integrin function. Furthermore, mutation of ASPβ148 to alanine in integrin $\alpha_4\beta_7$ resulted in constitutive activation of the integrin [78]. This suggests that in some integrins, loss of coordination of the ASPβ127-equivalent residue to the ADMIDAS ion is sufficient to cause integrin activation. Protonation of this residue at acidic extracellular pH is one mechanism by which loss of ADMIDAS ion coordination can occur. Studies with alanine mutation of ASPβ127 or the equivalent residue are a valuable complement to our MD data. However, we note that alanine substitution is not a direct parallel of the protonation that occurs at acidic pH_e, due to the fact that a protonated aspartate residue can participate in side-chain hydrogen bonding, but alanine cannot.

While MD allowed us to gain atomistic insight into the effect of acidic pH_e on integrin headpiece opening, this method has some limitations. First, the validity of these simulations depends on the accuracy of the MCCE pK_a predictions. A benchmarking study compared predicted pK_a values from several different computational programs with experimentally-derived pK_a values and found that MCCE has 71% accuracy to within 1 pK_a unit and 42% accuracy to within 0.5 pK_a units [178]. While MCCE compared favorably to other pK_a prediction programs, there is still a significant amount of error associated with these calculations. However, lacking experimental pK_a measurements for amino acids in the integrin $\alpha_v\beta_3$ headpiece, MCCE was the best method available to us.

Next, the simulations in this thesis were restricted to the integrin $\alpha_v\beta_3$ headpiece domains in order to be consistent with the previous work of Puklin-Faucher et al. [110], and to increase computational speed and efficiency. This neglects any effects that acidic pH_e may have on the integrin leg domains, which must straighten for the integrin activation process to be complete. The crystal structure that we used for our $\alpha_v\beta_3$ MD studies (PDB ID 1L5G) was the most complete integrin structure that was available at the time of our simulations; however, it lacked resolution for the PSI, EGF-1, and EGF-2 domains in the β_3 subunit leg. As a result, even if we had had greater computational resources, simulation of conformational changes for the complete extracellular domain would not have been possible. Since the time of our simulations, an $\alpha_v\beta_3$ crystal structure with these domains resolved has become available [179] (PDB ID 3IJE), in addition to a crystal structure for the complete extracellular portion of $\alpha_{IIb}\beta_3$ [91] (PDB ID 3FCS). Others have used these structures to study the $\alpha_v\beta_3$ and $\alpha_{IIb}\beta_3$ activation process by simulating the complete integrin extracellular domains and using external force to unbend the integrin leg domains [91, 112]. Without the application of force, it is unlikely the spontaneous straightening of the leg domains would have occurred within a timescale available to MD simulations [112].

In our MD study, only 8 simulations were conducted for each pH_e condition, although in Section 2.3 we suggest that 30 replicate simulations are necessary in order to adequately characterize rare events such as the headpiece opening conformational change. 30 simulations of 8 ns length for each pH_e condition would have been impractical with the available resources (~48 hr required to simulated 1 ns). As these simulations did not use external force to induce headpiece opening, there was no way to shorten the simulation timescale. Therefore, we tried to find a balance between simulating a long enough timescale to observe some headpiece opening while still conducting replicate simulations. However, it is possible that this limited number of simulations was inadequate for accurate characterization of headpiece opening propensity. Supplementing these simulations with complementary experimental approaches will address these methodological limitations and allow assessment of whether or not integrin activation is promoted at acidic pH_e for intact integrins on live cell surfaces.

2.5. SMD simulations of $\alpha_v\beta_3$-RGD: Within a single activation state, does acidic pH_e change $\alpha_v\beta_3$-RGD affinity via local changes to the binding pocket?

In Section 2.4, MD simulations were used to show that acidic pH_e promoted opening of the integrin $\alpha_v\beta_3$ headpiece. In the context of the full integrin, we predict that this would lead to an increase in the number of activated integrins present on the cell surface at acidic pH_e, which would alter overall cell-matrix binding. It is possible that acidic pH_e might independently change integrin-ligand affinity by locally altering the properties of the integrin binding pocket; for example, an activated integrin at pH_e 7.4 may have a different binding affinity than an activated integrin at pH_e 6.0. In this section, steered molecular dynamics is utilized to investigate the effect of acidic pH_e on $\alpha_v\beta_3$-RGD rupture forces and unbinding rates. SMD enables atomistic characterization of the effect of pH_e on unbinding mechanisms, and also allows us to easily decouple the effects of pH_e on activation from effects on unbinding, as integrin conformations can be directly observed in simulations.

2.5.1. Simulation system and pulling methods

Craig et al. previously used SMD simulations to study $\alpha_v\beta_3$-RGD unbinding [46]. While these simulations provided valuable information about unbinding mechanisms and the role of metal ions in the $\alpha_v\beta_3$-RGD interaction, the influence of extracellular conditions such as pH_e was not addressed. However, the simulations of Craig et al. were very valuable in informing our simulation setup. The molecular system for our SMD simulations was the same as for the headpiece opening simulations described in Section 2.4: the integrin $\alpha_v\beta_3$ headpiece domains in complex with a cyclic RGD pentapeptide. Initial bound configurations were chosen from the MD trajectories described in Section 2.4, but only conformations with a closed headpiece ($d < 4.28$ nm) were used as input for SMD simulations, so that results were not convoluted by the effects of headpiece opening on binding affinity. A computational spring of stiffness 4.14 N/m and velocity ranging from 0.2 – 2 m/s was used to pull the RGD ligand out of the integrin binding pocket. The spring stiffness and fastest velocity were chosen to enable comparison to the simulations of Craig et al. [46], and three loading rates spanning one order of magnitude were simulated in order to enable application of a modified Bell-Evans model to extract kinetic and energetic parameters of unbinding [139].

2.5.2. SMD results: rupture forces and unbinding rates

As described in Section 2.3, to accurately characterize properties such as rupture force F_R with atomistic simulation techniques, it is necessary to choose a representative set of initial configurations to use as input for production-run SMD simulations, which requires testing for a configuration-property correlation with a method such as clustering analysis. Here, $\alpha_v\beta_3$-RGD configurations taken from MD equilibration trajectories were clustered based on the positions of the atoms in the integrin binding pocket. SMD simulations were first conducted for the normal pH_e cluster centroids to generate an initial set of test configurations, and rupture force values were measured from these simulated data. Before testing for configuration-property correlations for the $\alpha_v\beta_3$-RGD system, we first validated our simulation protocol by comparing our force-extension data to Craig et al.'s results. Although we observe significant variation in simulated force-extension responses due to the multiple initial configurations that were used for SMD, in certain cases, our rupture force and extension agree very well with Craig et al.'s published values [46] (Figure 2.9).

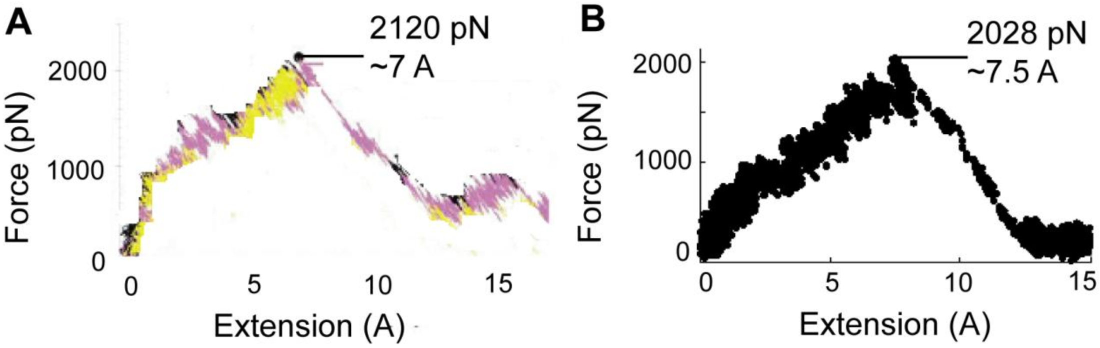

Figure 2.9 (A) SMD force vs. extension trace at loading rate $F' = 8.28$ N/s published by Craig et al [46]. (B) SMD force vs. extension trace obtained with our simulation protocol.

Craig et al. demonstrated that the coordination between the acidic ASP residue in the RGD ligand (ASP_{RGD}) and the divalent cations in the integrin binding pocket is critical to the $\alpha_v\beta_3$-RGD binding strength [46]. Although ASP_{RGD} contacted only the MIDAS ion in the initial crystal structure [45], in our equilibration MD trajectories ASP_{RGD} sometimes reoriented to contact both the MIDAS and LIMBS ions, or occasionally just the LIMBS ion[2]. Craig et al. reported that F_R was highest when ASP_{RGD} contacted both the MIDAS and LIMBS ions, lower when ASP_{RGD} contacted the MIDAS ion alone, and lower still when ASP_{RGD} contacted the LIMBS ion alone [46]. However, only one simulation was conducted for each of these cases, and as a result, the variation in F_R for each of these ion coordination states is unknown. In spite of this very limited sampling, Craig et al.'s data suggest that configuration-property correlations may exist for the $\alpha_v\beta_3$-RGD system. Therefore, we took this information into account as we designed test simulations to further characterize the relationship between initial bound configuration and F_R for this receptor-ligand pair.

Our set of cluster centroids included initial bound configurations in each of the three possible ASP_{RGD} ion coordination states. We used these centroids to test whether the correlation between initial ASP_{RGD} ion coordination state and output $\alpha_v\beta_3$-RGD F_R that was reported by Craig et al. could be reproduced using our simulation protocol. The set of cluster centroids was split into subgroups based on initial ASP_{RGD} ion coordination state, and the distribution of rupture forces for each subgroup was compared to the full distribution of rupture forces. The distributions for the MIDAS subgroup and LIMBS subgroup were narrower than that for the full set of rupture forces, although the MIDAS + LIMBS distribution was approximately as wide as that for the full set of rupture forces (Figure 2.10). Configurations with ASP_{RGD} coordinated to the MIDAS ion only tended to

---

[2] These ion coordination states will be referred to as follows: "MIDAS": ASP_{RGD} contacts only the MIDAS ion, "LIMBS": ASP_{RGD} contacts only the LIMBS ion, "MIDAS + LIMBS": ASP_{RGD} contacts both the MIDAS and LIMBS ions.

have lower rupture forces than those with ASP_{RGD} coordinated to the LIMBS ion only. This indicates that initial ASP_{RGD} ion coordination state does correlate with the $\alpha_v\beta_3$-RGD rupture force to some extent, although our more extensive sampling has revealed a different correlation than that reported by Criag et al. This correlation should be taken into account when characterizing $\alpha_v\beta_3$-RGD unbinding properties as a function of pH_e.

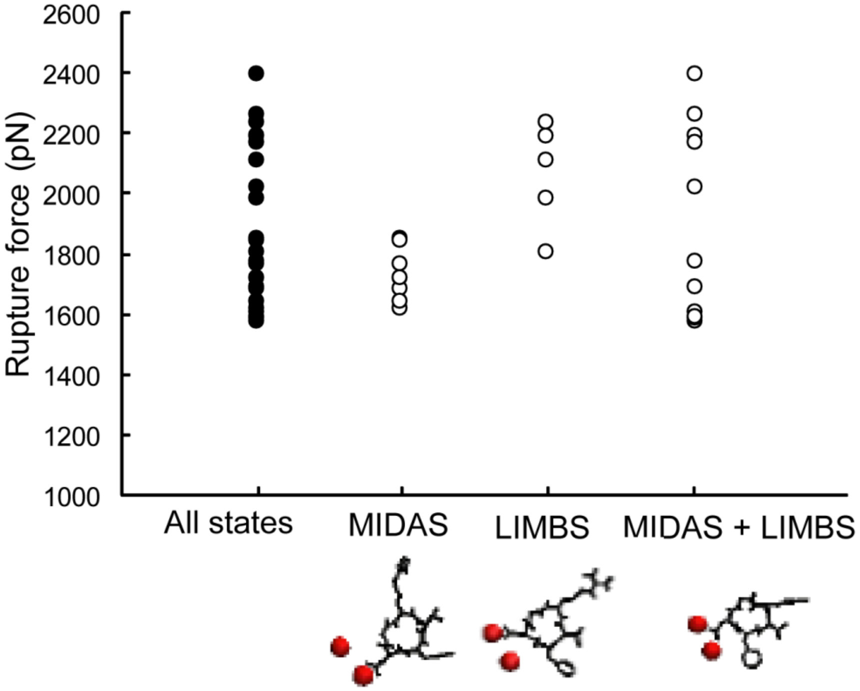

Figure 2.10 $\alpha_v\beta_3$-RGD rupture forces obtained from SMD simulations. Filled circles are rupture forces for the entire group of cluster centroids for normal pH_e. Open circles are subgroups of cluster centroid rupture forces, based on initial ASP_{RGD} ion coordination state. Ball-and-stick diagrams illustrate the RGD ligand (black sticks) and MIDAS (bottom red ball) and LIMBS (top red ball) ions. The distribution of rupture forces for the MIDAS subgroup and LIMBS subgroup is narrower than that for the full set of rupture forces.

We next tested whether further configurational differences within each ion coordination subset were correlated with rupture force. A single configuration was chosen from each subset, and 10 SMD simulations were run with this initial configuration, each with a different set of initial atomic velocities. We found that for each ion coordination subset, the rupture force variation among different configurations was approximately the same as the variation among different initial atomic velocities for a single initial configuration (Figure 2.11). Taken together with Figure 2.10, this indicates that the initial ASP_{RGD} ion coordination state is the dominant structural feature that determines binding affinity and output F_R, and that further configurational differences within each ion coordination state do not correlate with F_R. Therefore, the frequency of occurrence of each ion coordination state should be carefully accounted for when comparing rupture forces as a function of each pH_e, but the particular configurations within each ion coordination state can be chosen randomly.

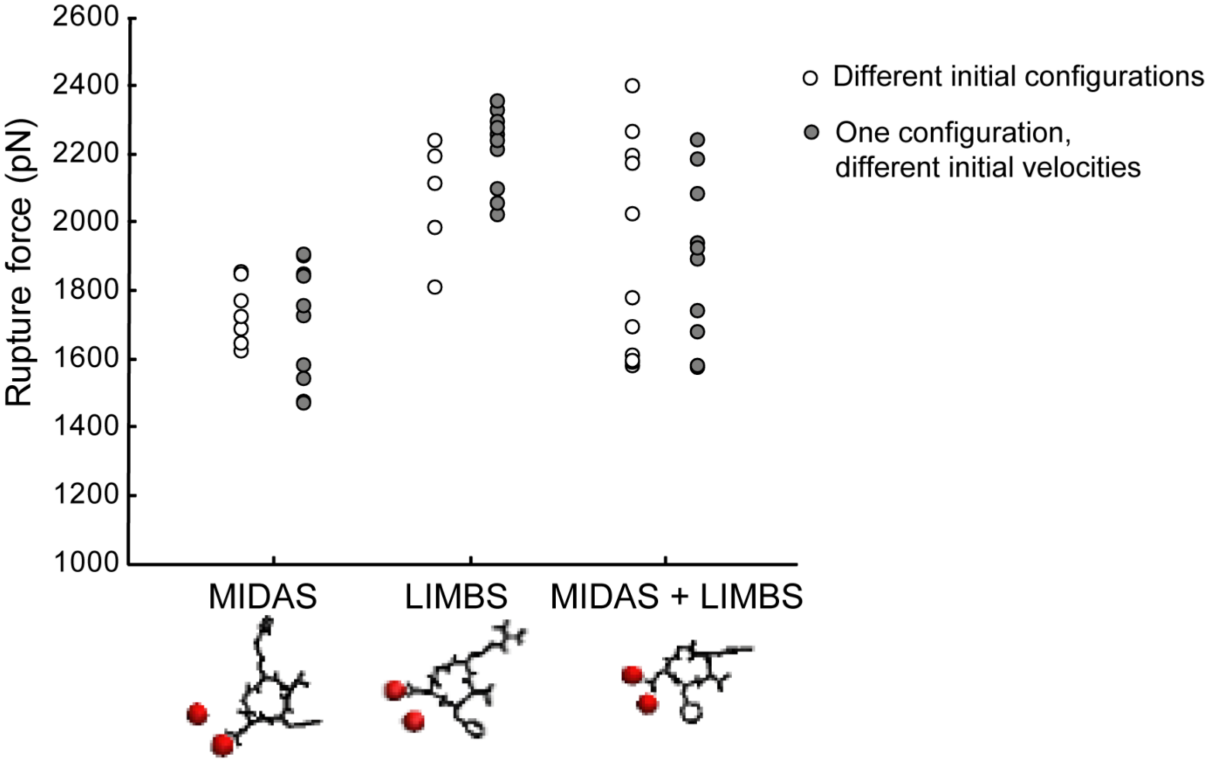

Figure 2.11 Comparison of rupture force distributions from cluster centroids with different atomic configurations (open circles) and a single configuration with different initial atomic velocities (gray filled circles) for each initial ion coordination state.

To characterize F_R as a function of $\mathrm{pH_e}$, SMD simulations were run for all cluster centroids from the normal and acidic $\mathrm{pH_e}$ equilibration trajectories at three loading rates. Cluster centroids with $\mathrm{ASP_{RGD}}$ coordinated to only the LIMBS ion were not used, as this particular ion coordination state did not occur at all in Craig et al.'s simulations or in the $\alpha_v\beta_3$-RGD crystal structure [45, 46], and it is unclear if this coordination would occur for a real integrin-ligand pair. Therefore, the set of initial configurations for SMD simulations included the MIDAS and MIDAS + LIMBS coordination states. Nineteen initial configurations were simulated for each $\mathrm{pH_e}$ condition at each loading rate. Rupture forces were weighted according to the frequency of occurrence of each ion coordination state in the equilibration simulation trajectories[3] to calculate average F_R for each $\mathrm{pH_e}$ condition at each loading rate.

There was no significant difference between average rupture forces at normal $\mathrm{pH_e}$ vs. acidic $\mathrm{pH_e}$ for any of the three loading rates tested. Average rupture forces were also plotted as a function of the logarithm of the loading rate (Figure 2.12). According to the Bell-Evans model, this dependence should be linear (Eq. 2.1), and our data fit reasonably well to this model. Parameters extracted using a modified Bell-Evans model [139] are given in Table 2.2. There was no statistically significant difference in the distance between the bound state and energetic maximum x_b for normal vs. acidic $\mathrm{pH_e}$. The unbinding rate k_{off} for

---

[3] Frequencies of occurrence in equilibration trajectories for each ion coordination state were: Normal $\mathrm{pH_e}$: 56.25% MIDAS, 43.75% MIDAS + LIMBS; Acidic $\mathrm{pH_e}$: 58.75% MIDAS, 41.25% MIDAS + LIMBS.

acidic pH_e is more than an order of magnitude greater than that for normal pH_e, but in spite of this apparently large change, the difference in k_{off} was not statistically significant. This is due to the fact that a small variation in F_R can give rise to a very large variation in k_{off}, due to the exponential function in the equation for k_{off}. Thus, the standard errors of the mean for k_{off} were extremely large (~700% of the mean), and we can only tentatively conclude that acidic pH_e does not significantly alter k_{off}.

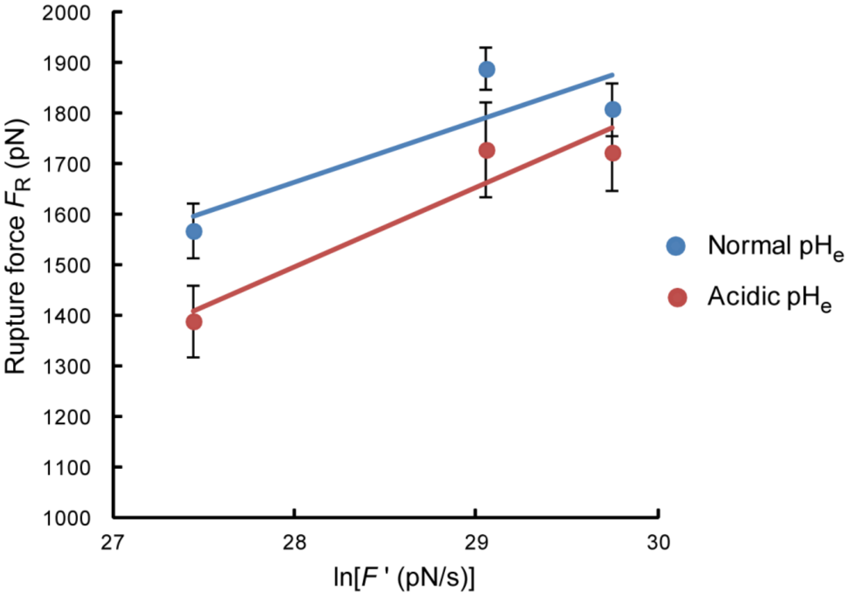

Figure 2.12 Average rupture forces as a function of ln(F') for normal and acidic pH_e simulations, with best fit lines. There was no significant difference between average rupture force at normal vs. acidic pH_e for any of the three loading rates tested. Error bars are SEM.

pH_e	Best fit slope	Best fit intercept	R^2	x_b (nm)	k_{off} (s^{-1})
Normal	121.45 ± 29.49	-1735.1 ± 852.8	0.7383	.034 ± 0.0082	$2.34 \times 10^4 \pm 1.65 \times 10^5$
Acidic	156.58 ± 35.8	-2886.4 ± 1030.2	0.9061	.026 ± 0.006	$9.15 \times 10^5 \pm 6.02 \times 10^6$

Table 2.2 Parameters from best fit lines and application of a modified Bell-Evans model [139]. Errors are SEM and were obtained by a bootstrapping sampling method (slope and intercept) and error propagation (x_b and k_{off}).

2.5.3. Discussion of SMD results

Our SMD simulation results clearly demonstrated that the integrin $\alpha_v\beta_3$-RGD unbinding force was correlated with the initial ion coordination state of ASP_{RGD}. Configurations with ASP_{RGD} coordinated to the MIDAS ion alone tended to have lower rupture forces than configurations with ASP_{RGD} coordinated to the LIMBS ion alone. Configurations with ASP_{RGD} coordinated to both the MIDAS and LIMBS ion displayed a wide range of rupture forces. Our data differ from the results of Craig et al., who reported that the rupture force was lowest when ASP_{RGD} was coordinated to the LIMBS ion alone [46].

This discrepancy is likely due to the fact that Craig et al. only conducted one simulation per condition and did not sample the F_R variation for each ion coordination state. Such limited sampling could easily have lead to mischaracterization of the dependence of F_R on ASP_{RGD} ion coordination. Our data characterizing this dependence have significantly extended the work of Craig et al. Although our findings are interesting, it is unclear if they can be tested experimentally, as a real integrin-ligand system may switch rapidly between different ion coordination states in an experimental timescale. Further, it is possible that the MIDAS + LIMBS and LIMBS coordination states are simulations artifacts, as there is no crystal structure evidence for these ASP_{RGD} coordinations.

Our SMD data do not support the conclusion that there is a difference in $\alpha_v\beta_3$ rupture force between normal and acidic pH_e, as there were no statistically significant differences in average F_R for any of the three loading rates we tested. Furthermore, there were no statistically significant differences in the x_b and k_{off} values calculated using a modified Bell-Evans model [139], although the standard errors of the mean for k_{off} were so large that no strong conclusion can be drawn from this finding.

For the simulations comparing normal and acidic pH_e, 19 initial configurations were simulated for each pH_e condition at each loading rate. However, given the dependence of F_R on initial ASP_{RGD} coordination and the recommendations outlined in Section 2.3, a truly accurate characterization of F_R distribution would require 30 simulations for each ion coordination state, which should then be weighted according to frequency of occurrence in equilibration simulations. Thus, three loading rates for two pH_e values would require 180 independent simulations, likely totaling more than 1 μs of simulated time. This amount of simulation was not feasible with our computational resources. Furthermore, accurate weighting of rupture forces requires accurate characterization of the frequency of occurrence of each ASP_{RGD} ion coordination state. It is unclear if our eight equilibration simulations at each pH_e condition (8 ns each) were sufficient to properly characterize these ion coordination states.

Our simulated average F_R values and calculated x_b and k_{off} values are certainly subject to error due to limited sampling. However, given the extremely large uncertainty in k_{off}, it is unlikely that further simulations would have enabled us to draw much better conclusions about the effect of extracellular pH on unbinding rates. In addition, SMD-derived k_{off} values will not match experimentally-derived parameters and thus have limited applicability [138, 140]. Furthermore, our SMD simulations were conducted with the closed headpiece conformation, as there is no crystal structure available for ligand-bound $\alpha_v\beta_3$ with a fully open headpiece. It is unclear if unbinding studies on this closed headpiece system are relevant to real integrin-ligand pairs, which would exist in the activated conformation. Therefore, there is limited knowledge to be gained from further SMD simulations, and we chose to focus on experimental approaches for further characterization of $\alpha_v\beta_3$-RGD unbinding as a function of pH_e.

2.6. Conclusions and transition to molecular-scale experiments

2.6.1. Conclusions

In this chapter, we first outlined a general methodology for choosing representative initial configurations to use for characterizing rare event property distributions in atomistic simulations, and offered guidelines for the number of simulations required for accurate characterization. We then conducted molecular dynamics simulations of the integrin $\alpha_v\beta_3$ headpiece in complex with an RGD peptide, and found that acidic extracellular pH promoted opening of the integrin headpiece. We posit that this effect is at least partially due to protonation of ASPβ127. In the protonated state, ASPβ127 cannot coordinate the ADMIDAS ion, which changes the dynamics of the critical α1-β1 loop and α1 helix. From our MD results, we predict that integrin activation will be promoted at acidic pH_e and that as a result, there will be more activated integrins on the live cell surfaces at acidic pH_e. Finally, we performed SMD simulations to study $\alpha_v\beta_3$-RGD unbinding as a function of pH_e, and found that rupture forces correlated to some extent with the initial ASP_{RGD} ion coordination state, underscoring the importance of divalent cations in modulating integrin binding affinity. Furthermore, we found that rupture forces and unbinding rates were statistically indistinguishable between normal and acidic pH_e, indicating that acidic pH_e does not directly alter $\alpha_v\beta_3$-RGD binding affinity via local changes to the integrin binding pocket. However, this conclusion remains tentative due to limited sampling.

2.6.2. Next question: Can these predictions be experimentally validated?

The atomistic simulation techniques utilized in this chapter allowed us to gain mechanistic insight into how acidic extracellular pH affects integrin activation and binding. In the next chapter, we utilize molecular-scale experimental methods to test the simulation predictions. First, flow cytometry is used to compare the amount of activated integrins on live cell surfaces at a range of pH_e values. Next, atomic force microscope (AFM)-enabled molecular force spectroscopy is used to measure $\alpha_v\beta_3$-RGD binding frequency and rupture force at acidic and normal pH_e values. These AFM forced unbinding experiments allow us to test our MD predictions about integrin activation as well as our SMD conclusions about the effect of acidic pH_e on $\alpha_v\beta_3$-RGD binding affinity.

2.7. Acknowledgments

E.B. Walton Vinocur contributed to the data analysis, interpretation of results, and manuscript editing for the study on using replicate simulations to characterize rare event property distributions (Section 2.3).

Chapter 3: Molecular-scale experiments

Sections 3.2 – 3.3 include material that was published in Ref. [85]. For that publication, R.K. Paradise designed experiments, collected, analyzed, and interpreted data, and wrote the manuscript.

3.1. Overview

In Chapter 2, atomistic-scale simulations were used to make predictions about the effects of acidic pH_e on activation propensity and binding affinity of integrin $\alpha_v\beta_3$. MD simulations demonstrated that the $\alpha_v\beta_3$ headpiece reached a partially open state more frequently at acidic pH_e, and we predicted that in the cellular context, this would lead an increased number of fully activated integrins. Furthermore, our SMD simulations indicated that for integrins in a single activation state, $\alpha_v\beta_3$-RGD rupture forces and unbinding rates do not vary significantly as a function of pH_e. In this chapter, we use flow cytometry and atomic force microscope (AFM)-enabled molecular force spectroscopy to test these simulation predictions for intact integrins on live cells. Flow cytometry experiments with the activation-specific antibody WOW-1 Fab demonstrate that the level of activated $\alpha_v\beta_3$ is higher for cells exposed to pH_e 6.0 than for cells exposed to pH_e 6.5 – 8.0. AFM-enabled molecular force spectroscopy experiments demonstrate that $\alpha_v\beta_3$-RGD binding frequency is higher at pH_e 6.0 than at pH_e 7.4, but that the mean $\alpha_v\beta_3$-RGD rupture force does not change. These data are consistent with our molecular dynamics simulations and indicate that acidic extracellular pH promotes activation of integrin $\alpha_v\beta_3$ in the live cell context.

3.2. Flow cytometry

3.2.1. Results

In order to investigate the effect of acidic extracellular pH on integrin activation on live cell surfaces, we conducted flow cytometry experiments using antibody WOW-1 Fab, which binds preferentially to the activated conformation of $\alpha_v\beta_3$. This antibody was created by modification of the $\alpha_{IIb}\beta_3$ ligand-mimetic antibody PAC1 Fab [109], and has been widely used in the literature to study $\alpha_v\beta_3$ conformational regulation [83, 90, 98, 180, 181].

Flow cytometry experiments were performed on $\alpha_v\beta_3$ CHO-B2 cells. These cells were engineered by others to express the β_3 integrin subunit, and the parental cell line CHO-B2 does not bind the RGD sequence [182]. To confirm the specificity of WOW-1 binding to activated $\alpha_v\beta_3$, control experiments were conducted measuring WOW-1 binding in the presence of different divalent cations (Figure 3.1A). WOW-1 binding was lowest on CHO-B2 pCDNA cells, which do not express the integrin β_3 subunit. Of the divalent ions tested, Ca^{2+} is known to stabilize the inactive integrin conformation [80, 86, 87], and cells in the presence of Ca^{2+} displayed the lowest level of WOW-1 binding. Mn^{2+} is known to promote integrin activation [80, 86, 87], and cells exposed to Mn^{2+} displayed the highest level of WOW-1 binding. An intermediate level of WOW-1 binding was observed in the presence of Mg^{2+}, and all the following pH_e experiments were performed with this ion. Although the difference in fluorescence intensity between Mn^{2+}-stimulated cells and negative control CHO-B2 pCDNA cells was small, the fold change we observed is comparable to that reported by others for this antibody [83, 109] (Figure 3.1B).

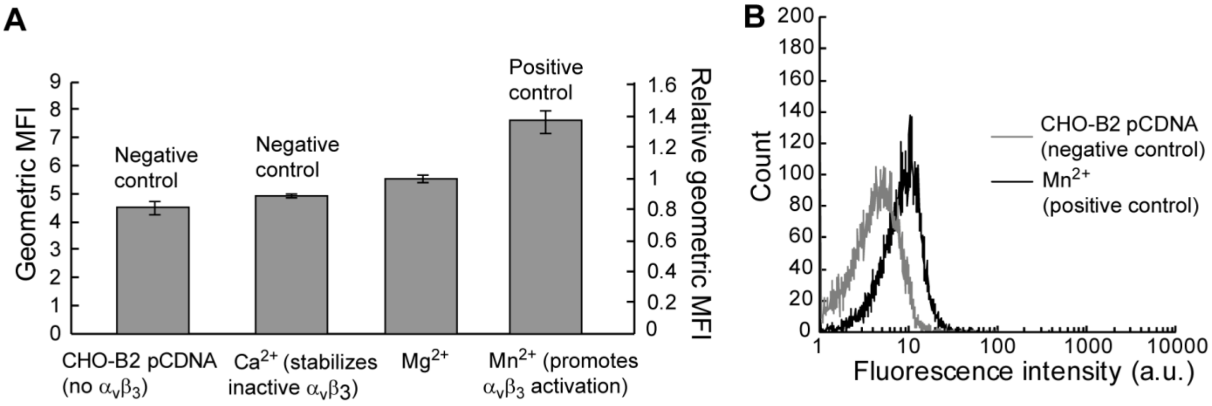

Figure 3.1 Control experiments confirming WOW-1 specificity. (A) WOW-1 Fab binding in the presence of various divalent cations. CHO-B2 pCDNA cells (negative control) do not express $\alpha_v\beta_3$, Ca^{2+} (negative control) stabilizes inactivate $\alpha_v\beta_3$, and Mn^{2+} (positive control) promotes $\alpha_v\beta_3$ activation. Data are displayed as the average geometric mean fluorescence intensity (MFI) of triplicate samples from a single representative experiment (primary axis), as well as the normalized geometric MFI expressed relative to the average value measured in the presence of Mg^{2+} ions (secondary axis), to enable direct comparison to Figure 3.2. (B) Representative flow cytometry fluorescence intensity histograms illustrating WOW-1 Fab binding for CHO-B2 pCDNA cells, which do not express the integrin β_3 subunit, and $\alpha_v\beta_3$ CHO-B2 cells exposed to Mn^{2+}, which activates integrin $\alpha_v\beta_3$. Error bars are SEM. Figure from Ref. [85].

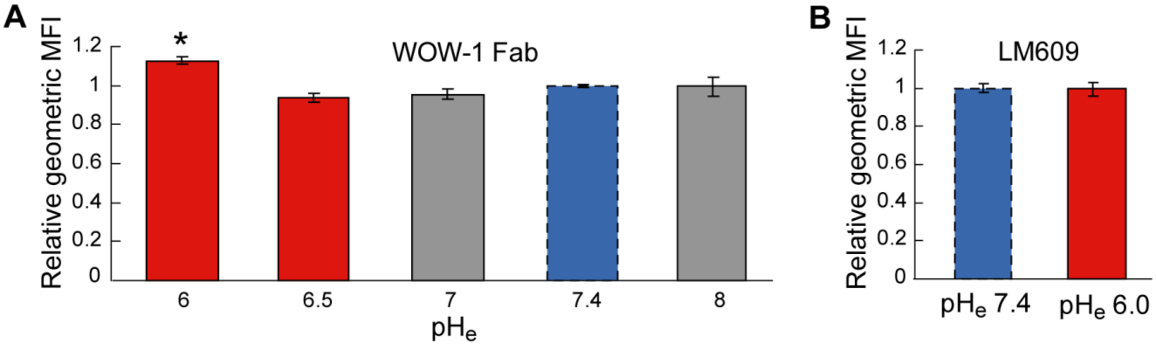

Figure 3.2 (A) WOW-1 Fab binding after exposure to pH_e 6.0 – 8.0. WOW-1 Fab binds preferentially to the activated conformation of $\alpha_v\beta_3$. Data are normalized geometric MFI at each pH_e expressed relative to the average value measured at pH_e 7.4. Average data were calculated from at least two independent experiments at each pH_e. Asterisk indicates $p < 0.01$ with respect to all other pH_e conditions. Red bars indicate acidic conditions, and blue bar outlined with dashed line indicates physiological pH_e 7.4. (B) LM609 binding after exposure to pH_e 6.0 or 7.4. LM609 is an antibody that binds all conformations of $\alpha_v\beta_3$. Data are expressed as in (A). Error bars are SEM. Figure from Ref. [85].

We next measured the level of activated $\alpha_v\beta_3$ on cell surfaces after exposure to pH_e values in the range 6.0 – 8.0. Cell shrinkage and detachment indicated a decrease in cell viability at $pH_e \leq 5.5$; therefore these lower pH_e values were not assessed via flow cytometry. The levels of WOW-1 binding after exposure to pH_e 6.5, 7.0, and 8.0 were statistically indistinguishable from that at normal physiological pH_e 7.4; however, exposure to pH_e 6.0 resulted in a significantly higher level of binding (Figure 3.2A). We used antibody LM609, which binds both the activated and inactivated conformation of $\alpha_v\beta_3$, to assess whether exposure to pH_e 6.0 changed the overall cell surface expression level of integrin $\alpha_v\beta_3$. We found that the $\alpha_v\beta_3$ expression level on the cell surface after exposure to pH_e 6.0 was indistinguishable from that at pH_e 7.4 (Figure 3.2B). Therefore, our flow cytometry results indicate that exposure to an acidic pH_e of 6.0 results in an increased level of activated $\alpha_v\beta_3$ on live cell surfaces.

3.2.2. Discussion of flow cytometry results

Our flow cytometry results indicated an increased number of activated $\alpha_v\beta_3$ integrins on live cell surfaces after exposure to pH_e 6.0 (Figure 3.2). This is consistent with our molecular dynamics data demonstrating that acidic extracellular pH promotes $\alpha_v\beta_3$ headpiece opening. It is important to note that in our flow cytometry assay it was necessary to perform the antibody-labeling step at pH_e 7.4 to ensure maximal antibody binding. The fact that our data showed an increase in WOW-1 binding after exposure to pH_e 6.0 in spite of the pH_e change during antibody binding indicates that the activated integrin conformation can persist to some extent after cells are returned to pH_e 7.4. This is consistent with the results of Tzima et al., which demonstrated that even after removal of an activating stimulus, $\alpha_v\beta_3$ integrins stay activated long enough to be labeled with WOW-1 Fab (i.e., ~30 min post-activating stimulus) [90]. However, the levels of activated $\alpha_v\beta_3$ we measured after exposure to pH_e 6.5 and pH_e 7.0 were not higher than that at pH_e 7.4, indicating that some level of reversal in activation state may occur after cells are returned to pH_e 7.4. Accordingly, it is plausible that acid-induced integrin activation also initially occurred in the pH_e 6.5 and 7.0 conditions, though to not as great a magnitude as for pH_e 6.0, so that detection in this assay was suppressed during the antibody binding step.

3.3. AFM-enabled molecular force spectroscopy

3.3.1. Introduction to AFM methodology

Atomic force microscope (AFM)-mediated molecular force spectroscopy (MFS) is the experimental counterpart to SMD simulations and enables characterization of interactions between single ligand-receptor pairs. In a typical AFM-MFS experiment, an AFM cantilever is functionalized with ligand molecules, often using flexible linkers such as polyethylene glycol (PEG). The cantilever is brought into contact with a surface or cell expressing receptors for the ligand of interest, thus creating the potential for a ligand-receptor binding event to occur (Figure 3.3A-B). After contacting the surface, the cantilever is retracted. If a ligand-receptor binding event occurs, this will exert a force on the cantilever during the retraction, which is released when the ligand-receptor complex ruptures. Throughout the approach-retract cycle, the cantilever deflection is recorded by a laser that is reflected off of the back of the cantilever onto a photodiode. This deflection can be multiplied by the cantilever spring constant to calculate the force applied to the cantilever, thus enabling measurement of the ligand-receptor rupture force F_R and effective stiffness of the bound complex k_{eff}. In the retraction portion of a force vs. displacement trace (Figure 3.3C), F_R is the magnitude of the jump in force, and k_{eff} is the absolute value of the slope immediately before rupture. Note that k_{eff} depends on the stiffness of the ligand-receptor complex, as well as the stiffness of the cantilever, cell, and flexible linker used for functionalization. The effective loading rate F'_{eff} is the product of k_{eff} and the cantilever velocity v. The rupture force is a function of loading rate, and it is possible to use F_R values obtained at different loading rates to extract kinetic and energetic parameters of unbinding through the application of modified Bell-Evans models [137-139].

AFM-MFS enables the study of ligand-receptor interactions at the single molecule level and can be performed with a variety of extracellular conditions. This approach is particularly valuable in combination with SMD simulations, as unbinding mechanisms characterized with SMD can be very useful for interpreting AFM-MFS force-displacement data. However, AFM-MFS experiments can be difficult to perform and are often very inefficient. In particular, achieving specific receptor-ligand binding can be very challenging, especially for experiments conducted on cell surfaces, where nonspecific adhesion is very likely to occur.

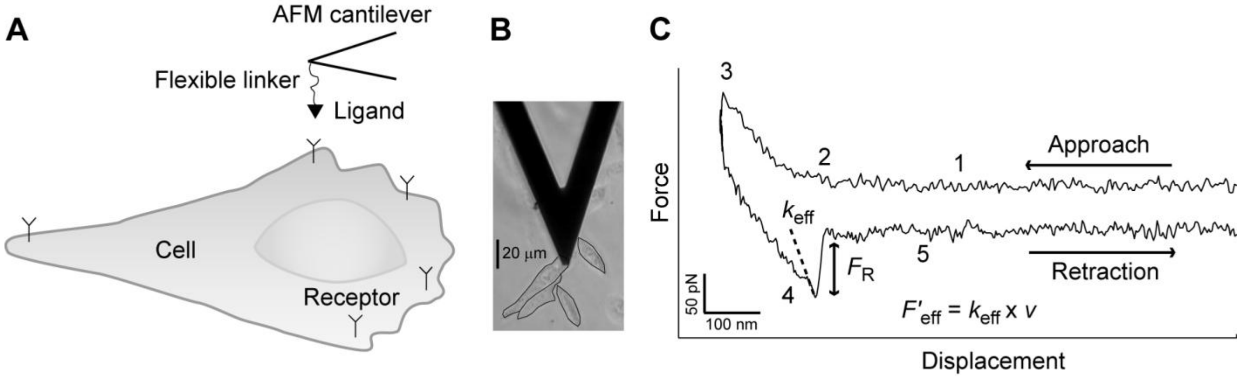

Figure 3.3 (A) Schematic depiction of a typical AFM molecular force spectroscopy setup with receptors expressed on the cell surface. (B) Optical image of an AFM cantilever positioned over an $\alpha_v\beta_3$ CHO-B2 cell. (C) A sample force-displacement trace during which a ligand-receptor binding interaction occurred. 1. Cantilever is above the cell surface; 2. Cantilever contacts the cell; 3. After indenting the cell briefly, cantilever begins to retract; 4. Immediately before rupture, the linker-ligand-receptor system is stretched; 5. The ligand-receptor complex has ruptured, and the cantilever is free of the cell. The offset in approach and retraction traces is due to fluid drag. Portions of figure are from Ref. [85].

MFS measurements have been performed on many integrin-ligand pairs such as $\alpha_5\beta_1$-fibronectin [106, 183, 184], $\alpha_4\beta_1$-VCAM-1 [107], and $\alpha_v\beta_3$-RGD ligand [114]. Of particular interest are the studies of Li et al. and Zhang et al., who reported that the integrin-ligand rupture force and binding frequency increased after integrin activation for $\alpha_5\beta_1$-fibronectin and $\alpha_4\beta_1$-VCAM-1, respectively [106, 107]. Thus, AFM-MFS can be used to assess integrin activation state as well as integrin-ligand unbinding properties.

3.3.2. Results

We conducted AFM-MFS experiments between RGD-functionalized cantilevers and $\alpha_v\beta_3$ CHO-B2 cells. In the RGD-functionalization protocol developed for this work, gold coated cantilevers are used to enable binding of a flexible PEG linker that is thiol terminated on one end and amine terminated on the other. In the second step of functionalization, the Sulfo-LC-SPDP cross-linker is bound to this PEG molecule. This cross-linker contains an amine reactive group on one end and a sulfhydryl-reactive group on the other and cross-links the amine terminated PEG linker to the cytsteine residue on a GRGDSPC peptide. The end result of this functionalization protocol is an RGD-containing peptide fuctionalized to the cantilever via a long flexible linker (Figure 3.4A). The linker increases the likelihood of receptor-ligand contact by giving the ligand spatial flexibility as the cantilever is brought toward the cell. To validate the functionalization chemistry, cantilevers were functionalized with the full protocol using a fluorescent GRGDSPC peptide, as well as with three negative control conditions: 1) no gold coating on the cantilever; 2) no PEG linker; 3) no Sulfo-LC-SPDP cross-linker. Comparison of fluorescent images demonstrated that the fully functionalized cantilevers had a better coating of GRGDSPC in all three cases (Figure 3.4B-D).

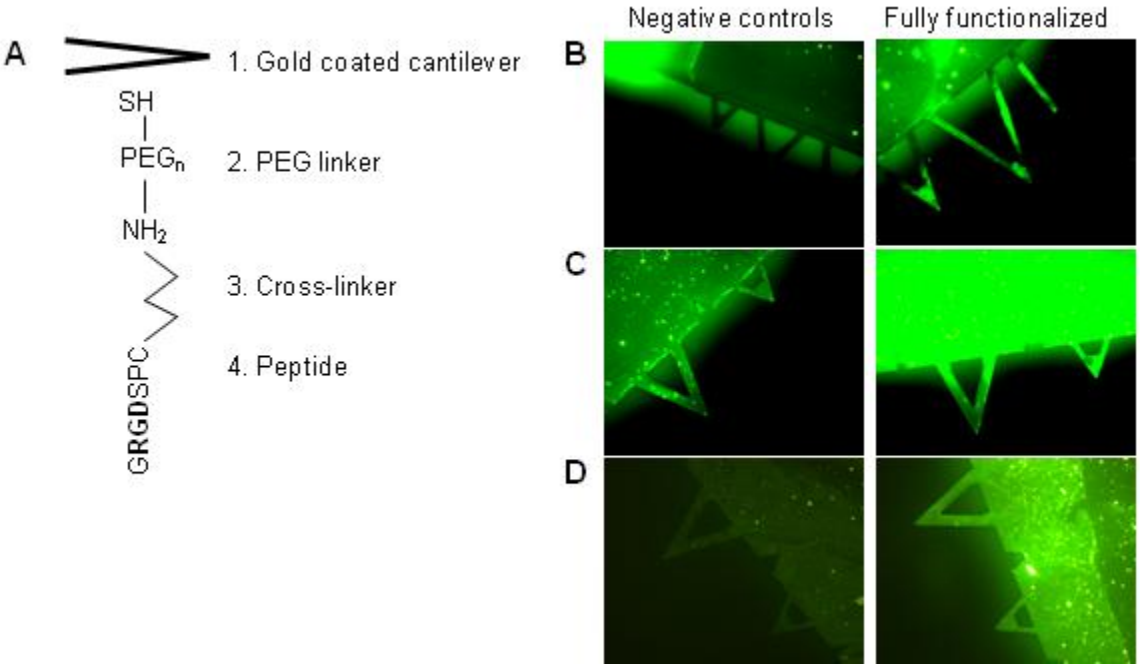

Figure 3.4 (A) Schematic of a RGD-functionalized cantilever illustrating the linkers used for functionalization chemistry. (B) Fully functionalized non-gold-coated cantilevers (left) compared with fully functionalized gold-coated cantilevers (right). (C) Gold-coated cantilevers functionalized without the PEG linker (left) compared with fully functionalized gold-coated cantilevers (right). (D) Gold-coated cantilevers functionalized without the cross-linker (left) compared with fully functionalized gold-coated cantilevers (right). Images within each pair (horizontal rows) were imaged on the same day and are displayed with the same contrast settings. However, different pairs were imaged on different days, and the three images of fully functionalized gold-coated cantilevers are not identical for this reason.

For our AFM-MFS experiments, the RGD-functionalized AFM cantilever was positioned over live $\alpha_v\beta_3$ CHO-B2 cells, far from the cell nucleus (Figure 3.3B), and 200 approach-retract cycles were performed for each cell. All experiments were conducted with cantilevers of the same stiffness and velocity, and thus had a single applied loading rate F'_{app}. Before characterizing $\alpha_v\beta_3$-RGD binding properties, it was first necessary to distinguish specific ligand-receptor binding events from nonspecific adhesion events between the cantilever and cell. The “gold standard” method for assessing specificity of interactions is to perform force spectroscopy before and after the addition of blocking agents, such as soluble ligands or antibodies, which occlude the receptor binding pockets and consequently prevent ligand binding. The goal of such experiments is to demonstrate that the interactions identified as specific occur infrequently after blocking. It is expected that specific receptor-ligand interactions will exhibit rupture forces F_R distributed around a characteristic value corresponding to the strength of the molecular complex at the particular loading rate used [106, 107]. Therefore, specific interactions in AFM-MFS experiments are usually identified by comparing histograms of rupture forces recorded before and after blocking, and identifying peaks that do not occur in the blocked condition. However, experiments conducted on live cell surfaces tend to have very high rates of nonspecific binding, and as a result, unblocked and blocked rupture force histograms may have considerable overlap. In such cases, it can be challenging to accurately identify specific interactions.

To minimize possible errors in identification of specific interactions in our experiments, we used the effective stiffness of the bound complex k_{eff} as an additional identifying characteristic that can be used to separate specific from nonspecific interactions, as we expect that k_{eff} should also be distributed around a characteristic value that reflects the stretching behavior of the receptor-ligand complex, molecular linkers, and cell immediately before rupture. Thus, the characteristic distributions of F_R and k_{eff} can be combined to effectively gate the specific interactions for each cell, despite the inherently large variation in experimental responses. This method of using both F_R and k_{eff} to identify specific binding interactions with high accuracy is novel and has not been previously demonstrated in the literature.

We conducted force spectroscopy measurements on cells before and after incubation with the antibody LM609, which blocks the RGD binding site on $\alpha_v\beta_3$. To simultaneously assess the measured F_R and k_{eff} distributions, we constructed heat maps illustrating the frequencies of occurrence of binding events with F_R and $k_{eff.}$within particular ranges (Figure 3.5). Analysis of heat maps for unbinding events before and after blocking demonstrated that events with $F_R > 50$ pN and $k_{eff} > 400$ pN/μm occurred frequently before, but not after, blocking the RGD binding site (Figure 3.5, region inside white lines). Quantification of the frequency of occurrence of interactions fulfilling these criteria for F_R and k_{eff} demonstrated that 16.80 ± 2.58% of the unblocked binding events pass this dual filter, compared to only 0.49 ± 0.49% of interactions after blocking (mean ± SEM). Therefore, rupture events with these characteristics were assumed to be specific $\alpha_v\beta_3$-RGD interactions, and all other events were assumed to be nonspecific (or more accurately, to be events which could not be objectively identified as specific). Additional negative controls were performed with cantilevers functionalized with linker molecules, but without GRGDSPC. In identical experiments conducted with these cantilevers, only 3.85 ± 1.75% (mean ± SEM) of the rupture events had $F_R > 50$ pN and $k_{eff} > 400$ pN/μm, confirming that events with these characteristics were specific receptor-ligand interactions that occurred infrequently in negative control experiments. Only these specific interactions were included in further analysis.

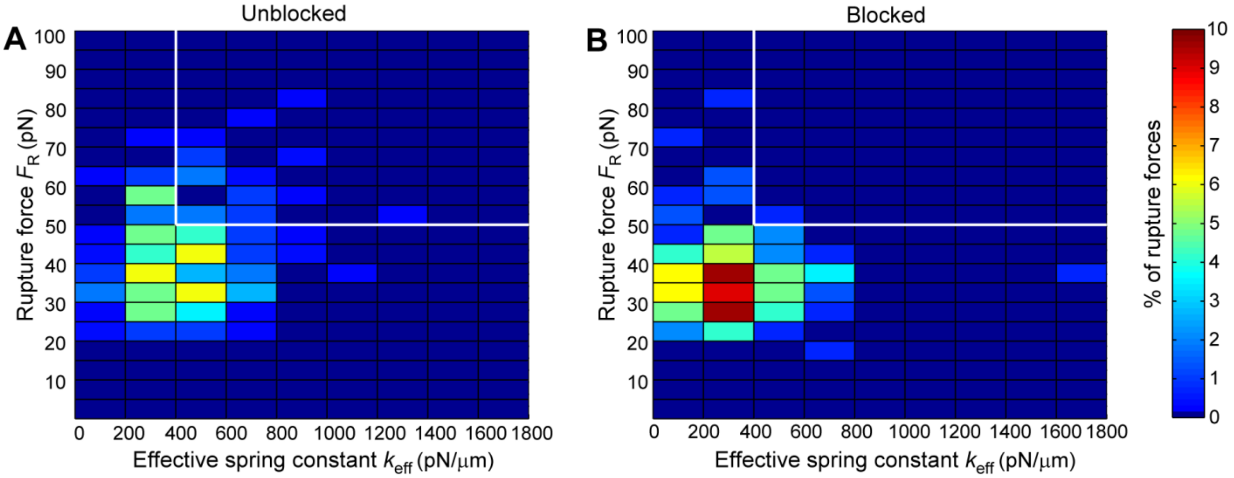

Figure 3.5 Heat maps illustrating the frequencies of binding events with F_R and k_{eff} within the indicated ranges. (A) Adhesion events before blocking the RGD binding site on $\alpha_v\beta_3$ with antibody LM609. (B) Adhesion events after blocking the RGD binding site on $\alpha_v\beta_3$ with antibody LM609. White lines outline region with $F_R >$ 50 pN and $k_{eff} >$ 400 pN/μm.

We performed AFM force spectroscopy experiments at pH_e 7.4 and pH_e 6.0. In addition, we performed a control experiment at pH_e 7.4 after incubation with antibody LIBS-6, which has been shown to activate $\alpha_v\beta_3$ [89]. As shown in Figure 3.5, within the single experimentally applied F'_{app} used for these experiments, we measured many values of k_{eff}, which results in a distribution of effective loading rates F'_{eff}. Measured specific rupture forces varied linearly with $\ln(F'_{eff})$, as predicted by the Bell-Evans model [137-139] (Figure 3.6A). However, the variation in F_R over this limited range of F'_{eff} was very small (<3 pN). Thus, for further analysis, all rupture forces were pooled together. Analysis of specific rupture forces revealed no significant differences in the mean rupture forces among the three conditions tested (Figure 3.6B). The similarity in mean rupture forces with and without LIBS-6 indicates that in our experimental system, $\alpha_v\beta_3$-RGD rupture forces do not detectably increase when the integrin is activated by antibody binding.

We also measured the $\alpha_v\beta_3$-RGD specific binding frequency f_b. Mean f_b at pH_e 7.4 increased after incubation with LIBS-6, demonstrating that a shift toward the activated state in the $\alpha_v\beta_3$ conformational equilibrium can be detected on intact cell surfaces as an increase in specific binding frequency. This is due to the much higher likelihood of the extended integrin conformations to bind the adhesive ligands, as compared to the bent conformation. Mean f_b was very low after blocking with LM609, confirming the specificity of the interactions chosen for analysis (Figure 3.6C).

We then normalized single-cell f_b values to the mean f_b measured at pH_e 7.4, to obtain the relative specific binding frequency $f_{b,rel}$; this normalization enabled us to combine data from replicate experiments conducted with different cantilevers. Comparison of $f_{b,rel}$ at pH_e 6.0 and pH_e 7.4 revealed that the mean $f_{b,rel}$ was significantly higher at pH_e 6.0 ($p < 0.05$, Figure 3.6D), although there was considerable variation in $f_{b,rel}$ among different cells within a given pH_e condition (Figure 3.6E). This trend was maintained in each of the three independent experiments we conducted. The shift in mean $f_{b,rel}$ cannot be explained by a change in the cell surface expression level of $\alpha_v\beta_3$, as demonstrated by our flow cytometry results with antibody LM609 (Figure 3.2B). In combination with the observation that binding frequency increases after activation by LIBS-6, these experimental data indicate that acidic extracellular pH$_e$ shifts the $\alpha_v\beta_3$ conformational equilibrium toward the activated state.

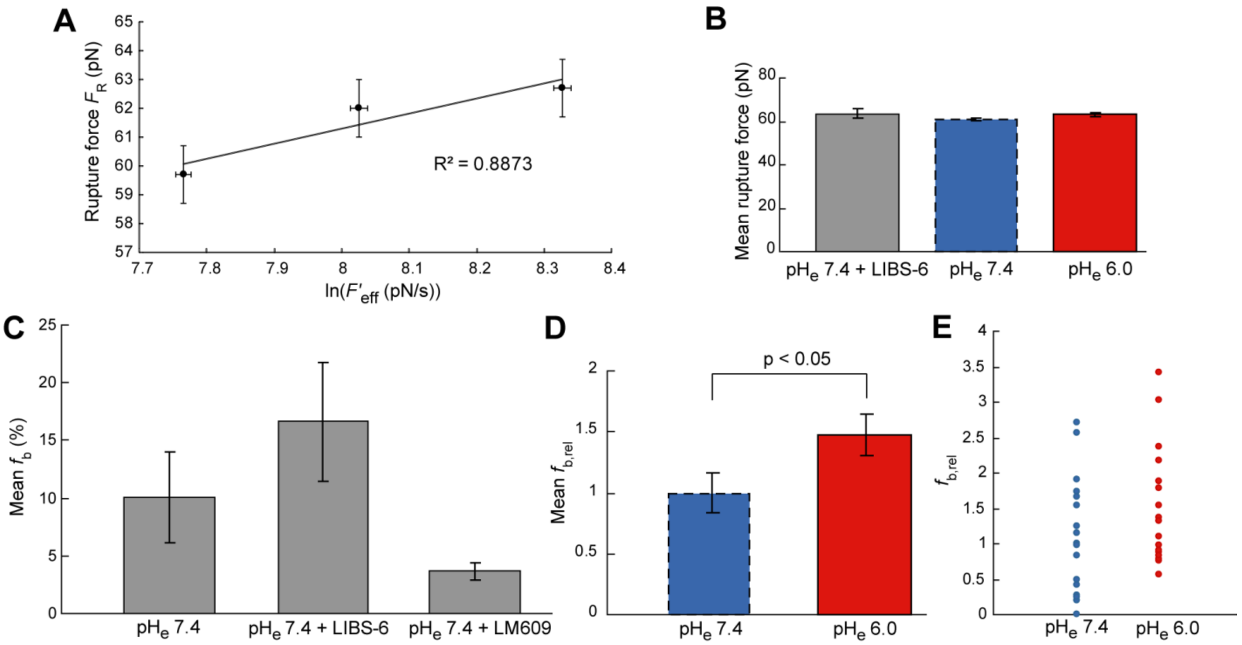

Figure 3.6 (A) Rupture forces at pH$_e$ 7.4 grouped by effective loading rate F'_{eff}. Data are consistent with the Bell-Evans model [137-139], even with the small range of F'_{eff} that we observed. (B) Mean rupture forces measured at pH$_e$ 7.4, pH$_e$ 7.4 after $\alpha_v\beta_3$ activation by antibody LIBS-6, and pH$_e$ 6.0. (C) Mean specific binding frequencies at pH$_e$ 7.4 before and after $\alpha_v\beta_3$ activation by antibody LIBS-6 or $\alpha_v\beta_3$ blocking by antibody LM609. (D) Mean specific binding frequencies at pH$_e$ 6.0 and pH$_e$ 7.4. Figure includes data from three independent experiments. For each experiment, the single-cell specific binding frequencies were normalized to the average value at pH$_e$ 7.4. These relative specific binding frequencies were then pooled and averaged. (F) Single cell specific binding frequencies used to calculate the average in (E). All error bars are SEM. Portions of figure are from Ref. [85].

3.3.3. Discussion of AFM-MFS results

Our AFM force spectroscopy data demonstrated that the specific $\alpha_v\beta_3$-RGD binding frequency increased at acidic pH$_e$, indicating an increase in the number of activated integrins (Figure 3.6). This finding is consistent with our flow cytometry results for cells exposed to pH$_e$ 6.0. We note that it is possible that the increase in integrin activation that we observed with AFM-MFS and with flow cytometry was not due to direct effects of acidic extracellular pH, but was rather due to acidification of intracellular pH and consequent changes to the integrin cytoplasmic domains or other intracellular molecules. For example, it is possible that intracellular pH changes altered talin-integrin binding in a way that increased the number of activated integrin receptors. However, our experiments are consistent with our molecular dynamics simulations demonstrating increased headpiece opening for $\alpha_v\beta_3$ in a cell-free system that did not include any cytoplasmic molecules (Section 2.4). Thus, these computational results suggest that extracellular acidification alone could have caused the increased integrin activation that we observed experimentally, although we do not have any direct proof of this for our molecular-level experiments. The role of intracellular acidification in our experiments will be further examined in Chapter 4.

Our AFM-MFS measurements also showed that the mean $\alpha_v\beta_3$-RGD rupture forces at pH_e 7.4 and pH_e 6.0 were very similar to that measured after $\alpha_v\beta_3$ activation by LIBS-6. We can speculate on a number of reasons underlying our observation that mean F_R did not increase upon activation. First, integrins are conformationally dynamic, and rearrange to the high-affinity state upon ligand binding [80]. Therefore, if RGD bound to a bent-closed or extended-closed integrin, the receptor may have rearranged to the extended-open conformation during our experimental contact time (>100 ms). Second, the bent-closed (low-affinity) conformation displays very low binding in other assays [80-82], so this conformation might not have been sampled substantively in our experiments. Finally, if RGD bound to a bent-closed or extended-closed integrin, and the receptor did not change conformation before unbinding, it is probable that the resulting rupture forces would be less than 50 pN and would not be distinguishable from nonspecific interactions in our analysis. Therefore, although the RGD ligand theoretically could have bound to any of the three integrin conformations, the measured mean specific F_R in our experimental system likely characterizes unbinding from the activated integrin conformation only, and thus would not be expected to reflect a shift in the conformational equilibrium.

In contrast to our results, previous AFM force spectroscopy studies by Li et al. and Zhang et al. reported that integrin activation increased the measured F_R for $\alpha_5\beta_1$-fibronectin [106] and $\alpha_4\beta_1$-VCAM-1 [107]. It is possible that there were fewer nonspecific interactions in those experiments, or that the rate of conformational switching is slower for the integrins they probed, enabling measurement of ligand unbinding from the low-affinity integrin conformation. We also note that Lehenkari and Horton reported an increase in $\alpha_v\beta_3$-RGD F_R at acidic pH_e [114]. It is possible that nonspecific adhesion was reduced in these experiments due to the use of fixed cells, and that this enabled measurement of rupture forces from different integrin activation states. If this was the case, then this early observation could be support our conclusion that acidic pH_e promotes integrin activation. However, the results of Lehenkari and Horton should be interpreted with caution. For example, in those experiments, the RGD peptides were noncovalently functionalized to the AFM cantilevers, which can result in detachment of RGD from the AFM probe during the repeated interactions with the cell surface and render it difficult to ensure specificity of measured rupture forces.

As discussed above, it is probable that the measured mean specific rupture forces at pH_e 7.4 and pH_e 6.0 characterize RGD unbinding from the activated conformation of $\alpha_v\beta_3$. Thus, these mean rupture forces can be compared with our SMD simulation results, which suggested that for integrins within a single conformational state, acidic extracellular pH does not change integrin-ligand binding affinity. Indeed, our experimental observation that there was no significant difference in mean F_R between pH_e 7.4 and pH_e 6.0 is consistent with our SMD rupture force results at normal and acidic pH_e. Because we only tested one applied loading rate in our AFM-MFS experiments, Bell's model cannot be used to calculate the energetic and kinetic unbinding parameters x_b and k_{off} (the range of F'_{eff} and F_R measured within the single experimentally applied loading rate and shown in Figure 3.6 is too narrow for accurate characterization of x_b and k_{off}). However, given the similarity in experimentally measured mean F_R at pH_e 7.4 and pH_e 6.0 at the single applied loading rate that was tested here, it is very unlikely that acidic extracellular pH directly alters x_b and k_{off} in this integrin-ligand system.

3.4. Conclusions and transition to subcellular-scale experiments

3.4.1. Conclusions

In this chapter, flow cytometry and AFM-enabled molecular force spectroscopy experiments were used to test simulation predictions about the effect of acidic extracellular pH on integrin $\alpha_v\beta_3$ activation and binding. AFM-MFS rupture force data demonstrated that the average $\alpha_v\beta_3$-RGD F_R does not change at pH_e 6.0 vs. pH_e 7.4, confirming our SMD simulation prediction that acidic extracellular pH does not directly alter $\alpha_v\beta_3$-RGD binding affinity via local changes to the integrin binding pocket. Furthermore, flow cytometry data showed that the level of activated $\alpha_v\beta_3$ on live cell surfaces increased for cells exposed to acidic pH_e, and AFM-MFS data demonstrated that $\alpha_v\beta_3$-RGD binding frequency increased at acidic pH_e. These results are consistent with our MD simulation predictions, and our combined simulation and experimental data thus suggest a model by which acidic extracellular pH promotes headpiece opening of integrin $\alpha_v\beta_3$ via protonation of ASPβ127. This could occur for integrins in the bent-closed or extended-closed conformation. The open headpiece destabilizes the bent conformation; therefore, acidic pH_e has the overall effect of shifting the integrin conformational equilibrium toward the high affinity extended-open state (Figure 3.7). In this manner, integrin $\alpha_v\beta_3$ can act as an extracellular pH sensor. Conformational regulation by extracellular pH is a novel mechanism of integrin activation that has not been previously described in the literature.

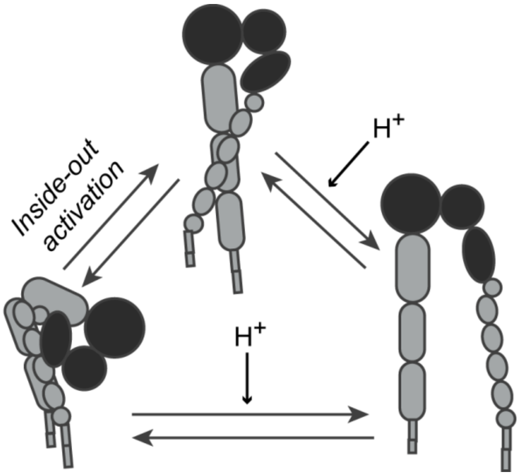

Figure 3.7 Model of pH_e-regulated integrin activation. Inside-out activation mechanisms can cause the bent-closed conformation to convert to the extended-closed conformation. Acidic extracellular pH can then promote headpiece opening to the extended-open conformation. In addition, acidic pH_e can stimulate headpiece opening on the bent-closed integrin, which is expected to lead to extension of the integrin legs. Through these dual mechanisms, acidic extracellular pH can shift the integrin conformational equilibrium to the high affinity extended-open state. Figure from Ref. [85].

3.4.2. Next question: How does increased integrin activation in acidic pH_e impact subcellular processes critical to cell adhesion and migration?

The experimental techniques utilized in this chapter allowed measurement of molecular-scale parameters such as the level of activated cell-surface $\alpha_v\beta_3$, $\alpha_v\beta_3$-RGD binding frequency, and $\alpha_v\beta_3$-RGD rupture force, and the results of these measurements enabled us to propose a model of acid-induced integrin activation. Next, we ask how this increased integrin activation in acidic extracellular pH affects two subcellular-scale processes that are critical to cell adhesion and migration: cell membrane dynamics and actin-integrin adhesion complex (AIAC) formation. In the next chapter, we use kymography to measure velocity and lifetime of cell membrane protrusions at acidic and normal pH_e, and assess the role of intracellular acidification in modulating membrane dynamics. We also transfect cells with a fluorescently labeled variant of the AIAC protein vinculin to enable characterization of AIAC number and size at acidic and normal pH_e. These subcellular-scale measurements extend our understanding of how acidic pH_e regulates cell-matrix interactions and resulting cellular processes.

Chapter 4: Subcellular-scale experiments

The material in Section 4.2.2 was published in Ref. [85]. For that publication, R.K. Paradise designed experiments, collected, analyzed, and interpreted data, and wrote the manuscript.

4.1. Overview

In Chapter 3, flow cytometry and AFM-enabled molecular force spectroscopy were used to study the effect of acidic extracellular pH (pH_e) on activation of integrin $\alpha_v\beta_3$ on live (non-fixed) cell surfaces. These molecular-scale experimental methods demonstrated that the amount of activated integrins increased at acidic pH_e, which was consistent with the molecular dynamics simulation results described in Chapter 2. In this chapter, we investigate how this increase in integrin activation affects two critical subcellular-scale processes that are modulated by integrin-ligand binding and are necessary for cell migration: cell membrane protrusion and focal adhesion formation. First, we use kymography to characterize $\alpha_v\beta_3$ CHO-B2 cell membrane protrusion lifetime and velocity at both normal and acidic pH_e. We also use this experimental technique to investigate whether intracellular acidification may play a role in causing the observed membrane dynamics effects. Kymography results demonstrate that cell membrane protrusion lifetime increases and protrusion velocity decreases in acidic pH_e, and that intracellular acidification alone is not sufficient to produce these results. Next, we transfect $\alpha_v\beta_3$ CHO-B2 cells with GFP-vinculin to enable visualization of actin-integrin adhesion complexes (AIACs), and characterize AIAC number and area for cells in normal and acidic pH_e. We find that cells in acidic pH_e on average have more AIACs than cells in normal pH_e 7.4, and that AIACs in acidic and normal pH_e can grow to the same average size. These data demonstrate that acidic extracellular pH can significantly alter subcellular-scale processes critical to cell migration.

4.2. Kymography

4.2.1. Background

In the first step of the cell migration process, the leading edge of a cell must protrude and form adhesions to the ECM or substratum. Membrane protrusion is often driven by actin polymerization, which is followed by integrin-ligand binding and formation of nascent adhesion sites just behind the leading edge [185]. Cell membranes often exhibit cycles of protrusion and retraction, and the retraction phases have been attributed to pulling forces exerted by myosin motors on actin fibers [48]. Several studies have shown that membrane dynamics can be modulated by cell-substratum adhesiveness[4] [48, 186-188]. For example, Bailly et al. demonstrated that for rat mammary carcinoma cells, cell-surface adhesion was not necessary for membrane protrusions to occur, as protrusion events were observed even when integrin binding was blocked or when cells were plated

---

[4] Here, the general term "adhesiveness" is considered to be a function of the number of receptor/ligand molecules available for binding as well as the receptor-ligand binding affinity. Adhesiveness increases with increased receptor/ligand numbers or higher binding affinity.

on nonadhesive surfaces. However, cell-surface adhesion stabilized protrusions, enabling them to last longer before retraction [186]. Harms et al. showed that for CHO cells, membrane protrusions were stabilized and had increased lifetime on substrata of increasing fibronectin coating concentration, but that the membrane protrusion velocity was independent of fibronectin coating concentration [187]. Gupton and Waterman-Storer demonstrated that for PtK$_1$ epithelial cells, membrane protrusion lifetime was positively correlated with fibronectin coating concentration [188]. Finally, Giannone et al. showed that for mouse embryonic fibroblasts, protrusion lifetime decreased on surfaces with a low fibronectin surface coating concentration, but protrusion velocity did not significantly change [48]. The general consensus among these studies is that protrusion lifetime increases in conditions of higher cell-substratum adhesiveness, but protrusion velocity does not change. Because changes in integrin activation propensity can also affect cell-matrix adhesiveness by modulating the number of integrin receptors in the high-affinity state, we asked how increased integrin activation at acidic pH$_e$ affects membrane protrusion dynamics.

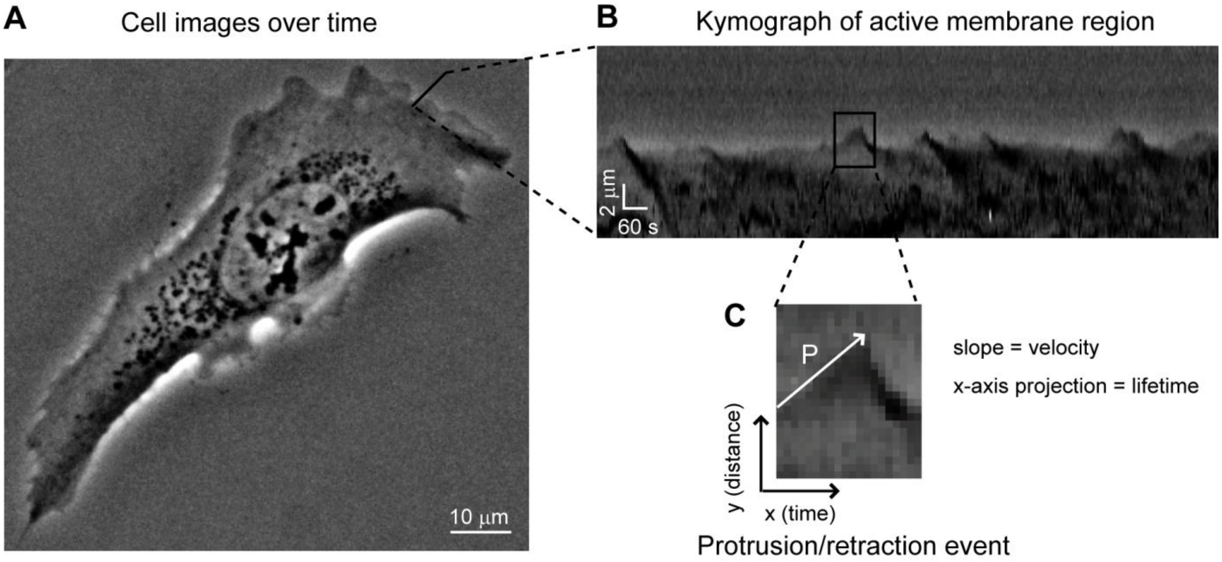

Figure 4.1 Images illustrating kymography experimental methods. (A) Images of $\alpha_v\beta_3$ CHO-B2 cells on fibronectin-coated glass (30 µg/ml) were taken at 40x magnification every 5 s for a duration of 25 min. A one-pixel-wide line was drawn perpendicular to the cell membrane at every location that exhibits activity. (B) This line was sequentially compiled for all image frames to produce a kymograph displaying individual protrusion events. (C) For each protrusion event (P), a straight line was drawn from the base to the peak. The slope of this line represents the protrusion velocity and the x-axis projection represents the lifetime.

In the studies described above, cell membrane protrusion dynamics was characterized using kymography. In a typical kymography experiment, cells are imaged at high magnification (e.g. 20x – 60x) at high frequency (e.g. every few seconds), enabling observation of short-timescale membrane protrusion/retraction cycles. For each location on the cell that exhibits protrusion events, a kymograph is produced by drawing a one-pixel-wide line perpendicular to the cell membrane. The images along this line at all timepoints are then sequentially compiled into a single image, illustrating the membrane dynamics at that specific location on the cell over time. To analyze individual protrusion events within each kymograph, a straight line is drawn from the base of each event to the peak. The slope of the line is the protrusion velocity, and the x-axis projection is the protrusion lifetime (Figure 4.1).

4.2.2. Results for normal and acidic pH_e

We used kymography to measure cell membrane protrusion parameters for $\alpha_v\beta_3$ CHO-B2 cells as a function of extracellular pH. For our experiments, $\alpha_v\beta_3$ CHO-B2 cells were plated on fibronectin-coated glass (30 µg/ml) in serum-free media and were allowed to adhere and spread for 2 – 3 hr before imaging. The cell media was then changed to serum-free bicarbonate free media at pH_e 7.4 or pH_e 6.5 and cells were imaged at 40x magnification every 5 s for a duration of 25 min. For each experiment, 10 – 20 cells were imaged and at least 200 individual protrusion events were analyzed for each pH_e condition to measure average protrusion lifetime and velocity. We used pH_e 6.5 for the acidic condition rather than pH_e 6.0 because cells were more active at pH_e 6.5, enabling collection of more membrane dynamics data.

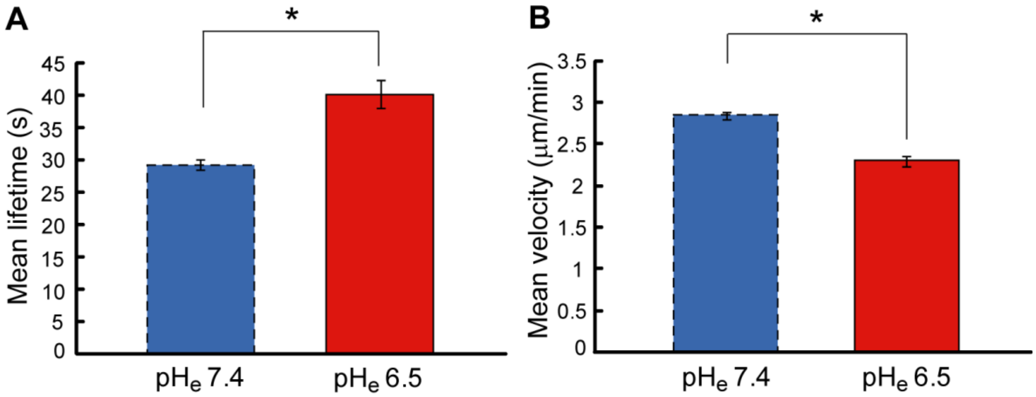

Figure 4.2 $\alpha_v\beta_3$ CHO-B2 cell membrane protrusion lifetime and velocity measured by kymography. Kymography measurements demonstrated that mean protrusion lifetime was significantly increased and mean protrusion velocity was significantly decreased at acidic extracellular pH (asterisks represent $p < 0.0001$). 501 individual protrusion events were measured for pH_e 7.4 and 204 events were measured for pH_e 6.5. Error bars are SEM.

Measurements of protrusion parameters demonstrated that mean protrusion lifetime was significantly increased for cells at pH_e 6.5 relative to pH_e 7.4 (40.12 ± 2.07 s and 29.24 ± 0.79 s respectively, mean ± SEM, Figure 4.2A), while mean protrusion velocity was significantly decreased (2.29 ± 0.07 µm/min and 2.85 ± 0.04 µm/min respectively, mean ± SEM, Figure 4.2B). In other words, protrusions grew more slowly and lasted longer when extended at acidic pH_e. Protrusion velocity is generally taken to represent actin polymerization rate [187], and our results therefore imply that actin polymerization rates slowed for cells at acidic pH_e. The increase in protrusion lifetime that we observed at pH_e 6.5 may be attributed to increased integrin activation in this condition, which would be expected to lead to more efficient formation of nascent adhesion sites at the cell membrane, and would thus stabilize growing protrusions [187].

4.2.3. Intracellular pH manipulation and kymography measurements

In the experiments discussed so far, the role of intracellular acidification is unknown. It is possible that our experimental changes to extracellular pH concurrently acidified intracellular pH (pH_i) in our cell system, and that this caused the increased integrin activation and altered membrane dynamics that we observed. For example, intracellular acidification could cause changes to talin-integrin binding, and thus modulate integrin activation from the intracellular rather than extracellular space. To test this possibility, we first measured intracellular pH for $\alpha_v\beta_3$ CHO-B2 cells over the timescales of our experiments. The fluorophore BCECF (2′,7′-bis-(2-carboxyethyl)-5-(and-6)-carboxyfluorescein) is commonly used for pH_i measurements [29, 35, 36, 189] . The acetoxymethyl ester form of the dye (BCECF-AM) is nonfluorescent and membrane permeable. Once inside the cell, BCECF-AM is cleaved by intracellular esterases to fluorescent BCECF (Figure 4.3A). BCECF has both a pH-sensitive excitation wavelength (~495 nm) and a pH-insensitive excitation wavelength (~440 nm), with an emission wavelength of ~535 nm. The pH-insensitive wavelength allows normalization for factors such as the amount of dye loaded into each cell, and the ratio of 495 nm/440 nm fluorescence intensities is approximately linear with intracellular pH in the range of pH_i 6.0 – 7.5 (Figure 4.3B). The ionophore nigericin allows rapid equilibration of intra- and extracellular pH and can be used for dye calibration [29, 35, 36, 190, 191].

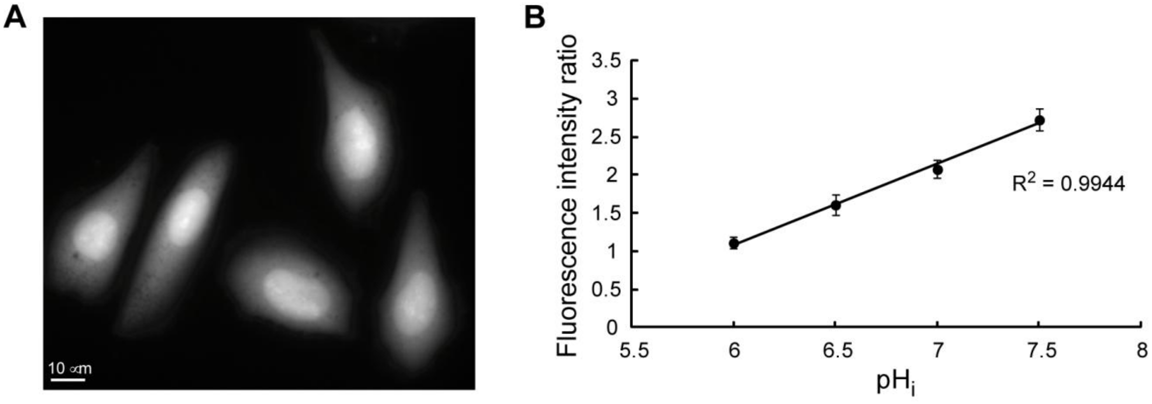

Figure 4.3 BCECF dye loading and calibration. (A) Fluorescent image (~495 nm excitation) illustrating BCECF loading into $\alpha_v\beta_3$ CHO-B2 cells. (B) Calibration of BCECF fluorescence intensity ratio in the pH_i range of interest. Fluorescence intensity ratio was calculated as the mean intensity of a cell imaged with ~495 nm excitation divided by the mean intensity of a cell imaged with ~440 nm excitation. Emission is at ~535 nm for both excitation wavelengths. The fluorescence intensity ratio was linear with pH_i. At least 28 cells were imaged for each calibration pH condition. Error bars are SEM.

For our measurements of intracellular pH, cells were incubated with 1 μM BCECF-AM for 30 min to allow the dye to cross the cell membrane. The concentration of BCECF-AM was optimized to give bright cell fluorescence with low exposure times (50 – 100 ms). Immediately following dye loading, cells were rinsed and imaged. Two fluorescent images were taken for each cell, both using a GFP filter encompassing 535 nm for the emitted light. The first image used a GFP filter encompassing 495 nm for the excitation beam, and the second image used a CFP filter encompassing 440 for the excitation beam. The filters were chosen to minimize cross-excitation. The mean intensity for each image was calculated, and the ratio of the GFP/CFP mean intensities was used to calculate pH$_i$. To calibrate intensity ratio at different pH$_i$ values, 10 μM nigericin was added in buffers with pH$_e$ 6.0 – 7.5, and cells were imaged as described above. A nigericin incubation time of 3 min was sufficient to equilibrate intra- and extracellular pH.

In the flow cytometry and AFM-enabled molecular force spectroscopy experiments discussed in Chapter 3, cells were exposed to pH$_e$ 6.0 over a timescale of 30 – 60 min. In our kymography measurements, cells were exposed to pH$_e$ 6.5 over a timescale of 30 – 90 min. Therefore, we measured intracellular pH for $\alpha_v\beta_3$ CHO-B2 cells exposed to pH$_e$ 6.0 or pH$_e$ 6.5 over these timescales. The pH$_i$ changes within the first 30 min of exposure to acidic extracellular pH were measured every ~1 min to inform interpretation of cellular-level experiments that will be discussed in Chapter 5, while pH$_i$ changes for longer exposure times were monitored every ~30 min. When cells were incubated in pH$_e$ 6.0, pH$_i$ dropped from ~7.5 – 7.0 within the first 10 min of exposure. After 30 min of exposure, pH$_i$ was ~6.6 (Figure 4.4A). For longer exposure times of ~60 – 90 min, pH$_i$ ranged from ~6.3 – 6.15. When cells were incubated in pH$_e$ 6.5 for ~30 – 90 min, pH$_i$ ranged from ~6.7 – 6.3 (Figure 4.4B). From these data, it is clear that intracellular pH was significantly acidified during the timescales of our flow cytometry, AFM-MFS, and kymography experiments.

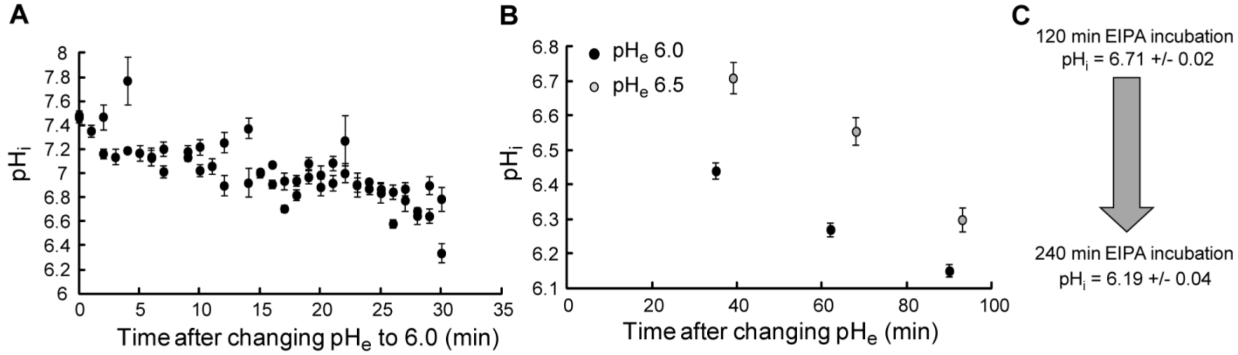

Figure 4.4 Intracellular pH measurements for cells exposed to acidic pH$_e$ and for cells incubated with the NHE1 inhibitor EIPA. (A) Intracellular pH measurements for $\alpha_v\beta_3$ CHO-B2 cells exposed to pH$_e$ 6.0 for 0 – 30 min. 3 – 14 cells were imaged at each timepoint. (B) Intracellular pH measurements for $\alpha_v\beta_3$ CHO-B2 cells exposed to pH$_e$ 6.0 or pH$_e$ 6.5 for 30 – 90 min. At least 36 cells were imaged at each timepoint. (C) Incubation with 50 μM EIPA (NHE1 inhibitor) for 120 – 240 min caused intracellular pH to reach the same range as that shown in (B) for cells exposed to pH$_e$ 6.5 for 30 – 90 min. All errors are SEM.

Next, we used EIPA (5-(N-Ethyl-N-isopropyl)amiloride) to block extrusion of H$^+$ from the NHE1 ion exchanger. This blocking causes accumulation of intracellular H$^+$ and consequent lowering of pH$_i$ [29, 36, 192-195]. Thus, the effects of intracellular and extracellular acidification can be decoupled. When cells were incubated with 50 μM EIPA for a period of 2 – 4 hr, pH$_i$ ranged from 6.7 – 6.2 (Figure 4.4C). This intracellular pH range is very similar to that observed after 30 – 90 min of exposure to pH$_e$ 6.5, as in our kymography measurements (Figure 4.4B). Therefore, we conducted further kymography experiments for cells treated with EIPA to determine whether intracellular acidification could cause the increased protrusion lifetime and decreased protrusion velocity that we observed previously.

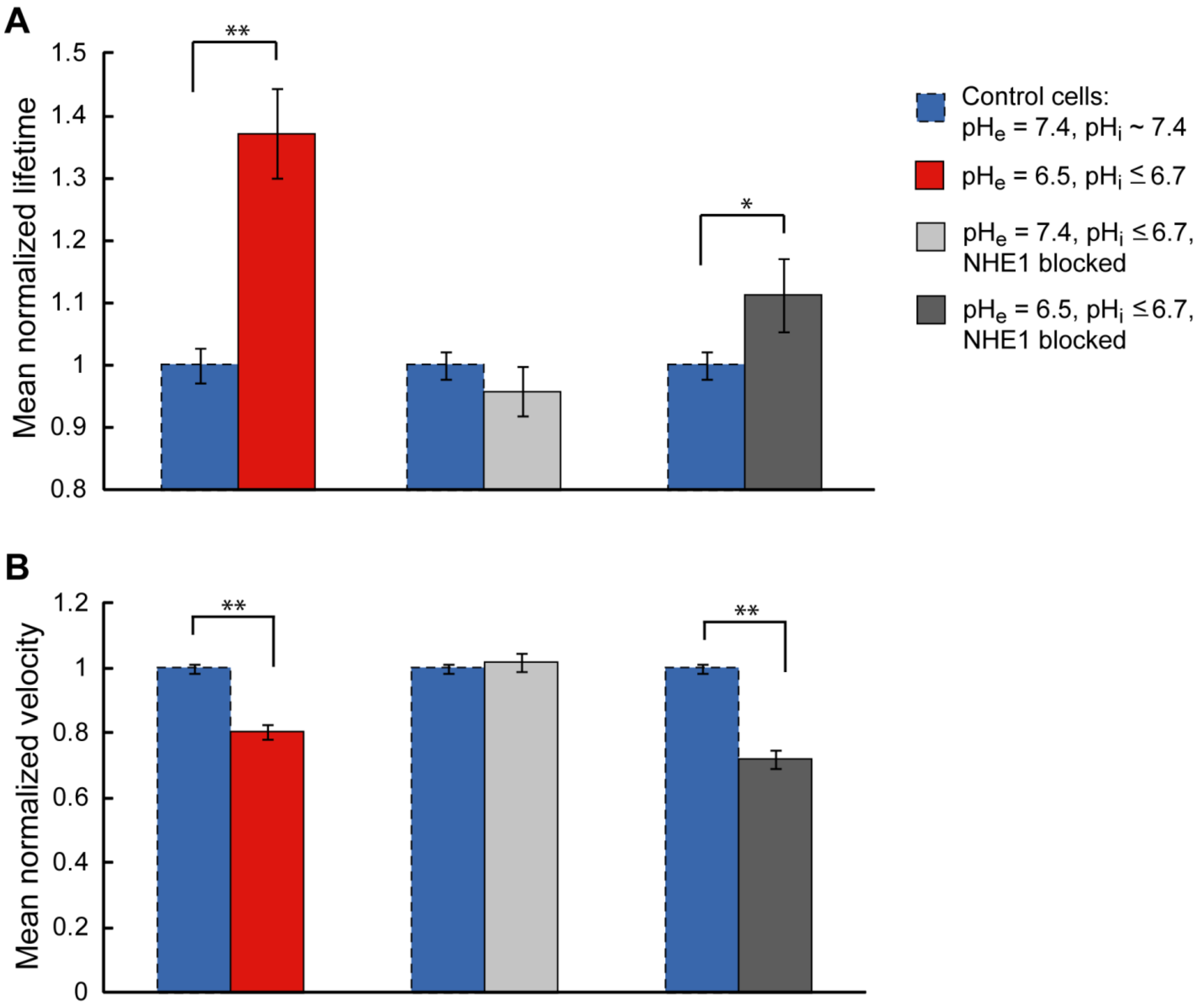

Figure 4.5 Average membrane protrusion lifetime and velocity measurements for cells in various extra- and intracellular pH conditions. As measurements were taken on different days, all data are normalized to the average value for control cells tested on the same day. (A) Left two bars: average membrane protrusion lifetime for cells in $pH_e = 6.5$ and $pH_i \leq 6.7$ compared to that for control cells ($pH_e = 7.4$, $pH_i \sim 7.4$). Data is the same as that shown in Figure 4.2. Center two bars: average membrane protrusion lifetime for cells in $pH_e = 7.4$ and $pH_i \leq 6.7$ with NHE1 blocked compared to that for control cells. Right two bars: average membrane protrusion lifetime for cells in $pH_e = 6.5$ and $pH_i \leq 6.7$ with NHE1 blocked compared to that for control cells. (B) Average protrusion velocity for the same conditions shown in (A). At least 100 protrusion events were measured for each experimental condition. All error bars are SEM. $^{**}p \leq 0.0001$, $^{*}p < 0.05$

Although protrusion frequency decreased by ~50% when cells were incubated with EIPA, we were able to characterize at least 100 protrusion events for each experimental condition. To enable ease of comparison for measurements taken on different days, all data were normalized to the average values for control cells tested on the same day. Absolute values for experiments are given in Table 4.1. In our original experiments, extracellular pH was acidified to 6.5, which concurrently lowered intracellular pH to ≤ 6.7. In that condition, protrusion lifetime was significantly increased and protrusion velocity was significantly decreased compared to cells with $pH_e = 7.4$ and $pH_i \sim 7.4$ (Figure 4.2 and Figure 4.5 left bars). In contrast, when intracellular pH was acidified by NHE1 blocking while extracellular pH was maintained at 7.4, the mean protrusion lifetime and velocity was similar to that of control cells (Figure 4.5 center bars). This suggests that intracellular acidification alone cannot account for the membrane dynamics differences we observed with extracellular acidification. However, it is possible that these differences were abrogated simply because NHE1 activity is required for these changes to occur. Therefore, we acidified the extracellular pH to 6.5 while also lowering pH_i via NHE1 blocking. With this extracellular acidification, differences in membrane protrusion lifetime and velocity were recovered even though NHE1 was still blocked (Figure 4.5 right bars). Taken together, these data demonstrate that intracellular acidification is not sufficient to cause cells to exhibit increased protrusion lifetime or decreased protrusion velocity. Thus, although pH_i does decrease over the 30 – 90 min timescale of our kymography experiments, this intracellular acidification cannot be responsible for the observed effects.

Condition		**Mean lifetime ± SEM (s)**	**Mean velocity ± SEM (μm/min)**
Pair 1	pH_e 7.4	29.24 ± 0.79, *N* = 501	2.85 ± 0.04, *N* = 501
	pH_e 6.5 ($pH_i \leq 6.7$)	40.12 ± 2.07, *N* = 204**	2.29 ± 0.07, *N* = 204**
Pair 2	pH_e 7.4	28.64 ± 0.61, *N* = 644	2.82 ± 0.04, *N* = 644
	pH_e 7.4 + EIPA ($pH_i \leq 6.7$, NHE1 blocked)	27.45 ± 1.16, *N* = 259	2.87 ± 0.08, *N* = 259
Pair 3	pH_e 7.4	26.72 ± 0.60, *N* = 534	3.54 ± 0.06, *N* = 534
	pH_e 6.5 + EIPA ($pH_i \leq 6.7$, NHE1 blocked)	29.72 ± 1.53, *N* = 109*	2.55 ± 0.10, *N* = 109**

Table 4.1 Average protrusion lifetime and velocity data for all experimental conditions shown in Figure 4.5. Asterisks indicate statistically significant differences compared to the pH_e 7.4 condition with that experimental pair. $^{**}p \leq 0.0001$, $^{*}p < 0.05$

4.2.4. Discussion of kymography results

Our kymography results for $\alpha_v\beta_3$ CHO-B2 cells at pH_e 7.4 and pH_e 6.5 demonstrated that membrane protrusion lifetime was increased for cells in acidic extracellular pH. Kymography measurements for cells treated with EIPA suggested that this effect requires extracellular acidification and cannot be caused by intracellular acidification alone. Several previous studies have shown that cell membrane protrusion lifetime increases with greater ligand coating concentrations [48, 186-188], and it has been suggested that this could be due to an increase in integrin-ligand binding at the leading edge, which stabilizes the membrane protrusions [187]. Our kymography results are consistent with this explanation, as greater integrin activation in acidic pH_e would increase integrin-ligand binding at the leading edge in a similar manner to greater fibronectin coating concentrations.

Kymography data also showed a decrease in membrane protrusion velocity for cells at pH_e 6.5, which indicates a decrease in actin polymerization rate. This effect was not observed in previous studies of membrane dynamics at varying ligand densities [48, 186-188], indicating that it is unlikely to be a direct result of increased cell-substratum adhesiveness in acidic pH_e. Interestingly, the decrease in protrusion velocity that we observed required extracellular acidification and was not observed when intracellular pH alone was acidified. Thus, in our experimental system, the intracellular process of actin polymerization was somehow regulated by extracellular pH. It is possible that integrin activation in acidic pH_e triggered intracellular signaling pathways that regulate actin polymerization dynamics, or that acidic pH_e changed the behavior of other transmembrane proteins that can regulate actin polymerization, such as growth factor receptors [196]. Further investigation of the mechanism of this effect is beyond the scope of this thesis, but is an interesting avenue for future research.

Our approach for using EIPA to deconvolute the effects of intracellular and extracellular acidification was used by Stock et al. in their study of melanoma cell migration as a function of pH_e. In this study, Stock et al. used EIPA to demonstrate that intracellular pH changes could not explain the effects of acidic pH_e on cell morphology and migration that they observed [29]. Although this approach was useful in our kymography studies and was the most practical experimental method available to us, we note that it has limitations. Most importantly, the number of protrusion events was reduced by ~50% for cells treated with EIPA, indicating that NHE1 has a role in regulating membrane dynamics. However, we were still able to measure lifetime and velocity for the protrusion events that did occur.

In our experiments with EIPA treatment, we did not directly measure the extent of integrin activation after intracellular acidification. However, protrusion lifetime is likely to be closely tied to integrin activation, as discussed above. Therefore, our measurements of protrusion lifetime for cells treated with EIPA suggest by extension that intracellular acidification alone is probably not sufficient to cause integrin activation via altered talin binding or other mechanisms. Our molecular dynamics simulations further support this conclusion, as increased headpiece opening was observed in acidic pH_e in the absence of transmembrane and intracellular integrin domains, and in the absence of other intracellular proteins.

4.3. Imaging of actin-integrin adhesion complexes

4.3.1. Background

At sites of integrin-ligand engagement, multi-protein assemblies form inside the cell, linking integrins to the actin cytoskeleton. These macromolecular adhesion sites can be generally referred to as actin-integrin adhesion complexes (AIACs), following the terminology of Geiger and Bershadsky [63]. There are distinct classes of AIACs, two of which are termed focal complexes and focal adhesions. Focal complexes are small ($<1\ \mu m^2$) and dynamic (lifetime <5 min), while focal adhesions are larger ($>1\ \mu m^2$) and more temporally stable (lifetime >15 min) [62, 188, 197-199]. Focal complexes and focal adhesions have some molecular components in common, such as the talin and vinculin adaptor proteins, which are understood to play a structural role in connecting integrins to actin, as well as signaling molecules such as focal adhesion kinase [62, 67]. However, focal adhesions also contain molecular components that are not present in focal complexes [62, 63, 67]. The transition from focal complex to focal adhesion requires activation of the GTPase Rho, which regulates actin polymerization and myosin contraction via downstream signaling pathways [63, 67, 200]. Focal adhesion development also requires mechanical force and is blocked when cell contractility is inhibited [201, 202]. AIACs are critical for cell migration, as they enable cells to transmit actomyosin-generated forces against their substrata or matrices, creating the traction necessary for translocation.

It has been shown that changes to cell-substratum adhesiveness can alter AIAC formation. For example, Gupton and Waterman-Storer showed that for PtK_1 epithelial cells, the number of AIACs increased as the surface fibronectin coating concentration [Fn] increased. At low [Fn], AIACs were located primarily at the cell periphery, while at high [Fn], AIACs were located throughout the cell. Furthermore, AIAC area decreased and lifetime increased for cells on surfaces with higher [Fn] [188]. Kato and Mrksich studied the adhesion of Swiss 3T3 fibroblasts to surfaces presenting either linear RGD peptides or higher affinity cyclic RGD peptides. Cells on surfaces presenting cyclic RGD peptides had twice as many AIACs than cells on surfaces presenting linear peptides, and the AIACs were smaller. AIACs for cells on cyclic RGD-presenting surfaces were also more evenly distributed throughout the cell, rather than being restricted to the cell periphery. Lowering the density of cyclic RGD resulted in AIACs similar to those observed on linear RGD [203].

In the studies discussed above, cell-substratum adhesiveness was modulated via alterations to ligand density or integrin-ligand binding affinity. As acidic extracellular pH can also modulate cell-substratum adhesiveness via promotion of integrin activation, we investigated the effect of acidic pH_e on AIAC formation for $\alpha_v\beta_3$ CH-B2 cells. The protein vinculin is a major component of both focal complexes and focal adhesions [62, 67], and a green fluorescent protein (GFP)-tagged vinculin construct has been widely used as an AIAC marker [62, 204-207]. Therefore, we transfected $\alpha_v\beta_3$ CHO-B2 cells with GFP-vinculin in order to visualize AIACs and characterize AIAC number and area at normal and acidic extracellular pH.

4.3.2. Results for normal and acidic pH_e

We used the method of lipofection to transfect $\alpha_v\beta_3$ CHO-B2 cells with GFP-vinculin plasmid DNA. With this transfection method, positively charged lipids form complexes with the negatively plasmid charged DNA molecules. These lipid complexes can then pass through the phospholipid bilayer of the cell membrane [208]. In our experiments the Lipofectamine© reagent (Invitrogen) was used for lipofection. Cells were detached ~24 h after transfection and plated on fibronectin-coated glass (30 μg/ml). After plating, cells were incubated in serum-free media pH_e 7.4 for 2 – 3 hr to allow cells to adhere and spread. Media was then changed to bicarbonate-free serum-free media at pH_e 7.4 or pH_e 6.5 and cells were fluorescently imaged at 60x magnification. For each experiment, we imaged at least ~35 cells per condition.

AIACs were clearly visible in fluorescent images of GFP-vinculin-transfected cells (Figure 4.6A). While some cells had AIACs mainly at the cell periphery (Figure 4.6A, left), others had AIACs in throughout the cell area (Figure 4.6A, right). To assess the effect of acidic extracellular pH on AIACs, GFP-vinculin-transfected cells were imaged after 20 – 40 min of exposure to pH_e 6.5 and compared to cells at pH_e 7.4. The mean number of AIACs per cell and mean AIAC area were quantified for cells at each pH_e. Figure 4.6B shows that cells in acidic pH_e had significantly more AIACs/cell than cells in pH_e 7.4 (52.36 ± 3.60 AIACs/cell and 35.83 ± 2.52 AIACs/cell, respectively, mean ± SEM). However, AIACs in pH_e 6.5 had a smaller average area than AIACs in pH_e 7.4 ($0.62 \pm 0.13\ \mu m^2$ and $0.71 \pm 0.02\ \mu m^2$, respectively, mean ± SEM). To test whether AIACs at pH$_e$ 6.5 had reached their maximal size or would grow larger if given more time, we imaged cells after 2 – 3 hr of exposure to pH$_e$ 6.5 or pH$_e$ 7.4. Figure 4.6C shows that with this longer exposure time, cells in pH$_e$ 6.5 still had more AIACs/cell than cells at pH$_e$ 7.4 (55.02 ± 3.74 AIACs/cell and 41.88 ± 2.93 AIACs/cell, respectively, mean ± SEM) but the mean AIAC areas were statistically indistinguishable for these two pH$_e$ values (0.68 ± 0.02 for pH$_e$ 6.5 vs. 0.70 ± 0.02 for pH$_e$ 7.4, mean ± SEM).

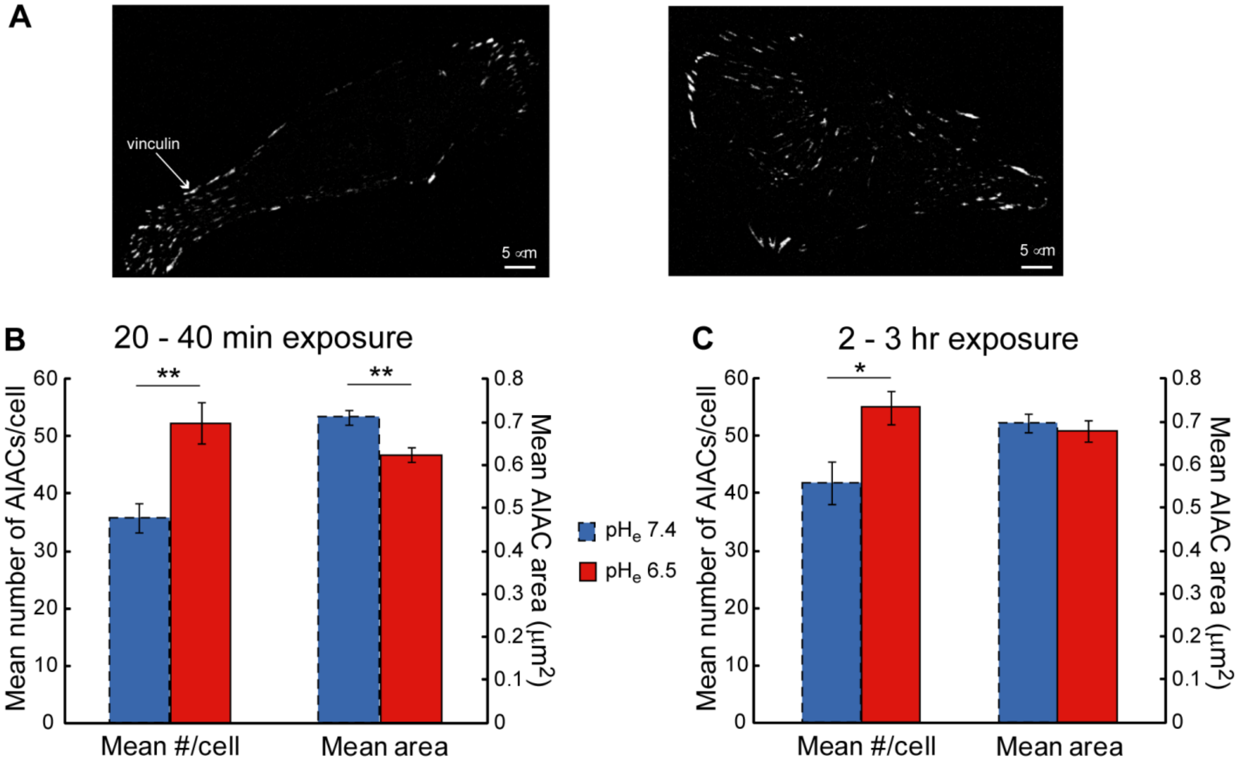

Figure 4.6 Characterization of actin-integrin adhesion complexes (AIACs) for cells in pH$_e$ 7.4 and pH$_e$ 6.5. (A) Representative fluorescent images of $\alpha_v\beta_3$ CHO-B2 cells transfected with GFP-vinculin. Some cells had AIACs mainly at the cell periphery (left), while others had AIACs throughout the cell body (right). (B) Mean number of AIACs per cell and mean AIAC area for cells exposed to pH$_e$ 7.4 or 6.5 for 20 – 40 min. *N* = 61 cells for pH$_e$ 7.4 and *N* = 56 cells for pH$_e$ 6.5. (C) Mean number of AIACs per cell and mean AIAC area for cells exposed to pH$_e$ 7.4 or 6.5 for 2 – 3 hr. *N* = 48 cells for pH$_e$ 7.4 and *N* = 63 cells for pH$_e$ 6.5. Error bars are SEM. *p < 0.01, **p < 0.001.

4.3.3. Discussion of AIAC imaging results

In these experiments, we were able to successfully image AIACs in $\alpha_v\beta_3$ CHO-B2 cells after transfecting cells with a GFP-vinculin construct. Our AIAC imaging experiments demonstrated that with 20 – 40 min of exposure to acidic pH$_e$, cells in pH$_e$ 6.5 developed more AIACs than cells at pH$_e$ 7.4, and the AIACs had smaller average area. After 2 – 3 hr of exposure, the average number of AIACs per cell for both pH$_e$ values remained approximately the same as for the shorter exposure time. However, the average area for AIACs in pH$_e$ 6.5 had increased to a size that was comparable to the pH$_e$ 7.4 condition. In other words, within 3 hr, the cells in acidic pH_e exhibited more AIACs of equivalent area to those in pH_e 7.4. One interpretation of our data is that acidic pH_e initiates AIAC formation but not does affect regulation of how large AIACs can grow. This is plausible in the context of our previous results demonstrating increased integrin activation in acidic pH_e. Increased integrin activation is likely to lead to increased integrin-ligand binding, which can facilitate or be followed by intracellular AIAC assembly.

Our finding of higher AIAC numbers in acidic pH_e is consistent with others' work showing higher AIAC numbers in conditions with increased cell-substrum adhesiveness (see discussion in Section 4.3.1) [188, 203]. However, previous studies found that AIAC area was smaller at higher cell-substratum adhesiveness, while we found that AIACs at both pH_e 6.5 and pH_e 7.4 reached the same average area after sufficient exposure times. This indicates that there may be some cell type-specific responses to increased cell-substratum adhesiveness, or that acidic pH_e has secondary effects beyond simply increasing adhesiveness that did not occur in the previous studies.

It is possible that intracellular acidification contributed to the changes in AIAC number and size that we observed. Even with only 20 – 40 min of exposure to pH_e 6.5, pH_i could have dropped to ~6.7, which may be low enough to alter interactions between AIAC proteins (Figure 4.4). The structure of the vinculin protein has been shown to be unaffected by pH in the range of 5.5 – 7.5 [209], but other AIAC proteins may be regulated by pH_i. For example, it has been demonstrated that talin-actin binding affinity is increased at acidic pH_i, and that this may result in increased AIAC lifetime in acidic pH_i [197]. However, in that study, the total number of AIACs was independent of pH_i and the mean AIAC size increased when pH_i was acidified, in contrast to our data at pH_e 6.5. This indicates that intracellular acidification is not sufficient to account for the changes we observed at acidic pH_e. Therefore, although it is certainly possible that intracellular pH-induced changes to talin or other molecules could alter AIAC dynamics, our suggestion that acidic pH_e-mediated integrin activation directly initiates AIAC formation remains valid and may be the dominant effect.

It is possible that acidic pH_e altered the dynamics of AIAC formation and dissolution rather than the initiation frequency alone. Because our data is limited to static images, we cannot draw any conclusions about AIAC dynamics. Although live cell transfection with GFP-vinculin technically should enable dynamic imaging of AIAC growth and dissolution, we were unable to conduct such experiments with our current microscope setup. The GFP-vinculin fluorophore photobleached very quickly in our experiments, such that it was not possible to collect multiple images of the same AIACs within a single cell. This is likely due to the intensity of the excitation light and the slow shutter speed in our microscope and camera. Further examination of AIAC dynamics as a function of pH_e is an interesting topic for future research that can be enabled by modifications to experimental equipment.

4.4. Conclusions and transition to cellular-scale experiments and modeling

4.4.1. Conclusions

In this chapter, we assessed the effect of acidic extracellular pH on subcellular–scale processes that are critical for cell migration. First, kymography was used to measure cell membrane protrusion lifetime and velocity and pH_e 7.4 and pH_e 6.5. Data demonstrated that protrusion lifetime increased at acidic pH_e, which is consistent with increased integrin activation in this condition. Membrane protrusion velocity decreased at acidic pH_e, indicating that actin polymerization is altered in this condition. Experiments with NHE1 blocking demonstrated that intracellular acidification is not sufficient to cause these changes to membrane protrusion lifetime or velocity.

Imaging of AIACs in GFP-vinculin-transfected cells demonstrated that cells in acidic pH_e developed more AIACs than cells at pH_e 7.4 and that AIACs in both extracellular pH conditions reached the same average size if given sufficient time (>40 min) for growth. Although we cannot draw conclusions about AIAC dynamics from these data, the increase in AIAC number suggests that acidic extracellular pH initiates AIAC formation, which is an expected consequence of increased integrin activation and binding. Thus, these kymography and AIAC imaging data are consistent with our atomistic simulations and molecular experiments and extend our knowledge to the subcellular length scale.

4.4.2. Next question: how does acidic extracellular pH impact cell spreading and migration?

In this thesis thus far, we have demonstrated that acidic extracellular pH significantly affects integrin activation propensity, cell membrane protrusions, and AIAC formation. We now ask how these changes to molecular- and subcellular-scale processes in acidic pH_e impact cellular-scale spreading and migration. In the next chapter, optical microscopy is used to assess cell spreading in both static and dynamic extracellular pH conditions. Furthermore, timelapse imaging is used to measure cell migration velocities and persistence times at normal and acidic pH_e over a range of fibronectin coating concentrations, and a mathematical model of cell migration is used to interpret these experimental results. Integration of our cellular-scale data with results from other length scales will enable us to make mechanistic predictions of how the acidic nature of the tumor and wound environments may regulate cell processes critical to cancer progression and wound healing.

4.5. Acknowledgments

A. Cherukara amplified and purified GFP-vinculin plasmid DNA and assisted with optimization of the GFP-vinculin transfection protocol for $\alpha_v\beta_3$ CHO-B2 cells. L. Wroblewska and A. Jagielska assisted with plasmid amplification and purification.

Chapter 5: Cellular-scale experiments and modeling

Sections 5.2 – 5.3.5 include material that was published in Ref. [85]. For that publication, R.K. Paradise designed experiments, collected, analyzed, and interpreted data, and wrote the manuscript.

5.1. Overview

In Chapter 2 and 3, results from atomistic-scale simulations and molecular-scale experiments demonstrated that acidic extracellular pH promotes activation of integrin $\alpha_v\beta_3$, which has the effect of increasing the adhesiveness between a cell and its substratum. In Chapter 4, we demonstrated that acidic pH_e increased cell membrane protrusion lifetime and decreased protrusion velocity, and that these effects could not be sufficiently explained by changes to intracellular pH. We also showed that cells in acidic pH_e developed more actin-integrin adhesion complexes than cells in pH_e 7.4. The effects of acidic pH_e on these subcellular-scale processes are likely to be related to greater numbers of activated integrins and increased cell-substratum adhesiveness in acidic pH_e. In this chapter, we investigate how increased integrin activation and the resulting subcellular changes in acidic pH_e affect cellular-scale spreading and migration. It is conceivable that increased cell-substratum adhesiveness could alter these complex cellular processes in a number of ways, such as changing cell spread area, morphology, migration speed, or persistence time. In this chapter, we characterize the effect of acidic pH_e on dynamic cell spreading at short timescales in terms of projected cell area, and at long timescales in terms of cell area and circularity, a parameter of cell morphology. We also measure cell migration speed and persistence time over a range of fibronectin surface coating concentrations in normal and acidic extracellular pH. Finally, we build on the cell migration model of Dimilla et al. [95] to assess the extent to which our cell migration speed data can be explained by increased integrin activation at acidic pH_e. We find that projected cell area increases within minutes of exposure to acidic pH_e conditions and oscillates in responses to cyclic pH_e changes. Several hours of exposure to acidic pH_e causes cell projected area to increase, and also results in an elongated cell morphology. Finally, the fibronectin concentration required for peak cell migration speed is lower for cells in acidic pH_e than for cells in pH_e 7.4, and the magnitude of the peak migration speed is also decreased. Modeling results indicate that the decrease in critical fibronectin concentration can be sufficiently explained by increased integrin activation in acidic pH_e, but that the decrease in migration speed is likely to be due to secondary effects of acidic pH_e.

5.2. Introduction

A number of previous studies have investigated the effects of acidic extracellular pH on cell adhesion and migration. These studies were discussed in detail in Section 1.3, and the major results will be summarized again here. In brief, adhesion between neutrophils and endothelial cells was increased when the extracellular environment was acidified [39], and the number and length of human breast cancer cell filopodia increased at acidic pH_e [42]. Acidic extracellular pH led to cytoskeletal rearrangement, stress fiber formation, and a reduction in motility for mouse microglial cells [43], and mouse metastatic melanoma cells displayed larger spread size, more elongated morphology, and increased invasion through collagen-coated filters at acidic pH_e [41]. Finally, human melanoma cells exhibited more lamellipodia, enhanced adhesion, and increased invasiveness through Matrigel at acidic extracellular pH, and migration speed was maximum at intermediate pH_e conditions [29, 40]. From these studies, it is clear that acidic extracellular pH can have significant effects on adhesion and migration of several different cell types. Here, we investigate the effects of acidic extracellular pH on cell spreading, morphology, and migration for the $\alpha_v\beta_3$ CHO-B2 cells that were used for the molecular- and subcellular-level studies discussed in Chapters 3 – 4.

5.3. Cell spreading and morphology

5.3.1. Background

Cell spreading and morphology are generally assessed using phase contrast microscopy of cells adhered to ligand-coated substrata. While these parameters are sometimes characterized only qualitatively, the extent of cell spreading can be quantified by measuring the projected cell area, and cell morphology can be quantified by calculating the cell circularity parameter C. Circularity is defined as $C = \frac{4\pi A}{P^2}$, where A is the projected cell area and P is the cell perimeter [29]. This parameter ranges from 0 – 1, and C close to 0 indicates a dendritic or elongated cell morphology, while C close to 1 indicates a rounded morphology. It has been shown that changes to cell-substratum adhesiveness can alter cell spreading and morphology. For example, Palecek et al. reported that CHO cells became more spread as the surface ligand coating concentration increased [96], and Madri et al. showed that the spread area of bovine aortic endothelial cells increased at higer fibronectin coating densities [210]. Furthermore, Huttenlocher et al. showed that CHO cells expressing a constitutively activated form of integrin $\alpha_{IIb}\beta_3$ were more spread than cells expressing wild-type $\alpha_{IIb}\beta_3$ [52], and Smith et al. showed that antibody-induced activation of integrin $\alpha_L\beta_2$ on migrating T lymphocytes resulted in an elongated cell morphology [211].

5.3.2. Results: cell spreading over short timescales

We first considered the dynamic cell spreading response to extracellular pH changes occurring over short timescales (on the order of min). For these experiments, the bicarbonate buffer in cell media was utilized to create a system in which extracellular pH varied over time. $\alpha_v\beta_3$ CHO-B2 cells were seeded on fibronectin-coated (30 μg/ml) glass-bottom dishes in serum-free media and allowed to adhere for 2 – 3 hr before imaging. Media pH was then changed to pH 6.0 every hour for a total duration of 8 hr; between media changes, the extracellular pH increased from 6.0 up to ~7.2 due to the bicarbonate buffer in the media and the presence of 5% CO_2. This extracellular pH increase was clearly visible as a change in color of the pH indicator present in the media (Figure 5.1A colorbar). Each time the media was changed to pH 6.0, many cells responded within minutes by spreading and elongating. This caused the projected cell area to increase (from ~650 μm^2 to ~900 μm^2 for the cell shown in Figure 5.1A), reaching a maximum about 30 min after each induced acidification to pH 6.0 (Figure 5.1A). As the media pH increased toward neutral pH, cells eventually began to shrink and thus the projected cell area decreased. This cell behavior was consistent and repeatable over 8 hr of media pH changes, resulting in oscillations of measured cell area that initiated within minutes. Control cells were plated in fibronectin-coated polystyrene dishes with tight-fitting lids that eliminated air exchange and CO_2-dependent pH_e buffering. This system enabled us to maintain media at steady pH_e 7.4. Control cells in steady pH_e conditions exhibited some changes in projected area over a time period of 8 hr, but these changes were of much smaller magnitude and did not occur in an oscillatory manner (Figure 5.1B).

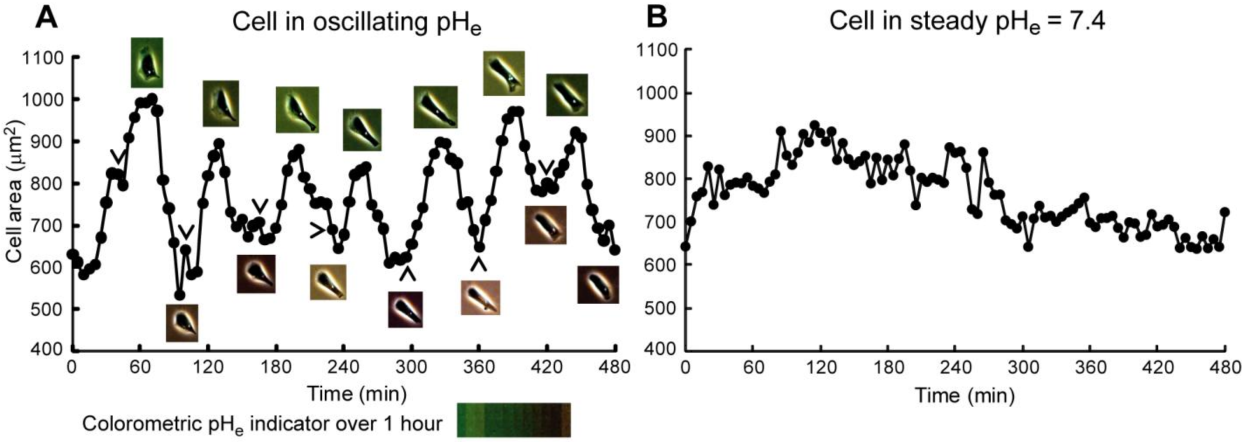

Figure 5.1 (A) Projected cell area for a representative cell over 8 hr, during which media pH_e was changed to pH 6.0 every hour. After each pH_e change, media pH_e drifted up to ~7.2 due to presence of bicarbonate buffer, as evidenced by the color change of the pH_e indicator in the media (shown for 1 hr). Images are snapshots of the cell at area minima and maxima. Arrowheads indicate points immediately before media pH_e was changed to pH_e 6.0. Each hour, cell area increased within minutes after pH_e was dropped to 6.0, and decreased as pH_e drifted up. Figure from Ref. [85]. (B) Cell area for a representative cell over 8 hr in conditions where the extracellular pH_e was maintained at a steady level of pH_e = 7.4. To maintain steady pH_e, cells were plated in polystyrene dishes with tight-fitting lids, which eliminated CO_2-dependent media buffering.

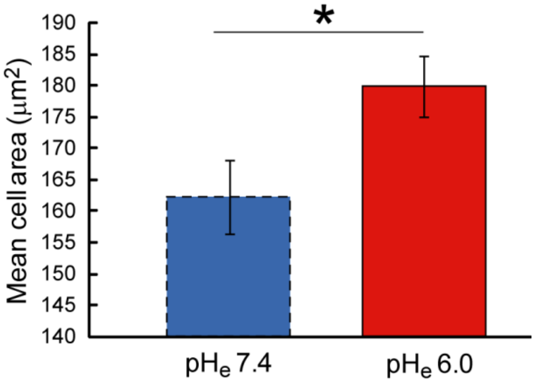

Figure 5.2 Mean spread area of $\alpha_v\beta_3$ CHO-B2 cells 30 min after plating from the suspended state onto fibronectin-coated glass in media at pH 6.0 or pH 7.4. Media initially set to pH 6.0 remained below pH 7.0 for the duration of the experiment. Mean cell area was significantly higher at pH_e 6.0 than at pH_e 7.4 ($p = 0.025$). *N* = 44 cells for pH_e 7.4 and *N* = 42 cells for pH_e 6.0. Error bars are SEM. Figure from Ref. [85].

Consistent with these measurements of extracellular pH-induced changes to spreading behavior for cells initially in the attached state, we observed that the short-timescale adhesion and spreading of cells seeded from the suspended state also varied with extracellular pH. For these experiments, cells were seeded onto fibronectin-coated glass (15 μg/ml) in serum-free media and imaged 30 min after seeding. Cells exhibited a significantly higher spread area when seeded in acidic media, as compared to media at pH 7.4 (180 μm^2 vs. 162 μm^2, Figure 5.2).

5.3.3. Discussion of short timescale cell spreading results

Measurements of the cell spreading response in a system with continuously changing pH_e demonstrated that the projected cell area oscillated in time with media pH changes, with larger cell area in more acidic media (Figure 5.1A). This is consistent with our model of increased cell-substratum adhesiveness due to increased integrin activation in acidic pH_e, which should result in greater cell spreading. The dynamic, rapid, and reversible cell response to acidic pH_e that we observed is unlikely to be a result of changes to intracellular pH, because cell area began to increase within minutes of extracellular acidification, and intracellular pH does not significantly change in this timescale (Figure 4.4A). Furthermore, the rapidity of the cell spreading response indicates that this effect is not mediated by internal cell processes such as changes in protein expression, which would take longer to manifest.

It is conceivable that the increase in cell spreading upon media acidification could be a result of increased actin polymerization causing greater membrane protrusion in this condition, rather than increased cell-substratum adhesiveness. However, kymography data in Chapter 4 demonstrated that membrane protrusion velocity actually decreased in acidic pH_e, indicating that the actin polymerization rate was slower rather than faster (Figure 4.2). Therefore, changes to the rate of actin polymerization cannot explain our dynamic cell spreading results. However, our kymography experiments also showed that protrusion lifetime increased in acidic pH_e, indicating enhanced lamellipodial stability, which is consistent with increased integrin activation and binding [187]. This increased protrusion stability during short-timescale protrusion/retraction cycles could conceivably lead to the larger-scale changes in projected cell area that were observed in these cell spreading experiments. This is also a likely explanation for the data demonstrating that cells in pH_e 6.0 had a larger spread area 30 min after plating from the suspended state than cells in pH_e 7.4 (Figure 5.2).

5.3.4. Results: cell spreading and morphology over long timescales

To measure the effects of acidic pH_e on cell spreading over longer timescales (several hours), we seeded $\alpha_v\beta_3$ CHO-B2 cells in serum-free media on fibronectin-coated polystyrene dishes with tight-fitting lids, which enabled us to maintain media pH_e at a steady level, as described in Section 5.3.2. Cells were allowed to adhere for 2 – 3 hr in pH_e 7.4 before the media was changed to pH_e 6.5 or 7.4. Extracellular media pH_e was then maintained for a duration of 8 hr, and the projected cell area was measured at the end of this time period. These experiments were conducted for fibronectin coating concentrations ranging from 0.1 – 30 μg/ml.

For both pH_e 7.4 and pH_e 6.5, the mean projected area increased with increasing fibronectin concentration (Figure 5.3A). This indicates that increased adhesiveness leads to more cell spreading. Furthermore, for all fibronectin concentrations except the lowest one (0.1 μg/ml), cells at pH_e 6.5 had a significantly higher mean projected area than cells at pH_e 7.4 (Figure 5.3A). Thus, acidic extracellular pH has a significant effect on cell spreading over 8-hr long timescales. To test the role of integrin $\alpha_v\beta_3$ in mediating the increased cell area observed at pH_e 6.5, additional experiments were conducted in which this integrin receptor was blocked by soluble GRGDSPC peptides at 25 μg/ml or 200 μg/ml. These experiments were conducted with 10 μg/ml fibronectin. For both pH_e 7.4 and pH_e 6.5, the projected cell area had an inverse dependence on GRGDSPC concentration; in other words, the cell area decreased as the blocking ligand concentration increased. However, cells at pH_e 6.5 had a larger mean projected area than cells at pH_e 7.4 for both concentrations of the blocking peptide (Figure 5.3B, columns 3-6). This could indicate that the increase in cell area observed at pH_e 6.5 does not require integrin $\alpha_v\beta_3$. Alternatively, it could indicate that even 200 μg/ml GRGDSPC does not completely block all of the available $\alpha_v\beta_3$ receptors. To test this, we measured the cell area at pH_e 7.4 and pH_e 6.5 for CHO-B2 pCDNA cells, which do not express $\alpha_v\beta_3$. For these cells, there was no significant difference in mean cell area between pH_e 6.5 and pH_e 7.4 (Figure 5.3B, columns 7-8). Thus, $\alpha_v\beta_3$ is indeed necessary for the mean spread area to increase in acidic extracellular pH, and 200 μg/ml GRGDSPC must be insufficient to completely block all $\alpha_v\beta_3$ receptors. This is consistent with the fact that cells in 200 μg/ml GRGDSPC remained attached to the fibronectin-coated surface. Finally, we measured cell area after activating integrin $\alpha_v\beta_3$ with Mn^{2+}. In this activating condition, the mean spread areas for pH_e 7.4 and pH_e 6.5 were high and the acidic pH_e-induced difference was abrogated (Figure 5.3B, columns 9-10). Thus, activation of $\alpha_v\beta_3$ is sufficient to cause a cell area increase comparable with that observed in pH_e 6.5.

In addition to the increase in projected cell area, many cells in pH_e 6.5 had developed an elongated morphology after 8 hr in this acidic pH_e condition (Figure 5.4A, images). This was quantified by calculating cell circularity (see Section 5.3.1). For both pH_e 7.4 and pH_e 6.5, the mean cell circularity decreased as fibronectin coating concentration increased. Furthermore, the mean cell circularity was lower at pH_e 6.5 than at pH 7.4 over all the fibronectin coating conditions tested, with the exception of the lowest concentration (Figure 5.4A). Thus, acidic extracellular pH causes cells to adopt a morphology characterized by low circularity. This is consistent with our qualitative observation that cells in pH_e 6.5 were more elongated than cells in pH_e 7.4. When integrin $\alpha_v\beta_3$ was blocked with 25 μg/ml GRGDSPC, mean cell circularity increased for both pHe values, but the circularity at pH_e 6.5 was still lower than that at pH_e 7.4 (Figure 5.4B, columns 3-4). However, with 200 μg/ml GRGDSPC, the pH-dependent difference was eliminated (Figure 5.4B, columns 5-6). The same effect was observed for CHO-B2 pCDNA cells (Figure 5.4B, columns 7-8). When integrin $\alpha_v\beta_3$ was activated with Mn^{2+} ions, mean cell circularity was low, and the pH-dependent difference was again eliminated (Figure 5.4B, columns 9-10). These data demonstrate that integrin $\alpha_v\beta_3$ is necessary and activation of $\alpha_v\beta_3$ is sufficient for cells to achieve low circularity.

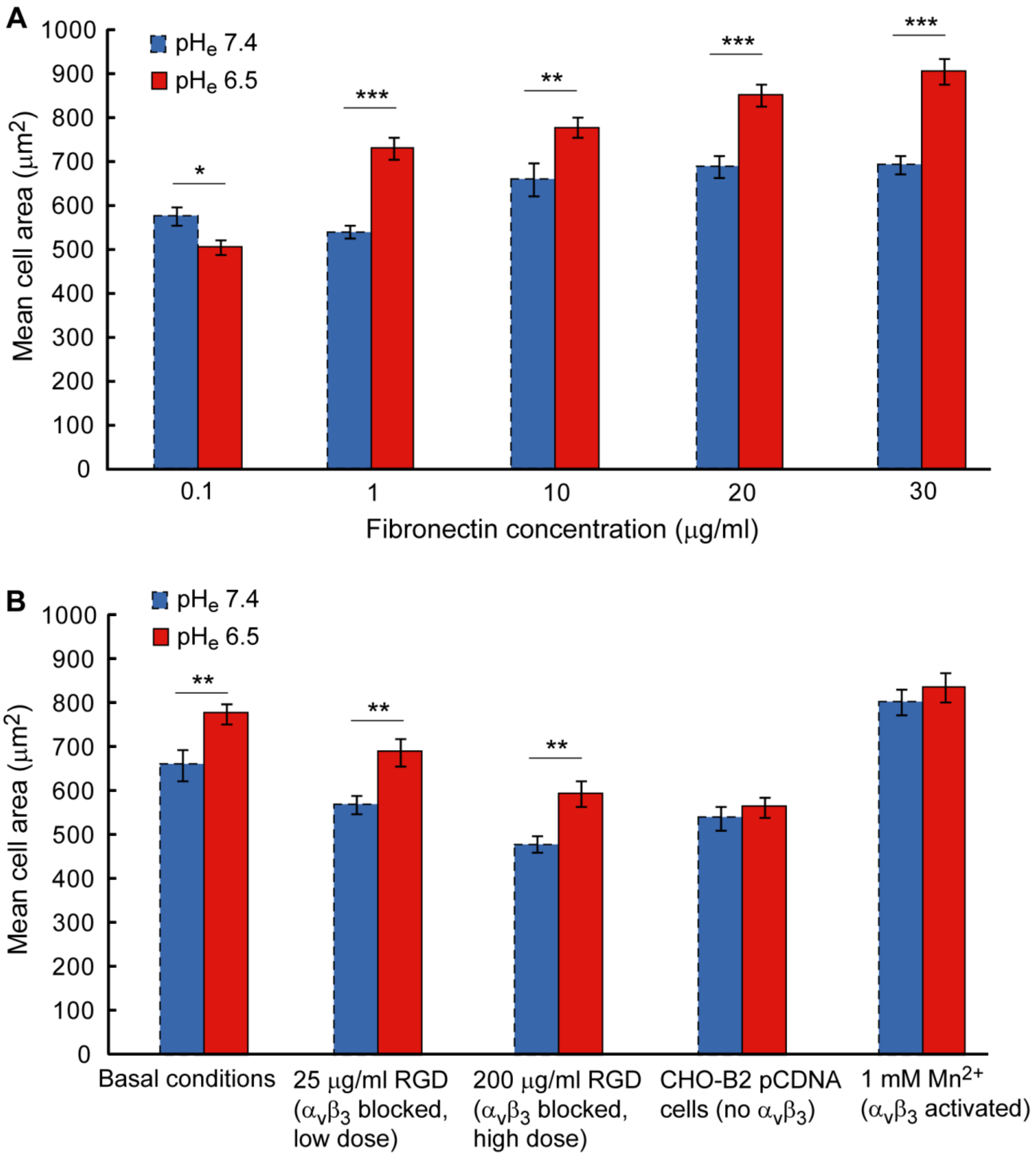

Figure 5.3 (A) Mean $\alpha_v\beta_3$ CHO-B2 cell projected area as a function of fibronectin surface coating concentration measured 8 hr after setting media pH$_e$ to 7.4 or 6.5. Cell area increased as fibronectin concentration increased for both pH$_e$ values. Cells at pH$_e$ 6.5 had larger cell area than cells at pH$_e$ 7.4 for all conditions, with the exception of 0.1 μg/ml fibronectin. (B) Mean $\alpha_v\beta_3$ CHO-B2 cell area at 10 μg/ml fibronectin measured 8 hr after setting media pH to 7.4 or 6.5. Soluble RGD peptide or Mn^{2+} was added in some cases, and one set of experiments was conducted with CHO-B2 pCDNA cells, as indicated. The difference in mean area at pH$_e$ 7.4 vs. pH$_e$ 6.5 for cells observed under basal conditions was eliminated for CHO-B2 pCDNA cells and for $\alpha_v\beta_3$ CHO-B2 cells incubated with 1 mM Mn^{2+}. At least 50 cells were measured for each condition, and all error bars are SEM. ***$p \leq 0.0001$, **$p < 0.01$, *$p < 0.05$.

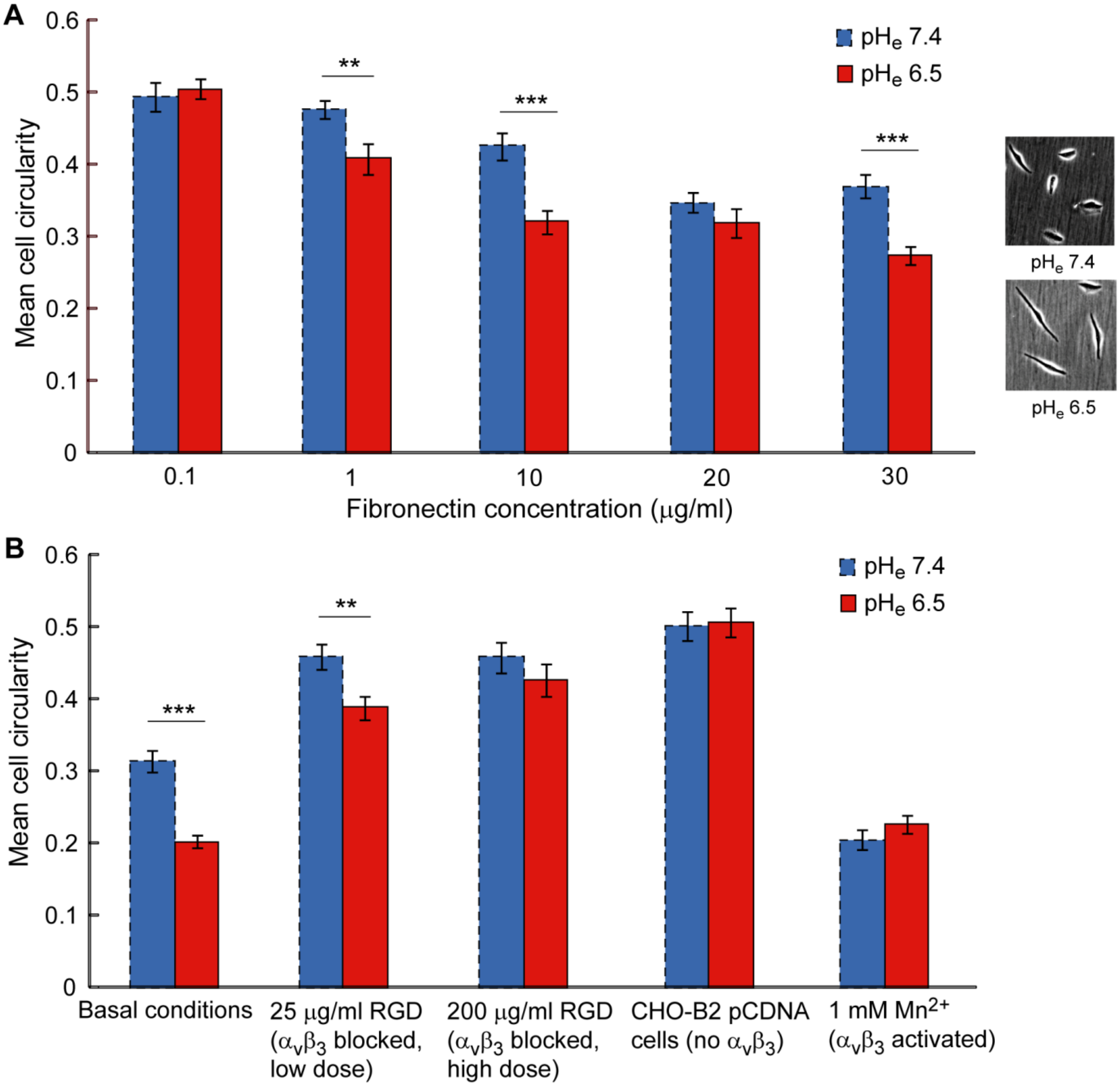

Figure 5.4 (A) Mean $\alpha_v\beta_3$ CHO-B2 cell circularity as a function of fibronectin surface coating concentration measured 8 hr after setting media pH to 7.4 or 6.5. Cell circularity decreased as fibronectin concentration increased for both pH$_e$ values. Cells at pH$_e$ 6.5 had lower cell circularity than cells at pH$_e$ 7.4 for all conditions, with the exception of 0.1 μg/ml fibronectin. Images show representative snapshots of $\alpha_v\beta_3$ CHO-B2 cells at pH$_e$ 7.4 or 6.5. (B) Mean $\alpha_v\beta_3$ CHO-B2 cell circularity at 10 μg/ml fibronectin measured 8 hr after setting media pH to 7.4 or 6.5. Soluble RGD peptide or Mn^{2+} was added in some cases, and one set of experiments was conducted with CHO-B2 pCDNA cells, as indicated. The difference in mean circularity at pH$_e$ 7.4 vs. pH$_e$ 6.5 for cells observed under basal conditions was eliminated for CHO-B2 pCDNA cells and for $\alpha_v\beta_3$ CHO-B2 cells incubated with 200 μg/ml RGD or 1 mM Mn^{2+}. At least 50 cells were measured for each condition, and all error bars are SEM. $^{***}p \leq 0.0001$, $^{**}p < 0.01$.

5.3.5. Discussion of long timescale cell spreading and morphology results

For our measurements of long-timescale cell area and circularity, the media was maintained at a steady acidic pH$_e$ level over several hours. As with the subcellular-scale experiments in Chapter 4, these experiments were conducted at pH_e 6.5 rather than pH_e 6.0 because cells were more active in pH_e 6.5. Although pH 6.0 is appropriate for experiments measuring molecular-level integrin activation and binding to antibodies or ligands, it may be too acidic for complex cellular-level processes such as spreading and migration, which involve many subcellular systems that could be independently and deleteriously affected by acidic pH_e. Our MD data indicate that the critical amino acid ASPβ127 will be protonated on the majority of integrins as long as the extracellular pH is less than the predicted pKa of this residue within the integrin (6.692); therefore, pH_e 6.5 is appropriate for testing the effect of acid-induced integrin activation on these long-timescale cellular-level processes.

We observed that cell area increased as fibronectin coating concentration increased, and that cells in pH_e 6.5 generally had a larger projected area than cells in pH_e 7.4. In addition, cell circularity decreased as fibronectin coating concentration increased, and cells in pH_e 6.5 generally had a lower cell circularity than cells in pH_e 7.4, which is consistent with the elongated morphology we observed for cells in acidic pH_e. Furthermore, experiments with $\alpha_v\beta_3$ blocking and non-$\alpha_v\beta_3$-expressing CHO-B2 pCDNA cells demonstrated that in our system, this integrin is necessary for cell area to increase and cell circularity to decrease. Finally, experiments with Mn^{2+} ions demonstrated that activation of $\alpha_v\beta_3$ was sufficient to cause these effects in a pH_e-independent manner. Our combined data indicate that these long-timescale changes to cell area and circularity can be reasonably attributed to increased cell-substratum adhesiveness resulting from acidic pH_e-induced integrin activation.

Interestingly, 200 μg/ml of the blocking peptide GRGDSPC abolished the pH_e dependence of cell circularity, but not cell area. However, the pH_e dependence of cell area was abolished for CHO-B2 pCDNA cells. These results suggest that the 200 μg/ml blocking peptide concentration was not enough to completely block all $\alpha_v\beta_3$ receptors on the cell surface, which is consistent with the fact that cells did not detach in this condition. This also suggests that cells require more integrins to achieve an elongated morphology than to simply spread out.

Our observation of increased cell area in acidic pH_e is consistent with the work of Kato et al., who demonstrated that mouse melanoma cells spread more in acidic pH_e [41]. In addition, our data showing that cells attained an elongated morphology characterized by lower circularity after long-timescale exposure to pH_e 6.5 is consistent with Stock et al.'s observation of lower melanoma cell circularity in acidic pH_e, and our model of acid-induced integrin activation is in agreement with Stock et al.'s speculation that acidic pH_e strengthened the integrin-ligand bond in their studies [29]. Furthermore, Smith et al. observed that antibody-induced integrin activation caused T cells to adopt an elongated morphology [211], which is consistent with our data showing that $\alpha_v\beta_3$ activation via $Mn2^+$ causes elongation of $\alpha_v\beta_3$ CHO-B2 cells. The physical basis for integrin activation causing cell elongation is not known. In our system, it is possible that acid-induced integrin activation and the resulting stabilization of membrane protrusions perturbed the inherent cell asymmetry, such that both the leading and trailing edge developed stable protrusions and actin-integrin adhesion complexes, making the trailing edge less likely to detach from the substratum. This could cause cells to stretch out and become elongated during the process of migration.

5.4. Cell migration

5.4.1. Background

Many studies have demonstrated that cell migration behavior can be well described by a persistent random walk model, in which cells migrate in the same direction over short timescales, but appear to randomly change direction when observed over longer timescales [96, 187, 212-214]. According to this model, the mean-squared displacement of cell centroids $<d^2(t)>$ should have the following dependence on time t:

$$<d^2(t)> = 2S^2P[t - P(1 - e^{-t/P})] \quad \text{(Eq. 5.1)}$$

where S is the cell migration speed and P is the persistence time, which is the characteristic time that a cell migrates in a particular direction [212]. Cell migration speed is generally calculated as the root mean-squared displacement during a particular time interval (usually chosen as the time between successive frames of a timelapse recording, e.g. 5 min) divided by the interval time, and persistence time can be extracted by fitting data to the persistent random walk equation (Eq. 5.1).

The biophysical cell migration model of DiMilla et al. predicted that cell migration speed would have a biphasic dependence on ECM ligand density, with a peak at intermediate density [95], and this result has been experimentally verified in many cell systems [96, 188, 213, 214]. At low ligand densities, the cell is unable to gain sufficient traction for migration, while at higher than optimal ligand densities, migration is limited by the ability of the cell trailing edge to detach from the substratum [215]. Modulating cell-substratum adhesiveness by changing integrin expression level or activation state can alter the ligand density required for maximum migration speed. For example, DiMilla et al. showed that increasing $\alpha_5\beta_1$ expression in CHO cells caused the biphasic cell migration speed curve to shift to the left, such that lower fibronectin coating concentrations were required for peak migration speed. Similar effects was observed for cells transfected with a mutated version of $\alpha_{IIb}\beta_3$ that had higher binding affinity than wild-type $\alpha_{IIb}\beta_3$, and for cells with $\alpha_{IIb}\beta_3$ activated by antibody binding. [96]. Huttenlocher et al. also demonstrated that the ligand density required for maximal migration[5] was decreased for CHO cells expressing a constitutively activated form of $\alpha_{IIb}\beta_3$ and for cells with activation induced by antibody binding, compared to control cells expressing wild-type $\alpha_{IIb}\beta_3$ [52].

The role of cell-substratum adhesiveness in modulating persistence time is less well characterized and appears to be system-dependent. Previous studies have found that persistence time may exhibit a monotonically increasing [187], biphasic [213, 214], or inverse biphasic dependence [213] on ECM ligand density, and the physical basis for these varied dependencies is currently not well understood.

---

[5] In the study by Huttenlocher et al., migration was characterized by the number of cells that reached the bottom chamber in a transwell assay, rather than by cell speed.

5.4.2. Experimental results

We measured cell migration speed and persistence time as a function of fibronectin coating concentration at normal and acidic extracellular pH. Our cell migration experiments were conducted for $\alpha_v\beta_3$ CHO-B2 cells plated on fibronectin-coated polystyrene dishes with tight fitting lids. Cells were allowed to adhere and spread at pH_e 7.4 for 2 – 3 hr before extracellular media pH was changed to pH_e 6.5 or pH_e 7.4. Media pH_e was then maintained for 8 hr, and cells were imaged every 5 min during this time period. From these images, cell centroid locations were tracked and cell migration speeds and persistence times were measured.

Results demonstrated that $\alpha_v\beta_3$ CHO-B2 cell migration speed had a biphasic dependence on fibronectin coating concentration, as expected. For cells in media maintained at pH_e 7.4, the peak migration speed of 16.97 μm/hr occurred at 1 μg/ml fibronectin, compared to the peak migration speed of 12.98 μm/hr at 0.1 μg/ml fibronectin for cells in pH_e 6.5 (Figure 5.5A). This leftward shift of peak speed to lower fibronectin concentrations indicates that cells at acidic extracellular pH required less ligand to achieve an optimal balance between traction and detachment. These data also demonstrate that cells in pH_e 6.5 migrated slower than cells at pH_e 7.4 for all the fibronectin concentrations tested; thus, the overall effect of acidic extracellular pH on cell migration speed is to shift the biphasic curve both down and to the left (Figure 5.5A). We also characterized cell persistence time as a function of fibronectin coating concentration at pH_e 7.4 and pH_e 6.5. We found that persistence time was biphasic with respect to fibronectin coating concentration, and that the location of peak persistence time was shifted from 19.54 min at 30 μg/ml fibronectin for cells in pH_e 7.4 to 13.99 min at 1 μg/ml fibronectin for cells in pH_e 6.5 (Figure 5.5B).

We also conducted migration experiments for $\alpha_v\beta_3$ CHO-B2 cells seeded on fibronectin-coated glass in serum-free media at pH_e 7.4. We used these measurements to identify the optimal ligand density for experiments requiring the optical quality of glass, such as the high magnification kymography and AIAC imaging experiments that were described in Chapter 4. For cells migrating on fibronectin-coated glass, the peak migration speed of 15.24 μm/hr occurred at 30 μg/ml fibronectin (Figure 5.5C), compared to the peak speed of 16.97 μm/hr at 1 μg/ml fibronectin for cells migrating on fibronectin-coated polystyrene (Figure 5.5A). Thus, maximum migration speed occurred at a higher ligand concentration for cells migrating on fibronectin-coated glass than for cells migrating on fibronectin-coated polystyrene, but the magnitude of the peak migration speed is similar on both surfaces. The persistence time for cells migrating on glass did not have a strong dependence on fibronectin concentration (Figure 5.5D), as none of the values of persistence time were statistically significantly different than any other values.

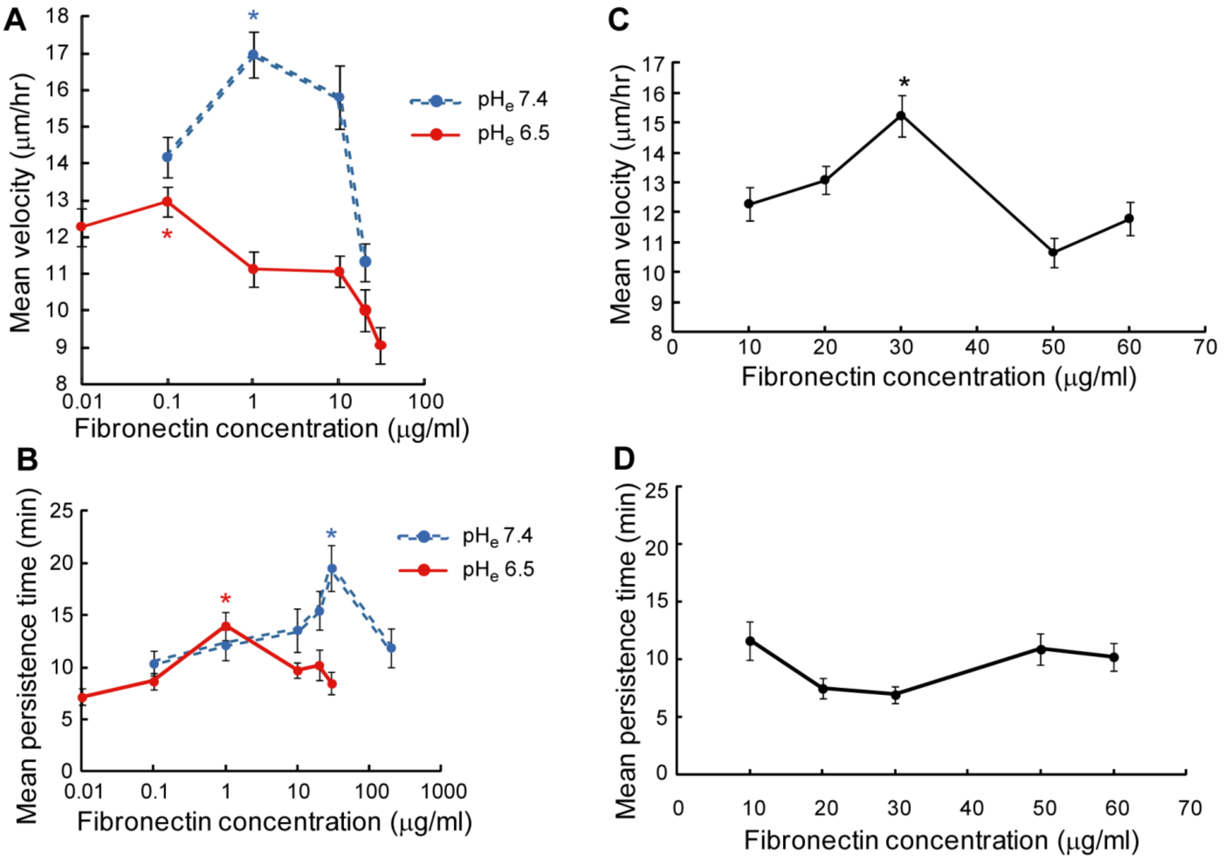

Figure 5.5 Mean speeds and persistence times for cells migrating on fibronectin-coated polystyrene (A,B) or fibronectin-coated glass (C,D). (A) Mean cell migration speed as a function of fibronectin coating concentration for cells migrating on fibronectin-coated polystyrene. Maximum migration speed occurred at a lower fibronectin concentration when cells were in acidic pH_e. Asterisks indicate peak migration speeds. Statistical significance of maximum migration speed value at pH_e 7.4: 0.1 vs. 1 μg/ml, $p < 0.05$; 1 vs. 20 μg/ml, $p < 0.001$; 1 vs. 30 μg/ml, $p < 0.001$. For pH_e 6.5: 0.1 vs. 1 μg/ml, $p < 0.1$; 0.1 vs. 10 μg/ml, $p < 0.05$; 0.1 vs. 20 μg/ml, $p < 0.001$; 0.1 vs. 30 μg/ml, $p < 0.001$. (B) Mean cell persistence time as a function of fibronectin coating concentration for cells migrating on fibronectin-coated polystyrene. Maximum persistence time occurred at a lower fibronectin concentration when cells were in acidic pH_e. Asterisks indicate peak persistence times. Statistical significance of maximum persistence times at pH_e 7.4: 0.1 vs. 30 μg/ml, $p<0.05$; 1 vs. 30 μg/ml, $p<0.05$. For pH_e 6.5: 0.01 vs. 1 μg/ml, $p<0.001$; 0.1 vs. 1 μg/ml, $p<0.01$; 1 vs. 10 μg/ml, $p<0.05$; 1 vs. 30 μg/ml, $p<0.01$. (C) Mean cell migration speed as a function of fibronectin coating concentration for cells migrating on fibronectin-coated glass in pH_e 7.4. Asterisk indicates peak migration speed. Statistical significance of maximum migration speed: 10 vs. 30 μg/ml, $p<0.01$; 30 vs. 50 μg/ml, $p<0.001$; 30 vs. 60 μg/ml, $p< 0.001$. (D) Mean cell persistence time as a function of fibronectin coating concentration for cells migrating on fibronectin-coated glass in pH_e 7.4. None of the values for persistence time are statistically significantly different than any other values. For (A) and (B), at least 40 cells were analyzed for each condition. For (C) and (D), at least 50 cells were analyzed for each condition. All error bars represent SEM.

5.4.3. Cell migration model

The effects of acidic extracellular pH on cell migration velocity in our experiments could be due to enhanced integrin activation and binding in this condition. However, it is also possible that acidic pH_e altered the cell in other ways (e.g. changing activity of signaling proteins, altering cellular metabolism, inducing or suppressing gene expression, etc.), and that these secondary effects caused the changes to migration velocity that we observed. In order to assess the extent to which our data can be explained by acid-induced integrin activation alone, we employed the biophysical cell migration model of DiMilla et al. [95]. In this model, the cell is approximated as a flat rectangular sheet with integrin receptors on both sides, on top of a substratum displaying immobilized ligand molecules (Figure 5.6A). The model takes into account only integrin trafficking, integrin-ligand binding, and contractile force generation, and does not consider other processes such as cytoskeletal dynamics or protein signaling.

The DiMilla et al. model is divided into two parts. In the first part, there is no contractile force, and the steady state receptor distribution is determined. In the model formulation, integrin receptors can undergo diffusion within the cell membrane, endocytosis, and reinsertion into the membrane. Membrane reinsertion can be polarized such that receptors are preferentially inserted into the cell leading edge. Receptors on the bottom side of the cell can also bind reversibly to the immobilized ligands, and binding affinity can vary between the lamellipod and uropod (Figure 5.6A). By using mass balances for free and bound receptors with appropriate kinetic constants and boundary conditions, it is possible to find the steady state receptor distribution over the cell surface.

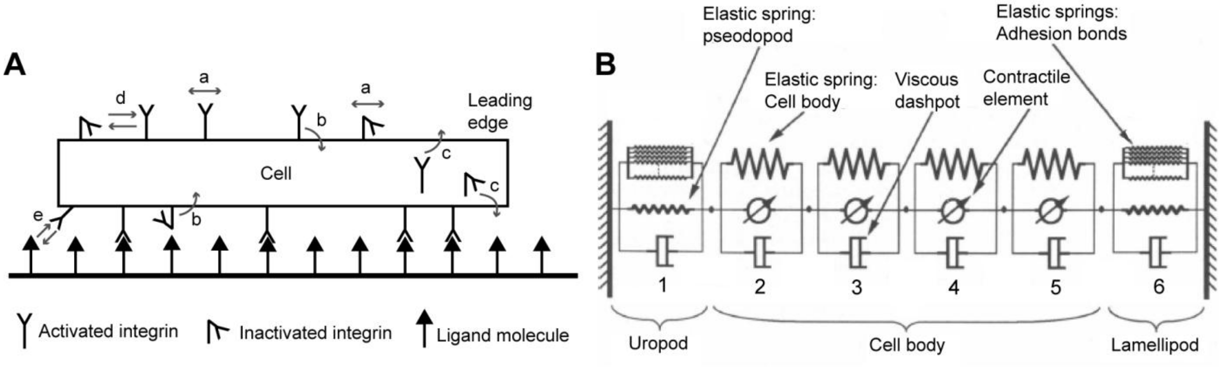

Figure 5.6 (A) Schematic of receptor adhesion and trafficking events that take place in our model formulation. For clarity, the cell is represented here with a separation between the top and bottom membranes; however, in the model, the cell is flat with no space between the top and bottom. Integrin receptors can diffuse within the cell membrane (a), undergo endocytosis (b), and be reinserted into the membrane (c). These events can occur for both activated and inactivated integrins, and reinsertion occurs preferentially at the leading edge of the cell. Receptors can switch between inactivated and activated conformations (e) and activated integrins can bind reversibly to ligand molecules (d) which are immobilized on an underlying substratum. (B) Schematic of the cell mechanics model used for calculation of cell displacement. The cell is divided into six compartments. Compartments #2 - #4 represent the cell body, compartment #1 is the trailing edge uropod, and compartment #6 is the leading edge lamellipod. All six compartments contain a spring and dashpot describing the intrinsic mechanical properties of the cell. The internal four cell body compartments also contain a contractile element, and the uropod and lamellipod compartments contain springs describing the adhesion bonds between the cell and substratum. Figure adapted from Ref. [95].

In the second part of the model, contractile force is introduced. The cell is divided into six compartments, with mechanical properties described by springs and dashpots (Figure 5.6B). The internal four compartments (#2 – #4 in Figure 5.6B) represent the cell body and include a contractile force element. Bound receptors are taken into account only for the outermost compartments, which represent the leading edge lamellipod (#6) and trailing edge uropod (#1). When contractile force is introduced, asymmetry in the ratio of adhesion to contractile force between the leading and trailing edges enables cell movement. With this cell mechanics model, it is possible to solve for the cell displacement during the time that contractile force is applied.

This model connects molecular-scale parameters (rates of integrin trafficking and binding) to cellular-scale output parameters (cell migration velocity), and is thus ideal for directly tying together our molecular-scale integrin activation results with our cell migration data. In order to extend this model to assess the effects of $\mathrm{pH_e}$-dependent integrin activation, we introduced two different integrin receptor states: activated and inactivated. Both integrin states were allowed to diffuse, undergo endocytosis, and be reinserted into the cell membrane [56]. However, because activated integrins have a much higher binding rate than inactivated integrins [80], only the activated state was allowed to bind ligand. Although the original DiMilla et al. model allows for differences in bond dissociation rates between the lamellipod and uropod, we kept the dissociation rate constant at all locations within the cell. Thus, the only source of asymmetry is the preferential insertion of integrins into the leading edge membrane.

In our model, integrins can switch between the two activation states, with rate constants estimated from rates of large-scale conformational changes for other proteins (10 – 100 $\mathrm{s^{-1}}$) [131-134] (Figure 5.6A). It was assumed that the activation rate k_a has an inverse dependence on $\mathrm{pH_e}$, such that more integrin receptors become activated in more acidic $\mathrm{pH_e}$. However, it is not clear exactly what form the dependence of k_a on $\mathrm{pH_e}$ should take. We know that the percentage of integrin $\alpha_\mathrm{v}\beta_3$ receptors with protonated ASPβ127 is expected to increase approximately linearly as $\mathrm{pH_e}$ decreases, for the $\mathrm{pH_e}$ range of interest.[6] Therefore, as a first approximation, we can use k_a values that produce a linearly increasing percentage of activated receptors with decreasing $\mathrm{pH_e}$. It is also possible that the inactivation rate k_i could decrease in acidic $\mathrm{pH_e}$. However, as decreasing k_i has the same net effect as increasing k_a (more activated integrins at steady state), we took k_i to be constant for these calculations. With these simple modifications, the DiMilla et al. model can be used to assess how much of an effect acid-induced integrin activation alone is likely to have on cell migration speed, and model predictions can be compared to our experimental data. Details of model equations and parameter choices can be found in Materials and Methods, Section 8.11.

By setting the inactivation rate k_i to zero, our model can be reduced back to the original DiMilla et al. model, enabling us to reproduce the DiMilla et al. results as validation of our code. Figure 5.7A displays the biphasic relationship between dimensionless cell velocity ν and dimensionless cell-substratum adhesiveness κ, plotted for several values of ψ, which is the ratio of lamellipodal to uropodal bond dissociation rate. Figure 5.7C displays the biphasic relationship between ν and κ, for several values of the total receptor number R_T. For comparison, the original figures from DiMilla et al. illustrating these relationships are shown in Figure 5.7B and Figure 5.7D. With our updated code, we were

---

[6] From the relation $= pKa + log\frac{[A^-]}{[HA]}$, where $[A^-]$ is the concentration of deprotonated molecules and [HA] is the concentration of protonated molecules.

able to achieve excellent agreement with the trends reported by DiMilla et al., although there were some slight differences in the exact velocity values. These minor differences are likely to be due to the updated packages (in Matlab) that we used for solving of model equations, as well as our implementation of certain constraints, details of which were not explicitly stated in the original report.

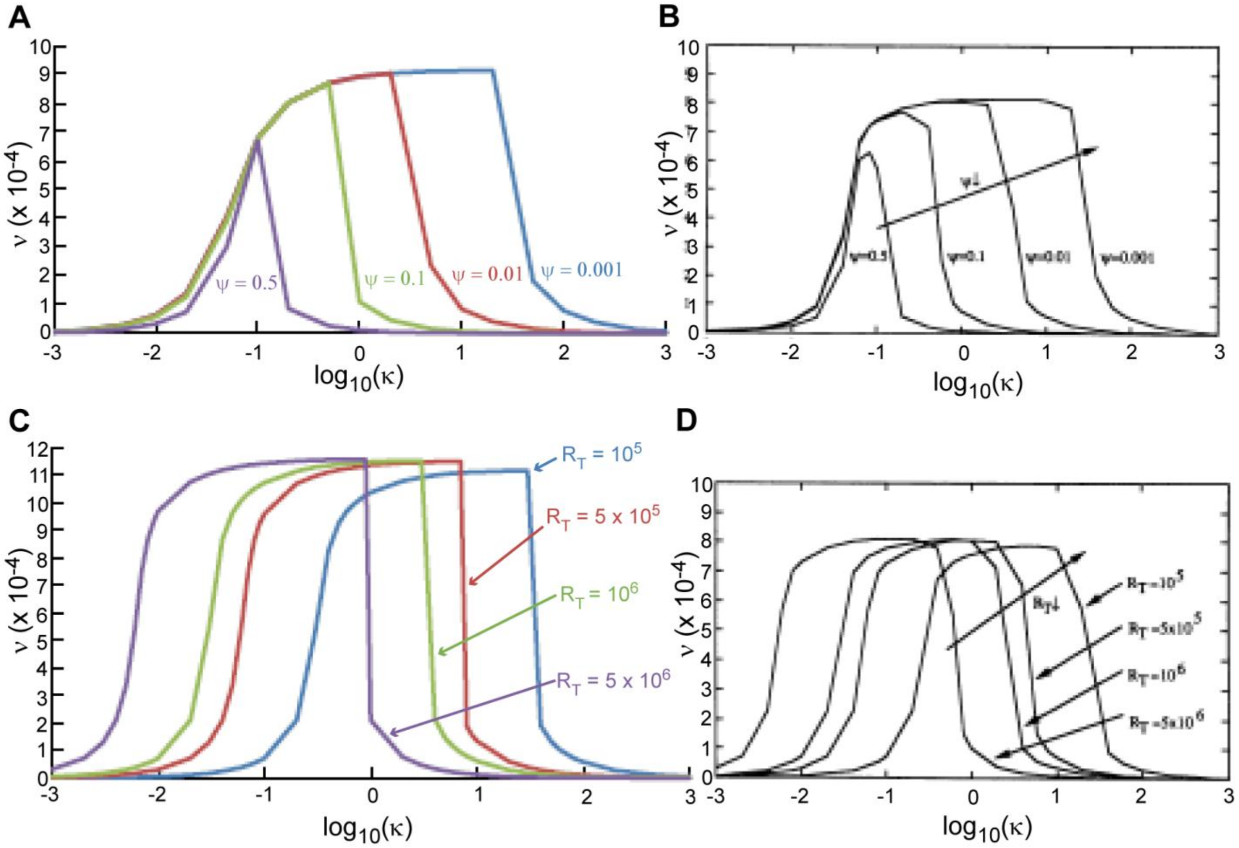

Figure 5.7 Reproduction of results from DiMilla et al. (Ref. [95]) produced with our updated code compared to original figures. (A) Dimensionless cell velocity ν as a function of dimensionless cell-substratum adhesiveness κ from our implementation of the DiMilla et al. model. Results are shown for several values of ψ, the ratio of uropodal to lamellipodial adhesiveness. (B) Original figure adapted from Ref. [95], illustrating ν as a function of κ for several values of ψ. (C) Dimensionless cell velocity ν as a function of dimensionless cell-substratum adhesiveness κ from our implementation of the DiMilla et al. model. Results are shown for several values of R_T, the total receptor number. (D) Original figure adapted from Ref. [95], illustrating ν as a function of κ for several values of R_T.

We can now proceed with calculations using the modified model that includes two integrin conformational states. Our first goal is to produce the computational parallel of Figure 5.5A, which shows our experimental measurements of cell migration velocity as a function of fibronectin surface coating concentration, for two extracellular pH values. To do this, we can calculate cell velocity as a function of ligand density, for several values of k_a, the integrin activation rate constant. Each value of k_a corresponds to a certain percentage of integrins being in the activated conformation at steady state. Before we can compare computational predictions to our experimental data, we must estimate the activation percentages that correspond to pH_e 7.4 and pH_e 6.5. For isolated $\alpha_v\beta_3$ molecules at pH 7.5, in the same ion conditions ($Ca^{2+} + Mg^{2+}$) as our cell migrations experiments, ~14% of the receptors had an extended conformation indicative of the activated state [80]. For $\alpha_v\beta_3$ molecules on a cell surface, the percentage is likely to be somewhat higher due to the addition of intracellular mechanisms of integrin activation. Thus, we will assume that ~20% of $\alpha_v\beta_3$ molecules are activated at pH_e 7.4.

We can use our molecular-level experimental data to estimate the fold change in activation percentage that occurs for acidic pH_e vs. pH_e 7.4. Although our molecular-level experiments were conducted at pH_e 6.0 rather than pH_e 6.5 (the condition used for cell migration measurements), these experimental data provide a reasonable first estimate of relative integrin activation percentages. Our flow cytometry experiments indicated that the level of activated $\alpha_v\beta_3$ was 1.13-fold higher for cells at pH_e 6.0 than cells at pH_e 7.4, while our AFM-MFS binding frequency data indicated that the level of activated $\alpha_v\beta_3$ was 1.48-fold higher for cells at pH_e 6.0 (Figure 3.2, Figure 3.6). Due to the fact that the antibody binding step for flow cytometry experiments was done at pH_e 7.4 (discussed in Section 3.2.2), the fold change estimate from this approach is likely to be an underestimate of the true value. We note that the value obtained from AFM-MFS is also not exact and has some error due to the limited sampling that was possible with this experimental approach. We can use the predicted pK_a value obtained from MCCE to calculate an upper bound for the fold change in activated integrins from pH_e 6.5 to 7.4. Assuming that protonated ASPβ127 always leads to activation of $\alpha_v\beta_3$ and neglecting other mechanisms of activation, we would expect ~16.4% of $\alpha_v\beta_3$ receptors to be activated at pH_e 7.4, and ~60.9% of the receptors to be activated at pH_e 6.5, equivalent to a 3.71-fold increase[7]. Taking these various estimates together, we will assume that the fold change in activation percentage from pH_e 7.4 to pH_e 6.5 is in the range of 1.5 – 3.5. Therefore, if 20% of $\alpha_v\beta_3$ molecules are activated at pH_e 7.4, then 30% – 70% will be activated at pH_e 6.5.

Figure 5.8 displays model calculations of cell velocity as a function of ligand density for k_a corresponding to 20% – 70% activated integrins. Increasing k_a causes the biphasic curve to shift to the left, such that peak migration speeds occur at lower adhesiveness κ, which is a function of ligand density n_s and the receptor-ligand dissociation constant K_D: $\kappa = n_s/K_D$. In our cell migration experiments, we observed a similar leftward shift of the biphasic curve for pH_e 6.5 vs. pH_e 7.4. Denoting the fibronectin concentration required for peak migration speed at pH_e 6.5 as $[Fn]_{6.5}$ and the corresponding concentration for pH_e 7.4 as $[Fn]_{7.4}$, our experimental data indicate that $\frac{[Fn]_{6.5}}{[Fn]_{7.4}} \approx 0.1$. As it is possible that the true peak speeds occur at fibronectin concentrations in between the ones that we tested, we will take 0.1 as an approximate, rather than exact, value for this ratio of critical fibronectin concentrations. Assuming that fibronectin concentration in solution is proportional to adhesiveness κ, we can compare this approximate ratio to our model predictions. If 20% of integrins are activated at pH_e 7.4, and ≥50% are activated at pH_e 6.5, the ratio of adhesiveness corresponding to the model-predicted leftward shift of maximum speed is $\frac{[\kappa]_{6.5}}{[\kappa]_{7.4}} = 0.25$. Given the limited resolution of the exact peak locations in our experimental

---

[7] From the relation $pH = pK_a + log\frac{[A^-]}{[HA]}$, where [$A^-$] is the concentration of deprotonated molecules and [HA] is the concentration of protonated molecules.

data, we feel that this ratio is in reasonable agreement with our experimentally measured ratio of 0.1. Thus, our model results indicate that increased integrin activation in pH$_e$ 6.5 is sufficient to cause the experimentally observed leftward shift of peak migration speed, without any contribution from intracellular signaling or other mechanisms.

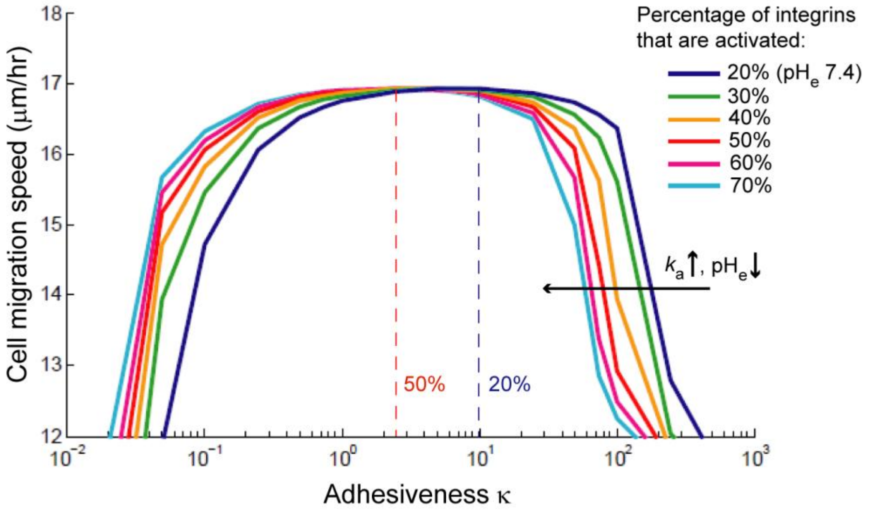

Figure 5.8 Cell migration model predictions for the effect of acidic extracellular pH on cell migration velocity. Decreasing extracellular pH is modeled as increasing the integrin activation rate k_a. This corresponds to an increasing percentage of total receptors becoming activated. pH$_e$ 7.4 is assumed to correspond to 20% activation. As pH$_e$ decreases, the biphasic curve of cell migration speed as a function of dimensionless adhesiveness shifts to the left. The adhesiveness values corresponding to peak migration speeds for 20% and 50% activation are indicated with dashed lines.

Our experimental data also showed that the magnitude of the peak migration speed for cells at pH$_e$ 6.5 was lower than that for cells at pH$_e$ 7.4 (Figure 5.5A). This decrease in peak migration speed is not predicted by the cell migration model to be a consequence of increased integrin activation alone. Thus, acidic pH$_e$ must have had some other effect on cells that caused migration speed to decrease. We can use the migration model to identify parameters that could have caused peak migration speed to decrease in our system (if these parameters were also altered in acidic pH$_e$). To do this, we calculated cell migration speed as a function of fibronectin density, while systematically varying each parameter in the model. We found that the following parameter changes can cause peak migration speed to decrease significantly: decreasing bond-cytoskeleton connection strength, increasing cell stiffness, increasing pseudopodal stiffness, increasing bond stiffness, decreasing contractile force, decreasing cell length, and increasing cell width (Figure 5.9).

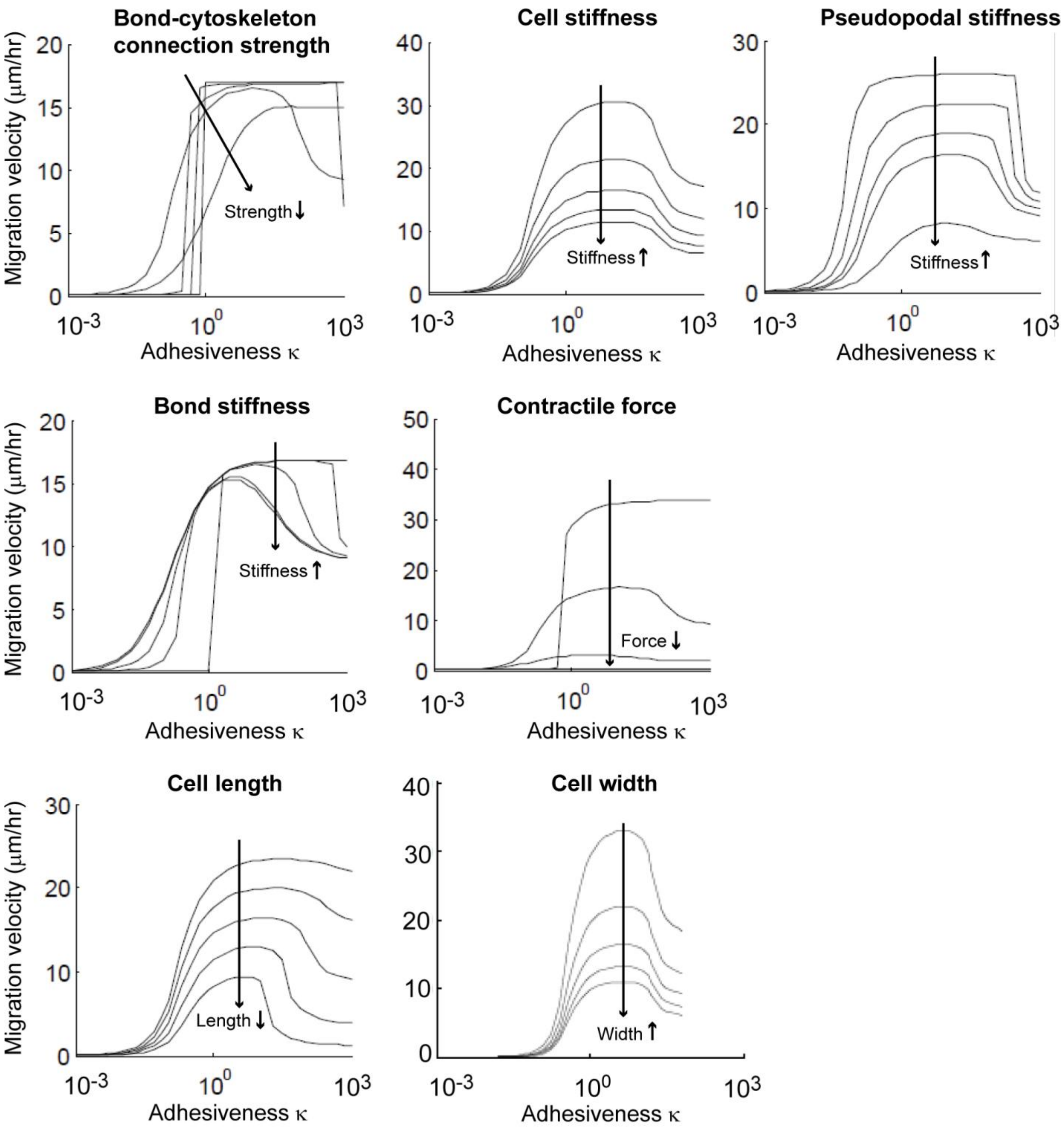

Figure 5.9 Parameters in the migration model that can cause peak cell migration speed to decrease. Cell migration speed is displayed as a function of dimensionless adhesiveness κ over a range of each parameter. The direction of parameter change (increase or decrease) that causes migration speed to decrease is indicated within each plot.

Parameter change that causes peak migration speed decrease	**Experimental data to test this**	**pH_e 7.4 value (mean ± SEM)**	**Acidic pH_e value (mean ± SEM)**	**Conclusion: does this parameter change occur with acidic pH_e?**
Decrease in bond-cytoskeleton connection strength	No data available	N/A	N/A	N/A
Increase in cell body stiffness	Indentation portion of AFM-MFS force-displacement data for pH_e 7.4 and 6.0	299.54 ± 25.16 Pa, $N = 10$ cells	275.00 ± 19.65 Pa, $N = 10$ cells	No; no significant difference in mean cell stiffness for pH_e 7.4 vs. 6.0 ($p > 0.05$)
Increase in pseudopodal stiffness	Assumed to vary in the same way as cell body stiffness	299.54 ± 25.16 Pa, $N = 10$ cells	275.00 ± 19.65 Pa, $N = 10$ cells	No; no significant difference in mean cell stiffness for pH_e 7.4 vs. 6.0 ($p > 0.05$)
Increase in bond stiffness	Slope of AFM-MFS force-displacement data immediately before bond rupture for pH_e 7.4 and 6.0	672.75 ± 19.97 pN/μm, $N = 166$	736.48 ± 24.44 pN/μm, $N = 207$	No; no significant difference in mean effective bond stiffness for pH_e 7.4 vs. 6.0 ($p > 0.05$)
Decrease in contractile force	PDMS wrinkling	N/A	N/A	Unknown; $\alpha_v\beta_3$ CHO-B2 cells did not measurably wrinkle the PDMS films
Decrease in cell length	Cell images in pH_e 7.4 and 6.5	52.68 ± 19.97 μm, $N = 91$	67.99 ± 2.52 μm, $N = 99$	No; cell length increases, not decreases, in pH_e 6.5 ($p < 0.0001$)
Increase in cell width	Cell images in pH_e 7.4 and 6.5	16.70 ± 0.60 μm, $N = 91$	16.23 ± 0.66 μm, $N = 99$	No; no significant difference in mean cell width for pH_e 7.4 vs. 6.5 ($p > 0.05$)

Table 5.1 Summary of parameter changes that cause peak migration speed to decrease in the cell migration model. Most of these parameters can be measured experimentally, and results indicate that none of these parameters were altered in acidic pH_e in a manner that is consistent with a decrease in peak migration speed.

With the exception of bond-cytoskeleton connection strength, all of these parameters can be assessed to some level with experimental data. Cell stiffness can be measured from analysis of the indentation portions of our AFM-MFS force-displacement data, and we can assume that pseudopodal stiffness will vary in the same way as cell body stiffness. Effective bond stiffness can be measured from the slope of our AFM-MFS data immediately before rupture, but it is important to note that this stiffness includes contributions from the PEG linker and cross-linker used for cantilever functionalization. Cell length and cell width can be measured from our images of cells after exposure to pH_e 6.5 or pH_e 7.4. Finally, contractile force can be assessed by culturing cells on a deformable poly(dimethyl siloxane) (PDMS) films. Cell-generated contraction can cause the PDMS to wrinkle, and the amount of force can be estimated from this deformation [216]. If experimental data indicate that one or more of the parameter changes displayed in Figure 5.9 occurs in acidic pH_e, this could at least partially explain the lowered migration speed that we observed in this condition.

Results of our data analyses are summarized in Table 5.1. We were not able to measure contractile force due to the fact that $\alpha_v\beta_3$ CHO-B2 cells did not measurably wrinkle the PDMS substratum in our experiments, even when the film thickness was decreased. This indicates that the amount of contractile force generated by these cells is too small to create wrinkles, although it is sufficient for cell migration. There were no statistically significant differences in cell stiffness, pseudopodal stiffness, bond stiffness, or cell width between pH_e 7.4 and pH_e 6.0 or 6.5. The mean cell length in pH_e 6.5 was significantly larger than that in pH_e 7.4, but according to the model predictions, this change in cell length would cause cell migration speed to increase, not decrease. Thus, none of the experimentally testable parameters were significantly altered in acidic pH_e in a manner that can explain a decrease in peak migration speed. From these data, it remains possible that altered contractile force generation and/or bond-cytoskeleton connection strength is responsible for the decrease in migration speed in acidic pH_e. However, as there are many molecular and cellular processes that are not included in the model, it is also likely that one or more of these other factors could be responsible for decreasing cell migration speed in acidic extracellular pH.

5.4.4. Discussion of cell migration results

Our cell migration experiments demonstrated that the fibronectin concentration required for maximum migration speed was decreased at acidic pH_e; i.e., the location of the peak in the biphasic curve was shifted to the left (Figure 5.5A). Our results from the updated DiMilla et al. cell migration model suggest that increased integrin activation could cause a leftward shift of peak migration speed that is comparable with our experimental data (Figure 5.8). Furthermore, Palecek et al. showed that antibody-induced integrin activation in $\alpha_{IIb}\beta_3$ CHO cells also decreased the ligand concentration required for maximum migration speed to a similar extent as observed in our experiments [96]. Therefore, our measurement of a leftward shift of peak migration speed can be sufficiently explained by a model of increased integrin activation at acidic pH_e, which results in increased cell-substratum adhesiveness and consequently less ligand required for efficient migration.

In our experiments, we also observed that the maximum cell speed measured at pH_e 6.5 was lower than the maximum speed measured at pH_e 7.4 (Figure 5.5A). Such an effect was not observed in the studies by Palecek et al. [96] or in our migration model predictions (Figure 5.8), indicating that the reduction in peak migration speed we observed at acidic pH_e cannot be explained by increased integrin activation alone. The cell migration model was used to explore some possible reasons for this effect (Figure 5.9), and comparison with experimental data indicated that none of the experimentally testable model-identified hypotheses could explain the decrease in migration speed that we observed in acidic pH_e (Table 5.1). However, we were not able to measure the effect of pH_e on contractile force, due to the fact that $\alpha_v\beta_3$ CHO-B2 cells did not visibly wrinkle the PDMS films used in our assay. We also did not have any experimental data regarding the strength of the bond-cytoskeletal connection, which likely corresponds to the lumped contributions of many AIAC proteins. Thus, the possibility remains open that changes to contractile force generation or bond-cytoskeletal connection strength caused the reduction in migration speed that we observed for cells at pH_e 6.5. Furthermore, acidic extracellular pH likely affects processes that were not considered in this biophysical model of cell migration, such as cell signaling or metabolism. Although the reduction in peak migration speed indicates that acidic pH_e may affect complex cellular behaviors such as migration via more than one mechanism, it does not preclude the possibility of integrin activation via extracellular acidification.

For cells migrating on polystyrene, the persistence time had a biphasic dependence on fibronectin coating concentration, and the location of peak persistence time was shifted to lower fibronectin concentrations for cells in pH_e 6.5 compared to cells in pH_e 7.4 (Figure 5.5C). This biphasic dependence of persistence time on ligand concentration is consistent with the work of DiMilla et al., who found that the persistence time of human smooth muscle cells was biphasic with respect to fibronectin and collagen type IV coating concentration [214], as well as the work of Ware et al., who found that the persistence time of NR6 fibroblasts was biphasic with respect to Amgel concentration [213]. However, for cells migrating on glass, we found no significant dependence of persistence time on fibronectin concentration (Figure 5.5D). It is possible that the persistence time for cells migrating on glass does indeed have a biphasic dependence on fibronectin coating concentration, but that we did not test a large enough concentration range for this dependence to be revealed. Future work can extend our results to a wider range of fibronectin concentrations to test this hypothesis.

It is unlikely that any of our cellular-scale (or subcellular-scale) results can be explained by acid-induced changes to fibronectin, as both guanidine hydrochloride-induced denaturation experiments and computational electrostatic calculations have demonstrated that the fibronectin protein structure is generally unchanged for pH 6.0 and higher [217, 218]. Finally, it is important to note that our migration experiments were conducted on 2-D surfaces. While cell migration speed in 3-D matrices still has a biphasic dependence on cell-matrix adhesiveness, migration in 3-D also requires matrix metalloproteinases (MMPs) to digest the matrix and reduce steric hindrance [219]. It has been shown that secretion and catalytic activity for some MMPs have pH-dependence and can be upregulated in acidic pH_e [40, 220, 221]. This would cause increased digestion of the ECM at acidic pH_e and consequently less ligands available for integrin binding. Thus, increased integrin activation in acidic pH_e may be a mechanism that could compensate for this loss of ECM ligands. Further exploration of the role of acid-induced integrin activation in 3-D cell migration is a very interesting topic for future study.

5.5. Role of intracellular pH in long-timescale experiments

As described above, it is unlikely that intracellular acidification played a significant role in our short-timescale cell spreading experiments, in which we observed changes to cell area in $t < 30$ min. However, the long-timescale cell spreading and migration experiments spanned several hours, which is more than enough time for the intracellular environment to become acidified to $pH_i < 6.5$ (Figure 4.4B). This could affect activity of intracellular proteins in ways that could alter cell spreading and migration behavior. For example, some members of the calpain family of proteases exhibit pH-dependent activity, with optimum activity around pH 7.4 [222]. As many proteins involved in migration are calpain substrates [223], changes in calpain activity at acidic pH_e could certainly affect cell motility. It has also been shown that the binding between talin and actin is pH-dependent, with increased affinity at lower pH, and it was suggested that this results in increased lifetime of actin-integrin adhesion complexes [197]. Changes in talin-actin binding could affect force transmission during actomyosin-mediated contraction, which could alter migration behavior. It is possible that the reduction in migration speed observed for cells at acidic pH_e was a result of changes to intracellular proteins such as calpains, talin, or others. It is also possible that intracellular acidification changes cellular metabolism such that less ATP is available for actomyosin contraction and other motility-related processes. Thus, while our long-timescale cell spreading and migration results are generally consistent with a model of acid-induced integrin activation, we cannot exclude the possibility that intracellular acidification contributed to causing the cellular responses that we observed. However, our short-timescale cell spreading data and kymography measurements (Chapter 4) indicate that pH_e alone can certainly modulate at least the early stages of migration initiation.

5.6. Conclusions and transition to pH_e gradient experiments

5.6.1. Conclusions

In this chapter, we investigated the effects of acidic extracellular pH on cell spreading and migration. We demonstrated that $\alpha_v\beta_3$ CHO-B2 cells exhibited a dynamic and reversible response to changes in extracellular pH_e, and that extracellular acidification resulted in increased cell spreading over short timescales. These effects could have been mediated by increased integrin activation and resulting stabilization of membrane protrusions in acidic pH_e. We further showed that acidic extracellular pH caused cell area to increase and cell circularity to decrease, and that activation of integrin $\alpha_v\beta_3$ was sufficient to cause these results. Finally, we demonstrated that the critical fibronectin concentration required for maximum migration speed is reduced for cells in acidic extracellular pH, and that cells in acidic pH_e migrated slower than cells in pH_e 7.4 for all the fibronectin concentrations that we tested. Modeling results indicate that the reduction in critical fibronectin concentration can be reasonably attributed to increased integrin activation in acidic pH_e, but that the reduction in migration speed is likely to be due to secondary effects of acidic extracellular pH. Overall, these data show that cellular-scale spreading and migration behavior for $\alpha_v\beta_3$ CHO-B2 cells was altered in a manner that is largely consistent with increased integrin activation in acidic pH_e.

5.6.2. Next question: How do cells migrate in pH_e gradients?

The experiments discussed in Chapters 3 – 5 all used $\alpha_v\beta_3$ CHO-B2 cells as a model cell type that enabled study of integrin $\alpha_v\beta_3$ without any contribution from other RGD-binding integrins. In addition, these experiments were all focused on the effects of bulk changes to pH_e. In Chapter 6, we consider the pH_e profiles that cells are likely to encounter in the *in vivo* tumor and wound healing contexts that motivated this work, particularly pH_e gradients. Increased integrin activation, membrane protrusion stabilization, and AIAC formation in acidic pH_e could cause cells to preferentially migrate toward the acidic end of pH_e gradients. As a result, acidic pH_e may serve as a cue that helps direct cells toward poorly vascularized areas during the process of angiogenesis, which is critical to tumor growth and wound healing. In the next chapter, we investigate cell migration behavior in pH_e gradients similar to those that have been measured in tumors. Experiments are conducted for the model $\alpha_v\beta_3$ CHO-B2 cells, as well as endothelial cells, which play an important role during angiogenesis. With these experiments, we move toward an experimental system that is more relevant to the tumor and wound sites of interest, allowing us to consider the implications that our combined results have for cell behavior in these contexts.

5.7. Acknowledgments

J. Breucop collected and analyzed data for the short timescale measurements of cell spreading from the detached state (Figure 5.2). Dr. M. Whitfield conducted PDMS wrinkling experiments (Table 5.1), wrote the code for the cell migration model, conducted tests of parameter variation, and aided in interpretation of results (Section 5.4.3). A.S. Zeiger analyzed indentation data to calculate cell stiffness at pH_e 7.4 and pH_e 6.0 (Table 5.1).

Chapter 6: Cell migration in an extracellular pH gradient

6.1. Overview

Thus far, we have used atomistic-scale simulations and molecular-scale experiments to demonstrate that acidic extracellular pH promotes activation of integrin $\alpha_v\beta_3$. We have also shown that acidic extracellular pH alters membrane protrusion dynamics, actin-integrin adhesion complex formation, cell spreading, and cell migration in a manner that is consistent with increased $\alpha_v\beta_3$ integrin activation. In this chapter, we extend our experiments from homogeneous pH_e conditions to the more complex pH_e environments that exist in the tumor and wound contexts. We investigate the cell migration response to extracellular pH gradients, which have been shown to exist *in vivo* at tumors and are likely to exist in wound sites as well. Using the Dunn chamber to establish gradients from pH_e 6.0 – 7.5, we assess whether cells exhibit directional migration preference toward lower pH_e. We consider the model $\alpha_v\beta_3$ CHO-B2 cell line, as well as bovine retinal microvascular endothelial cells (BRECs), which are relevant to angiogenesis in the tumor and wound healing contexts, and murine NIH-3T3 fibroblasts, which are relevant to the wound healing environment. We find that the average position of $\alpha_v\beta_3$ CHO-B2 cells and BRECs moves progressively toward the acidic end of the pH_e gradient over time, and that these cells preferentially polarize toward lower pH_e. In contrast, NIH 3T3 fibroblasts do not exhibit preferential migration toward either side of the gradient. These data suggest that extracellular pH gradients may help direct migration of angiogenic endothelial cells to poorly vascularized regions of tumors or wounds.

6.2. Background

As described in Chapter 1, the average extracellular pH in tumors and wounds is often significantly more acidic than in normal tissue environments. This is partially due to the fact that tumors and wounds characteristically contain regions of damaged or irregular vasculature, resulting in a hypoxic microenvironment (i.e., the partial pressure of oxygen (pO_2) is decreased from normal levels) [2, 6, 14-18, 24, 27]. However, although the bulk extracellular pH in these environments is generally acidic, the pH_e environment is not uniform. Rather, high resolution methods for measuring pH_e have shown significant spatial variations in pH_e profiles within tumors [1, 18]. In particular, pH_e gradients exist within tumors, with pH_e decreasing about 0.7 units over a distance of about 350 μm from a tumor blood vessel in the case of human colon adenocarcinoma xenografts grown in mice. In this example, the partial pressure of oxygen (pO_2) also dropped over this distance, by about 14 mmHg [1] (Figure 6.1A). Furthermore, pH_e gradients have been measured at the interfaces between tumors and normal tissue, with pH_e increasing about 0.4 units over a distance of about 1 mm toward the normal tissue, for human prostate tumors grown in mice [6]. The presence of oxygen gradients at wound sites implies that similar pH_e gradients occur in these environments as well [23, 26, 28] (Figure 6.1B). However, pH_e profiles were not measured in these wound healing studies, and cannot be estimated from measurements of pO_2 alone, as the relation between pO_2 and pH_e depends on cellular metabolism.

We have shown that acidic extracellular pH promotes activation of integrin $\alpha_v\beta_3$; thus, the overall adhesiveness between a cell and the surrounding ECM is increased in regions of acidic pH_e. Consistent with this finding, acidic extracellular pH also leads to membrane protrusion stability and increased actin-integrin adhesion complex formation. Studies with fibronectin surface gradients have demonstrated that cells preferentially migrate toward higher concentrations of fibronectin coating, which have higher adhesiveness, owing to higher spatial density of adhesive ligands [224, 225]. In the context of our previous results, this suggests that cells in a pH_e gradient may preferentially migrate toward the acidic end of the gradient, if the change in pH_e over the cell length creates a large enough difference in adhesiveness. This could be particularly important for endothelial cells migrating within or toward tumors or wounds to initiate vascularization in hypoxic areas or for fibroblasts migrating into wounds to begin matrix repair and remodeling. Therefore, we examined migration behavior of $\alpha_v\beta_3$ CHO-B2 cells, bovine retinal microvascular endothelial cells (BRECs), and murine NIH-3T3 fibroblasts in pH_e gradients.

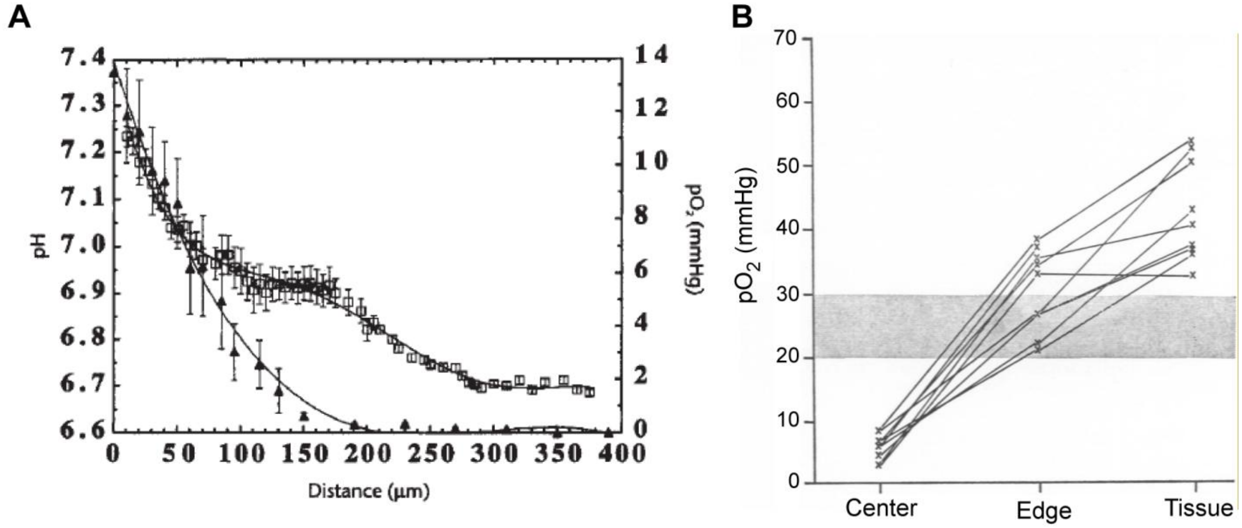

Figure 6.1 Extracellular pH and pO_2 gradients that have been measured in tumors and wounds. (A) Extracellular pH (open squares) and pO_2 (closed triangles) gradients measured in human tumor xenografts. Distance was measured moving away from the nearest blood vessel, with 0 μm taken as the center of the nearest vessel. Figure adapted from Ref. [1]. (B) pO_2 gradients measured in 4-day-old wounds in rats. Measurements were taken at the wound center, wound edge, and surrounding normal tissue. Shaded area represents the average pO_2 for unwounded control tissues (25 ± 5.4 mmHg, mean ± SD). Figure adapted from Ref. [23].

6.3. Results

6.3.1. Gradient stability

In order to establish a pH_e gradient, we used the commercially available Dunn chamber, which is designed to create linear gradients of soluble factors. The Dunn chamber consists of two concentric wells separated by a bridge of 20 μm depth and approximately 1 mm width. When the inner well is filled with a low concentration solution and the outer well is filled with a high concentration solution, a linear concentration gradient forms across the bridge region. The chamber also contains a post of 20 μm depth located at the center of the inner well, which is not exposed to a gradient and thus serves as a control (Figure 6.2A). For analysis of migration data, the initial position of each migrating cell was set at the origin, and images were rotated such that the vertical y-axis was parallel with the gradient at time 0. With this coordinate system assumed for each cell analyzed, increasing y-coordinate value correlates with increasing acidity (Figure 6.2B).

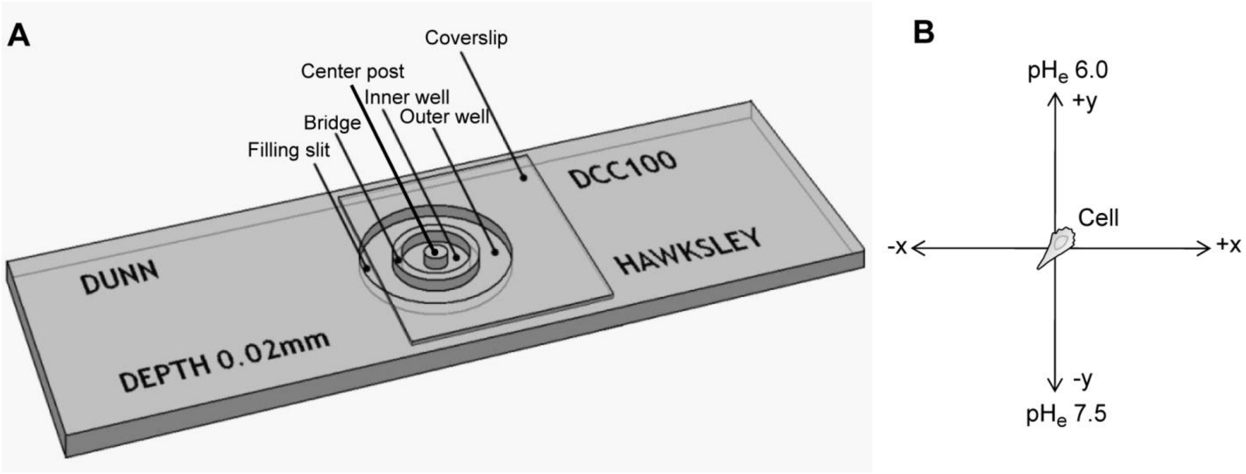

Figure 6.2 Experimental system used to establish pH$_e$ gradients. (A) Illustration of the Dunn chamber used to establish pH$_e$ gradients. When the inner and outer wells are filled with solutions of different concentrations, a linear concentration gradient forms across the bridge. Figure is adapted from www.hawksley.co.uk (B) Schematic of orientation used for analysis of cell tracks. Based on the cell position at time 0, images were rotated such that the gradient was oriented vertically, with the acidic end at the top of the image, and with the initial cell position at the origin.

For our experiments, we established a gradient between pH$_e$ 6.0 – 7.5. This 1.5 pH unit gradient over ~1 mm is similar in magnitude to some gradients reported for tumors *in vivo* [1] (Figure 6.1A). The pH$_e$ gradient was imaged using the pH-sensitive fluorophore BCECF (2′,7′-bis-(2-carboxyethyl)-5-(and-6)-carboxyfluorescein), which was used to measure intracellular pH in Chapter 4. BCECF has excitation wavelengths at 495 nm and 440 nm, and the ratio of the 495/440 nm fluorescence intensities is linear with solution pH in the range of interest (Figure 6.3A). For our measurements, BCECF was added to bicarbonate-free serum-free media (pH$_e$ 6.0 – 7.5) at a concentration of 10 μM. To establish a gradient, the inner well of the Dunn chamber was filled with pH$_e$ 7.5 media and the outer well was filled with pH$_e$ 6.0 media. For control measurements, both wells were filled with media at the same pH$_e$. After the wells were filled with media at the desired pH$_e$, the chamber was sealed with a glass coverslip.

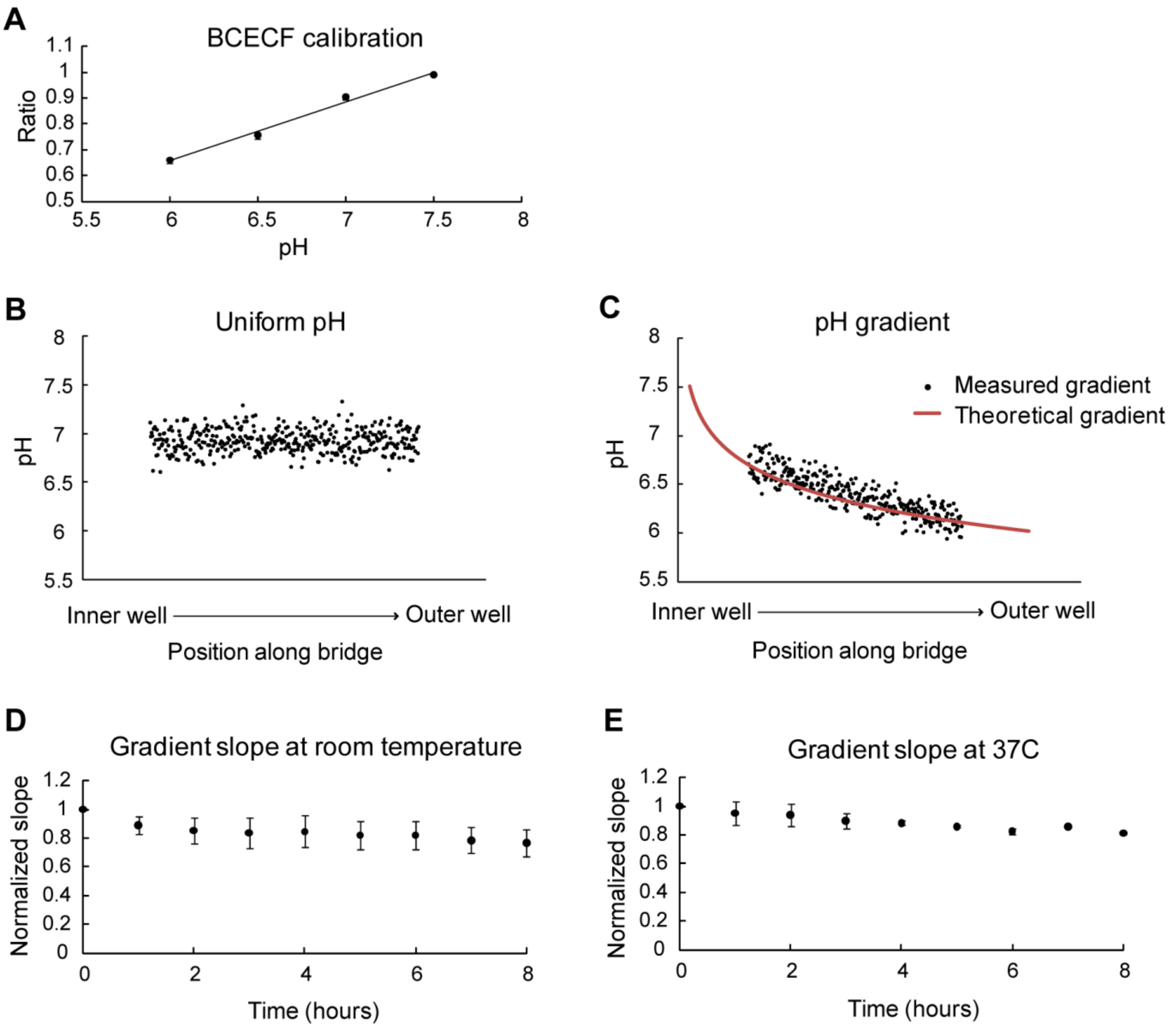

Figure 6.3 Imaging pH_e gradients using the pH-sensitive fluorophore BCECF. (A) Calibration of BCECF light intensity ratio over a pH_e range of 6.0 – 7.5. Light intensity ratio was linear with respect to pH_e in this range. (B) Linescan of BCECF light intensity ratio over the center of the Dunn chamber bridge, when both wells of the chamber were filled with solution of pH_e 7.0. The pH_e profile over the center of the bridge was flat. (C) Linescan of BCECF light intensity ratio over the center of the Dunn chamber bridge, when the inner well was filled with pH_e 7.5 solution and the outer well was filled with pH_e 6.0 solution. The pH_e gradient that formed over the center of the bridge was approximately linear and was in good agreement with the theoretical logarithmic gradient from pH_e 7.5 to pH_e 6.0 (red line). (D) Stability of the pH_e gradient at room temperature. The gradient slope at each timepoint was normalized to the slope at time 0. The slope decreased to 77% of the original value after 8 hr. Data are average values from two independent experiments. (E) Stability of the pH_e gradient at 37°C. The gradient slope at each timepoint was normalized to the slope at time 0. The slope decreased to 81% of the initial original value after 8 hr. Data are average values from two independent experiments. Error bars are SEM.

When we measured BCECF fluorescence profiles over the bridge in the Dunn chamber, we found that the fluorescence ratio at the bridge edges deviated from expected values, likely due to variable depth at these edge regions. Thus, we were only able to measure pH_e in the center of the bridge. In chambers with the same pH_e in both wells, the pH_e profile over the center of the bridge was flat (Figure 6.3B, data shown for pH_e 7.0), while in chambers with pH_e 7.5 in the inner well and pH_e 6.0 in the outer well, the pH_e profile showed a clear gradient, with pH_e decreasing toward the outer well as expected (Figure 6.3C). Because the gradient of hydrogen ion concentration gradient is expected to be linear in the Dunn chamber, the gradient in pH_e should be logarithmic. The measured pH_e gradient in the center of the bridge was in good agreement with the theoretical logarithmic pH_e gradient that should have formed over the full length of the bridge (Figure 6.3C). The pH_e profile in the center of the bridge can be well approximated as linear, and to assess gradient stability we measured the slope of this linear gradient every hour for a duration of 8 hr. We evaluated gradient stability at room temperature and at 37°C, and two independent experiments were conducted at each temperature. At room temperature, the gradient slope decreased to 77% of the initial value over a period of 8 hr (Figure 6.3D), while at 37°C, the slope decreased to 81% of the original value (Figure 6.3E). These data demonstrate that the pH_e gradient is quite stable over an 8-hr time period, allowing for long-timescale imaging of cell migration in the gradient.

6.3.2. $\alpha_v\beta_3$ CHO-B2 cells

We next assessed the migration behavior of $\alpha_v\beta_3$ CHO-B2 cells in the pH_e gradient. These cells serve as an ideal model system with which to test how acid-induced activation of $\alpha_v\beta_3$ affects the directionality and velocity of cells migrating in a pH_e gradient. For each experiment, a glass coverslip was coated with 30 μg/ml fibronectin. Cells were plated on the coverslip in serum-free media at pH_e 7.4 and allowed to adhere and spread for 2 – 3 hr before the coverslip was transferred to the Dunn chamber. The inner well of the Dunn chamber was filled with bicarbonate-free serum-free media at pH_e 7.5, and the outer well was filled with the same media at pH_e 6.0. The chamber was then sealed with the coverslip on which cells were adhered. Cells were imaged at 4x magnification every 5 min for 8 hr. Three independent experiments were conducted, and a total of 133 cells in the pH_e gradient were tracked.

Measurement of the mean coordinates over time for cells in the gradient demonstrated that the mean y-coordinate increased over time, indicating that the cell population on average moved progressively toward the acidic end of the gradient (Figure 6.4A). The average positions were significantly greater than zero for all timepoints after ~3 hr ($p < 0.05$). In contrast, the average x-coordinates were not significantly different than zero at any of the timepoints, indicating that the cells moved approximately equal amounts in the positive and negative x directions (Figure 6.4B). In other words, there was no preferred direction for cell movement perpendicular to the gradient.

Next, we created an angular histogram displaying the distribution of angles θ (relative to the horizontal) traversed for each 1-hr segment of the cell trajectory (Figure 6.4C, box). As this histogram takes into account the direction but not magnitude of each 1-hr increment of displacement, it allows assessment of directional preference independent of any effects that the gradient may have on cell velocity. This histogram demonstrates that the positive angles of cell movement were more common than negative angles, indicating directional bias toward the acidic end of the gradient (Figure 6.4C). The Rayleigh statistical test for this angular distribution gives $p = 2.4 \times 10^{-6}$, indicating that this distribution significantly deviates from a uniform distribution.

Measurement of the mean coordinates for the cells located within the center control post demonstrated that the average x- and y-coordinates for these cells were not significantly different than zero at any time point (Figure 6.4D-E). Furthermore, the histogram of cell displacement angles does not indicate a direction preference, with $p > 0.05$ from the Rayleigh test (Figure 6.4F). Thus, cells that were not exposed to a pH_e gradient migrated approximately equal amounts in all directions.

We also assessed the percentage of cells that displayed preferential migration toward acid, in order to understand the level of response in this system. After 8 hr of migration, 66% of the cells in the gradient had moved to a final position with a positive y-coordinate, i.e., toward the acidic end of the gradient (Figure 6.4G). This is significantly higher than the expected 50% if the cells were moving in a random manner ($p < 0.0004$). Cell migration in the direction perpendicular to the gradient did not indicate a directional preference, as the percentage of cells that had moved to either side at the 8-hr timepoint was not significantly different that 50%. Similarly, at the center post, which is not exposed to a gradient and serves as a control, the percentage of cells that had moved to a final position with a positive y-coordinate was not significantly different than 50% (Figure 6.4G).

Cells at different positions along the gradient are exposed to different ranges of extracellular pH during migration. To assess the effect of gradient position on directionality and velocity of cell migration, the positions along the bridge were divided into five equal bins, and each cell was assigned to a bin based on its initial position. Because cell migration distance over 8 hr (~26 μm) is small compared to the width of the bridge (~1000 μm), the initial cell position is a reasonable marker for the cell location in the gradient throughout the imaging duration. The percentage of cells that had moved to a position with lower pH after 8 hr did not have a significant dependence on the cell location within the gradient (Figure 6.4H). However, the velocity was dependent on the cell position: cells initially located on the acidic end of the gradient moved significantly slower than cells initially located closer to pH_e 7.5 (Figure 6.4I). Therefore, the initial position within the gradient affects cell velocity, but not directionality.

6.3.3. Bovine retinal microvascular endothelial cells (BRECs)

Although $\alpha_v\beta_3$ CHO-B2 cells are an ideal model system to study the role of integrin $\alpha_v\beta_3$ in cell migration, they only express one RGD-binding integrin and are therefore not representative of the cell types that would be found in tumors and wounds. Furthermore, $\alpha_v\beta_3$ CHO-B2 cells do not have functional relevance in the tumor or wound healing contexts. Therefore, we next studied the migration behavior of bovine retinal microvascular endothelial cells (BRECs) in the pH_e gradient. These primary cells are relevant to both tumors and wounds, as endothelial cell migration is critical to angiogenesis in these environments. Though BRECs contain a mixed population of fibronectin-binding integrins, Enaida et al. have demonstrated that expression of $\alpha_v\beta_3$ is higher than expression of $\alpha_v\beta_5$, $\alpha_2\beta_1$, and $\alpha_5\beta_1$ in these cells [226]. Thus, we hypothesized that BRECs would respond to the pH_e gradient in a manner similar to that of $\alpha_v\beta_3$ CHO-B2 cells.

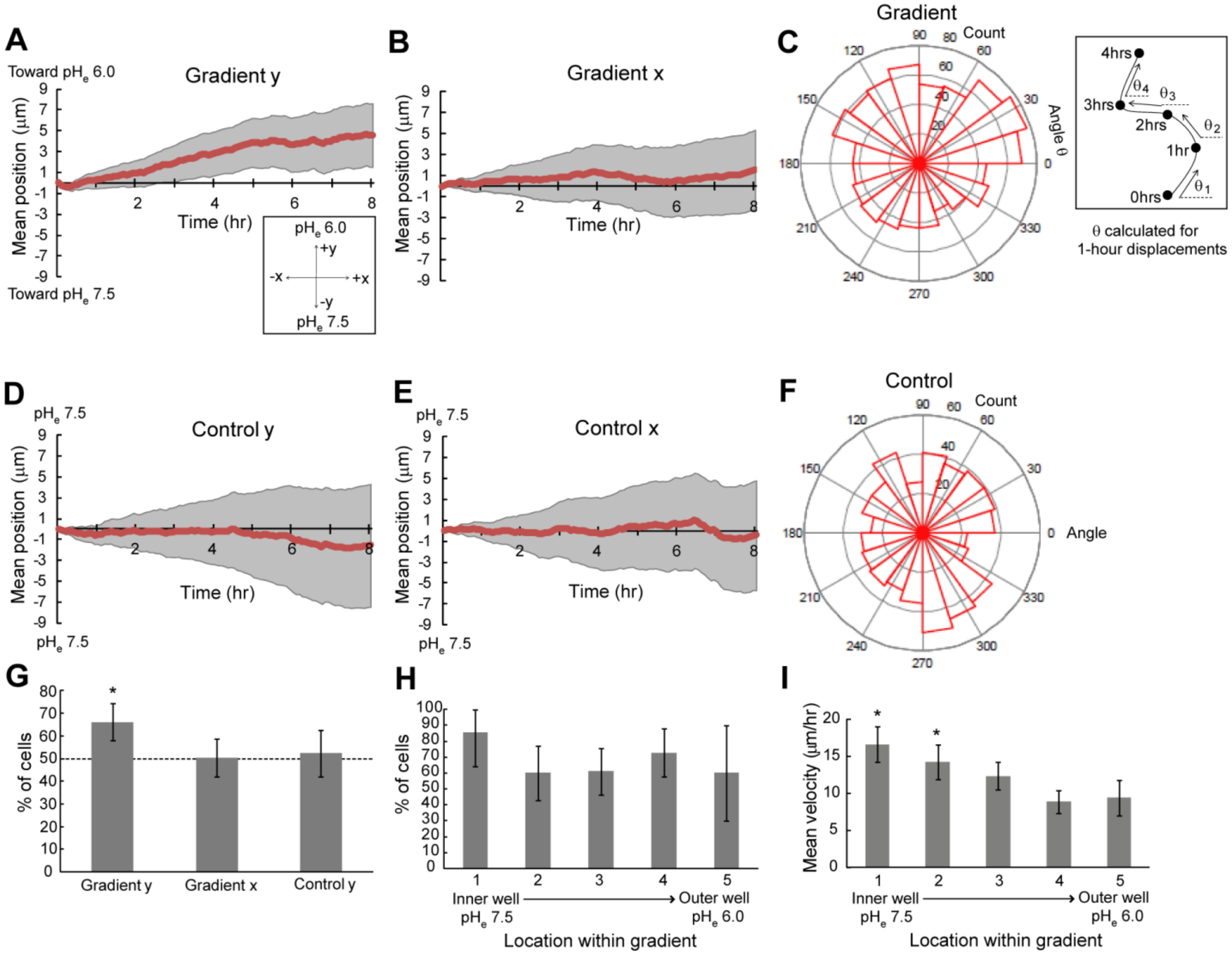

Figure 6.4 Results for $\alpha_v\beta_3$ CHO-B2 cells migrating in a pH$_e$ gradient. For cells in the pH$_e$ gradient, the y-axis is parallel to the gradient direction and the x-axis is perpendicular to the gradient direction. Cells in the control region are not exposed to a gradient. (A) Mean y-coordinate (red line) with 95% confidence intervals (gray shaded regions) over time for $\alpha_v\beta_3$ CHO-B2 cells in the pH$_e$ gradient. The mean y-coordinate is significantly different than zero for all timepoints at which the error bars do not encompass the x-axis. Box illustrates the coordinate system used for data analysis. (B) Mean x-coordinate over time for $\alpha_v\beta_3$ CHO-B2 cells in the pH$_e$ gradient. The mean x-coordinate is not significantly different than zero at any of the timepoints. (C) Angular histogram for $\alpha_v\beta_3$ CHO-B2 cells in the pH$_e$ gradient. The distribution of angles is significantly different than a uniform distribution (Rayleigh test $p = 2.4 \times 10^{-6}$). Box illustrates calculation of angles from cell trajectories. For each 1-hr displacement, angles were calculated with respect to the horizontal. (D) Mean y-coordinate over time for $\alpha_v\beta_3$ CHO-B2 cells over the center control post. The mean y-coordinate is not significantly different than zero at any of the timepoints. (E) Mean x-coordinate over time for $\alpha_v\beta_3$ CHO-B2 cells over the center control post. The mean x-coordinate is not significantly different than zero at any of the timepoints. (F) Angular histogram for $\alpha_v\beta_3$ CHO-B2 cells over the center control post. The distribution of angles is not significantly different than a uniform distribution. (G) Percentage of $\alpha_v\beta_3$ CHO-B2 cells that attained a position with positive x- or y-coordinate at the 8-hr timepoint. After 8 hr of migration, significantly more than 50% of the cells over the bridge had a positive y-coordinate ($p < 0.0004$), but the percentage of cells with a positive x-coordinate is not significantly different than 50%. For cells over the center control post, the percentage of cells with a positive y-coordinate is not significantly different than 50%. Asterisk indicates $p < 0.0004$ with respect to 50%. (H) Percentage of $\alpha_v\beta_3$ CHO-B2 cells in the pH$_e$ gradient that attained a position with positive y-coordinate at the 8-hr timepoint as a function of cell location within the gradient. No significant dependence on position was observed. (I) Mean $\alpha_v\beta_3$ CHO-B2 cell velocity as a function of cell

location within the gradient. Cells closer to the inner well (pH_e 7.5) moved significantly faster than those closer to the outer well (pH_e 6.0). Asterisk at location 1 indicates $p < 0.05$ with respect to locations 4 and 5. Asterisk at position 2 indicates $p < 0.05$ with respect to location 4. Gradient data are for 133 cells, and control data are for 88 cells, each pooled from 3 independent experiments. All error bars are 95% CI.

BREC migration experiments were conducted using the same conditions as described above for $\alpha_v\beta_3$ CHO-B2 cells. Briefly, for each experiment, BRECs were plated on a fibronectin-coated glass coverslip (30 μg/ml), which was used to seal a Dunn chamber with the inner well at pH_e 7.5 and the outer well at pH_e 6.0. Two independent experiments were conducted, yielding a total of 120 cells in the pH_e gradient. Cells were imaged every 5 min over a duration of 8 hr, and cell tracks were analyzed as described above.

For BRECs in the gradient, the mean y-coordinate increased over time, indicating progressive movement toward the acidic end of the gradient (Figure 6.5A). The average y-coordinates at all timepoints after ~2.5 hr were significantly greater than zero ($p < 0.05$), but the average x-coordinates were not significantly different than zero at any of the timepoints (Figure 6.5B). The angular histogram for BRECs in the gradient showed that displacements with positive angles occurred more frequently than displacements with negative angles, indicating directional preference toward the acidic end of the gradient independent of contributions from pH_e-dependent cell velocity (Figure 6.5C). This angular distribution was significantly different than a uniform distribution, with $p = 0.0011$. For cells over the center control post, the mean coordinates were not significantly different than zero for any of the measured time points, and the angular histogram did not deviate significantly from a uniform distribution (Figure 6.5D-F). Thus, we conclude that BRECs preferentially migrate toward lower pH_e.

After 8 hr of migration, 61% of BRECs in the pH_e gradient had moved to a final position with a positive y-coordinate. This was significantly higher than 50% ($p < 0.02$), but lower than the 66% observed for $\alpha_v\beta_3$ CHO-B2 cells. For both control conditions, the percentage of cells that had moved to either side after 8 hr was not significantly different from 50% (Figure 6.5G). The effects of cell position in the gradient on directionality and velocity were similar to those observed with $\alpha_v\beta_3$ CHO-B2 cells. The percentage of cells that had moved to a final position with lower pH_e after 8 hr did not show a significant dependence on the cell location within the gradient (Figure 6.5H). However, cell migration speed was significantly slower for cells that were located on the acidic end of the gradient (Figure 6.5I).

6.3.4. NIH-3T3 fibroblasts

We also studied the migration behavior of NIH-3T3 fibroblasts in the pH_e 6.0 – 7.5 gradient, motivated by the important role of fibroblasts in matrix repair and remodeling during wound healing. Fibroblast experiments were conducted with the same conditions described above for $\alpha_v\beta_3$ CHO-B2 cells and for BRECs. For each experiment, cells were plated on a fibronectin-coated glass coverslip (30 μg/ml), which was used to seal a Dunn chamber with the inner well at pH_e 7.5 and the outer well at pH_e 6.0. Three independent experiments were conducted, yielding a total of 147 cells in the pH_e gradient.

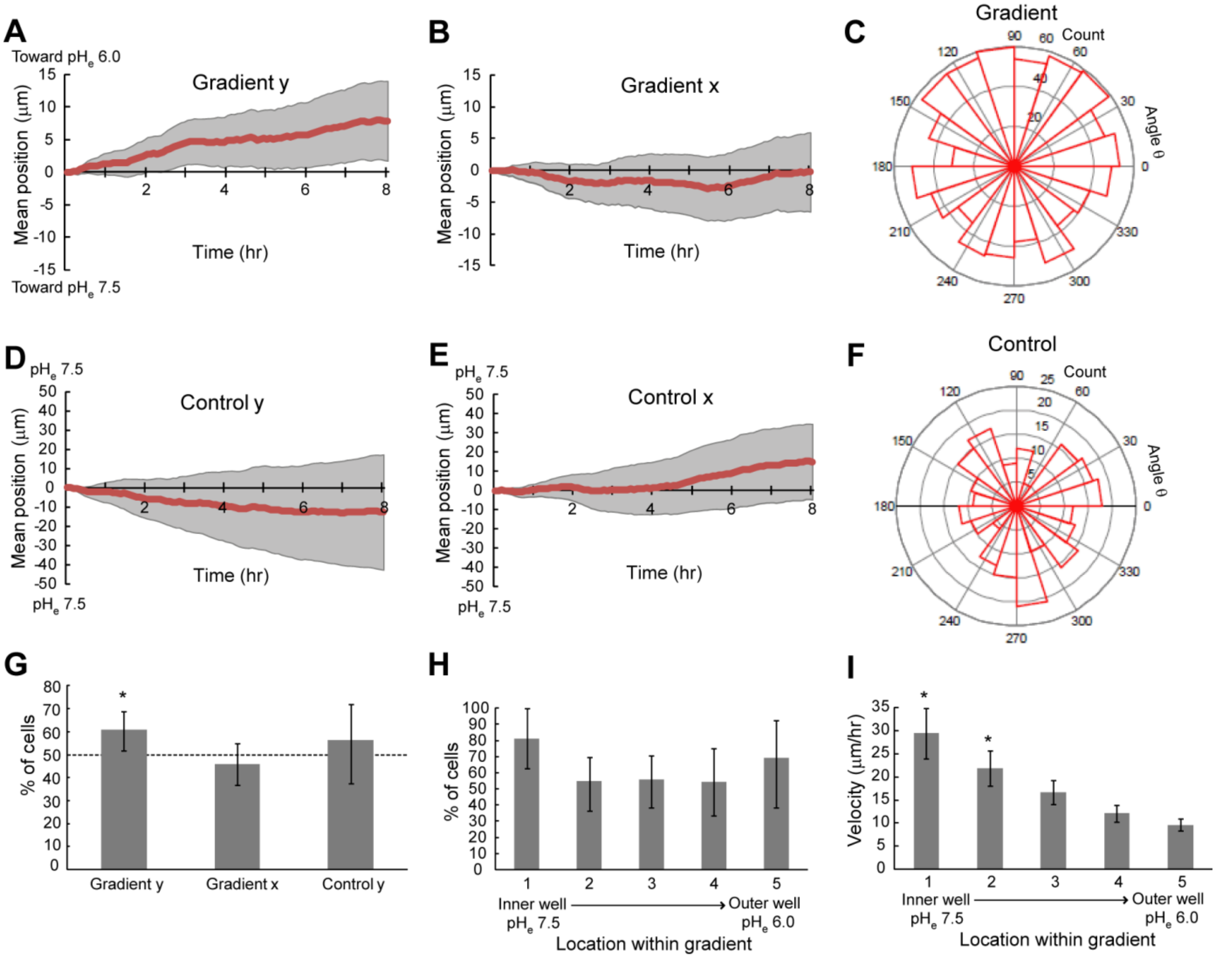

Figure 6.5 Results for BRECs migrating in pH$_e$ gradient. For cells in the pH$_e$ gradient, the y-axis is parallel to the gradient direction and the x-axis is perpendicular to the gradient direction. Cells in the control region are not exposed to a gradient. (A) Mean y-coordinate (red line) with 95% confidence intervals (gray shaded regions) over time for BRECs in the pH$_e$ gradient. The mean y-coordinate is significantly different than zero for all timepoints at which the error bars do not encompass the x-axis. (B) Mean x-coordinate over time for BRECs in the pH$_e$ gradient. The mean x-coordinate is not significantly different than zero at any of the timepoints. (C) Angular histogram for BRECs in the pH$_e$ gradient. The distribution of angles is significantly different than a uniform distribution (Rayleigh test $p = 0.0011$). (D) Mean y-coordinate over time for BRECs over the center control post. The mean y-coordinate is not significantly different than zero at any of the timepoints. (E) Mean x-coordinate over time for BRECs over the center control post. The mean x-coordinate is not significantly different than zero at any of the timepoints. (F) Angular histogram for BRECs over the center control post. The distribution of angles is not significantly different than a uniform distribution. (G) Percentage of BRECs that attained a position with positive x- or y-coordinate at the 8-hr timepoint. After 8 hr of migration, significantly more than 50% of the cells over the bridge had a positive y-coordinate, but the percentage of cells with a positive x-coordinate is not significantly different than 50%. For cells over the center control post, the percentage of cells with a positive y-coordinate is not significantly different than 50%. Asterisk indicates $p < 0.02$ with respect to 50%. (H) Percentage of BRECs in the pH$_e$ gradient that attained a position with positive y-coordinate at the 8-hr timepoint as a function of cell location within the gradient. No significant dependence on position was observed. (I) Mean BREC velocity as a function of cell location within the gradient. Cells closer to the inner well (pH$_e$ 7.5) moved significantly faster than those closer to the outer well (pH$_e$ 6.0). Asterisk at location 1 indicates $p < 0.05$ with respect to locations 2, 3, 4, and 5. Asterisk at position 2 indicates $p < 0.05$ with respect to locations 4 and 5. Gradient data are for 120 cells, and control data are for 32 cells, each pooled from 2 independent experiments. Error bars are 95% CI.

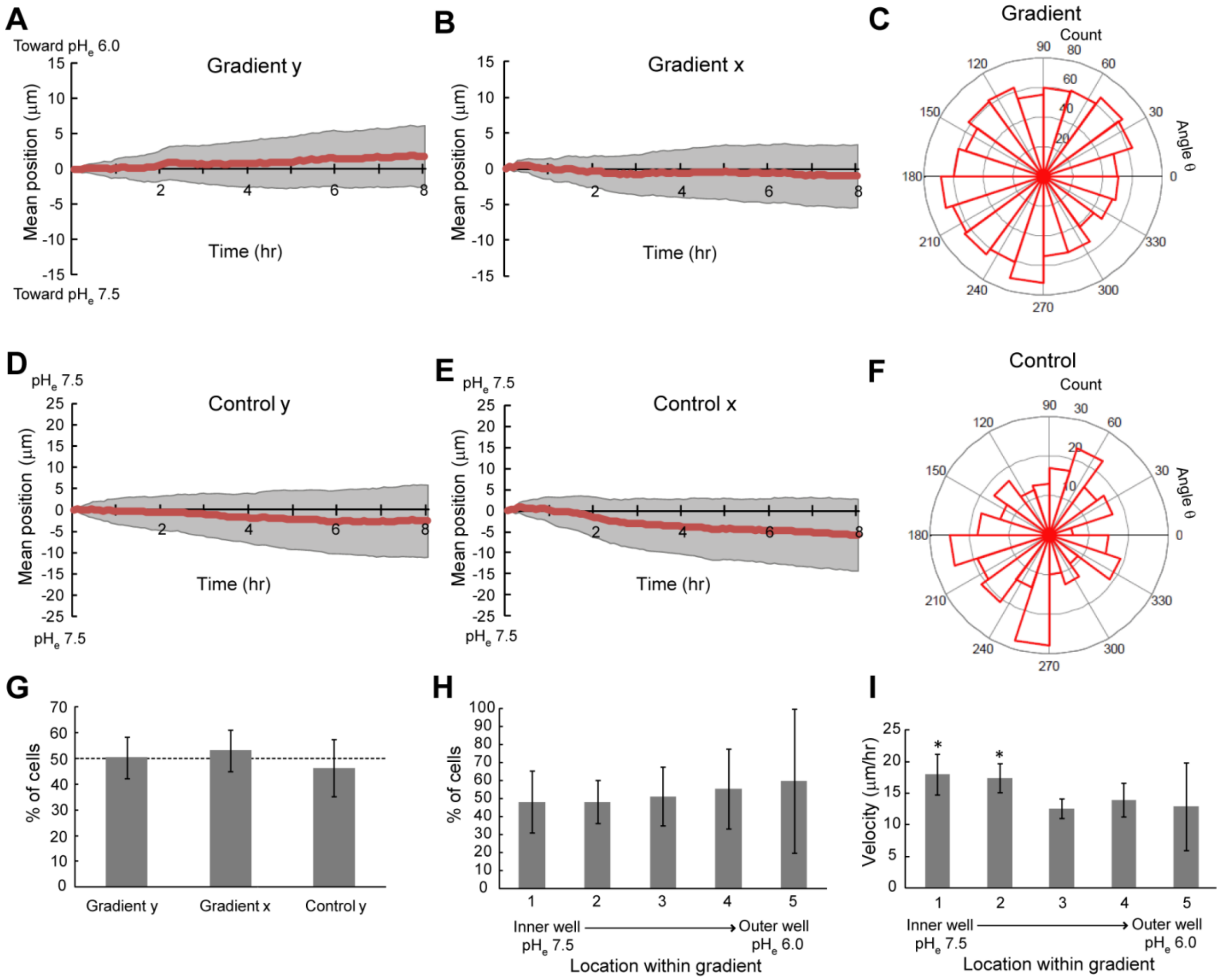

Figure 6.6 Results for NIH-3T3 fibroblasts migrating in a pH_e gradient. For cells in the pH_e gradient, the y-axis is parallel to the gradient direction and the x-axis is perpendicular to the gradient direction. Cells in the control region are not exposed to a gradient. (A) Mean y-coordinate (red line) with 95% confidence intervals (gray shaded regions) over time for NIH-3T3 fibroblasts in the pH_e gradient. The mean y-coordinate is not significantly different than zero for any of the timepoints. (B) Mean x-coordinate over time for NIH-3T3 fibroblasts in the pH_e gradient. The mean x-coordinate is not significantly different than zero at any of the timepoints. (C) Angular histogram for NIH-3T3 fibroblasts in the pH_e gradient. The distribution of angles is not significantly different than a uniform distribution. (D) Mean y-coordinate over time for NIH-3T3 fibroblasts over the center control post. The mean y-coordinate is not significantly different than zero at any of the timepoints. (E) Mean x-coordinate over time for NIH-3T3 fibroblasts over the center control post. The mean x-coordinate is not significantly different than zero at any of the timepoints. (F) Angular histogram for NIH-3T3 fibroblasts over the center control post. The distribution of angles is not significantly different than a uniform distribution. (G) Percentage of NIH-3T3 fibroblasts that attained a position with positive x- or y-coordinate at the 8-hr timepoint. After 8 hr of migration, the percentage of cells in the gradient that had a positive y-coordinate is not significantly different from 50%. The percentage of cells with a positive x-coordinate is also not significantly different than 50%. For cells over the center control post, the percentage of cells with a positive y-coordinate is not significantly different than 50%. (H) Percentage of NIH-3T3 fibroblasts in the pH_e gradient that attained a position with positive y-coordinate at the 8-hr timepoint as a function of cell location within the gradient. No significant dependence on position was observed. (I) Mean NIH-3T3 velocity as a function of cell location within the gradient. Cells closer to the inner well (pH_e 7.5) moved significantly faster than those closer to the outer well (pH_e 6.0). Asterisk at location 1 indicates $p < 0.05$ with respect to location 3. Asterisk at position 2 indicates $p < 0.05$ with respect to location 3. Gradient

data are for 147 cells, and control data are for 52 cells, each pooled from 3 independent experiments. All error bars are 95% CI.

In contrast to the $\alpha_v\beta_3$ CHO-B2 cells and the BRECs, NIH-3T3 fibroblasts did not show a directional preference in the gradient. For fibroblasts migrating in the pHe gradient, the mean y-coordinates did not differ significantly from zero at any of the timepoints (Figure 6.6A), and the angular histogram was not significantly different from a uniform distribution (Figure 6.6C). Furthermore, the percentage of cells that had moved to a final position with lower pHe after 8 hr of migration was not significantly different than 50% (Figure 6.6G). As with the other two cell types, the percentage of cells that had moved to a final position with lower pH_e after 8 hr did not show a significant dependence on the cell position within the gradient (Figure 6.6H). Cell migration speed was dependent on cell position in the gradient, but the trend was not as strong as for the $\alpha_v\beta_3$ CHO-B2 cells or the BRECs (Figure 6.6I). All control conditions indicated random migration, as expected (Figure 6.6B,D,E,F,G).

It is possible that the acid-induced integrin activation that we characterized for integrin $\alpha_v\beta_3$ does not occur for all the integrins that expressed by NIH-3T3 fibroblasts. Although there is a lack of quantitative data comparing integrin subtypes in NIH-3T3 fibroblasts, the literature suggests that integrin $\alpha_5\beta_1$ might be the predominant integrin expressed for these cells [125, 227, 228]. If $\alpha_5\beta_1$ is not regulated by acidic pH in the same way or to the same extent as $\alpha_v\beta_3$, this could explain why the fibroblasts did not migrate with a directional preference. This hypothesis can be tested by blocking or suppressing $\alpha_5\beta_1$ such that the cells must use other integrins (such as $\alpha_v\beta_3$) for migration, and then testing whether the cells display directional preference in the pH_e gradient. Therefore, we investigated NIH-3T3 fibroblast migration in the pH_e gradient after blocking $\alpha_5\beta_1$ with a function-blocking antibody.

Before beginning migration experiments, we first assessed cell morphology after $\alpha_5\beta_1$ blocking to assess qualitatively how blocking of this particular integrin affects cell spreading and adhesion. NIH-3T3 fibroblasts were plated on fibronectin-coated glass (30 μg/ml) in serum-free media at pH_e 7.4 and allowed to adhere for 2 – 3 hr before the $\alpha_5\beta_1$-blocking antibody was added at a concentration of 10 μg/ml. After ~20 hr of incubation with the $\alpha_5\beta_1$-blocking antibody, almost all of the cells were adhered to the substratum and were spread out. In contrast, images of control cells that were not exposed to antibody showed many detached cells[8], and the attached cells appeared qualitatively to be less well spread (Figure 6.7A-B). This indicates that the $\alpha_5\beta_1$ antibody somehow promoted adhesion and spreading for these cells.

---

[8] The large number of detached cells is due to the 20 hr of incubation without serum.

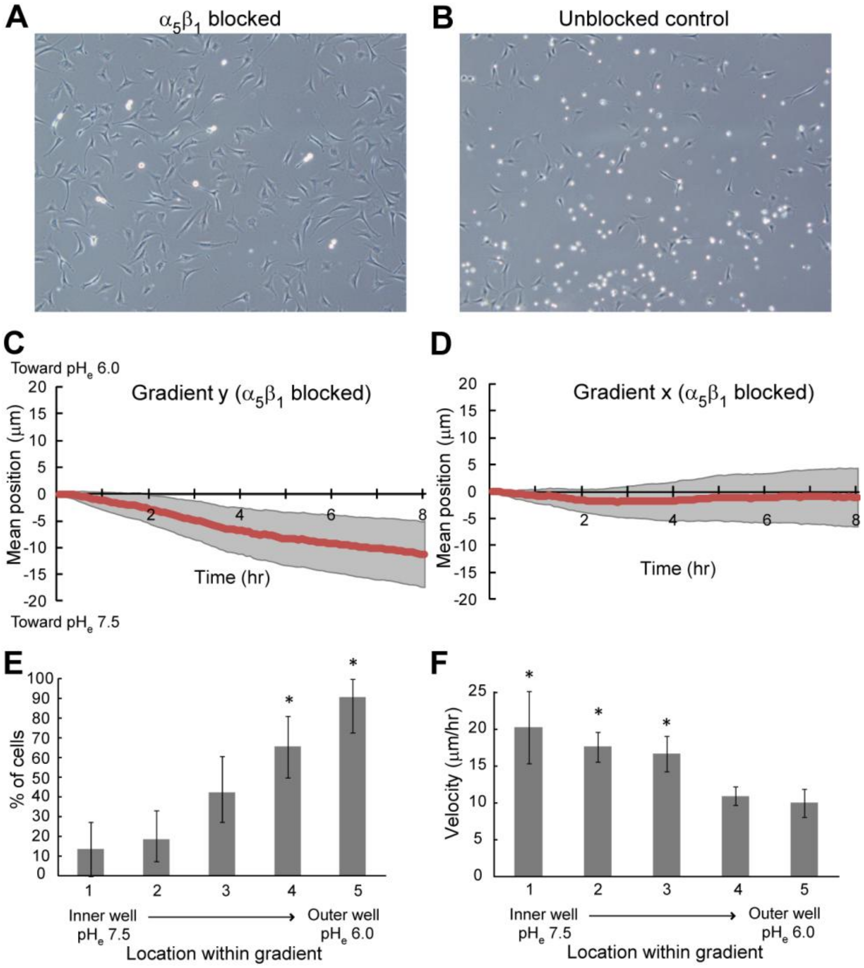

Figure 6.7 Results for NIH-3T3 fibroblasts migrating in a pH_e gradient in the presence of $\alpha_5\beta_1$-blocking antibody. For cells in the pH_e gradient, the y-axis is parallel to the gradient direction and the x-axis is perpendicular to the gradient direction. (A) Phase contrast image of NIH-3T3 fibroblasts taken after ~20 hr of incubation with $\alpha_5\beta_1$-blocking antibody. Cells are predominantly adhered and spread out. (B) Phase contrast image of NIH-3T3 fibroblasts that were not exposed to $\alpha_5\beta_1$-blocking antibody. Many cells are detached, and attached cells appear to be less well spread than those in (A). (C) Mean y-coordinate (red line) with 95% confidence intervals (gray shaded regions) over time for NIH-3T3 fibroblasts with $\alpha_5\beta_1$ blocked in the pH_e gradient. The mean y-coordinate is significantly lower than zero for all timepoints after ~2.5 hr. (D) Mean x-coordinate over time for NIH-3T3 fibroblasts with $\alpha_5\beta_1$ blocked in the pH_e gradient. The mean x-coordinate is not significantly different than zero at any of the timepoints. (E) Percentage of NIH-3T3 fibroblasts with $\alpha_5\beta_1$ blocked in the pH_e gradient that attained a position with positive y-coordinate at the 8-hr timepoint as a function of cell location within the gradient. A significant dependence on position was observed, with percentage increasing for cells that are located in more acidic portions of the gradient. Asterisk at location 4 indicates $p < 0.005$ with respect to locations 1 and 2. Asterisk at location 5 indications $p < 0.005$ with respect to location 3 and $p < 0.0001$ with respect to locations 1 and 2. (E) Mean NIH-3T3 velocity as a function of cell location within the gradient. Cells closer to the inner well (pH_e 7.5) moved significantly faster than those closer to the outer well (pH_e 6.0). Asterisk at location 1 indicates $p < 0.001$ with respect to locations 4 and 5. Asterisk at position 2 indicates $p < 0.01$ with respect to location 4 and $p < 0.05$ with respect to location 5. Asterisk as location 3 indicates $p < 0.05$ with respect to location 4. Gradient data are for 125 cells pooled from 2 independent experiments. All error bars are 95% CI.

We next evaluated directional cell migration for fibroblasts migrating in the pH_e gradient with $\alpha_5\beta_1$ blocked. Experiments were conducted with the same conditions as described above for the other cell types, but with the addition of 10 μg/ml $\alpha_5\beta_1$-blocking antibody to the media in both wells of the Dunn chamber. Two independent experiments were conducted, yielding a total of 125 cells in the pH_e gradient. For the cell population as a whole, the mean y-coordinate decreased over time, indicating that the cell population moved away from the acidic end of the gradient, on average. The mean y-coordinates at all timepoints after ~2.5 hr were significantly lower than zero ($p < 0.05$), while the average x-coordinates were not significantly different than zero at any of the timepoints (Figure 6.7C-D). Thus, there was no preferred direction for cell movement perpendicular to the gradient. In contrast to the $\alpha_v\beta_3$ CHO-B2 cells and the BRECs, the percentage of NIH-3T3 fibroblasts that moved to a position with lower pH_e had a significant dependence on the initial cell position within the gradient. For the group closest to pH_e 7.5 (location #1 in Figure 6.7E), only ~14% of the cells had moved toward acid after 8 hr. In contrast, for the group closest to pH_e 6.0 (location #5 in Figure 6.7E), 91% of the cells had moved toward acid after 8 hr. Thus, cells on both ends of the gradient displayed nonrandom directionality, but in opposite directions. The average movement of the cell population as a whole toward higher pH_e (Figure 6.7C) was due to the fact that cells closer to pH_e 7.5 moved faster (i.e., had larger displacements per time interval) than cells closer to pH_e 6.0 (Figure 6.7F).

6.4. Discussion

6.4.1. Mechanism for migration toward acid

Using the Dunn chamber, we were able to establish pH_e gradients from pH_e 6.0 – 7.5 that were very stable over a time period of 8 hr. This level of gradient stability initially seemed surprising, as the diffusion coefficient for H^+ ions in water is very high (9.3×10^{-5} cm^2/s) [229]. However, it has been shown that hydrogen ion diffusion can be constrained by reactions with mobile buffers or other chemicals in solution. This can lower the effective diffusion coefficient of the hydrogen ion by about two orders of magnitude to ~10^{-6} cm^2/s [229-231]. Therefore, maintenance of a pH_e gradient in buffered cell media over several hours is within the range of diffusion estimates reported in the literature.

Our cell migration measurements in pH_e gradients demonstrated that the average position of $\alpha_v\beta_3$ CHO-B2 cells moved toward the acidic end of the gradient over time, while the average position in control conditions did not deviate significantly from zero (Figure 6.4A,B,D,E). Similar results were observed for BRECs, a physiologically relevant cell type that expresses a mixed population of integrins (Figure 6.5A,B,D,E). There are three possible mechanisms for how the pH_e gradient could cause a progressive movement of the average cell position toward lower pH_e:

Mechanism 1 (Figure 6.8A): The results discussed in Chapters 2 and 3 showed that acidic extracellular pH promotes activation of integrin $\alpha_v\beta_3$. Thus, a cell in a pH_e gradient would experience differential pH_e-regulated integrin activation over the length of the cell body, which could cause a cell to alter its polarization direction, possibly by orienting the leading edge toward the more acidic end of the gradient. By this mechanism of preferential orientation toward acid, the mean cell position could move toward acid independent of any velocity effects.

Mechanism 2 (Figure 6.8B): According to the mathematical model of cell migration that we introduced in Chapter 6, cell migration depends on the asymmetry in the ratio of adhesiveness to contractility. If asymmetry is increased, the cell will move farther within a given time interval [95]. In our extended version of the model, which includes a pH_e-dependent integrin activation rate k_a, a pH_e gradient can be easily modeled by allowing k_a to be position dependent. In this way, it is possible for the integrin activation rate to be higher at one end of the cell than at the other. Our model predicts that for a cell polarized with the leading edge at the acidic end of the gradient[9], the pH_e gradient will enhance the asymmetry in adhesiveness required for migration, as integrins at the leading edge will be activated with greater frequency than integrins at the trailing edge. The opposite effect will occur for cells polarized with the leading edge toward higher pH_e. Thus, cells polarized toward lower pH_e are predicted to have greater net displacements than cells polarized in the opposite direction (Figure 6.9). By this mechanism, the mean cell position could move toward acid even if the direction of polarization was random.

Mechanism 3 (Figure 6.8C): For both $\alpha_v\beta_3$ CHO-B2 cells and BRECs, cells migrating in more acidic regions of the gradient displayed significantly reduced migration speed. This is consistent with the $\alpha_v\beta_3$ CHO-B2 cell migration speed measurements discussed in Chapter 5. Because of this pH_e-dependent velocity, it is possible that cells could migrate randomly (with no preferred direction), but cells that encounter regions of lower pH_e become effectively trapped there due to decreased migration speed. By this mechanism, the mean cell position could move toward acid even if the direction of polarization is random and the cell velocity is independent of polarization direction.

Each of these three mechanisms would result in the mean cell y-coordinate increasing over time, as we observed. It is also possible that more than one of these mechanisms occurs simultaneously in our experimental system. With our gradient migration data, we can assess which of these mechanisms is likely to be dominant in our experiments. First, our angular histograms demonstrate that for both $\alpha_v\beta_3$ CHO-B2 cells and BRECs, movements with positive angles occurred more frequently than those negative angles. As these histograms do not take into account the distance traveled over each time interval of 1 hr, these data indicate that cells exhibited some level of directional preference and were not polarizing with equal likelihood toward and away from acid. Thus, mechanism 1 is at least partially responsible for the migration toward acid that we observed in our experiments.

As for mechanism 2, our 1-hr increments of displacement data (y-component only) indicate whether cell displacement was greater toward acid than away from acid. For $\alpha_v\beta_3$ CHO-B2 cells, the average displacement toward acid was 3.08 ± 0.18 μm, and the average displacement away from acid was 2.91 ± 0.14 μm (mean ± SEM). Although the displacement toward acid is larger, the difference is not statistically significant. This indicates that mechanism 2 does not contribute appreciably to the net movement toward

---

[9] In the model, the direction of polarization is set by allowing integrin receptors to be preferentially inserted at the leading edge. This leads to an increase in total receptor numbers at the leading edge.

acid for $\alpha_v\beta_3$ CHO-B2 cells. However, for BRECs, the average displacement toward acid was 5.82 ± 0.27 μm, compared to 4.78 ± 0.29 μm away from acid (mean ± SEM). This difference is statistically significant ($p = 0.0084$), indicating that mechanism 2 does indeed contribute to the net migration toward acid for BRECs, along with mechanism 1.

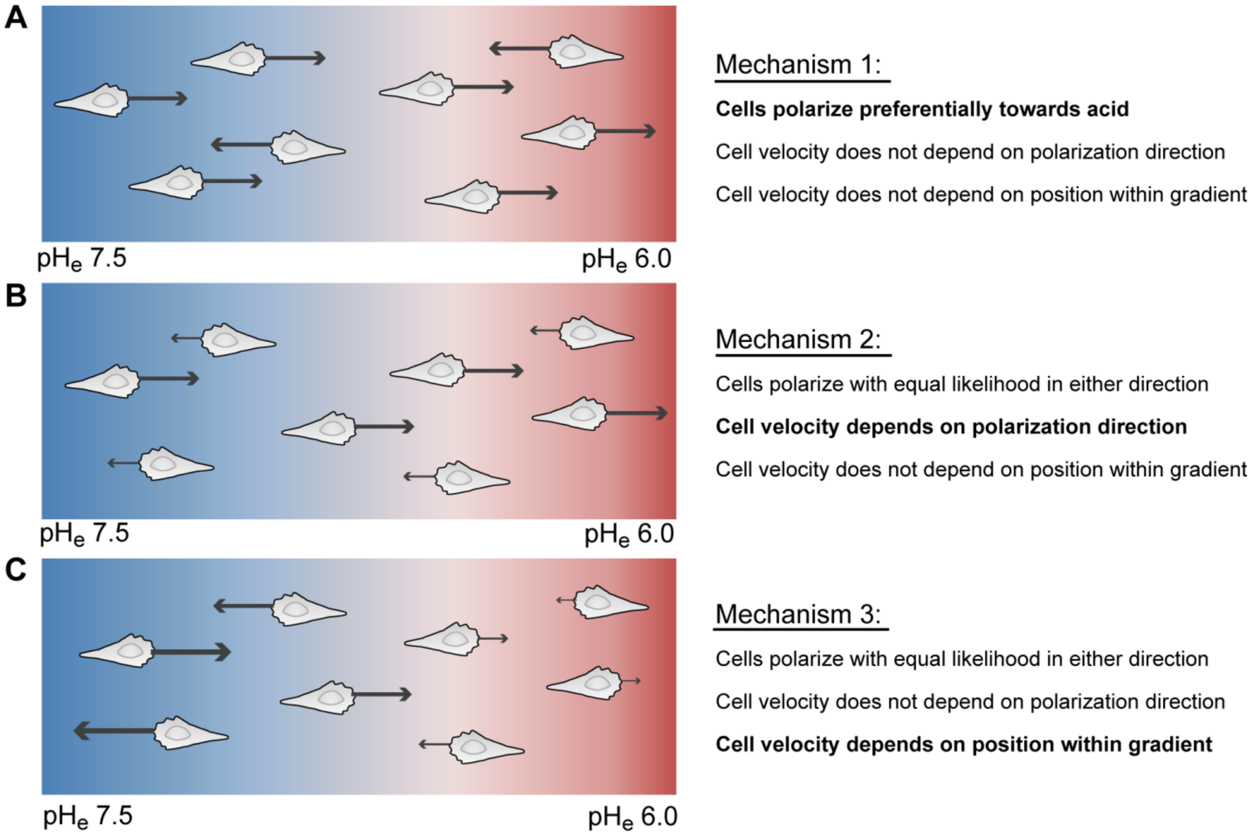

Figure 6.8 Schematic depiction of the three possible mechanisms underlying the shift in mean cell position toward acid over time. The blue end of the gradient is pH_e 7.5 and the red end is pH_e 6.0. Arrows indicate the magnitude of cell velocity, with larger arrows indicating higher speed. The direction of the arrows indicates the direction of the leading edge (i.e., the direction of polarization). Cell movement is restricted to one dimension for simplicity. (A) Cells polarize preferentially toward acid, but cell velocity does not depend on polarization direction or position within gradient. (B) Cell velocity is higher for cells polarized toward acid, but velocity is independent of the position within the gradient. In this scenario, cells polarize equally in both directions. (C) Cell velocity depends on the position within the gradient, decreasing for cells in more acidic positions. However, cell velocity does not depend on polarization direction, and cells polarize equally in both directions.

The experimentally measured displacements are compared to the mathematical model predictions in Figure 6.9. For clarity of comparison, we normalized the data to the mean values for cells polarized away from acid (i.e. mean displacement for cells polarized away from acid = 1). The model cannot be used to make quantitative predictions for BRECs, because the pH_e dependence and other parameters in the model were optimized for $\alpha_v\beta_3$ CHO-B2 cells. However, the qualitative trends for the model compared to our BREC data are in good agreement. As for the $\alpha_v\beta_3$ CHO-B2 cells, although there was no statistically significant difference in the mean displacement toward and away from acid, we note that it is still possible that the physical basis for mechanism 2 is valid for these cells. It could be that a small difference in displacements does indeed exist but could not be resolved with statistical significance in our experiments.

It is unlikely that the chemokinetic mechanism 3 is dominant in our experimental systems. Over the 8-hr timescale of our migration experiments, BRECs traveled over an average distance that was less than 5% of the gradient width, and $\alpha_v\beta_3$ CHO-B2 cells traveled over less than 3.5% of the gradient width. Thus, it is highly improbable that any individual cell experienced pH_e changes large enough to significantly decrease the cell velocity (in other words, over the limited region of the gradient that each cell explored during our experiments, cell velocity was approximately constant). As a result, it is unlikely that mechanism 3 contributed significantly to causing the shift in mean cell position that we observed. However, it is important to note that for migration over longer timescales (e.g., 48 hr), this mechanism may play a larger role, as a cell would be more likely to encounter regions of the gradient that result in decreased velocity.

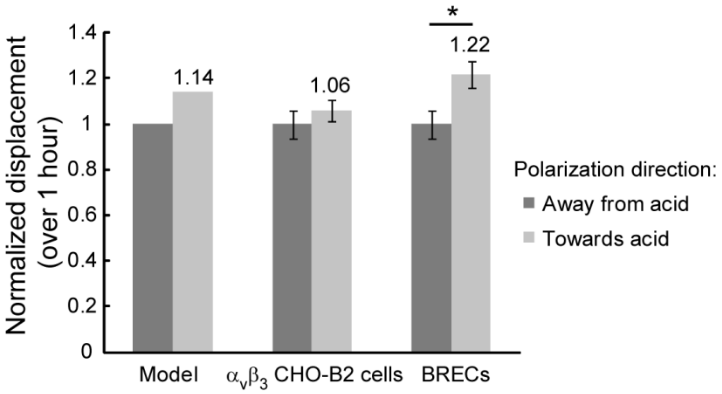

Figure 6.9 Mean cell displacements (over a 1-hr period) for cells polarized away from acid compared to cells polarized toward acid. Data are normalized to the values for cells polarized away from acid. Our cell migration model predicts that mean displacement toward acid will be greater than that away from acid (left bars), assuming that cells are equally positioned throughout the gradient. Our experimental data for $\alpha_v\beta_3$ CHO-B2 cells show that the mean displacement toward acid is greater than the mean displacement away from acid, but this difference is not statistically significant (middle bars). Measurements for BRECs show that the mean displacement toward acid is significantly greater than the mean displacement away from acid (right bars). Asterisk indicates $p = 0.0084$. Error bars are SEM.

In summary, our data indicate that mechanism 1 is dominant for $\alpha_v\beta_3$ CHO-B2 cells in our experimental system, and that mechanisms 1 and 2 both contribute significantly for BRECs. As mechanism 1 occurs for both the cell types we studied here, it is important to consider how differential acid-induced integrin activation over the length of a cell could regulate polarization such that the cell preferentially migrates toward acid. In Chapter 4, we found that acidic pH_e stabilized membrane protrusions, which is consistent with increased cell-matrix adhesiveness in this condition. Thus, membrane protrusions would exhibit longer lifetime on the end of the cell that is exposed to more acidic pH_e, and this could cause reorientation such that this end of the cell becomes the leading edge. Increased formation of actin-integrin adhesion complexes on membrane protrusions at this end of the cell would further reinforce this effect. In this manner, increased integrin activation in acidic pH_e could regulate cell directional orientation via alterations to subcellular-scale processes that are critical to migration.

6.4.2. Extent of response in the cell population

In our experiments, we observed that about 66% of the $\alpha_v\beta_3$ CHO-B2 cell population and about 61% of the BREC population oriented toward the acidic side of the pH_e gradient[10] during migration (Figure 6.4G, Figure 6.5G). This orientation percentage varied as a function of location within the gradient, ranging from 60% – 86% for $\alpha_v\beta_3$ CHO-B2 cells and from 54% - 81% for BRECs (Figure 6.4H and Figure 6.5H, respectively). We now ask: if the gradient is sufficient to cause preferential orientation toward acid, why do some cells migrate in the opposite direction? In other words, why is there a less than perfect response to the gradient? One possible answer to this question is that there are statistical fluctuations in the hydrogen ion concentration $[H^+]$ local to the cell, and thus at any given time, some cells sense the gradient while other do not. If the fluctuations are large enough, it is even possible that some cells may sense a gradient in the wrong direction. This idea was examined in detail by D. A. Lauffenburger in Ref. [232]. In this paper, a model was created to estimate concentration fluctuations and calculate the probability of correct orientation in a concentration gradient. Here, we use this model to estimate the extent of cellular response that can be expected after taking concentration fluctuations into account for a gradient from pH_e 6.0 – 7.5.

In this model, it is assumed that if the difference in bound receptors between the two halves of a cell exceeds a threshold value of N^*, the cell will automatically orient toward the side with more bound receptors. The cell does not make instantaneous concentration measurements, but averages the measurements made over a time T. If the average bound receptor difference during time T does not exceed the threshold N^*, then the cell is assumed to orient randomly (i.e., without a preference toward either side). Note that this model evaluates the likelihood of mechanism 1 described above (Figure 6.8), but does not consider mechanism 2 or mechanism 3. We used Equations 31 – 32 in Ref. [232] for our calculations. Details of the equation derivation will not be described here, but can be found in Ref. [232].

For application of this model to a pH_e gradient, the binding reaction of interest is that between H^+ and ASPβ127, the amino acid in the integrin $\alpha_v\beta_3$ headpiece that we postulate is at least partially responsible for the acid-induced activation of this integrin. The parameters used for calculations are N^*, T, N_o (total number of receptors per cell), K_d (acid dissociation constant), k_f (kinetic rate constant of binding), k_r (kinetic rate constant of dissociation), and ε (one half of the fractional concentration change over the cell length). Estimated values for these parameters are listed in Table 6.1.

In Chapter 2, we used Multi-Conformation Continuum Electrostatics (MCCE) to estimate the effective pK_a value for ASPβ127 within the $\alpha_v\beta_3$ integrin. From this pK_a value, we can easily obtain the acid dissociation constant K_d using the relation $\mathrm{pK_a} = -\log(K_\mathrm{d})$. However, the binding and dissociation kinetic rate constants are not well characterized. By calculating the diffusion rate constant using an expression developed by DeLisi et al. [233]

---

[10] Here, cells that moved to a more acidic position after 8 hr of migration are considered to have oriented toward the acidic side of the gradient.

and comparing it to an estimated value for the overall binding rate constant from Fersht [132], we determined that the binding appears to be reaction-limited rather than diffusion-limited.[11] This enabled us to calculate the dissociation rate constant as $k_r = (K_d k_f)/N_o$ [232]. We used a range of k_f values in our calculations, as it is unclear if the estimated value reported for H^+ binding to a carboxylate group is accurate for an amino acid within a complex protein environment. We also tested a range of values for N^* and T, as it is difficult to determine what the appropriate values should be for our experimental system.

Parameter	Estimated values	Notes
N^*	10 – 80 receptors	Varied based on values from Ref. [232]
T	1 s – 1 hr	Range similar to that tested in Ref. [232]
N_o	10000 receptors	From Ref. [104]
K_d	2.03 x 10^{-7} M	From pKa = 6.692, calculated by MCCE (Chapter 2)
k_f	3 x 10^{9} – 3 x 10^{12} $M^{-1}min^{-1}$	From Ref. [132]
k_r	6.1 x 10^{-2} – 6.1 min^{-1}	$k_r = (K_d k_f)/N_o$
ε	2.48 x 10^{-2}	Gradient from pH_e 6.0 – 7.5 over 1 mm distance, with a cell of 50 μm length

Table 6.1 Parameter values used for calculation of cell orientation percentages in a pH_e gradient.

We calculated the percentage of cells orienting toward acid as a function of $[H^+]$ (i.e. as a function of initial position within the gradient), for a variety of parameter values. For the highest value of k_f that we considered for these calculations, the percentage of cells orienting toward acid exhibits a sharp transition between perfect response and random orientation (Figure 6.10A). As k_f decreases, this transition becomes more gradual, and the region with perfect sensing becomes smaller. Orientation percentage drops at more acidic positions in the gradient because as more receptors become protonated, it becomes increasingly difficult to achieve a sufficient difference in protonated receptor number between the leading and trailing edges of the cell. The influence of threshold bound receptor difference number N^* is displayed in Figure 6.10B. For low N^*, sensing of the gradient is easier to achieve, and nearly perfect orientation toward acid is predicted for all positions. As N^* increases, the region with perfect sensing narrows, and orientation percentage drops to 50% at the more acidic side of the gradient. The effect of decreasing the time-averaging period T is similar to the effect of decreasing k_f. For long T, perfect sensing is achieved over a large portion of the gradient, and then the orientation

---

[11] To assess whether the binding is diffusion- or reaction-limited, we estimated the forward diffusion rate constant k_+ using the following expression: $k_+ = 4\pi a D \Big/ \left(1 + \frac{\pi a}{Ns}\right)$, where a is the cell radius, D is the H^+ diffusion coefficient, N is the number of free receptors, and s is the receptor radius. Using a = 2.5 x 10^{-3} cm, D = 9.3 x 10^{-7} – 9.3 x 10^{-5} cm^2/s, N = 10000, and s = 3 x 10^{-7} cm, we obtain k_+ = 2.92 x 10^{14} – 2.92 x 10^{16} $M^{-1}min^{-1}$. Comparing this to the overall rate constant of H^+ binding to a carboxylate group, k_f = 3 x 10^{12} $M^{-1}min^{-1}$, we see that $k_f \ll k_+$, indicating that the binding is not diffusion limited. We were not able to obtain a similar comparison for the reverse diffusion rate constant k_- vs. the overall dissociation rate constant k_r, because measured values for k_r were not available. Thus, we proceeded with calculations assuming that binding was reaction-limited, rather than diffusion-limited.

percentage sharply drops to 50%. As T decreases, the level of fluctuations increases, and the region with perfect sensing narrows.

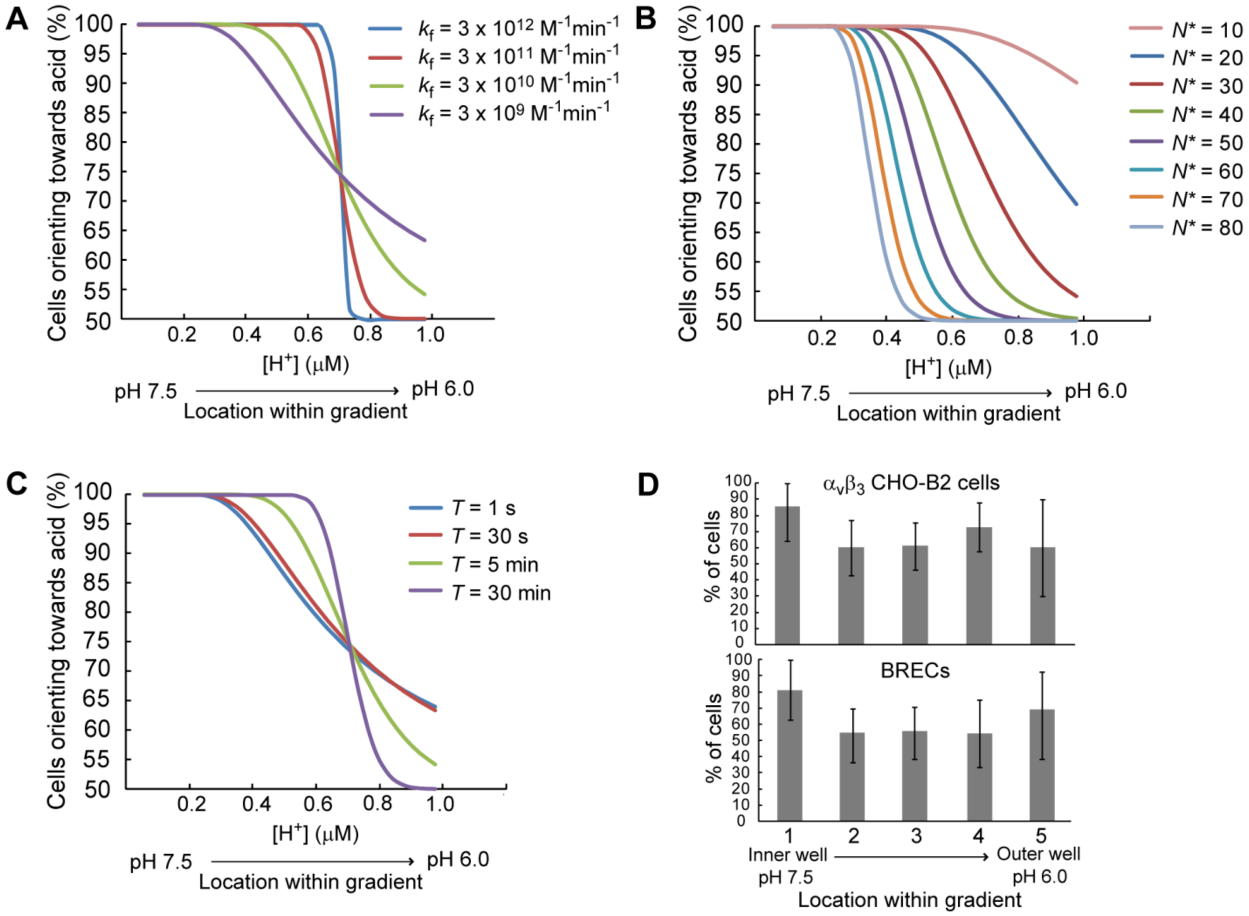

Figure 6.10 (A) Percentage of cells orienting toward acid as a function of position within the gradient, for various values of k_f, with T = 5 min and N^* = 30. (B) Percentage of cells orienting toward acid as a function of position within the gradient, for various values of N^*, with T = 5 min and k_f = 3 x 10^{10} M^{-1}min^{-1}. (C) Percentage of cells orienting toward acid as a function of position within the gradient, for various values of T, with k_f = 3 x 10^{10} M^{-1}min^{-1} and N^* = 30. (D) Top: reproduction of Figure 6.4H. Percentage of $\alpha_v\beta_3$ CHO-B2 cells in the pH$_e$ gradient that attained a position with positive y-coordinate at the 8-hr timepoint as a function of cell location within the gradient. Bottom: reproduction of Figure 6.5H. Percentage of BRECs in the pH$_e$ gradient that attained a position with positive y-coordinate at the 8-hr timepoint as a function of cell location within the gradient.

These model predictions can be compared to our measurements of cell orientation percentage as a function of location within the gradient, which are reproduced in Figure 6.10D. The percentages that we measured at different locations within the gradient have large 95% confidence intervals due to the limited number of cells that we could image in each gradient location (typically <15 cells per experiment within a bin width of ~200 μm). Thus, it is difficult to clearly identify the dependence of orientation percentage on position within the gradient. Tentatively, our experimental data suggest that the orientation percentage is greatest at the higher pH$_e$ region of the gradient and decreases at other positions within the gradient. Our model predictions indicate that there are ranges of parameters that produce orientation percentages that are reasonably close to our experimentally measured values. Therefore, our data are consistent with the concept that a gradient from pH_e 6.0 – 7.5 is sufficient to produce preferential cellular orientation toward acid (mechanism 1 in Figure 6.8), and that fluctuations in hydrogen ion concentration could be one reason that cells displayed less than perfect orientation in our experiments. However, it is important to recognize that concentration fluctuations are likely not the only reason for orientation percentage to be less than 100% in our experiments. For example, a difference in protonated receptor number higher than N^* between the two ends of the cell probably does not guarantee automatic re-orientation in a real cell system. Furthermore, while the model allows for differences in the numbers of protonated receptors between the front and back of the cell, the total number of receptors at the front and back are assumed to be equal. This is unlikely to be the case for a real cell system, in which the distribution of cell surface integrin receptors is often not uniform across the cell length.

6.4.3. Lack of response for NIH-3T3 cells

NIH-3T3 fibroblasts did not exhibit a directional preference when migrating in the pH_e gradient. This indicates that there are some cell-type-specific mechanisms involved in regulating the cell response to extracellular pH_e. Although the fibroblast cell migration speed decreased at acidic pH_e, this effect was not as strong as that observed for the other two cell types, which also indicates that NIH-3T3 cells are not as sensitive to changes in extracellular pH_e. We can suggest three hypotheses for why NIH-3T3 fibroblasts did not exhibit preferred directionality in the pH_e gradient.

First, it is possible that the predominant integrin that NIH-3T3 fibroblasts use during migration is not activated by acidic extracellular pH. It has been suggested that $\alpha_5\beta_1$ is the dominantly expressed fibroblast integrin [125, 227, 228], and thus we attempted conducting gradient migration experiments after blocking $\alpha_5\beta_1$. Images of NIH-3T3 fibroblasts after incubation with an $\alpha_5\beta_1$-blocking antibody demonstrated that more cells were adhered and cells were more spread out after blocking, compared to control cells that were not treated with the antibody (Figure 6.7A-B). This could indicate that $\alpha_5\beta_1$ blocking promotes overexpression of other integrins, or stimulates expression of other proteins involved in cell adhesion and spreading (e.g., adhesion complex or cytoskeletal proteins). Gradient migration experiments indicated that when $\alpha_5\beta_1$ was blocked, cells closer to pH_e 7.5 moved toward lower acid concentrations, while cells closer to pH_e 6.0 moved toward higher acid concentrations (Figure 6.7E). Thus, the likelihood of migration toward lower pH_e depended on the initial position of each cell within the gradient, and these data are inconclusive with regard to the original question of whether $\alpha_5\beta_1$ blocking allows NIH-3T3 fibroblasts to migrate toward the acidic end of a pH_e gradient. Although resolving the reason for this dual directional preference is beyond the scope of this thesis, we can suggest one explanation for this effect that could be tested in the future. It is possible that when $\alpha_5\beta_1$ is blocked, $\alpha_v\beta_3$ and one other integrin become dominant in NIH-3T3 fibroblasts. This other integrin might contain the α_6 subunit, which has been shown to be expressed in NIH-3T3 cells [227, 228], or it could be that the blocking antibody stimulated expression of a different integrin subtype. The non-$\alpha_v\beta_3$ integrin could be regulated by pH_e in a different way than $\alpha_v\beta_3$; for example, this integrin could have a higher propensity for activation in basic rather than acidic pH_e. Therefore, $\alpha_v\beta_3$ would be the dominant integrin for cells on the more acidic end of the gradient, while the other integrin would be dominant for cells closer to pH_e ~7.5. In this situation, it is conceivable that cells on the two ends of the gradient could show opposite directional preference. To test this, various fibroblast integrins could be sequentially blocked or suppressed in order to test the resulting effect on migration in a pH_e gradient.

It is important to note that interpretation of our $\alpha_5\beta_1$ blocking experiments is further complicated by the fact that it is unclear whether the $\alpha_5\beta_1$ antibody was affected by acidic pH_e. It is possible that the antibody binding affinity might have varied within the pH_e gradient, in which case some cells might have been blocked more effectively than others. For this reason, it may be necessary to consider different experimental designs to further investigate the role of $\alpha_5\beta_1$ in fibroblast migration. For example, siRNAs could be used to suppress expression of $\alpha_v\beta_3$, thus eliminating the need for function blocking antibodies. Alternatively, NIH-3T3 gradient experiments could be conducted with vitronectin as the surface ligand, rather than fibronectin. This would reduce the number of integrins that could be used for migration [47]. Another possibility is to test the gradient response for $\alpha_5\beta_1$ CHO-B2 cells. $\alpha_5\beta_1$ is the only fibronectin-binding integrin for these cells; thus, although this experiment would not be conducted with fibroblasts, it would indicate whether preferential directionality in a pH_e gradient is possible for cells that use only $\alpha_5\beta_1$ for migration.

A second hypothesis for the lack of NIH-3T3 fibroblast response in the pH_e gradient is that the ligand density used in our experiments was not optimized for fibroblast migration. The fibronectin concentration used in our experiments (30 μg/ml) is the concentration at which $\alpha_v\beta_3$ CHO-B2 cells showed peak migration velocity; therefore, we expected that changes in adhesiveness would have the greatest impact on cell migration at this concentration. However, this critical fibronectin concentration may be different for fibroblasts. It is possible that the fibronectin density used for the gradient experiments was too high, such that cell-surface adhesiveness at both ends of the cell was already so great that small changes in integrin activation could not measurably impact cell behavior. To assess this, NIH-3T3 cell migration speed should be measured at a range of fibronectin concentrations, and the concentration corresponding to the peak speed should be used for further gradient experiments.

Ware et al. and Maheshwari et al. studied the migration behavior of NR6 fibroblasts, which are derivatives of 3T3 fibroblasts that lack endogenous epidermal growth factor receptor (EGFR) [213, 234, 235]. For NR6 cells that were engineered to express exogenous EGFR, migration velocity did not depend on ligand concentration, unless the cells were stimulated with soluble EGF [213, 234]. This suggests that without stimulation, NR6 cells maintain a balance between adhesion and contractility that remains constant in conditions of varying cell-substratum adhesiveness. As EGFR-transfected NR6 cells are very similar to NIH-3T3 fibroblasts, it is likely that these two cell lines will exhibit similar migration behavior. Thus, NIH-3T3 fibroblasts may not show biphasic migration velocity on surfaces with different fibronectin densities. By extension, if small changes to cell-substratum adhesiveness do not alter NIH-3T3 cell migration behavior, then these cells may be insensitive to pH_e gradients. In this case, it would be interesting to test whether EGF stimulation changes the NIH-3T3 cell migration response to ligand density or extracellular pH, as it does with NR6 fibroblasts.

Finally, a third hypothesis for the lack of NIH-3T3 fibroblast response in the pH_e gradient is that integrin expression (or pH_e-independent mechanisms of integrin activation) might be more strongly polarized in NIH-3T3 fibroblasts than in $\alpha_v\beta_3$ CHO-B2 cells or BRECs, such that pH_e-induced integrin activation cannot alter cell orientation in a significant way. This could be assessed by imaging integrin localization (perhaps by fluorescent labeling) in the three cell types that we studied here and comparing expression at the leading vs. trailing edge of cells.

6.4.4. Implications for tumor growth and wound healing

Our observations of preferential cell migration toward acid in a pH_e gradient were not limited to the model $\alpha_v\beta_3$ CHO-B2 cell line. We observed similar preferential migration behavior with BRECs, which are primary cells that express a physiologically relevant mixed population of integrins. Endothelial cell migration toward acidic extracellular pH has important implications for angiogenesis in tumor and wound environments. In wound healing, pH_e drops at 2-10 days post-injury [25-27]. This coincides with the period in which endothelial cells migrate into wounds, which occurs between days 4-14 [19, 20]. As acidic pH_e is often correlated with hypoxia, this could serve as a signal directing cells toward regions where new blood vessels are especially needed (Figure 6.11). Thus, the acidic pH_e present in wound sites could help accelerate wound healing, and the same condition in tumors could accelerate tumor growth via angiogenesis. Interestingly, integrin $\alpha_v\beta_3$ is required for angiogenesis, and is upregulated on angiogenic endothelial cells [124]. One role of this integrin may be to act as a pH_e sensor and consequently direct endothelial cell migration toward acidic pH_e.

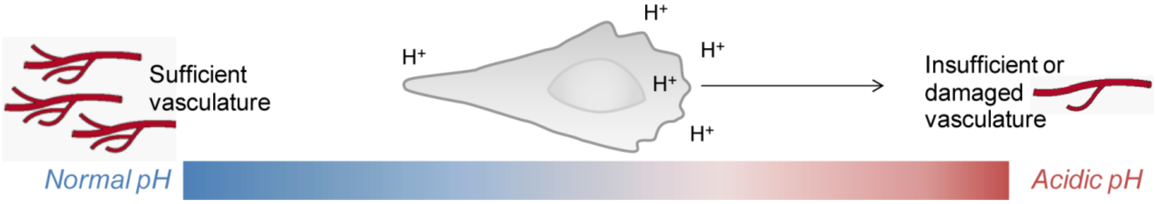

Figure 6.11 Schematic of how an extracellular pH gradient could direct cell migration toward regions of insufficient or damaged vasculature.

The gradient from pH_e 6.0 – 7.5 over 1 mm (1.5 pH units/mm) that was used in our experiments is similar to some pH_e gradients that have been measured in tumors [1]. However, shallower pH_e gradients also exist in some tumor and wound environments, such as the gradient of ~0.4 pH units/mm measured at the tumor-host interface for human prostate tumors grown in mice [6]. The concentration fluctuation model discussed above (Section 6.4.2) can be used to estimate the extent to which cells would respond to shallower pH_e gradients. Assuming that all gradients exist over a 1 mm distance, we calculated the percentage of cells orienting toward acid as a function of position within the pH_e gradient, for various gradients ranging from pH_e 6.0 – 7.5 to pH_e 7.25 – 7.5 over 1 mm. Results indicate that greater than 50% orientation toward acid is possible for all the gradients we tested (Figure 6.12). For the shallowest gradient ($\mathrm{pH_e}$ 7.25 – 7.5), the percentage of cells that orient toward acid is quite low (~55%), but for the gradient from $\mathrm{pH_e}$ 7.0 – 7.5, the orientation percentage is 65% - 75%. Therefore, preferential migration toward acid is not limited to the steepest $\mathrm{pH_e}$ gradients in the tumor or wound environments, but could conceivably occur for shallower gradients as well.

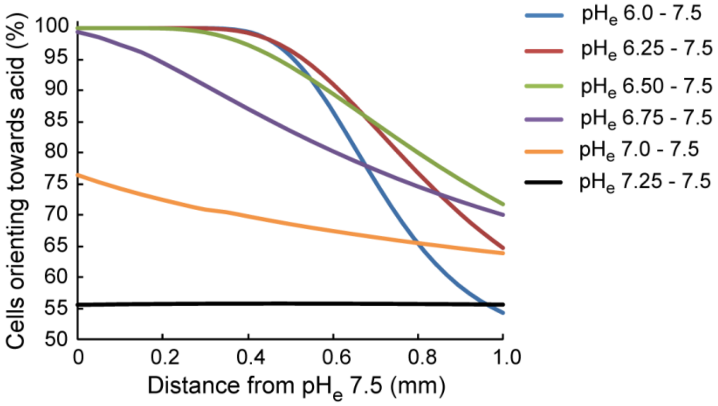

Figure 6.12 Percentage of cells orienting toward acid as a function of position within the indicated gradients, with $k_f = 3 \times 10^{10}\ \mathrm{M^{-1}min^{-1}}$, T = 5 min, and N^* = 30. All gradients are over 1 mm distance.

Our results indicate that acidic $\mathrm{pH_e}$ can serve as a direct directional cue for endothelial cell migration by activating integrin $\alpha_v\beta_3$ receptors (and possibly other integrins) expressed on cell surfaces. However, it is important to recognize that other stimulators of angiogenesis, such as vascular endothelial growth factor (VEGF), are also regulated by pH. For example, acidic pH led to increased expression and secretion of VEGF in several human cancer cell lines [236-238]. VEGF binding to endothelial cells and to fibronectin increased at acidic pH [239, 240], and VEGF expression increased at acidic pH for brain tumors *in vivo* [236]. Several other angiogenic factors, such as interleukin 8, platelet-derived endothelial cell growth factor, and basic fibroblast growth factor, are also regulated by pH [241-243]. Thus, integrin activation is one of several ways in which acidic extracellular pH could regulate angiogenesis in tumor and wound environments, and the interplay between various pH-regulated factors is an interesting subject for future work.

6.5. Conclusions

In this chapter, we demonstrated that $\alpha_v\beta_3$ CHO-B2 cells and bovine retinal microvascular endothelial cells migrated toward the acidic end of a $\mathrm{pH_e}$ gradient. Both cell types displayed preferential polarization toward acid, and BRECs also had greater displacements toward acid than away from acid, which is consistent with predictions from our cell migration model. NIH-3T3 fibroblasts did not display preferential directional orientation in the $\mathrm{pH_e}$ gradient, and understanding the reasons for this lack of gradient response is an interesting avenue for future investigation. The directional migration that we observed for $\alpha_v\beta_3$ CHO-B2 cells and BRECs in the $\mathrm{pH_e}$ gradient is consistent with our previous data that indicated acid-induced integrin activation, membrane protrusion stabilization, and adhesion complex formation in a bath of uniform acidic pH_e. Our experimental pH_e gradient closely mimicked pH_e profiles that exist in tumors, and our results indicate that acidic extracellular pH could serve as a cue directing angiogenic endothelial cells to poorly vascularized regions. In this way, pH_e gradients could promote tumor growth and wound healing by modulating angiogenesis.

In the next chapter, we will summarize the results of this work from the atomistic to cellular scale. We will then discuss the implications of our results over these length scales for regulation of cellular function in the tumor and wound healing contexts, as well as the implications for how the Na^+/H^+ exchanger NHE1 may regulate asymmetry in adhesiveness for normal cell migration. We will also consider the ways in which our data inform the interpretation of the six previously published studies of cell adhesion and migration in acidic pH_e that were introduced in Chapter 1. Finally, the major contributions of this thesis work will be summarized and ideas for future studies will be discussed.

6.6. Acknowledgments

Dr. M. Whitfield wrote the code for the cell migration model and aided in interpretation of results (Section 6.4.1).

Chapter 7: Overarching discussion

7.1. Major findings

7.1.1. Summary of previous chapters

This thesis was motivated by the well established observation that extracellular pH is generally acidic in the tumor and wound healing environments. This acidity is largely due to anaerobic cellular metabolism in these environments, which tend to be hypoxic because of damaged or insufficient vasculature. We were further motivated by the fact that cells in healthy, undamaged tissues can experience locally acidified pH_e due to the hydrogen ions extruded by the Na^+/H^+ exchanged NHE1. Although several studies have investigated cell adhesion and migration in acidic extracellular $pH_{e,}$ the molecular mechanisms underlying the observed effects were not fully clear. In particular, the role of integrin receptors in mediating the cellular response to acidic pH_e was not known. Using computational and experimental approaches ranging from the atomistic- to cellular-scale, this thesis explored the hypothesis that acidic extracellular pH can directly regulate integrin-ligand interactions, and that this can significantly affect cell adhesion and migration in acidic environments. The major results from each chapter are summarized here:

Chapter 2: Atomistic-scale simulations: We used molecular dynamics (MD) simulations to investigate the effect of acidic extracellular pH on integrin $\alpha_v\beta_3$ headpiece opening and $\alpha_v\beta_3$-RGD unbinding. Multi-Conformation Continuum Electrostatics (MCCE) was used to predict pK_a values for the amino acids in the $\alpha_v\beta_3$ headpiece, taking the molecular environment of each residue into account. Using pK_a values obtained from MCCE, we established atomistic models that simulated effective normal physiological pH_e and effective acidic pH_e. Simulation trajectories indicated that acidic pH_e promoted opening of the $\alpha_v\beta_3$ headpiece, and that protonation of ASPβ127 was at least partially responsible for this effect. Steered molecular dynamics (SMD) simulations of $\alpha_v\beta_3$-RGD unbinding indicated that the bond rupture force depended on the ion coordination state of ASP_{RGD}. However, there was no significant difference in average rupture forces or unbinding rates between normal and acidic pH_e, indicating that acidic pH_e does not directly alter the $\alpha_v\beta_3$-RGD binding affinity via direct changes to the $\alpha_v\beta_3$ binding pocket. Thus, the major effect of acidic extracellular pH is to promote $\alpha_v\beta_3$ headpiece opening, which we predicted would cause complete integrin activation. Due to the heavy computational requirements of these atomistic-scale simulations, our trajectories were restricted to brief durations (8 ns for each headpiece opening simulation), and our sampling of ion coordination states was limited. We therefore turned to experimental approaches to test simulations predictions and further explore the effects of acidic pH_e on $\alpha_v\beta_3$ activation and binding.

Chapter 3: Molecular-scale experiments: We used flow cytometry and atomic force microscope (AFM)-enabled molecular force spectroscopy to test the hypothesis that acidic pH_e will result in increased numbers of activated integrins on live cell surfaces, compared to normal pH_e 7.4. Flow cytometry experiments with the activation-specific antibody WOW-1 Fab showed that live $\alpha_v\beta_3$ CHO-B2 cells exposed to pH_e 6.0 had more activated $\alpha_v\beta_3$

integrins than cells at pH_e 7.4. Experiments with the LM609 antibody demonstrated that the total surface expression level of $\alpha_v\beta_3$ was unchanged for cells exposed to pH_e 6.0. AFM-enabled molecular force spectroscopy experiments showed that the $\alpha_v\beta_3$-RGD binding frequency was increased for cells in pH_e 6.0 compared to cells in pH_e 7.4, but the rupture force was unchanged. These molecular-scale experimental data are in agreement with our atomistic-scale simulation predications, and suggest that acidic extracellular pH_e promotes headpiece opening and consequential activation of integrin $\alpha_v\beta_3$.

Chapter 4: Subcellular-scale experiments: We used kymography to assess the effect of acidic pH_e on $\alpha_v\beta_3$ CHO-B2 cell membrane dynamics, and transfected cells with GFP-vinculin to investigate the effect on actin-integrin adhesion complex (AIAC) number and area. Kymography results demonstrated that membrane protrusion lifetime increased and velocity decreased for cells at pH_e 6.5, compared to cells at pH_e 7.4. Longer protrusion lifetime is an expected direct consequence of increased integrin activation in acidic pH_e, as it has been shown by others that protrusion lifetime increases in conditions of higher cell-substratum adhesiveness [48, 186-188]. Decreased protrusion velocity could be an effect of downstream signaling after integrin activation, or a secondary effect of acidic pH_e unrelated to increased integrin activation. We also measured membrane protrusion lifetime and velocity after acidifying intracellular pH by blocking the Na^+/H^+ exchanger NHE1, and results showed that intracellular acidification cannot account for the changes to membrane dynamics that we observed for cells at pH_e 6.5. Fluorescent imaging of $\alpha_v\beta_3$ CHO-B2 cells transfected with GFP-vinculin showed that cells in pH_e 6.5 developed more AIACs than cells in pH_e 7.4. After 20 – 40 min of media acidification, AIACs at pH_e 6.5 exhibited a smaller average projected area than those at pH_e 7.4, but this difference was abolished after 2 – 3 hr of acidification. These results indicate that acidic pH_e initiates formation of new AIACs, and it is plausible that this is a result of increased integrin activation and binding in this condition. Combined results from this chapter show that acidic extracellular pH has significant effects on subcellular-scale processes that are critical to cell migration, and that these effects are largely consistent with our model of acid-induced integrin activation.

Chapter 5: Cellular-scale experiments: We used optical microscopy to investigate the effects of acidic extracellular pH on $\alpha_v\beta3$ CHO-B2 cell spreading, morphology, and migration. We found that the cell projected area oscillated in response to cyclic changes in media pH_e, with larger cell area in more acidic media conditions, which could be a result of the increased membrane protrusion lifetime in acidic pH_e that we characterized in Chapter 4. We also determined that cells in pH_e 6.5 had greater projected area than cells in pH_e 7.4 over a range of fibronectin coating concentrations. Furthermore, over the same range of fibronectin coating concentrations, cells in pH_e 6.5 were more elongated than cells in pH_e 7.4, which was quantified as lower cell circularity. Experiments with CHO-B2 pCDNA cells, which do not express $\alpha_v\beta_3$, demonstrate that this integrin is necessary for cell area to increase and cell circularity to decrease in acidic pH_e. Furthermore, experiments with Mn^{2+}, which activates $\alpha_v\beta_3$, demonstrated that activation of this integrin is sufficient to cause these changes to cell area and circularity in acidic pH_e. Cell migration experiments at pH_e 6.5 and pH_e 7.4 showed that peak cell migration speed occurred at a lower fibronectin concentration for cells at pH_e 6.5; i.e. the biphasic curve of speed vs. fibronectin concentration was shifted to the left. In addition, cells at pH_e 6.5 migrated slower than cells at pH_e 7.4 for all the fibronectin concentrations that we tested. We used a modified version of the a biophysical model of cell migration proposed by DiMilla et al. [95] to assess the extent to which these effects of acidic pH_e on cell migration could be attributed to increased integrin activation. Results indicated that the shift of peak migration speed to a lower fibronectin concentration in pH_e 6.5 could be a direct result of acid-induced integrin activation, but that the general decrease of migration speed is not attributable to pH_e-dependent integrin activation alone. This decrease in migration speed does not preclude increased integrin activation in this condition, but is likely to be due to a secondary effect of acidic pH_e such as altered metabolism. Overall, these cellular-scale experiments demonstrate that acidic extracellular pH affects cell spreading, morphology, and migration in a manner that is consistent with our atomistic-, molecular-, and subcellular-scale results.

Chapter 6: Cell migration in a pH_e gradient: The previous chapters investigated the molecular and cellular response to changes in pH_e of the bulk media, a spatially homogeneous cue. In Chapter 6, we considered the pH_e gradients that exist in the tumor and wound healing environments of interest. We used the Dunn chamber to establish gradients between pH_e 6.0 – 7.5, and investigated the migration behavior of $\alpha_v\beta_3$ CHO-B2 cells, bovine retinal microvascular endothelial cells (BRECs), and NIH-3T3 fibroblasts in these gradients. NIH-3T3 fibroblasts did not show a directional preference in the pH_e gradient; the reasons for this are currently unclear and are beyond the scope of this thesis. For both $\alpha_v\beta_3$ CHO-B2 cells and BRECs, the average position of the cell population moved progressively toward the acidic end of the gradient over time. For $\alpha_v\beta_3$ CHO-B2 cells, this effect was primarily due to preferential polarization toward acid. For BRECs, this effect was due to preferential polarization toward acid as well as larger cell displacements toward acid than away from acid. Taking these results together with our previous data, we propose that increased $\alpha_v\beta_3$ activation, greater membrane protrusion stability, and increased AIAC formation in acidic pH_e could cause cells to orient such that the part of the cell exposed to more acidic pH_e becomes the leading edge during migration. The results of our pH_e gradient experiments have interesting implications. In particular, the preferential migration of BRECs toward acid suggests that pH_e gradients could be an important cue for directional migration of vascular endothelial cells during angiogenesis in tumor growth or wound healing contexts.

In summary, we have investigated the effects of acidic extracellular pH, an important chemical cue found in the tumor and wound microenvironments, on atomistic-, molecular-, subcellular-, and cellular-scale processes. This research has identified integrin $\alpha_v\beta_3$ as a major pH_e sensor that is activated in acidic conditions. Activation of $\alpha_v\beta_3$ acts as a signal that converts information about extracellular pH into subcellular- and cellular-scale responses (Figure 7.1). For some responses, we have shown via experiments or modeling that activation of $\alpha_v\beta_3$ is sufficient to cause the observed effects (Figure 7.1, solid black arrows). For other responses, the observed results are consistent with increased integrin activation, and we can reasonably hypothesize that they are direct downstream effects of increased $\alpha_v\beta_3$ activation in acidic pH_e. However, we have not conclusively proven these connections (Figure 7.1, solid gray arrows). Furthermore, it is plausible that some of the cellular-scale responses that we observed may be mediated in part by the subcellular-scale responses to acidic pH_e (Figure 7.1, dashed gray arrows). Finally, we also uncovered some subcellular- and cellular-scale responses to acidic pH_e that cannot be directly attributed to increased integrin activation at this time, and may be due to alteration of other processes, such as intracellular signaling or metabolic pathways (Figure 7.1, dashed black arrows). Overall, we have characterized the effects of acidic extracellular pH in a multi-scale manner that draws connections between atomistic protonation events, molecular conformational changes and binding events, subcellular membrane protrusion processes and AIAC formation, and cellular spreading and migration.

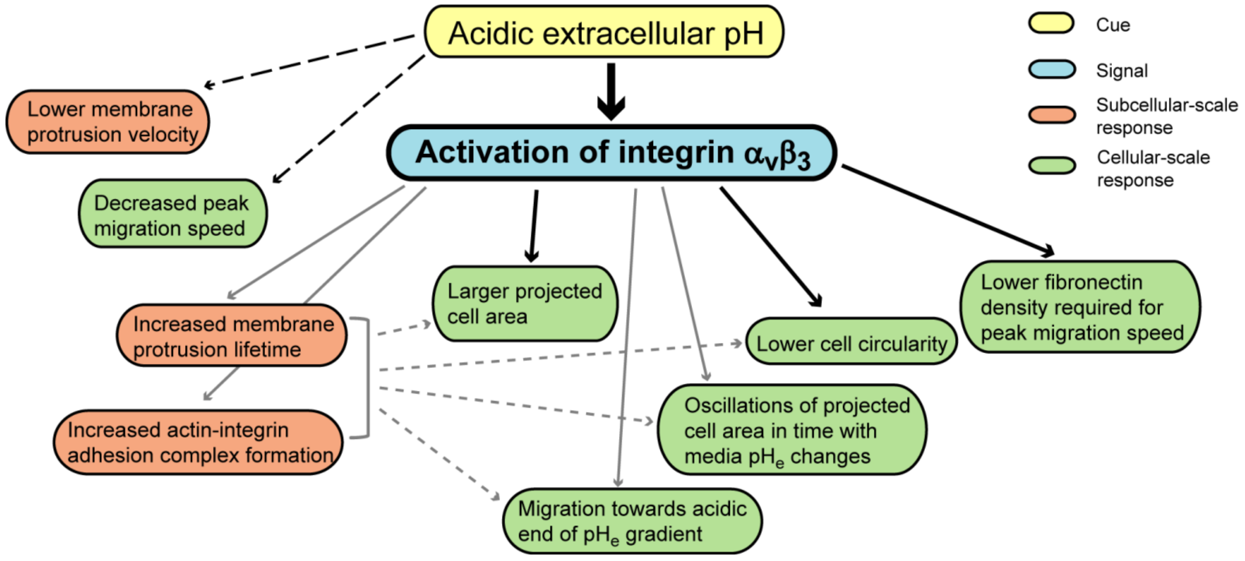

Figure 7.1 Schematic diagram illustrating major thesis results in a cue-signal-response framework. Acidic extracellular pH is a chemical cue found in several physiological contexts. The major effect of acidic pH_e uncovered in this thesis is activation of integrin $\alpha_v\beta_3$, which acts as a signal mediating several subcellular- and cellular-scale responses. For some responses, we have shown that activation of $\alpha_v\beta_3$ is sufficient to cause the observed effects, and these connections are indicated with black solid arrows. Gray solid arrows indicate subcellular- and cellular-scale responses that we speculate are direct downstream effects of increased integrin activation in acidic pH_e. Gray dashed arrows indicate places where subcellular-scale responses may possibly contribute to the observed cellular-scale responses. Dashed black arrows indicate responses to acidic pH_e that we cannot directly attribute to increased integrin activation at this time.

7.1.2. Role of intracellular acidification

Our experimental changes to extracellular pH concurrently altered intracellular pH (pH_i), as shown in Figure 4.4. Therefore, it is possible that some of the effects of acidic pH_e that we measured were actually caused by intracellular acidification and consequent alterations to intracellular processes. This possibility was addressed for each set of results in the discussion portions of the previous chapters, and we will review the general conclusions here.

We directly assessed the role of pH_i in modifying subcellular-scale membrane dynamics, and results demonstrated that intracellular acidification cannot account for the increased membrane protrusion lifetime and decreased protrusion velocity that we observed for cells at pH_e 6.5, compared to cells at pH_e 7.4. As membrane protrusion lifetime is closely related to integrin activation and binding, these data also suggest that activation of integrin $\alpha_v\beta_3$ can be modulated by extracellular acidification alone. This supposition is further reinforced by our molecular dynamics simulations of $\alpha_v\beta_3$ headpiece opening, which did not include any intracellular components. Thus, we can reasonably assume that intracellular acidification did not contribute significantly to our molecular-level flow cytometry and AFM-mediated force spectroscopy results demonstrating increased levels of activated $\alpha_v\beta_3$ for cells in acidic pH_e. However, the possibility remains that acidic pH_i may have played a role in our observation that cells in pH_e 6.5 had more AIACs than cells in pH_e 7.4. It is conceivable that AIAC dynamics in response to acidic pH_e may be modulated both extracellularly (more sites for AIAC initiation due to increased integrin activation and binding) and intracellularly (alterations to protein-protein binding within AIACs).

As for our cellular-level results, our observations of cell area oscillations in response to media pH_e changes are unlikely to have been caused by intracellular effects, due to the fact that cell area began to increase within 10 min of media acidification, before there were any significant changes to $pH_{i.}$ In contrast, intracellular pH was acidified significantly during the 8-hr time span of our cell spreading, morphology, and migration experiments. However, we showed that integrin activation is sufficient to cause cell area to increase and circularity to decrease, and our migration model predictions indicated that integrin activation is sufficient to cause the biphasic cell velocity vs. fibronectin concentration curve to shift to the left. Therefore, as integrin activation can be mediated solely by extracellular pH, we can assume that these direct downstream cellular-scale responses also do not require intracellular pH changes. However, our observation of decreased cell migration speed in acidic pH_e over all fibronectin concentrations cannot be explained by increased integrin activation alone, and was thus probably caused by changes to intracellular proteins and processes. Finally, we cannot exclude the possibility that intracellular pH changes contributed to the directional migration we observed for $\alpha_v\beta_3$ CHO-B2 cells and BRECs in the pH_e gradient, although we suspect that these results were largely due to direct downstream effects of pH_e-induced integrin activation, namely increased membrane protrusion stability.

In summary, we can reasonably surmise that the following effects of acidic pH_e most likely do not require intracellular pH changes: increased activation of integrin $\alpha_v\beta_3$, increased membrane protrusion lifetime, decreased membrane protrusion velocity, oscillations of projected cell area in response to cyclic media pH_e changes, larger projected cell area, lower cell circularity, and leftward shift of the biphasic cell velocity vs. fibronectin concentration curve. However, intracellular acidification may possibly have contributed to these other effects of acidic pH_e: increased AIAC formation, decreased peak cell migration speed, and preferential migration toward acid in a pH_e gradient. Further clarification of the role of extracellular vs. intracellular pH in mediating these subcellular- and cellular-scale responses is an avenue for further research that is especially relevant to the tumor environment, because tumor cells generally maintain pH_i at normal levels although pH_e can be significantly decreased.

7.1.3. Extension to other integrins

This thesis focused on integrin $\alpha_v\beta_3$, which is structurally well-characterized and is expressed on many types of tumor and wound healing cells. However, $\alpha_v\beta_3$ is not the only integrin expressed by cells in the physiological contexts of interest. Therefore, it is important to consider whether our key finding – that acidic pH_e promotes $\alpha_v\beta_3$ headpiece opening and activation – extends to other integrins. Our molecular dynamics results indicated that protonation of ASPβ127 and resulting configurational changes are critical events in acid-induced activation of integrin $\alpha_v\beta_3$. This amino acid is a conserved acidic residue in seven of the eight integrin β subunits (all except β8, Appendix B), and protonation of this residue is therefore possible for almost all integrins. However, the effective pK_a of this amino acid will depend on its specific local environment. As a result, each integrin β subunit could require a different extracellular pH for ASPβ127 to be protonated on the majority of receptors, and the configurational changes following protonation may vary among different β subunits. This idea of subunit specificity is consistent with activation and binding data for integrins in which ASPβ127 (or the equivalent residue in other β subunits) was mutated to alanine. These data were discussed in detail in Chapter 2, and the general conclusion was that the effect of alanine mutation depended on the specific β subunit being tested. Therefore, although there is structural homology among different members of the integrin family of proteins, regulation of activation is not necessarily identical for all integrins. However, we note that our model of acid-induced $\alpha_v\beta_3$ activation is consistent with subcellular- and cellular-level effects of acidic pH_e that others have measured for cell types expressing different integrins (see Section 7.2 for details). Although none of these studies directly studied integrin activation, the consistency with our data suggests that activation of other integrins may indeed be promoted by acidic extracellular pH, and that this may be responsible for some of the responses to acidic pH_e that have been described in the literature. Clarification of the subunit specificity of acid-induced integrin activation is an important area for future investigation that will enable better prediction of how various physiologically relevant cell types respond to acidic extracellular pH.

7.2. Previous work in the context of our results

In Chapter 1, we outlined six prior studies by other researchers that investigated the effects of extracellular pH on cell adhesion and migration. Part of the motivation of this thesis research was to elucidate the molecular mechanisms underlying these observations. Here, we will reassess these studies within the context of our work to evaluate whether increased integrin activation could have contributed to the previously reported effects of acidic pH_e.

Study #1: Serrano et al. reported that adhesion between human endothelial cells and neutrophils was strengthened in acidic pH_e [39]. As this adhesion is mediated by binding between β2 integrins on neutrophils and ICAM-1 ligands on endothelial cells, it is certainly possible that acid-induced integrin activation played a role in strengthening cell-cell adhesion in this study. To test this, one could assess whether the amount of activated neutrophil β2 integrins increases in acidic pH_e, using methods similar to those described in Chapter 3 of this study.

Study #2: Stock et al. reported that human melanoma cells had more lamellipodia and exhibited greater spreading acidic pH_e. The number of adherent cells in collagen matrices and the amount of matrix deformation caused by cell-exerted forces both also increased in acidic pH_e, indicating general enhancement to cell adhesion. Furthermore, Stock et al. showed that cell migration speed had a biphasic dependence on extracellular pH in their experimental system [29]. All of these results can be explained by increased integrin activation in acidic pH_e. Greater numbers of lamellipodia could be a result of increased membrane protrusion stability due to enhanced integrin activation and binding, and this could also lead to greater cell spreading and adhesion. The biphasic dependence of cell migration speed on extracellular pH is very similar to the biphasic dependence on ligand density that has been well described in the literature [96, 188, 213, 214], as both ligand density and pH_e-modulated integrin activation alter cell-substratum adhesiveness. Interestingly, Stock et al. speculated that strengthening of integrin-ligand bonds in acidic pH_e could explain their cell adhesion and migration results, and our model of acid-induced integrin activation is consistent with this speculation.

Study #3: Rofstad et al. showed that acidic extracellular pH increased invasiveness of human melanoma cells in Matrigel [40]. Although this could be attributed to the increased proteinase secretion that occurred in acidic pH_e, enhanced integrin activation could also have played a role. In particular, this enhanced integrin activation could have helped make up for the decrease in ligand availability that likely occurs after enzymatic matrix digestion.

Study #4: Kato et al. demonstrated that acidic extracellular pH caused increased migration of mouse melanoma cells through collagen-coated filters in Boyden chambers. These investigators also observed increased gelatinase secretion in acidic pH_e [41]. As with the Rofstad et al. study described above, acid-induced integrin activation and increased matrix digestion could both have contributed to the effect of pH_e on cell invasion.

Study #5: Glunde et al. reported that the number and length of filopodia increased at acidic pH_e for human breast cancer cells [42]. The increased filopodial length could have been a result of increased membrane protrusion stability resulting from enhanced integrin activation in acidic extracellular pH, and kymography experiments similar to those described in Chapter 4 could be used to evaluate this possibility.

Study #6: Faff and Nolte showed that acidic pH_e caused cytoskeletal rearrangement, stress fiber formation, and reduced motility for mouse microglial cells [43]. The reported cytoskeletal changes could have been a downstream effect of increased integrin activation in acidic pH_e, but could also have been consequence of the decreased intracellular pH that occurred in this study. Similarly, the reduced motility is likely to have been a result of perturbations to intracellular processes resulting from acidic pH_i.

In conclusion, many of the results reported in these six studies are consistent with our model of acid-induced integrin activation. Integrin activation in acidic pH_e could have been the primary mechanism of pH_e sensing and information transfer in some of these experimental systems, and changes to integrin-ligand binding could have directly caused many of the effects on adhesion and migration that were observed in these previously published studies. Thus, the results of this thesis can lend insight into and aid interpretation of previously reported work.

7.3. Implications

7.3.1. Regulation of integrin activation and binding in varied environments

Integrin activation can be regulated by a diverse set of extracellular signals, including divalent cations [73, 78, 80, 86-88], ligand molecules [80], fluid shear stress [90], and mechanical force [91]. The results of this thesis work have added to this list by revealing extracellular pH to be important and novel regulator of integrin activation. The ability of integrins to respond to such disparate chemomechanical activation cues suggests that cell-matrix binding can be finely tuned in environments that present different combinations of these activation signals. As a result, integrins could facilitate precise regulation of cell adhesion and migration in many pathological and physiological contexts. Elucidation of the ways in which various integrin activation mechanisms are coordinated will be critical to the goal of understanding and modulating cell adhesion and migration in diverse microenvironments.

7.3.2. Tumor growth and wound healing

Our results indicate that acidic extracellular pH could significantly alter cell adhesion and migration in the tumor and wound environments via regulation of integrin activation. In particular, our findings indicate that pH_e gradients in tumors or wounds could help direct some cell types, such as vascular endothelial cells, toward poorly vascularized regions during angiogenesis, which is the sprouting of new vessels from existing vasculature. Such pH_e gradients exist at the interfaces between tumors and normal tissue [6], as well as at locations between blood vessels within tumors [1, 18] (Figure 7.2A). In addition, although pH_e gradients have not been directly measured in wound sites, the existence of pO_2 gradients in these regions [23, 26, 28] implies the presence of pH_e gradients, as anaerobic metabolism in hypoxic environments leads to extracellular acidification (Figure 7.2B). Our data show that endothelial cells preferentially orient toward the acidic end of pH_e gradients, and will thus tend to migrate toward regions in need of angiogenesis (Figure 7.2C). Our results also show that cell migration speed slows in more acidic regions of the gradient, which could keep cells confined within the regions requiring new vessel formation, rather than migrating away. Thus, by altering endothelial cell migration and consequent angiogenesis, acidic pH_e could promote tumor growth and disease progression, as well as wound healing.

7.3.3. The role of NHE1 in cell migration

The implications of this research are not limited to the tumor and wound environments. Rather, our model of acid-induced integrin activation has very interesting implications for how the Na+/H+ exchanger NHE1 may regulate migration of normal, healthy cells. Because NHE1 localized to adhesion sites [30, 33], it extrudes hydrogen ions into the environment proximal to integrin receptors. Furthermore, NHE1 localizes to the leading edge of migrating cells [31, 35, 36], and its ion exchange activity creates cell surface pH_e gradients. Measurements for human melanoma cells indicate that there could be a difference in local pH_e of approximately 0.2 units over a single cell length, even if the bulk extracellular environment has a spatially constant pH_e [37, 38]. According to our integrin activation results, this local acidification at the leading edge would result in increased number of activated integrins, and a corresponding increase in cell-surface adhesiveness (Figure 7.3). It is well known that asymmetry in the ratio of adhesiveness to contractility is required for cell migration; thus, NHE1 polarization could be one mechanism that creates or enhances this asymmetry. In this manner, acidic pH_e may help define the cell leading edge and regulate migration for normal cells in healthy tissues.

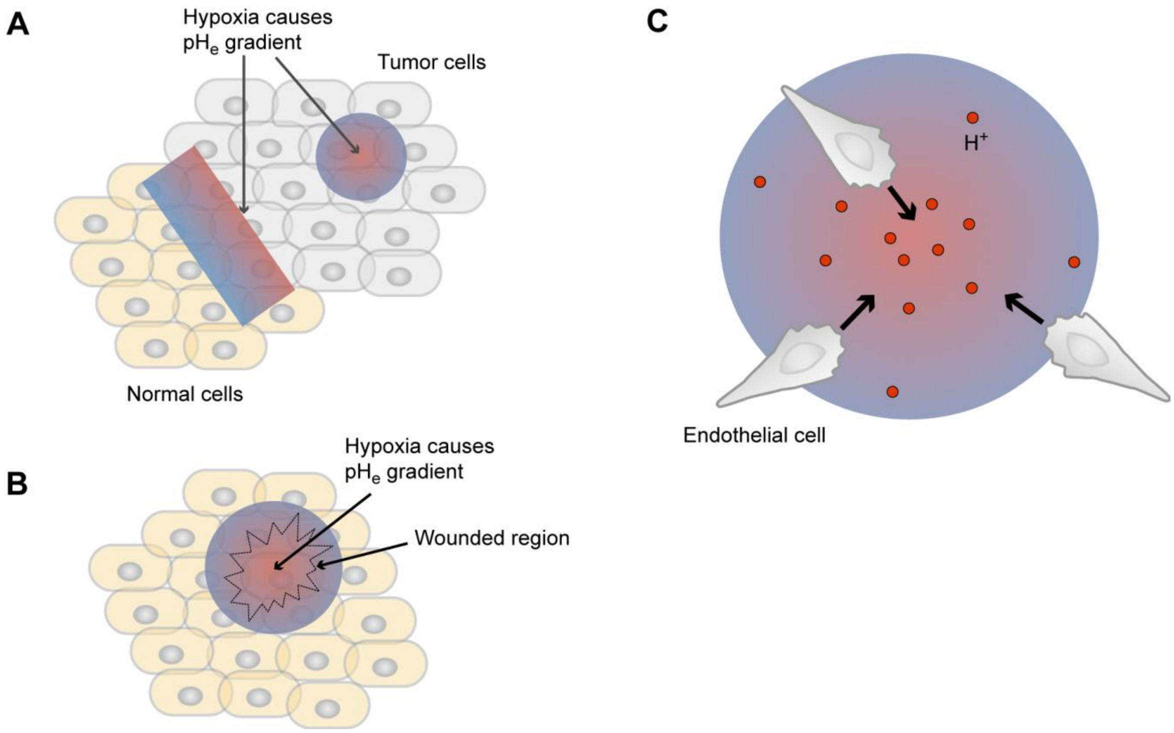

Figure 7.2 Schematic illustration of pH_e gradients in tumors and wounds, and the effect such gradients have on endothelial cell migration. (A) In the tumor context, pH_e gradients form at the interfaces between tumor cells (gray) and normal tissue (peach), as well as at insufficiently vascularized regions within tumors. Red represents the more acidic part of the gradient, while blue represents extracellular pH close to 7.4. (B) It is likely that pH_e gradients exist at wound sites, due to anaerobic cellular metabolism in the hypoxic environment resulting from damaged vasculature. (C) Our data show that endothelial cells preferentially migrate toward the acidic part of a pH_e gradient, likely due to increased integrin activation and membrane protrusion stabilization in acid.

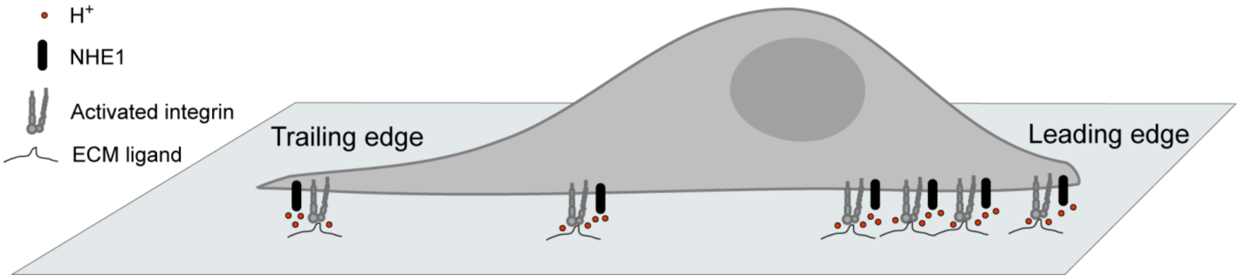

Figure 7.3 Schematic depiction of the possible role of NHE1 in integrin activation during cell migration. NHE1 localizes to the leading edge of migrating cells and extrudes hydrogen ions proximal to integrin receptors. The locally acidified environment caused by NHE1 activity may activate integrins preferentially at the leading edge, thus creating an asymmetry in cell-surface adhesiveness.

7.4. Suggestions for future study

There are several avenues for future research that can expand upon the results of this thesis and explore the implications of our work in more detail. Of particular relevance are research topics investigating whether our results extend to different integrins and cell types, and studies using experimental systems that more realistically represent the physiological environments of interest. Here, we describe what we consider to be four of the most promising and interesting topics for future work.

7.4.1. Exploration of other integrins

This thesis focused on integrin $\alpha_v\beta_3$, and it is currently unknown whether activation of other integrins can be regulated by extracellular pH. It is possible that different integrins become activated at different pH_e, and that some integrins may not exhibit a pH_e-induced activation response (or the pH_e level required for activation may not be in a physiologically relevant range). It will be very interesting to understand the full range of pH_e response among different integrins, and this will greatly aid predictions about how different cell types will respond to acidic extracellular pH. This research could be done with similar methods to those used in this thesis; for example, AFM-enabled molecular force spectroscopy on cell types exhibiting different integrins to measure binding frequencies and rupture forces as a function of extracellular pH. It is also possible to use methods that directly image the protein structure for purified integrins, such as electron microscopy, which has been used in other studies of integrin activation [80, 81].

7.4.2. Fibroblast migration in pH_e gradients

As detailed in Chapter 6, NIH-3T3 fibroblasts did not migrate with a directional preference in the pH_e gradient, and the addition of an $\alpha_5\beta_1$-blocking antibody caused the cells to exhibit a dual response to the gradient: cells on one end of the gradient migrated toward acid, while cells on the other end of the gradient migrated away from acid. The reasons for these responses to the pH_e gradient, both before and after $\alpha_5\beta_1$ blocking, are not well understood. Resolving this problem will enable us to better understand the variation of response among different cell types that are relevant to the tumor and wound environments. Several ideas for further exploration of fibroblast migration in pH_e gradients were outlined in Chapter 6. These include exploring the role of different fibroblast integrins by suppressing expression of specific integrins, or alternatively, using different ECM ligands to promote selective use of certain integrins (e.g., only α_v integrins will be used for binding if vitronectin is the ligand). Furthermore, we suggested assessing the NIH-3T3 fibroblast response to different fibronectin coating concentrations, to understand in a general sense how cell-surface adhesiveness regulates migration of these cells. The reader can refer to Section 6.4.3 for further details of proposed future experiments.

7.4.3. 3-D cell migration

The experiments conducted in this thesis were for cells adhered to or migrating on 2-D substrata. While this is an appropriate choice for fundamental research using model systems, it is not representative of 3-D tissue environments. Therefore, extending our results to 3-D cell migration will be an important focus for future research. It will be particularly interesting to understand how increased matrix metelloproteinase activity in acidic pH_e [40, 220, 221], which is necessary for reducing steric hindrance of 3-D matrices but concurrently reduces ligand availabilility, balances with increased integrin activation to enable cell migration. It will also be important to test the cellular response to pH_e gradients in 3-D systems to more fully understand how gradients regulate cell behavior in the tumor and wound environments. Experimental matrices that have been used for 3-D cell migration experiments include collagen gels [244], poly(ethylene glycol)-based hydrogels [245], and Matrigel [219], and 3-D concentration gradient devices have been developed [246]. These tools could certainly be used for studying the role of acidic extracellular pH in modulating 3-D cell migration, although some optimization and modification of microscopes, software, and image analysis methods may be required.

7.4.4. ECM stiffness

In addition to having acidic extracellular pH, tumor ECM is generally stiffer than that of normal tissues. For example, normal breast tissue exhibits Young's modulus E of ~0.15 kPa, but breast tumors can exhibit E as large as ~4 kPa [247]. Normal liver tissue exhibits E of ~2.5-5kPa, but liver tumors exhibit E of ~55-75 kPa [248]. Furthermore, the stiffness of the ECM in wound sites also increases after fibroblasts enter the injured tissue and exert contractile forces on the matrix [249, 250]. Previous research has suggested that receptor-ligand unbinding kinetics can be regulated by the stiffness of the material presenting the binding molecules [139], indicating that ECM stiffness could modulate integrin-ligand unbinding. Investigation of this potential mechanical regulation is an intriguing parallel to our work with acidic pH_e, and it will be interesting to explore the combined effect that these two cues have on molecular and cellular behavior. To characterize the role of mechanical stiffness in regulating integrin-ligand interactions, AFM-enabled molecular force spectroscopy techniques could be used to measure integrin-ligand unbinding forces and rates. These molecular-scale experiments could be conducted with ligand-functionalized cantilevers of varying stiffness, or alternatively, cells could be attached to cantilevers and ligands could be presented on gels of varying stiffness. Subcellular- and cellular-scale parameters could be measured for cells adhered to gels of varying stiffness. Further studies could use experimental systems that include increased mechanical stiffness as well as acidic extracellular pH. Such research will greatly further our understanding of how the chemomechanical properties of the tumor and wound environments can alter integrin-ligand interactions and downstream cell processes.

7.5. Contributions

This thesis work has resulted in several major contributions to the field of cell-matrix interactions. First, we have developed several new methods for the study of integrin conformation and integrin-ligand binding as a function of extracellular conditions, which include: 1) a method for using clustering analysis to select a representative set of initial configurations for input into molecular dynamics simulations, enabling characterization of rare-event property distributions; 2) a protocol for covalent functionalization of AFM cantilevers with RGD ligands; 3) a method for using both rupture force and effective loading rate to identify specific binding events in AFM-enabled molecular force spectroscopy experiments; 4) application of the Dunn chamber to create stable pH gradients for cell migration experiments. More broadly, this thesis has demonstrated the integration of computational and experimental methods over lengthscales ranging from single atoms to whole cells to gain detailed understanding of how an extracellular chemical cue affects molecular behavior and downstream cellular processes. This general methodology enabled us to draw connections between molecular-, subcellular-, and cellular-scale parameters, and can serve as an example for study of other complex problems in molecular and cellular biology.

In addition to the development of general methods and specific protocols, this work has characterized a novel mechanism of integrin activation, and we have demonstrated for the first time that integrins can act as pH_e sensors. This can explain many of the ways that acidic pH_e affects subcellular and cellular processes, which were previously understood poorly. We have additionally shown for the first time that some cell types preferentially migrate toward acid in pH_e gradients. Our findings firmly establish extracellular pH as a critical regulator of molecular and cellular function, and have laid the groundwork for further investigation of this topic. Our combined studies spanning multiple length scales have increased knowledge of how normal migrating cells may use NHE1 proton pumps to generate or increase asymmetry in adhesiveness between the leading and trailing edges, which is an important advance to the fundamental understanding of directed cell migration. Furthermore, our work has led to new predictive knowledge of how the acidic nature of the tumor and wound environments may regulate behavior of surrounding cells, especially migration of endothelial cells during angiogenesis. This underscores the importance of the extracellular environment in regulating cell behaviors, and is a significant contribution to tumor and wound healing biology. It is our aim that this thesis work will inspire a plentitude of future research, both in elucidating basic biological mechanisms for chemomechanical regulation of cellular processes and in development of new strategies for treatment of cancer and wound healing diseases.

Chapter 8: Materials and methods

8.1. Antibodies and reagents

WOW-1 Fab and LIBS-6 antibodies were provided by Dr. Sanford Shattil (University of California at San Diego) and Dr. Mark Ginsberg (University of California at San Diego), respectively. GFP-vinculin plasmid was provided by Dr. Benjamin Geiger (Weizmann Institute of Science). Reagents for bacterial transformation and GFP-vinculin plasmid amplification were obtained from Dr. Ron Weiss (Massachusetts Institute of Technology). All other reagents were purchased from the manufacturers listed in Table 8.1.

Reagent	Manufacturer	Catalog number
anti-$\alpha_v\beta_3$ antibody LM609	Millipore	MAB1976
anti-$\alpha_5\beta_1$ antibody BMB5	Millipore	MAB2514
Alexa 488 goat anti-mouse IgG (H + L) F(ab')$_2$ fragment	Invitrogen	A11017
SH-PEG-NH$_2$ linker	Nanocs	PG2-AMSL-5k
sulfo-LC-SPDP cross-linker	Pierce Biotechnology	21650
GRGDSPC peptide	Phoenix Pharmaceuticals	025-28
DMEM (high-glucose)	Invitrogen	11995-081
DMEM (low-glucose)	Invitrogen	11885-092
DMEM (high-glucose, bicarbonate-free)	Invitrogen	12800-017
DMEM (low-glucose, bicarbonate-free)	Invitrogen	31600-034
Opti-MEM	Invitrogen	31985-062
antibiotics-antimyotics	Invitrogen	15240-062
non-essential amino acids	Invitrogen	11140-050
G418 (geneticin)	Invitrogen	10131-035
zeocin	Invitrogen	R25001
fibronectin from human plasma	Sigma	F2006
HEPES	Sigma	H3537
EIPA	Sigma	A3085
paraffin	Sigma	327212
beeswax	Sigma	243248
BCECF-AM	Invitrogen	B1170
BCECF (free acid)	Invitrogen Biotium	B1151 (Invitrogen) 51010 (Biotium)
nigericin	Invitrogen	N1495
fetal bovine serum for CHO cell culture	Hyclone	SH30070.03
bovine calf serum for fibroblast cell culture	American Type Culture Collection	30-2030
bovine calf serum for endothelial cell culture	Sigma	C8056
Lipofectamine and Plus reagents	Invitrogen	15338-100
Plasmid Midi Kit	Qiagen	12143

Table 8.1 Manufacturers and catalog numbers for the reagents used in this thesis work.

8.2. MD simulations

8.2.1. Biotin-streptavidin simulations

The biotin-streptavidin tetramer (PDB ID 1STP [160]) was simulated at 300K in explicit water for 101 ns using the GROMACS molecular dynamics package, version 3.3 [251, 252], as described previously [253]. The portion of the equilibration trajectory with t > 15 ns was determined to have begun exploring its equilibrium phase space in at least a local minimum, as calculated by the protocol of Walton et al. [253]. Every five frames of this portion of the equilibration trajectory were used as input for clustering analysis, for a total of 489 configurations. The GROMACS tool g_cluster was used for single linkage hierarchical clustering, and clusters with at least 10 members were chosen for SMD simulations. The similarity measure for the clustering algorithm used here was the root mean square deviation (RMSD) of residues after least squares fitting between pairs of configurations. A configuration was assigned to a cluster if its RMSD with respect to any cluster member was within a cutoff, and the cluster centroid was defined as the member with the lowest average RMSD with respect to all other cluster members. The RMSD cutoff c_{RMSD} was chosen in order to produce ~10 clusters with at least 10 members each. RMSD cutoff for each clustering group: whole complex, c_{RMSD} = 7.5 Å; occupied binding pocket, c_{RMSD} = 3.5Å; unoccupied binding pocket, c_{RMSD} = 2.5 Å.

SMD simulations of forced biotin dissociation from the streptavidin receptor were performed as previously described [139]. Briefly, one subunit of the streptavidin tetramer was subjected to loading forces through a force transducer (i.e., a Hookean spring). The center of mass of one streptavidin monomer was fixed, but the system was allowed to rotate about the center of mass. The tensile loading direction was defined as the normalized vector between the initial center of mass of the fixed streptavidin subunit and the O2 atom of the biotin bound primarily to that subunit. The biotin molecule was displaced via a Hookean spring of spring constant k = 1686 kJ mol^{-1}nm^{-2} (2.8 N/m) with a velocity $\vec{v}$ = 0.8 m/s.

The resulting trajectories were analyzed to extract the force exerted by the spring and the reaction coordinate of the ligand as functions of simulation time. The reaction coordinate χ is defined as the distance of the biotin O2 atom from its initial position, $\chi = [(x - x_0)^2 + (y - y_0)^2 + (z - z_0)^2]^{1/2}$. Forces were examined every 200 fs, and rupture force F_R was taken as the maximum force recorded during a particular trajectory, which was ultimately followed by dissociation of the complex.

To find the mean and standard deviation of each distribution of rupture forces we fit the linear portion (0-80%) of the cumulative distribution function (CDF) to a straight line. The rupture force distribution for a single ligand-receptor complex is expected to be approximately Gaussian [254], and by Taylor expansion of the Gaussian CDF, the slope of the best fit line can be approximated as $1/(\sigma(2\pi)^{1/2})$. The mean was calculated as the force value for which the CDF equaled 50%. We were able to use the non-symmetric interval 0-80% due to the presence of a cutoff function at non-zero force caused by the added harmonic potential in SMD [255].

8.2.2. Integrin simulations

Molecular dynamics simulations were conducted using GROMACS version 3.3 [251, 252] and were run on 2.66 GHz Intel Xeon X5355 processors. The input crystal structure for MD simulations was the extracellular portion of integrin $\alpha_v\beta_3$ in complex with an RGD ligand (PDB ID 1L5G [45]). Mn^{2+} ions were replaced with Mg^{2+}, and only the α propeller (residues 1 – 438 in the α subunit), β hybrid, and βA domains were simulated (residues 55 – 434 in the β subunit). The PRODRG server [256] was used to generate the RGD ligand topology.

Multi-Conformation Continuum Electrostatics (MCCE) [173, 174] was used to predict pK_a values for all the titratable amino acid residues in the integrin-ligand system. To incorporate the protein environment into pK_a prediction calculations, MCCE gives flexibility to the protein structure by allowing each residue to exist in multiple positions (within a predefined set) and ionization states. Each combination of amino acid position and ionization state is called a conformer, and a particular set of conformers comprises a protein microstate. For each protein microstate, MCCE calculates electrostatic energies using a Poisson-Boltzmann continuum formulation, as well as nonelectrostatic energy terms. Finally, Monte Carlo sampling is employed to find the distribution of conformer states during a simulated titration. This is used to estimate a pK_a value for each residue.

MCCE is freely available online at http://www.sci.ccny.cuny.edu/~mcce/index.php. MCCE can run at several levels which consider different numbers of amino acid conformers. A greater number of conformers results in more accurate pK_a prediction, but requires more computational power. For our pK_a predictions, we first ran MCCE on the integrin-ligand system at the "quick" level, which uses the minimum number of conformers. We then ran MCCE again at the quick level using a "gold list" of particular residues of interest. This allowed additional conformers to be generated for just the residues within 4 Å of those in the gold list, and increases pK_a prediction accuracy without requiring excessive computational resources. In effect, this enables double checking of the pK_a values for residues of interest. Residues chosen for the gold list included those that interacted with the RGD ligand or the divalent cations in the $\alpha_v\beta_3$-RGD crystal structure [45] or in the simulations of Criag et al. [46]. Residues with pK_a values from the first MCCE quick run that were significantly different than the pK_a values for amino acids in solution were also included in the gold list. The gold list included the following amino acids: ASPα150, TYRα178, ALAα215, ASPα218, PHEα177, GLNα180, ARGβ216, ASNβ215, ALAβ218, PROβ219, ASPβ158, GLUβ220, ASPβ217, TYRβ122, SERβ123, SERβ121, ASPβ251, ASPβ119, ASPβ126, ASPβ127, LYSβ181, HISβ192, HISβ255, GLUα123, HISβ244, HISβ274, HISα91, ASPα186, GLUβ174, HIS α113, and HISβ280. Calculated pK_a values from the gold list run were used to determine amino acid protonation states during simulations.

To simulate an effective acidic pH_e, all residues with $pK_a > 6.2$ were protonated. To simulate the normal physiological pH_e of ~7.4, all residues with $pK_a > 8.2$ were protonated. GLUβ400 and GLUβ409 were not protonated in spite of their elevated pK_a values; this is because these residues are close to the C-terminus of the simulation system and are thus artificially solvent exposed. A third simulation system designed to test the role of ASPβ127 had this residue protonated, in addition to all residues with $pK_a > 8.2$.

After protonation, the protein was solvated with Simple Point Charge water molecules in a box of dimensions 10.235 nm x 11.513 nm x 8.298 nm. Na^+ and Cl^- were added at a physiological concentration of 0.137 M to provide charge neutrality. After adding water molecules and ions, there were a total of ~93650 atoms in each simulation system (only polar hydrogen atoms were explicitly included). For each pH_e system, a two step steepest descents minimization of the X-ray diffraction structure was performed. In the first step, the integrin, RGD, and Mg^{2+} ions were held fixed and the maximum force in the system was reduced to less than 2000 kJ $mol^{-1}nm^{-1}$. In the second step, the full system was free to move and the maximum force in the system was reduced to less than 1500 kJ $mol^{-1}nm^{-1}$. After minimization, a 10 ps molecular dynamics simulation was performed with position restraints on the side chains of ARG_{RGD} and ASPα218, as suggested by Puklin-Faucher et al. [110]. Eight simulations of 10 ps duration were conducted for each pH_e, each with a different seed for random initialization of atomic velocities. The final frame at 10 ps was taken as input for further simulation, resulting in eight different input configurations for each pH_e. An MD simulation of 8 ns duration was performed for each input configuration. During MD simulations, ARG_{RGD} and ASPα218 position restrains were removed, and center of mass rotation and translation of the receptor were restrained. Simulations were performed under constant pressure and temperature, using periodic boundary conditions and Particle Mesh Ewald electrostatics with a short range interaction cutoff of 0.9 nm. Systems were considered to be equilibrated when the RMSD of the receptor, ligand, and ions with respect to the initial configuration reached a plateau (usually requiring 2 – 3 ns).

To quantify the headpiece opening that occurred during MD simulations, we calculated the y-component of the distance d between a portion of the β-propeller domain (residues α250-438) and a portion of the hybrid domain (residues β55-106 and β356-434). The centers of mass of these regions were used for the distance calculation, and d was calculated at every recorded frame (every 5 ps) of each MD trajectory.

To select configurations for SMD simulations, he equilibrated portion of each trajectory was used as input for clustering analysis. RMSD of binding cleft residues after least-squares fitting was used as the similarity measure for clustering. The binding cleft included the 3 Mg^{2+} ions in the β subunit as well as all integrin residues that have been reported to interact with the RGD ligand or with the ions[45, 46]. These residues were ASPα150, TYRα178, ALAα215, ASPα218, PHEα177, GLNα180, ARGβ216, ASNβ215, ALAβ218, PROβ219, ASPβ158, GLUβ220, ASPβ217, TYRβ122, SERβ123, SERβ121, ASPβ251, ASPβ119, ASPβ126, and ASPβ127. Clusters with 10+ members were chosen for further analysis. For each trajectory, the RMSD cutoff was chosen in order to have 5 – 8 clusters of this size. Cluster centroids were used as input configurations for SMD simulations. Seeds for random generation of initial atomic velocities were varied as noted.

The initial position of the force transducer (spring) in all SMD simulations coincided with the center of mass of the RGD ligand. The centers of mass of the α and β subunits were held fixed. The tensile loading direction was defined as the vector between the initial center of mass of these two fixed points and the center of mass of the RGD ligand. The transducer was defined by stiffness k = 2492 kJ $mol^{-1}nm^{-2}$ (4.14 N/m) with $\vec{v}$ = 0.2 – 2 m/s; this corresponds to F' = 0.828 – 8.28 N/s. The resulting trajectories were analyzed to extract the force exerted by the spring and the reaction coordinate of the ligand as functions of simulation time. The reaction coordinate χ is defined as the distance of the center of mass of the RGD ligand from its initial position, $\chi = [(x - x_0)^2 + (y - y_0)^2 + (z - z_0)^2]^{1/2}$. Forces were examined every 200 fs, and rupture force F_R was taken as the maximum force recorded during a particular trajectory, which was ultimately followed by dissociation of the complex.

For simulations comparing rupture forces at acidic and normal pH_e, initial configurations with ASP_{RGD} coordinated to only the LIMBS ion were excluded. Thus, the set of initial configurations at each pH_e included the MIDAS and MIDAS + LIMBS ion coordination states. Nineteen initial configurations (cluster centroids from the clustering procedure described above) were used for SMD simulations at each pH_e. Rupture forces were weighted according to the frequency of occurrence of each ion coordination state in the equilibration simulation trajectories to calculate mean F_R for each pH_e condition at each loading rate. Frequencies of occurrence for each ion coordination state were 56.25% MIDAS and 43.75% MIDAS + LIMBS for normal pH_e and 58.75% MIDAS and 41.25% MIDAS + LIMBS for acidic pH_e. Best fit lines for F_R vs. $\ln(F')$ were calculated with Microsoft Excel. Standard errors for the best fit slopes and intercepts were calculated using a bootstrapping sampling procedure [257]. For each pH_e, 10000 sets of F_R vs. $\ln(F')$ data were generated by randomly sampling with replacement from the original SMD-generated data set. For each data set, rupture forces were weighted using the frequencies given above in order to calculate the mean F_R at each F'. Best fit lines were calculated for each of these sets of mean F_R vs. F'. Thus, 10000 values of slope and intercept were generated for each pH_e. The standard deviation of these 10000 bootstrapped slopes and intercepts is equal to the standard error of the SMD-derived slopes and intercepts [257].

Equations 2.2 and 2.3 were used to calculate the distance between the bound state and energetic maximum x_b and the kinetic unbinding rate k_{off}. Propagation of error equations was used to calculate the standard errors in x_b and k_{off} from the standard errors in slope and intercept:

$$\sigma_{k_{off}}{}^2 = \sigma_m{}^2\left(\frac{\partial k_{off}}{\partial m}\right)^2 + \sigma_b{}^2\left(\frac{\partial k_{off}}{\partial b}\right)^2 \qquad \text{(Eq. 8.1)}$$

$$\sigma_{x_b}{}^2 = \sigma_m{}^2\left(\frac{\partial x_b}{\partial m}\right)^2 + \sigma_b{}^2\left(\frac{\partial x_b}{\partial b}\right)^2 \qquad \text{(Eq. 8.2)}$$

where $\sigma_{k_{off}}$ is the standard error in k_{off}, σ_{x_b} is the standard error in x_b, σ_m is the standard error in slope, and σ_b is the standard error in intercept.

8.3. Cell culture

$\alpha_v\beta_3$ CHO-B2 cells and CHO-B2 pCDNA cells were provided by Dr. Linda Griffith (Massachusetts Institute of Technology), as subcultures of cell lines developed by Dr. Jean Schwarzbauer (Princeton University) and Dr. Siobhan Corbett (University of Medicine and Dentistry of New Jersey), respectively. $\alpha_v\beta_3$ CHO-B2 cells have been engineered to express the integrin β_3 subunit; the parental cell line CHO-B2 does not bind RGD [182]. Cell culture media consisted of high-glucose bicarbonate-buffered DMEM containing L-glutamine and sodium pyruvate, supplemented with 10% fetal bovine serum, 1% antibiotics-antimyotics, and 1% non-essential amino acids. Media also included 500 μg/mL zeocin or 250 μg/mL G418 (geneticin) for $\alpha_v\beta_3$ CHO-B2 or CHO-B2 pCDNA cells, respectively. Cells were maintained in an incubator at 37°C with 5% CO_2. Cells were passaged at 70% confluency and were centrifuged at 800 rpm for 5 min after detachment. Cells passaged at ratios of 1:4, 1:10, or 1:20 reached 70% confluency after 1 day, 2 days, or 3 days, respectively. $\alpha_v\beta_3$ CHO-B2 cells were maintained for no more than 25 passages, as β_3 integrin expression can be lost with further passaging.

Bovine retinal microvascular endothelial cells (BRECs) were provided by Dr. Ira Herman (Tufts University). Cell culture media consisted of low-glucose bicarbonate-buffered DMEM containing L-glutamine and sodium pyruvate, supplemented with 10% bovine calf serum and 12.5 mM HEPES. Cells were maintained in an incubator at 37°C with 5% CO_2. Cells were passaged at 70 – 100% confluency at a ratio of 1:5 and were centrifuged at 800 rpm for 6 min after detachment. Cells were maintained for no more than 18 passages due to minimize senescence.

NIH-3T3 fibroblasts were purchased from the American Type Culture Collection (ATCC). Cell culture media consisted of high-glucose bicarbonate-buffered DMEM supplemented with 10% bovine calf serum. Cells were maintained in an incubator at 37°C with 5% CO_2. Cells were passaged at 70% confluency and centrifuged at 1200 rpm for 8 min after detachment. Cells passaged at a density of 4×10^3 cells/cm^2 reached 70% confluency after 3 days.

All cell types were passaged with the following procedure: First, cell media was aspirated and cells were rinsed with Ca^{2+}/Mg^{2+}-free PBS. PBS was aspirated and trypsin/EDTA was added (1 ml for cells in a P60 dish or T25 flask, 1.5 ml for cells in a T75 flask). Dishes/flasks were placed in a 37°C incubator until cells detached. After detachment, media (formulations given above for each cell type) was added at an equivalent volume to the trypsin/EDTA and cells were transferred to a centrifuge tube. Cells were centrifuged at the speeds and durations given above. Supernatent was aspirated and cells were resuspended in 1 ml media. Cells were then plated into tissue-culture treated dishes or flasks at the densities given above. Before plating cells, 5 ml media was added to P60 dishes and T25 flasks and 15 ml media was added to T75 flasks.

8.4. Flow cytometry

Flow cytometry experiments were performed with $\alpha_v\beta_3$ CHO-B2 cells, and CHO-B2 pCDNA cells were used as a negative control. WOW-1 Fab was used as a primary antibody to label activated $\alpha_v\beta_3$, and LM609 was used to label all conformations of $\alpha_v\beta_3$. Alexa 488 goat anti-mouse IgG (H + L) F(ab')$_2$ fragment was used as the secondary antibody.

The buffer used for all flow cytometry experiments consisted of 137 mM NaCl, 2.7 mM KCl, 3.3 mM NaH_2PO_4, 3.8 mM HEPES, 5.5 mM glucose, 1 mg/ml BSA, and 0.75 mM divalent cations ($CaCl_2$, $MgCl_2$, or $MnCl_2$, as noted). Buffer was adjusted to desired pH using 1 M HCl and NaOH. Experiments were conducted at pH 6.0, 6.5, 7.0, 7.4, and 8.0. Cells were prepared for flow cytometry analysis as follows: cells were washed with (Ca^{2+}, Mg^{2+}-free) PBS, and detached with trypsin/EDTA. Trypsin was diluted, and cells were centrifuged at 800 rpm for 5 min. Cells were resuspended in buffer at desired pH, and 10 μl of each cell type was removed for counting in a hemocytometer. Cells were then centrifuged and resuspended at desired pH at a concentration of 2.3566×10^6 cells/ml and incubated at room temperature for 20 min. All following steps were performed with pH 7.4 buffer. Cells were centrifuged and resuspended at 13.158 x 10^6 cells/ml or 5 x 10^6 cells/ml for WOW-1 Fab and LM609 experiments, respectively. 0.5 x 10^6 cells were incubated with 12 μl WOW-1 Fab or 2 μg LM609 for 30 min at room temperature or on ice, respectively. During antibody incubations, cells were agitated every 10 min. After incubation, 200 μl buffer was added and cells were centrifuged. Cells were then resuspended in 100 μl buffer, with 100 μl of secondary antibody solution (1:300 dilution in PBS). Cells were incubated in secondary antibody for 30 min on ice, and agitated every 10 min. After incubation, 200 μl of buffer was added and cells were centrifuged. Cells were resuspended in 0.5 ml buffer and analyzed on a BD FACSCalibur flow cytometer. All experiments were performed with triplicate samples, and at least two independent experiments were performed for each pH (pH 6.0, N = 2; pH 6.5, N = 2; pH 7.0, N = 3; pH 7.4, N = 6; pH 8.0, N = 2). For each experiment, the average $\alpha_v\beta_3$ CHO-B2 geometric mean fluorescence intensity (MFI) was normalized to the average CHO-B2 pCDNA geometric MFI. This quantity is referred to as the normalized geometric MFI.

8.5. AFM-enabled molecular force spectroscopy

All AFM force spectroscopy measurements were performed on an MFP-3D (Asylum Research, Inc.) system using Olympus TR400PB gold-coated silicon nitride cantilevers, with spring constant $k \sim 25$ pN/nm. Cantilever spring constant varied by approximately +/- 10% from this value. Cantilevers were cleaned in piranha solution (70% sulfuric acid, 30% hydrogen peroxide) and then rinsed thoroughly with 18 MΩ Millipore water. Rinses in following steps were performed in PBS + 1 mM EDTA. To conjugate a polyethylene glycol (PEG) linker to the cantilever surface, a 1 mM solution of SH-PEG-NH_2 (3.4 kDa) in PBS-EDTA was allowed to react with cantilevers for one hour at room temperature. Cantilevers were rinsed and then allowed to react with a solution of Sulfo-LC-SPDP cross-linker for 30 min at room temperature. Solution was prepared by dissolving Sulfo-LC-SPDP in ultrapure water at 20 mM, and diluting this solution 1:40 in PBS-EDTA. Cantilevers were rinsed and then incubated in a 1 mg/ml solution of GRGDSPC peptide overnight at room temperature. Cantilevers were rinsed thoroughly once again to remove excess peptide before use. Functionalization was confirmed using fluorescent GRGDSPC peptides.

Experiments were performed at room temperature in buffer containing 137 mM NaCl, 2.7 mM Kcl, 3.3 mM NaH_2PO_4, 3.8 mM HEPES, and 1 mM $MgCl_2$. Buffer was adjusted to pH 7.4 or pH 6.0 using 1 M HCl and NaOH. Experiments were conducted on $\alpha_v\beta_3$ CHO-B2 cells adhered to 60 mm-diameter tissue-culture treated polystyrene Petri dishes (Falcon). Cells were incubated at room temperature for 20 – 30 min before measurements were taken. In experiments with LIBS-6 and LM609, antibody was added at 25 μg/ml or 20 μg/ml respectively, and allowed to react for 30 min at room temperature. Three independent experiments comparing pH conditions were performed, with each replicate experiment at each pH including 200 spectra on each of 5 – 10 cells. For each cell, 200 force cycles were conducted in a 10 x 20 grid on a 2 x 2 μm area. For each force cycle, the AFM cantilever was positioned above a cell away from the nucleus. Cantilevers were moved toward the cell at a velocity v = 5 μm/s until a trigger force of 150 pN was reached. Cantilevers were then held on the cell surface for 0.1 s before retraction at 5 μm/s. All unbinding measurements were conducted at the same applied loading rate. Cantilevers were held above the cell surface for 1 s to allow cells to recover between measurements. Unbinding events were detected as jumps in the retraction portion of the force-displacement data.

Output force-displacement (F-d) data were analyzed with a customized Matlab script. For every F-d response exhibiting a visible unbinding event (jump in force during retraction), rupture force F_R was calculated as the difference between the average force following rupture and the minimum point at rupture. Effective loading rate F' was calculated as the product of the slope immediately before rupture (k_{eff}) and the cantilever velocity v. Unbinding events with $F_R > 50$ pN and $F' > 2000$ pN/s were taken to be specific $\alpha_v\beta_3$-RGD interactions. Single-cell specific binding frequency f_b was calculated as the number of specific unbinding events on a given cell normalized to the total number of unbinding events observed on that cell. Single-cell relative specific binding frequency $f_{b,rel}$ was calculated as the single-cell f_b normalized to the average f_b value at pH 7.4. Mean f_b and $f_{b,rel}$ are averages taken over several cells at each condition.

8.6. Kymography

Unless otherwise noted, media for kymography experiments consisted of high-glucose bicarbonate-buffered DMEM containing L-glutamine and sodium pyruvate, supplemented with 1% antibiotics-antimyotics, 1% non-essential amino acids, and 500 μg/ml zeocin. Media pH was adjusted using 1 M HCl or NaOH. Glass-bottom P60 dishes (MatTek) were coated with 30 μg/ml fibronectin in PBS for 1 hr at room temperature. Dishes were then rinsed twice with PBS. $\alpha_v\beta_3$ CHO-B2 cells were plated on dishes in serum-free media and allowed to adhere for 2 – 3 hr in a 37°C incubator with 5% CO_2 before media was changed to bicarbonate-free serum-free media at pH 6.5 or 7.4. Cells were imaged in phase contrast on an Olympus IX51 inverted microscope at 40x magnification in an incubator at 37°C. Three independent experiments comparing pH 7.4 and pH 6.5 were conducted. For each experiment, approximately 10 – 20 cells were imaged and at least 100 individual protrusion events were analyzed for each condition. Images were collected every 5 s for a duration of 25 min. Each kymograph was produced in Metamorph by drawing a one-pixel-wide line perpendicular to the cell membrane at an active membrane region. The images along this line at all timepoints were then sequentially compiled into a single image, illustrating the membrane dynamics at that specific location on the cell. For each visible protrusion event on a kymograph, a straight line was drawn from the beginning of the event to its peak, or to the beginning of a plateau. Events with a height of less than 4 pixels were neglected. The slope of this line represents the protrusion velocity. Protrusion lifetime was quantified as the x-axis projection of this line, with the addition of plateau duration, if applicable. For experiments with NHE1 blocking, EIPA was added at a concentration of 50 μM, and kymography experiments were conducted as described above for cells that were incubated with EIPA for 2 – 4 hr.

8.7. Measurement and manipulation of pH_i

The fluorophore BCECF (2′,7′ - bis - (2 - carboxyethyl) - 5 - (and - 6) - carboxyfluorescein) was used for pH_i measurements. The acetoxymethyl ester form of the dye (BCECF-AM) is nonfluorescent and membrane permeable. Once inside the cell, BCECF-

AM is cleaved by intracellular esterases to fluorescent BCECF. BCECF has both a pH-sensitive excitation wavelength (~495 nm) and a pH-insensitive excitation wavelength (~440 nm), with an emission wavelength of ~535 nm. The pH-insensitive wavelength allows normalization for factors such as the amount of dye loaded into each cell, and the ratio of 495 nm/440 nm fluorescence intensities is approximately linear with intracellular pH. The ionophore nigericin allows rapid equilibration of intra- and extracellular pH and can be used for dye calibration [29, 35, 36, 190, 191].

Buffer for loading BCECF-AM into cells consisted of 135 mM NaCl, 4 mM KCl, 1 mM $MgCl_2$, 1 mM $CaCl_2$, 10 mM Hepes, and 10 mM glucose. Loading buffer was adjusted to pH 7.4 using 1 M HCl and NaOH. Buffer for dye calibration consisted of 140 mM KCl, 1 mM $MgCl_2$, 1 mM $CaCl_2$, 10 mM Hepes, and 10 mM glucose. Calibration buffer was adjusted to pH 6.0, 6.5, 7.0, and 7.5 using 1 M HCl and KOH (calibration with nigericin requires high [K^+] and low [Na^+]). 5 mM BCECF-AM stock solution was made by dissolving BCECF-AM in anhydrous DMSO. 10 mM nigericin stock solution was made by dissolving nigericin in ethanol.

To load dye into cells, $\alpha_v\beta_3$ CHO-B2 cells were incubated in warm loading buffer with 1 μM BCECF-AM (1:5000 from stock) for 30 min at 37°C (without 5% CO_2). This concentration was optimized to give bright cell fluorescence with low exposure times (50-100 ms), and was not toxic to cells. Cells were then rinsed three times with warm loading buffer (no BCECF-AM). After rinses, dishes were filled with warm loading buffer at the desired pH for imaging.

Cells were first imaged with ~495 nm excitation and ~535 nm emission wavelengths (FITC excitation/emission filter), and then imaged with ~440 nm excitation and ~535 emission wavelengths (CFP excitation filter and FITC emission filter). Filters were selected to minimize cross-excitation. Cells were imaged on an Olympus IX81 inverted microscope at 40x magnification with a 50-100 ms exposure time. Exposure time was chosen to give bright fluorescence without exceeding the light intensity limit of the camera.

For calibration, loading buffer was removed and dishes were filled with warm calibration buffer with 10 μM nigericin (1:1000 from stock) at pH 7.0. Cells were imaged as described above after 3 min of incubation with nigericin. This was repeated with calibration buffer with 10 μM nigericin at pH 6.0, 7.5, and 6.5. High and low pH calibration solutions were alternated to ensure that the changes in cell fluorescence were not due to a systematic increase or decrease.

Image analysis was done using Image J. Background fluorescence was first subtracted from each image. Cells were traced, and the mean intensity value over the cell area for each fluorescence channel was measured. For each cell, the 495 nm/440 nm intensity ratio was calculated. Calibration images were analyzed in the same way, and intensity ratio data vs. pH were fit to a straight line. This calibration curve was used to convert intensity ratio to pH_i for other images.

The NHE1 inhibitor EIPA (5-(N-Ethyl-N-isopropyl)amiloride) was used to modulate intracellular pH. EIPA blocks extrusion of H^+ from the NHE1 ion exchanger, which causes accumulation of intracellular H^+ and consequent lowering of pH_i [29, 36, 192-195]. 25 mM EIPA stock solution was made by dissolving EIPA in DMSO. Cells were incubated with 25 – 50 μM EIPA in culture media for 1.5 – 24 hr, and then BCECF-AM loading was performed as described above, but with the addition of EIPA in the loading buffer (included during loading, rinsing, and imaging). Intracellular pH was then measured as described above. Kymography experiments were conducted for cells that had been incubated with 50 μM EIPA for 2 – 4 hr, which corresponded to pH_i 6.7 – 6.2.

8.8. GFP-vinculin transfection and AIAC imaging

Unless otherwise noted, $\alpha_v\beta_3$ CHO-B2 cell media for AIAC experiments consisted of high-glucose bicarbonate-buffered DMEM containing L-glutamine and sodium pyruvate, supplemented with 10% fetal bovine serum, 1% antibiotics-antimyotics, 1% non-essential amino acids, and 500 μg/mL zeocin. Media pH was adjusted using 1 M HCl or NaOH.

GFP-vinculin plasmid with ampicillin resistance was obtained from Dr. Benjamin Geiger (Weizmann Institute of Science), and was blotted onto filter paper before shipping. To extract DNA from filter paper, the portion of paper containing plasmid was cut out, placed in a small Eppendorf tube, and submerged in ~40 μl Tris/EDTA. The tube was then gently vortexed to aid extraction of DNA. Filter paper was soaked in Tris/EDTA for ~10 min at 50°C, and vortexed occasionally during this time.

To transform bacteria, ~5 μl of Tris/EDTA solution (now containing DNA) was removed from the tube and incubated with competent XL-10 *E. coli* cells. Cells were obtained from Dr. Ron Weiss (Massachusetts Institute of Technology). The tube containing cells was gently tapped to mix cells with solution. Cells were incubated on ice for 30 min, and then heat shocked at 42°C for 30 s. 400 μl of Super Optimal Broth with added glucose was added, and cells were shaken at 37°C for 40 – 60 min. Cells were then plated on LB-agar with ampicillin and grown for ~15 hr at 37°C. Colonies were then cultured in growth medium with 1:500 ampicillin overnight to amplify DNA. GFP-vinculin plasmid DNA was purified using the Qiagen Plasmid Midi Kit, following the manufacturer's instructions. DNA concentration after purification was ~500 ng/μl.

For GFP-vinculin transfection, $\alpha_v\beta_3$ CHO-B2 cells were plated on tissue-culture treated 6-well plates (Falcon) in 2 ml antibiotic-free serum-free media per well. For each well, 1.5 μg (3 μl) plasmid DNA was diluted in 500 μl Opti-MEM media and mixed thoroughly. Plus Reagent was gently mixed and 1.5 μl was added to the diluted DNA. Solution was mixed gently and incubated for 5 min at room temperature. Next, Lipofectamine was gently mixed and 2 μl was added to the diluted DNA. Solution was mixed thoroughly and incubated for 30 min at room temperature. DNA solution was added dropwise to the each well containing cells, and the plate was gently rocked back and forth to mix solution with cell media. Cells were incubated for 18 – 24 hr in a 37°C incubator with 5% CO_2, and then media was changed to complete growth media. Before imaging, glass bottom 6-well or 12-well plates (MatTek) were coated with 30 μg/ml fibronectin in PBS for 1 hr at room temperature. Dishes were then rinsed twice with PBS. Transfected cells were plated in wells in serum-free media and allowed to adhere for 2 – 3 hr in a 37°C incubator with 5% CO_2. Media was then changed to bicarbonate-free serum-free media at pH 7.4 or 6.5. Cells were imaged on an Olympus IX51 inverted microscope in an incubator at 37°C using a 60x oil immersion objective and a GFP filter cube with 1000 ms exposure time. Three independent experiments were conducted for each duration of exposure to acidic

pH_e, and at least 35 cells were imaged for each condition within each experiment. Data shown in figures are from a single experiment.

Images were analyzed using ImageJ. For detection of AIACs, background was subtracted from images using the rolling ball method (Subtract Background under the Process menu). Image pixel values were then thresholded such that AIACS were displayed in black and the background was displayed in white (Adjust Threshold under the Image menu). AIACs were then detected and AIAC areas were measured using the Analyze Particles function under the Analyze menu.

8.9. Cell spreading, morphology, and migration measurements

Unless otherwise noted, media for cellular-scale experiments consisted of high-glucose bicarbonate-buffered DMEM containing L-glutamine and sodium pyruvate, supplemented with 1% antibiotics-antimyotics, and 1% non-essential amino acids. 500 μg/mL zeocin was added to media for experiments with $\alpha_v\beta_3$ CHO-B2 cells and 250 μg/ml G418 (geneticin) was added to media for experiments with CHO-B2 pCDNA cells. Media pH was adjusted using 1 M HCl or NaOH.

8.9.1. Cell spreading with cyclic pH_e changes

For pH oscillation experiment, 60 mm-diameter glass-bottom Petri dishes (MatTek) were coated with 30 μg/ml fibronectin in PBS for 1 hr at room temperature. Dishes were then rinsed twice with PBS. $\alpha_v\beta_3$ CHO-B2 cells were plated on dishes in serum-free media at a density of approximately 6000 cells/cm^2 and allowed to adhere for 2 – 3 hr in a 37°C incubator with 5% CO_2. Media was then changed to pH 6.0 and refreshed to pH 6.0 every hour; between media changes, pH increased to ~7.2. Cells were imaged in phase contrast every 5 min for 8 hr on an Olympus IX51 inverted microscope in an incubator at 37°C with 5% CO_2. Cells that divided or touched other cells were excluded from analysis. Projected cell area was measured using ImageJ. For cell tracking, background was subtracted from all images in a given timelapse stack using the rolling ball method (Subtract Background under the Process menu). Image pixel values were then thresholded such that cells were displayed in black and the background was displayed in white (Adjust Threshold under the Image menu). Cell areas were measured using the Analyze Particles function under the Analyze menu. An independent experiment with 10 μg/ml fibronectin coating showed similar cell area oscillations.

8.9.2. Cell spreading from the detached state

No. 1 glass coverslips or glass-bottom P60 dishes (MatTek) were coated with 15 μg/ml fibronectin in PBS for 1 hr at room temperature. Coverslips or dishes were then rinsed twice with PBS. $\alpha_v\beta_3$ CHO-B2 cells were plated on coverslips or dishes in serum-free media with an initial pH of 6.0 or 7.4 and allowed to adhere for 30 min in an incubator at 37°C with 5% CO_2 before imaging in phase contrast on an Olympus IX51 inverted microscope. Media initially set to pH 6.0 remained below pH 7.0 for the duration of the incubation. Projected cell area was measured using ImageJ. Two independent experiments were performed. In each experiment, approximately 40 cells were measured for each pH.

Independent experiments showed consistent results, and data presented are from a single experiment.

8.9.3. Cell spreading and morphology over long timescales

50 mm-diameter Petri dishes (not tissue-culture treated) with tight-fitting lids (Pall Life Sciences) were coated with 0.1 – 30 μg/ml fibronectin in PBS for 1 hr at room temperature. Dishes were then rinsed twice with PBS. $\alpha_v\beta_3$ CHO-B2 cells were plated on dishes in serum-free media at a density of approximately 6000 cells/cm^2 and allowed to adhere for 2 – 3 hr in a 37°C incubator with 5% CO_2 before media was changed to pH 6.5 or 7.4. After media pH change, Petri dish lids were tightened to eliminate air exchange and consequent pH drift, and cells were incubated at 37°C. Eight hr after the media change, cells were imaged in phase contrast on an Olympus IX51 inverted microscope. For experiments with $\alpha_v\beta_3$ blocking or activation, dishes were coated with 10 μg/ml fibronectin as described above. $\alpha_v\beta_3$ CHO-B2 cells or CHO-B2 pCDNA cells were plated on dishes in serum-free media at a density of approximately 6000 cells/cm^2 and allowed to adhere for 2 – 3 hr in a 37°C incubator with 5% CO_2 before media was changed to bicarbonate-free serum-free media at pH 6.5 or 7.4. $MnCl_2$ (1 mM) or soluble GRGDSPC peptide (200 μg/ml) was also added during this media exchange for some sample conditions. Cells were incubated in 37°C and imaged as described above. Images were analyzed with ImageJ to measure projected area A and circularity C ($C = 4\pi A/P^2$, where P is the cell perimeter). Cells touching other cells were excluded from analysis. At least 50 cells were analyzed for each experimental condition.

8.9.4. Cell migration

For migration experiments with cells on polystyrene, 50 mm-diameter Petri dishes (not tissue-culture treated) with tight-fitting lids (Pall Life Sciences) were coated with 0.01 – 200 μg/ml fibronectin in PBS for 1 hr at room temperature. Dishes were then rinsed twice with PBS. $\alpha_v\beta_3$ CHO-B2 cells were plated on dishes in serum-free media at a density of approximately 6000 cells/cm^2 and allowed to adhere for 2 – 3 hr in a 37°C incubator with 5% CO_2 before media was changed to pH 6.5 or 7.4. After media pH change, Petri dish lids were tightened to eliminate air exchange and consequent pH drift. Cells were imaged on an Olympus IX51 inverted microscope in phase contrast every 5 min for 8 hr in an incubator at 37°C. 10 – 15 unique fields were imaged for each experiment. For migration experiments with cells on glass, 60 mm-diameter glass-bottom dishes (MatTek) were coated with 10 – 60 μg/ml fibronectin in PBS for 1 hr at room temperature. Experiments were conducted as described for cells on polystyrene, but cells were imaged in the presence of 5% CO_2.

For all migration experiments, images were analyzed using ImageJ, and cells that divided or touched other cells were excluded from analysis. Cell tracking was performed as described in Section 8.9.1, but cell centroids rather than projected cell areas were measured using the Analyze Particles function. Mean-squared displacements of cell centroids as a function of time ($\langle d^2(t) \rangle$) were calculated with a customized Matlab script using the method of non-overlapping intervals [212, 258]. The root mean-squared displacement for the shortest interval was divided by the interval time (5 min) to obtain cell speed S. Mean-squared displacements as a function of time were fit to a persistent random walk model: $<d^2(t)> = 2S^2P[t - P(1 - e^{-t/P})]$ [212]. Cells with a goodness-of-fit $R^2 < 0.5$ were not included in the calculation of mean cell speed. At least 40 cells with $R^2 > 0.5$ were analyzed for each condition.

8.10. Cell migration in an extracellular pH gradient

Media formulations for pH_e gradient migration experiments are the same as those given in Section 8.3, without the addition of serum. Media contained bicarbonate buffer unless otherwise noted. Media pH was adjusted using 1 M HCl or NaOH.

8.10.1. Dunn chamber setup and gradient imaging

For gradient imaging, BCECF (free acid) was added to bicarbonate-free serum-free $\alpha_v\beta_3$ CHO-B2 cell media at a concentration of 10 μM, and the Dunn chamber was set up according to the manufacturer's instructions. Briefly, both wells were filled with bicarbonate-free serum-free media at pH 7.5, and a coverslip (with or without cells) was placed upside down over the wells, leaving a thin slit open at the outer well. The sides of the coverslip, with the exception of the slit at the outer well, were sealed to the chamber slide using a melted wax mixture consisting of 1:1:1 paraffin:beeswax:Vaseline, and the outer well was drained with a Kimwipe held at the open slit. The outer well was then filled through the slit with bicarbonate-free serum-free pH 6.0 media using a syringe. Finally, the slit was sealed with melted wax. For each dye calibration measurement, both wells were filled with a solution of a single pH and sealed with a coverslip.

The bridge region was imaged at 4x magnification at excitation wavelengths of ~440 nm and ~495 nm, both with an emission wavelength of ~535 nm. The 495 nm wavelength is pH sensitive and the 440 nm wavelength is pH insensitive. The ratio of the 495/440 nm light intensities is linear with pH and thus serves as a pH indicator. To assess gradient stability, images were taken every hour over a duration of 8 hr for chambers at room temperature and at 37°C. Two independent experiments were performed at each temperature. Gradient images were analyzed with ImageJ. The profile of light intensity ratio over the bridge was measured, and slope was calculated by a linear fit to the data. Data points near the edges of the bridge were excluded due to artifacts in light intensity, likely resulting from variable depth at these edge regions.

8.10.2. Cell migration measurements and image analysis

No. 2 coverslips were coated with 30 μg/ml fibronectin in PBS for 1 hr at room temperature, then rinsed twice with PBS. Cells were plated on coverslips in serum-free media and allowed to adhere for 2 – 3 hr in a 37°C incubator with 5% CO_2 before being placed in the Dunn chamber. Media loaded into the Dunn chamber wells consisted of bicarbonate-free DMEM, supplemented as described in Section 8.3 for each cell type, but with no serum. Cells were imaged in phase contrast at 4x magnification every 5 min for 8 hr in an incubator at 37°C. 6 – 10 unique fields were imaged for each experiment, and 2 – 3 independent experiments were conducted for each cell type. For NIH-3T3 migration experiments with integrin $\alpha_5\beta_1$ blocked, the blocking antibody BMB5 was added to the media loaded into the Dunn chamber wells at 10 μg/ml, and cells were incubated in the chamber at 37°C for 30 min prior to imaging.

For each cell over the bridge region, images were rotated such that the gradient was oriented vertically, with the acidic end at the top of the image. For cells over the center post, images were rotated in a similar manner, such that a line drawn from the middle of the post through the cell was oriented vertically in the images, with the outside edge of the post at the top of the image. Rotation for all images in the timelapse stack for each cell was based on the cell position at time 0. The initial position of each cell was set to the origin at (0,0) before cell tracking. Cell centroids were tracked using ImageJ using the procedure described in Section 8.9.4, and cells that divided, touched other cells, or migrated less than 10 μm from their initial location were excluded from further analysis. After excluding these cells, a total of at least 120 cells in the gradient region were analyzed for each cell type. Mean-squared displacements as a function of time ($<d^2(t)>$) were calculated using the method of non-overlapping intervals [212, 258]. The root mean-squared displacement for the shortest interval was divided by the interval time (5 min) to obtain cell speed S. For each cell type, data from 2-3 independent experiments were pooled to obtain percentages and averages shown in figures.

8.10.3. Statistical analysis

To compare cell population percentages with a null hypothesis of 50%, the z-statistic was calculated as: $z = \frac{p-p_0}{\sqrt{p_0(1-p_0)/n}}$, where p is the observed fraction, p_0 is the expected fraction of 0.5, and n is the number of cells measured [165]. The two-tailed P-value was then calculated from a table of standard normal curve areas.

To compare mean cell x- and y- coordinates with a null hypothesis of zero, the z-statistic was calculated as: $z = \frac{\hat{x}-\mu_0}{s/\sqrt{n}}$, where $\hat{x}$ is the mean measured coordinate, μ_0 is the expected value of 0, s is the standard deviation of cell position, and n is the number of cells measured [165]. The two-tailed p value was then calculated from a table of standard normal curve areas.

To compare cell migration speeds, p values were calculated with a Bonferonni post-test following one-way ANOVA. To assess dependence of population percentages on cell position, the Marascuilo procedure for multiple comparisons was applied using the program at http://www.stattools.net/Multiprop_Pgm.php.

All error bars shown in figures represent 95% confidence intervals. To construct confidence intervals for percentage data, a bootstrapping sampling method was used [257]. Briefly, for each set of cell positions at the 8-hr timepoint, 10000 bootstrapped data sets were created by randomly sampling the original data set with replacement. The population percentage that moved in the direction of interest was calculated for each bootstrapped data set. The 95% confidence interval was taken as the range encompassing the middle 95% of the values calculated for the 10000 bootstrapped data sets.

8.11. Migration model

As described in Section 5.4.3, the original DiMilla et al. cell migration model [95] has two parts. In the first part, receptor diffusion, trafficking, and binding are considered, and the steady state receptor distribution under zero contractile force is determined. In the second part, contractile force is introduced and cell displacement is determined. To extend the migration model of DiMilla et al. to assess the effects of $\mathrm{pH_e}$-dependent integrin activation, we introduced two different integrin receptor states: activated and inactivated. Both integrin states were allowed to diffuse, undergo endocytosis, and be reinserted into the cell membrane [56]. However, because activated integrins have a much higher binding rate than inactivated integrins [80], only the activated state was allowed to bind ligand. Although the original DiMilla et al. model allows for differences in bond dissociation rates between the lamellipod and uropod, we kept the dissociation rate constant at all locations within the cell. Thus, the only source of asymmetry is preferential insertion of integrins into the leading edge membrane.

In our model, integrins can switch between the two activation states, with rate constants estimated from rates of large-scale conformational changes for other proteins (10 – 100 $\mathrm{s^{-1}}$) [131-134] (Figure 5.6A). Values for the activation rate k_a were chosen to produce a linearly increasing percentage of activated receptors with decreasing $\mathrm{pH_e}$. The inactivation rate k_i was assumed to be constant for these calculations. To model migration in an extracellular pH gradient, k_a was assumed to be position-dependent.

Table 8.2 lists our modified equations and the original DiMilla et al. equation numbers for the first part of the migration model. In model equations, the density of free inactivated receptors on the dorsal (top) and ventral (bottom) surfaces of the cell are denoted as n_{ri}^{d} and n_{ri}^{v}, respectively. The density of free activated receptors on the dorsal and ventral surfaces are denoted as n_{ra}^{d} and n_{ra}^{v}, respectively. The density of bound receptors on the ventral surfaces is denoted as $n_b$and the ligand density is denoted as n_s. Bonds form at a rate k_f and dissociate at an intrinsic rate k_{ro}. Free receptors diffuse at a rate D_r and undergo endocytosis at a rate k_e. Receptors are reinserted over a fraction of the cell length λ from the leading edge, and v is the overall forward cell velocity. The cell has length L and width W.

Table 8.3 lists our modified equations and the original DiMilla et al. equation numbers for the second part of the migration model. In model equations, the number of bonds in the uropod and lamellipod are denoted as R_{bu} and R_{bl}, respectively. The total number of receptors on the ventral sides of the uropod and lamellipod are denoted as R_{Tu} and R_{Tl}, respectively. The spring constant for the bond-cytoskeletal connections is denoted as k_c, the bond spring constant as k_{sp}, Boltzmann's constant as k_b, and temperature as T. The displacement of the nodes connecting the uropod and lamellipod to the cell body are denoted as u_1 and u_1, respectively. Finally, ψ is the ratio of intrinsic bond dissociation rates between the front and back of the cell (set to 1 in our model), $\beta = 1 + \frac{k_i}{k_a}$, and $\kappa = \frac{k_f n_s}{k_{ro}}$.

DiMilla et al. equation number	Modified equation
Eq. 3a for inactivated receptors	$\frac{\partial n_{ri}^{d}}{\partial t} = D_r \nabla^2 n_{ri}^{d} - k_e n_{ri}^{d} + k_i n_a^{d} - k_a n_i^{d} + \frac{k_e}{2\lambda LW} \int_0^L \int_{-W/2}^{W/2} (n_{ri}^{d} + n_{ri}^{v})\, dy\, dx$ (Eq. 8.1)
Eq. 4a for inactivated receptors	$\frac{\partial n_{ri}^{v}}{\partial t} = D_r \nabla^2 n_{ri}^{v} - k_e n_{ri}^{v} + k_i n_a^{v} - k_a n_i^{v} + \frac{k_e}{2\lambda LW} \int_0^L \int_{-W/2}^{W/2} (n_{ri}^{d} + n_{ri}^{v})\, dy\, dx$ (Eq. 8.2)
Eq. 3a for activated receptors	$\frac{\partial n_{ra}^{d}}{\partial t} = D_r \nabla^2 n_{ra}^{d} - k_e n_{ra}^{d} + k_a n_i^{d} - k_i n_a^{d} + \frac{k_e}{2\lambda LW} \int_0^L \int_{-W/2}^{W/2} (n_{ri}^{d} + n_{ri}^{v})\, dy\, dx$ (Eq. 8.3)
Eq. 4a for activated receptors	$\frac{\partial n_{ra}^{v}}{\partial t} = D_r \nabla^2 n_{ra}^{v} - k_f n_s n_{ra}^{v} + k_{ro} n_b - k_e n_{ra}^{v} + k_a n_i^{v} - k_i n_a^{v} + \frac{k_e}{2\lambda LW} \int_0^L \int_{-W/2}^{W/2} (n_{ra}^{d} + n_{ra}^{v})\, dy\, dx$ (Eq. 8.4)
Eq. 3b for inactivated receptors	$\frac{\partial n_{ri}^{d}}{\partial t} = D_r \nabla^2 n_{ri}^{d} - k_e n_{ri}^{d} + k_i n_a^{d} - k_a n_i^{d}$ (Eq. 8.5)
Eq. 4b for inactivated receptors	$\frac{\partial n_{ri}^{v}}{\partial t} = D_r \nabla^2 n_{ri}^{v} - k_e n_{ri}^{v} + k_i n_a^{v} - k_a n_i^{v}$ (Eq. 8.6)
Eq. 3b for activated receptors	$\frac{\partial n_{ra}^{d}}{\partial t} = D_r \nabla^2 n_{ra}^{d} - k_e n_{ra}^{d} + k_a n_i^{d} - k_i n_a^{d}$ (Eq. 8.7)
Eq. 4b for activated receptors	$\frac{\partial n_{ra}^{v}}{\partial t} = D_r \nabla^2 n_{ra}^{v} - k_f n_s n_{ra}^{v} + k_{ro} n_b - k_e n_{ra}^{v} + k_a n_i^{v} - k_i n_a^{v}$ (Eq. 8.8)
Eq. 5	$\frac{\partial n_b}{\partial t} = k_f n_s n_{ra}^{v} - k_{ro} n_b + v \frac{\partial n_b}{\partial x}$ (Eq. 8.9)

Table 8.2 Modified equations for the first part of the cell migration model.

Model equations were nondimensionalized as described in Ref. [95] and were solved in Matlab. Parameter values used for data generation with our migration model are given in Table 8.4. Whenever possible, experimentally measured values for integrin $\alpha_v\beta_3$ and CHO cells were used. Parameters for which measured values were not available were set within the range used in the original DiMilla et al. model. Parameter values were chosen such that model predictions fit our experimental data for $\alpha_v\beta_3$ CHO-B2 cell migration speed as a function of fibronectin coating concentration (Figure 5.5) and extracellular pH (Figure 6.4). For modeling migration in the extracellular pH gradient, adhesiveness κ was set at 100.

DiMilla et al. equation number	Modified equation	
Eq. 15a	$R_{bu}\{u_1\} = \dfrac{R_{Tu}}{1 + \beta\psi^{-1}\kappa^{-1}\exp\left(\dfrac{k_c^2 u_1^2}{k_{sp}k_bT}\right)}$	(Eq. 8.10)
Eq. 15b	$R_{bl}\{u_5\} = \dfrac{R_{Tl}}{1 + \beta\kappa^{-1}\exp\left(\dfrac{k_c^2 u_5^2}{k_{sp}k_bT}\right)}$	(Eq. 8.11)
Eq. 17a	$R_{Tu} = \displaystyle\int_{5L/6}^{L}\int_{-W/2}^{W/2}(n_{ri}^{v} + n_{ra}^{v} + n_b)\,dy\,dx$	(Eq. 8.12)
Eq. 17b	$R_{Tl} = \displaystyle\int_{0}^{L/6}\int_{-W/2}^{W/2}(n_{ri}^{v} + n_{ra}^{v} + n_b)\,dy\,dx$	(Eq. 8.13)

Table 8.3 Modified equations for the second part of the cell migration model.

Parameter	Description	Value
T	Temperature	310 K
D_r	Free receptor diffusivity	3 x 10^{-14} m^2/s (from Ref. [259])
k_e	Endocytosis rate	5.5 x 10^{-4} s^{-1} (from Ref. [260])
R_T	Total # receptors on cell	1 x 10^{4} (from Ref. [104])
λ	Fraction of leading edge for receptor insertion	0.1
g_E	Dimensionless strength of connection between bond and cytoskeleton	4 x 10^{-3}
E	Cell elasticity	462.5 N/m^2 (from Ref. [261])
u	Viscosity of cell	2.44 kg/ms (from Ref. [261])
F_c	Force generated in each cell node	3.4 x 10^{-9} N
g_S	Dimensionless intrinsic pseudopod stiffness	0.02
k_sp	Bond spring constant	0.1 N/m^2
k_ro	Unstressed bond dissociation rate	1 x 10^{-3} s^{-1}
L	Length of cell	50 x 10^{-6} m (from experiments)
W	Width of cell	20 x 10^{-6} m (from experiments)
x_grids	# grids in length direction	24
y_grids	# grids in width direction	12
κ	Dimensionless adhesiveness	varied between 10^{-3} – 10^{3}
t_c	Contraction time	300 s
t_m	Movement cycle time	600 s
ψ	Lamellipod to uropod bond dissociation ratio	1
k_i	Integrin inactivation rate	10 s^{-1}
k_a	Integrin activation rate	linear function of pH$_\mathrm{e}$, with k_a = 2.5 s^{-1} at pH$_\mathrm{e}$ 7.4 and k_a = 10 s^{-1} at pH$_\mathrm{e}$ 6.5.

Table 8.4 Parameters used for data generation with the modified DiMilla et al. cell migration model.

8.12. Statistical analysis

Unless otherwise noted, p values for comparison of two conditions were calculated with an unpaired t-test. For comparison of three or more conditions, p values were calculated with a Bonferroni post-test following one-way ANOVA. Graphpad Prism was used for statistical analysis.

References

1. Helmlinger, G., et al., *Interstitial pH and pO2 gradients in solid tumors in vivo: High-resolution measurements reveal a lack of correlation.* Nat Med, 1997. **3**(2): p. 177-182.
2. Dewhirst, M.W., et al., *The relationship between the tumor physiologic microenvironment and angiogenesis.* Hematology/Oncology Clinics of North America, 2004. **18**(5): p. 973-990.
3. Warburg, O., *On the origin of cancer cells.* Science, 1956. **123**(3191): p. 309-14.
4. Galarraga, J., et al., *Glucose metabolism in human gliomas: Correspondence of in situ and in vitro metabolic rates and altered energy metabolism.* Metabolic Brain Disease, 1986. **1**(4): p. 279-291.
5. Bustamante, E. and P.L. Pedersen, *High aerobic glycolysis of rat hepatoma cells in culture: Role of mitochondrial hexokinase.* Proceedings of the National Academy of Sciences, 1977. **74**(9): p. 3735-3739.
6. Gatenby, R.A., et al., *Acid-Mediated Tumor Invasion: a Multidisciplinary Study.* Cancer Res, 2006. **66**(10): p. 5216-5223.
7. McLean, L.A., et al., *Malignant gliomas display altered pH regulation by NHE1 compared with nontransformed astrocytes.* Am J Physiol Cell Physiol, 2000. **278**(4): p. C676-688.
8. Reshkin, S.J., et al., *Phosphoinositide 3-Kinase Is Involved in the Tumor-specific Activation of Human Breast Cancer Cell Na+/H+ Exchange, Motility, and Invasion Induced by Serum Deprivation.* J. Biol. Chem., 2000. **275**(8): p. 5361-5369.
9. Reshkin, S.J., et al., *Na+/H+ exchanger-dependent intracellular alkalinization is an early event in malignant transformation and plays an essential role in the development of subsequent transformation-associated phenotypes.* FASEB J, 2000. **14**(14): p. 2185-97.
10. Kaplan, D.L. and W.F. Boron, *Long-term expression of c-H-ras stimulates Na-H and Na(+)-dependent Cl-HCO3 exchange in NIH-3T3 fibroblasts.* Journal of Biological Chemistry, 1994. **269**(6): p. 4116-24.
11. Negendank, W.G., *MR spectroscopy of musculoskeletal soft-tissue tumors.* Magn Reson Imaging Clin N Am, 1995. **3**(4): p. 713-25.
12. Prescott, D.M., et al., *The Relationship between Intracellular and Extracellular pH in Spontaneous Canine Tumors.* Clinical Cancer Research, 2000. **6**(6): p. 2501-2505.
13. Gerweck, L.E. and K. Seetharaman, *Cellular pH Gradient in Tumor versus Normal Tissue: Potential Exploitation for the Treatment of Cancer.* Cancer Research, 1996. **56**(6): p. 1194-1198.
14. Gillies, R.J., Z. Liu, and Z. Bhujwalla, *31P-MRS measurements of extracellular pH of tumors using 3-aminopropylphosphonate.* Am J Physiol Cell Physiol, 1994. **267**(1): p. C195-203.
15. Thistlethwaite, A.J., et al., *pH distribution in human tumors.* International Journal of Radiation Oncology*Biology*Physics, 1985. **11**(9): p. 1647-1652.
16. Wike-Hooley, J.L., et al., *Human tumour pH and its variation.* Eur J Cancer Clin Oncol, 1985. **21**(7): p. 785-91.

17. Wike-Hooley, J.L., J. Haveman, and H.S. Reinhold, *The relevance of tumour pH to the treatment of malignant disease.* Radiother Oncol, 1984. **2**(4): p. 343-66.
18. Martin, G.R. and R.K. Jain, *Noninvasive Measurement of Interstitial pH Profiles in Normal and Neoplastic Tissue Using Fluorescence Ratio Imaging Microscopy.* Cancer Res, 1994. **54**(21): p. 5670-5674.
19. Singer, A.J. and R.A. Clark, *Cutaneous wound healing.* N Engl J Med, 1999. **341**(10): p. 738-46.
20. Broughton, G., 2nd, J.E. Janis, and C.E. Attinger, *The basic science of wound healing.* Plast Reconstr Surg, 2006. **117**(7 Suppl): p. 12S-34S.
21. Mutsaers, S.E., et al., *Mechanisms of tissue repair: from wound healing to fibrosis.* The International Journal of Biochemistry & Cell Biology, 1997. **29**(1): p. 5-17.
22. Diegelmann, R.F. and M.C. Evans, *Wound healing: an overview of acute, fibrotic and delayed healing.* Front Biosci, 2004. **9**: p. 283-9.
23. Remensnyder, J.P. and G. Majno, *Oxygen gradients in healing wounds.* Am J Pathol, 1968. **52**(2): p. 301-23.
24. Schneider, L., et al., *Influence of pH on wound-healing: a new perspective for wound-therapy?* Archives of Dermatological Research, 2007. **298**(9): p. 413-420.
25. Sayegh, N., et al., *Wound pH as a predictor of skin graft survival.* Curr Surg, 1988. **45**(1): p. 23-4.
26. Hunt, T.K., B. Zederfeldt, and T.K. Goldstick, *Oxygen and healing.* The American Journal of Surgery, 1969. **118**(4): p. 521-525.
27. Hunt, T.K., et al., *Respiratory gas tensions and pH in healing wounds.* The American Journal of Surgery, 1967. **114**(2): p. 302-307.
28. Kühne, H.H., U. Ullmann, and F.W. Kühne, *New aspects on the pathophysiology of wound infection and wound healing — The problem of lowered oxygen pressure in the tissue.* Infection, 1985. **13**(2): p. 52-56.
29. Stock, C., et al., *Migration of human melanoma cells depends on extracellular pH and Na+/H+ exchange.* The Journal of Physiology, 2005. **567**(1): p. 225-238.
30. Stock, C. and A. Schwab, *Role of the Na+/H+ exchanger NHE1 in cell migration.* Acta Physiologica, 2006. **187**(1-2): p. 149-157.
31. Denker, S.P. and D.L. Barber, *Cell migration requires both ion translocation and cytoskeletal anchoring by the Na-H exchanger NHE1.* The Journal of Cell Biology, 2002. **159**(6): p. 1087-1096.
32. Denker, S.P., et al., *Direct Binding of the Na-H Exchanger NHE1 to ERM Proteins Regulates the Cortical Cytoskeleton and Cell Shape Independently of H+ Translocation.* Molecular Cell, 2000. **6**(6): p. 1425-1436.
33. Plopper, G.E., et al., *Convergence of integrin and growth factor receptor signaling pathways within the focal adhesion complex.* Mol. Biol. Cell, 1995. **6**(10): p. 1349-1365.
34. Montcourrier, P., et al., *Breast cancer cells have a high capacity to acidify extracellular milieu by a dual mechanism.* Clin Exp Metastasis, 1997. **15**(4): p. 382-92.
35. Grinstein, S., et al., *Focal localization of the NHE-1 isoform of the Na+/H+ antiport: assessment of effects on intracellular pH.* Embo J, 1993. **12**(13): p. 5209-18.
36. Lagana, A., et al., *Regulation of the formation of tumor cell pseudopodia by the Na(+)/H(+) exchanger NHE1.* J Cell Sci, 2000. **113**(20): p. 3649-3662.

37. Stock, C., et al., *pH Nanoenvironment at the Surface of Single Melanoma Cells.* Cellular Physiology and Biochemistry, 2007. **20**(5): p. 679-686.
38. Stüwe, L., et al., *pH dependence of melanoma cell migration: protons extruded by NHE1 dominate protons of the bulk solution.* The Journal of Physiology, 2007. **585**(2): p. 351-360.
39. Serrano, C.V., Jr., et al., *pH dependence of neutrophil-endothelial cell adhesion and adhesion molecule expression.* Am J Physiol Cell Physiol, 1996. **271**(3): p. C962-970.
40. Rofstad, E.K., et al., *Acidic extracellular pH promotes experimental metastasis of human melanoma cells in athymic nude mice.* Cancer Res, 2006. **66**(13): p. 6699-707.
41. Kato, Y., et al., *Induction of 103-kDa gelatinase/type IV collagenase by acidic culture conditions in mouse metastatic melanoma cell lines.* J Biol Chem, 1992. **267**(16): p. 11424-30.
42. Glunde, K., et al., *Extracellular acidification alters lysosomal trafficking in human breast cancer cells.* Neoplasia, 2003. **5**(6): p. 533-45.
43. Faff, L. and C. Nolte, *Extracellular acidification decreases the basal motility of cultured mouse microglia via the rearrangement of the actin cytoskeleton.* Brain Research, 2000. **853**(1): p. 22-31.
44. Hynes, R.O., *Integrins: bidirectional, allosteric signaling machines.* Cell, 2002. **110**(6): p. 673-87.
45. Xiong, J.-P., et al., *Crystal Structure of the Extracellular Segment of Integrin alpha Vbeta 3 in Complex with an Arg-Gly-Asp Ligand.* Science, 2002. **296**(5565): p. 151-155.
46. Craig, D., et al., *Structural Insights into How the MIDAS Ion Stabilizes Integrin Binding to an RGD Peptide under Force.* Structure, 2004. **12**(11): p. 2049-2058.
47. Humphries, J.D., A. Byron, and M.J. Humphries, *Integrin ligands at a glance.* Journal of Cell Science, 2006. **119**(19): p. 3901-3903.
48. Giannone, G.g., et al., *Lamellipodial Actin Mechanically Links Myosin Activity with Adhesion-Site Formation.* Cell, 2007. **128**(3): p. 561-575.
49. Choma, D.P., K. Pumiglia, and C.M. DiPersio, *Integrin $\alpha 3\beta 1$ directs the stabilization of a polarized lamellipodium in epithelial cells through activation of Rac1.* Journal of Cell Science, 2004. **117**(17): p. 3947-3959.
50. Ikari, Y., K.O. Yee, and S.M. Schwartz, *Role of alpha5beta1 and alphavbeta3 integrins on smooth muscle cell spreading and migration in fibrin gels.* Thromb Haemost, 2000. **84**(4): p. 701-5.
51. Parnaud, G., et al., *Blockade of $\beta 1$ Integrin-Laminin-5 Interaction Affects Spreading and Insulin Secretion of Rat β-Cells Attached on Extracellular Matrix.* Diabetes, 2006. **55**(5): p. 1413-1420.
52. Huttenlocher, A., M.H. Ginsberg, and A.F. Horwitz, *Modulation of cell migration by integrin-mediated cytoskeletal linkages and ligand-binding affinity.* The Journal of Cell Biology, 1996. **134**(6): p. 1551-1562.
53. Stefansson, S. and D.A. Lawrence, *The serpin PAI-1 inhibits cell migration by blocking integrin [alpha]v[beta]3 binding to vitronectin.* Nature, 1996. **383**(6599): p. 441-443.
54. Tiwari, S., et al., *Divalent cations regulate the folding and activation status of integrins during their intracellular trafficking.* Journal of Cell Science, 2011. **124**(10): p. 1672-1680.

55. Cluzel, C., et al., *The mechanisms and dynamics of (alpha)v(beta)3 integrin clustering in living cells.* J Cell Biol, 2005. **171**(2): p. 383-92.
56. Ng, T., et al., *PKC[alpha] regulates [beta]1 integrin-dependent cell motility through association and control of integrin traffic.* Embo J, 1999. **18**(14): p. 3909-3923.
57. Woods, A.J., et al., *PKD1/PKC[mu] promotes [alpha]v[beta]3 integrin recycling and delivery to nascent focal adhesions.* Embo J, 2004. **23**(13): p. 2531-2543.
58. Du, J., et al., *Integrin activation and internalization on soft ECM as a mechanism of induction of stem cell differentiation by ECM elasticity.* Proceedings of the National Academy of Sciences, 2011. **108**(23): p. 9466-9471.
59. Pellinen, T. and J. Ivaska, *Integrin traffic.* Journal of Cell Science, 2006. **119**(18): p. 3723-3731.
60. Caswell, P.T., et al., *Rab-coupling protein coordinates recycling of Î±5Î²1 integrin and EGFR1 to promote cell migration in 3D microenvironments.* The Journal of Cell Biology, 2008. **183**(1): p. 143-155.
61. Zamir, E. and B. Geiger, *Components of cell-matrix adhesions.* Journal of Cell Science, 2001. **114**(20): p. 3577-3579.
62. Galbraith, C.G., K.M. Yamada, and M.P. Sheetz, *The relationship between force and focal complex development.* J. Cell Biol., 2002. **159**(4): p. 695-705.
63. Geiger, B. and A. Bershadsky, *Assembly and mechanosensory function of focal contacts.* Current Opinion in Cell Biology, 2001. **13**(5): p. 584-592.
64. Lee, S.E., R.D. Kamm, and M.R.K. Mofrad, *Force-induced activation of Talin and its possible role in focal adhesion mechanotransduction.* Journal of Biomechanics, 2007. **40**(9): p. 2096-2106.
65. Critchley, D.R., et al., *Integrin-mediated cell adhesion: the cytoskeletal connection.* Biochem Soc Symp, 1999. **65**: p. 79-99.
66. Critchley, D.R., *Cytoskeletal proteins talin and vinculin in integrin-mediated adhesion.* Biochem Soc Trans, 2004. **32**(Pt 5): p. 831-6.
67. Zamir, E. and B. Geiger, *Molecular complexity and dynamics of cell-matrix adhesions.* J Cell Sci, 2001. **114**(20): p. 3583-3590.
68. Guo, W. and F.G. Giancotti, *Integrin signalling during tumour progression.* Nat Rev Mol Cell Biol, 2004. **5**(10): p. 816-826.
69. Giancotti, F.G. and E. Ruoslahti, *Integrin Signaling.* Science, 1999. **285**(5430): p. 1028-1033.
70. Xiong, J.-P., et al., *Crystal Structure of the Extracellular Segment of Integrin alpha Vbeta 3.* Science, 2001. **294**(5541): p. 339-345.
71. Mould, A.P. and M.J. Humphries, *Regulation of integrin function through conformational complexity: not simply a knee-jerk reaction?* Current Opinion in Cell Biology, 2004. **16**(5): p. 544-551.
72. Carman, C.V. and T.A. Springer, *Integrin avidity regulation: are changes in affinity and conformation underemphasized?* Current Opinion in Cell Biology, 2003. **15**(5): p. 547-556.
73. Valdramidou, D., M.J. Humphries, and A.P. Mould, *Distinct roles of beta1 metal ion-dependent adhesion site (MIDAS), adjacent to MIDAS (ADMIDAS), and ligand-associated metal-binding site (LIMBS) cation-binding sites in ligand recognition by integrin alpha2beta1.* J Biol Chem, 2008. **283**(47): p. 32704-14.

74. Shimaoka, M., et al., *Structures of the αL I Domain and Its Complex with ICAM-1 Reveal a Shape-Shifting Pathway for Integrin Regulation.* Cell, 2003. **112**(1): p. 99-111.
75. Humphries, M.J., *Insights into integrin-ligand binding and activation from the first crystal structure.* Arthritis Res, 2002. **4 Suppl 3**: p. S69-78.
76. Humphries, M.J., et al., *Integrin structure: heady advances in ligand binding, but activation still makes the knees wobble.* Trends in Biochemical Sciences, 2003. **28**(6): p. 313-320.
77. Takagi, J. and T.A. Springer, *Integrin activation and structural rearrangement.* Immunological Reviews, 2002. **186**(1): p. 141-163.
78. Chen, J., A. Salas, and T.A. Springer, *Bistable regulation of integrin adhesiveness by a bipolar metal ion cluster.* Nat Struct Biol, 2003. **10**(12): p. 995-1001.
79. Mould, A.P., et al., *Role of ADMIDAS cation-binding site in ligand recognition by integrin alpha 5 beta 1.* J Biol Chem, 2003. **278**(51): p. 51622-9.
80. Takagi, J., et al., *Global Conformational Rearrangements in Integrin Extracellular Domains in Outside-In and Inside-Out Signaling.* Cell, 2002. **110**(5): p. 599-611.
81. Takagi, J., H.P. Erickson, and T.A. Springer, *C-terminal opening mimics 'inside-out' activation of integrin alpha5beta1.* Nat Struct Biol, 2001. **8**(5): p. 412-6.
82. Luo, B.-H., T.A. Springer, and J. Takagi, *Stabilizing the open conformation of the integrin headpiece with a glycan wedge increases affinity for ligand.* Proceedings of the National Academy of Sciences of the United States of America, 2003. **100**(5): p. 2403-2408.
83. Tadokoro, S., et al., *Talin Binding to Integrin {beta} Tails: A Final Common Step in Integrin Activation.* Science, 2003. **302**(5642): p. 103-106.
84. Mould, A.P., et al., *Conformational Changes in the Integrin βA Domain Provide a Mechanism for Signal Transduction via Hybrid Domain Movement.* Journal of Biological Chemistry, 2003. **278**(19): p. 17028-17035.
85. Paradise, R.K., D.A. Lauffenburger, and K.J. Van Vliet, *Acidic Extracellular pH Promotes Activation of Integrin $\alpha_v\beta_3$.* PLoS ONE, 2011. **6**(1): p. e15746.
86. Mould, A.P., S.K. Akiyama, and M.J. Humphries, *Regulation of integrin alpha 5 beta 1-fibronectin interactions by divalent cations. Evidence for distinct classes of binding sites for Mn2+, Mg2+, and Ca2+.* J Biol Chem, 1995. **270**(44): p. 26270-7.
87. Mould, A.P., et al., *Integrin activation involves a conformational change in the alpha 1 helix of the beta subunit A-domain.* J Biol Chem, 2002. **277**(22): p. 19800-5.
88. Plow, E.F., et al., *Ligand Binding to Integrins.* Journal of Biological Chemistry, 2000. **275**(29): p. 21785-21788.
89. Frelinger, A.L., et al., *Monoclonal antibodies to ligand-occupied conformers of integrin alpha IIb beta 3 (glycoprotein IIb-IIIa) alter receptor affinity, specificity, and function.* Journal of Biological Chemistry, 1991. **266**(26): p. 17106-17111.
90. Tzima, E., et al., *Activation of integrins in endothelial cells by fluid shear stress mediates Rho-dependent cytoskeletal alignment.* Embo J, 2001. **20**(17): p. 4639-47.
91. Zhu, J., et al., *Structure of a complete integrin ectodomain in a physiologic resting state and activation and deactivation by applied forces.* Mol Cell, 2008. **32**(6): p. 849-61.
92. Moser, M., et al., *Kindlin-3 is essential for integrin activation and platelet aggregation.* Nat Med, 2008. **14**(3): p. 325-30.

93. Nieswandt, B., et al., *Loss of talin1 in platelets abrogates integrin activation, platelet aggregation, and thrombus formation in vitro and in vivo.* J. Exp. Med., 2007. **204**(13): p. 3113-3118.
94. Ley, K., et al., *Getting to the site of inflammation: the leukocyte adhesion cascade updated.* Nat Rev Immunol, 2007. **7**(9): p. 678-689.
95. DiMilla, P.A., K. Barbee, and D.A. Lauffenburger, *Mathematical model for the effects of adhesion and mechanics on cell migration speed.* Biophys J, 1991. **60**(1): p. 15-37.
96. Palecek, S.P., et al., *Integrin-ligand binding properties govern cell migration speed through cell-substratum adhesiveness.* Nature, 1997. **385**(6616): p. 537-40.
97. Pilch, J., R. Habermann, and B. Felding-Habermann, *Unique Ability of Integrin* $\alpha v \beta 3$ *to Support Tumor Cell Arrest under Dynamic Flow Conditions.* Journal of Biological Chemistry, 2002. **277**(24): p. 21930-21938.
98. Felding-Habermann, B., et al., *Integrin activation controls metastasis in human breast cancer.* Proceedings of the National Academy of Sciences, 2001. **98**(4): p. 1853-1858.
99. Parsons, J.T., *Focal adhesion kinase: the first ten years.* Journal of Cell Science, 2003. **116**(8): p. 1409-1416.
100. Harburger, D.S. and D.A. Calderwood, *Integrin signalling at a glance.* Journal of Cell Science, 2009. **122**(2): p. 159-163.
101. Schwartz, M.A., *Integrin signaling revisited.* Trends in Cell Biology, 2001. **11**(12): p. 466-470.
102. Eliceiri, B.P., *Integrin and Growth Factor Receptor Crosstalk.* Circulation Research, 2001. **89**(12): p. 1104-1110.
103. Alam, N., et al., *The integrin-growth factor receptor duet.* J Cell Physiol, 2007. **213**(3): p. 649-53.
104. Zhang, Z., et al., *The alpha v beta 1 integrin functions as a fibronectin receptor but does not support fibronectin matrix assembly and cell migration on fibronectin.* The Journal of Cell Biology, 1993. **122**(1): p. 235-242.
105. Chen, L.L., et al., *Multiple activation states of integrin alpha4beta1 detected through their different affinities for a small molecule ligand.* J Biol Chem, 1999. **274**(19): p. 13167-75.
106. Li, F., et al., *Force measurements of the alpha5beta1 integrin-fibronectin interaction.* Biophys J, 2003. **84**(2 Pt 1): p. 1252-62.
107. Zhang, X., et al., *Molecular Basis for the Dynamic Strength of the Integrin {alpha}4{beta}1/VCAM-1 Interaction.* Biophys. J., 2004. **87**(5): p. 3470-3478.
108. Vinogradova, O., et al., *A structural basis for integrin activation by the cytoplasmic tail of the Î±IIb-subunit.* Proceedings of the National Academy of Sciences, 2000. **97**(4): p. 1450-1455.
109. Pampori, N., et al., *Mechanisms and Consequences of Affinity Modulation of Integrin alpha Vbeta 3 Detected with a Novel Patch-engineered Monovalent Ligand.* J. Biol. Chem., 1999. **274**(31): p. 21609-21616.
110. Puklin-Faucher, E., et al., *How the headpiece hinge angle is opened: new insights into the dynamics of integrin activation.* J. Cell Biol., 2006. **175**(2): p. 349-360.
111. Puklin-Faucher, E. and V. Vogel, *Integrin activation dynamics between the RGD-binding site and the headpiece hinge.* J Biol Chem, 2009.

112. Chen, W., et al., *Molecular Dynamics Simulations of Forced Unbending of Integrin $\alpha V\beta 3$.* PLoS Comput Biol, 2011. **7**(2): p. e1001086.
113. Jin, M., I. Andricioaei, and T.A. Springer, *Conversion between Three Conformational States of Integrin I Domains with a C-Terminal Pull Spring Studied with Molecular Dynamics.* Structure, 2004. **12**(12): p. 2137-2147.
114. Lehenkari, P.P. and M.A. Horton, *Single Integrin Molecule Adhesion Forces in Intact Cells Measured by Atomic Force Microscopy.* Biochemical and Biophysical Research Communications, 1999. **259**(3): p. 645-650.
115. Bauer, K., C. Mierke, and J. Behrens, *Expression profiling reveals genes associated with transendothelial migration of tumor cells: a functional role for alphavbeta3 integrin.* Int J Cancer, 2007. **121**(9): p. 1910-8.
116. Rolli, M., et al., *Activated integrin {alpha}v{beta}3 cooperates with metalloproteinase MMP-9 in regulating migration of metastatic breast cancer cells.* Proceedings of the National Academy of Sciences, 2003. **100**(16): p. 9482-9487.
117. Pecheur, I., et al., *Integrin avb3 expression confers on tumor cells a greater propensity to metastasize to bone.* The FASEB Journal, 2002.
118. Albelda, S.M., et al., *Integrin Distribution in Malignant Melanoma: Association of the {beta}3 Subunit with Tumor Progression.* Cancer Res, 1990. **50**(20): p. 6757-6764.
119. Nip, J., et al., *Human melanoma cells derived from lymphatic metastases use integrin alpha v beta 3 to adhere to lymph node vitronectin.* J Clin Invest, 1992. **90**(4): p. 1406-13.
120. Witkowski, C.M., et al., *Characterization of integrin subunits, cellular adhesion and tumorgenicity of four human prostate cell lines.* Journal of Cancer Research and Clinical Oncology, 1993. **119**(11): p. 637-644.
121. McCabe, N.P., et al., *Prostate cancer specific integrin [alpha]v[beta]3 modulates bone metastatic growth and tissue remodeling.* Oncogene, 2007. **26**(42): p. 6238-6243.
122. Liapis, H., A. Flath, and S. Kitazawa, *Integrin alpha V beta 3 expression by bone-residing breast cancer metastases.* Diagnostic molecular pathology : the American journal of surgical pathology, part B, 1996. **5**(2): p. 127-35.
123. Brooks, P.C., et al., *Integrin alpha v beta 3 antagonists promote tumor regression by inducing apoptosis of angiogenic blood vessels.* Cell, 1994. **79**(7): p. 1157-64.
124. Brooks, P., R. Clark, and D. Cheresh, *Requirement of vascular integrin alpha v beta 3 for angiogenesis.* Science, 1994. **264**(5158): p. 569-571.
125. White, D.P., P.T. Caswell, and J.C. Norman, *$\alpha v\beta 3$ and $\alpha 5\beta 1$ integrin recycling pathways dictate downstream Rho kinase signaling to regulate persistent cell migration.* The Journal of Cell Biology, 2007. **177**(3): p. 515-525.
126. Gailit, J., et al., *Human Fibroblasts Bind Directly to Fibrinogen at RGD Sites through Integrin Î±vÎ^{2}3.* Experimental Cell Research, 1997. **232**(1): p. 118-126.
127. Dalton, S.L., et al., *Cell adhesion to extracellular matrix regulates the life cycle of integrins.* Molecular Biology of the Cell, 1995. **6**(12): p. 1781-91.
128. Krishnan, R., E. Walton, and K. Van Vliet, *Characterizing rare-event property distributions via replicate molecular dynamics simulations of proteins.* Journal of Molecular Modeling, 2009. **15**(11): p. 1383-1389.
129. Krishnan, R., et al., *Modeling and simulation of chemomechanics at the cell-matrix interface.* Cell Adhesion and Migration, 2008. **2**(2).

130. van der Spoel, D., et al., *Gromacs User Manual version 3.3.* www.gromacs.org, 2005.
131. Wolf-Watz, M., et al., *Linkage between dynamics and catalysis in a thermophilic-mesophilic enzyme pair.* Nat Struct Mol Biol, 2004. **11**(10): p. 945-9.
132. Fersht, A., *Structure and Mechanism in Protein Science*. 1999, New York: W.H. Freeman and Company.
133. Hammes, G.G., *Multiple Conformational Changes in Enzyme Catalysisâ€* Biochemistry, 2002. **41**(26): p. 8221-8228.
134. Gilbert, S.P., et al., *Pathway of processive ATP hydrolysis by kinesin.* Nature, 1995. **373**(6516): p. 671-6.
135. Grubmüller, H., B. Heymann, and P. Tavan, *Ligand Binding: Molecular Mechanics Calculation of the Streptavidin-Biotin Rupture Force.* Science, 1996. **271**(5251): p. 997-999.
136. Isralewitz, B., M. Gao, and K. Schulten, *Steered molecular dynamics and mechanical functions of proteins.* Curr Opin Struct Biol, 2001. **11**(2): p. 224-30.
137. Bell, G.I., *Models for the specific adhesion of cells to cells.* Science, 1978. **200**(4342): p. 618-627.
138. Evans, E. and K. Ritchie, *Dynamic strength of molecular adhesion bonds.* Biophys. J., 1997. **72**(4): p. 1541-1555.
139. Walton, E.B., S. Lee, and K.J. Van Vliet, *Extending Bell's model: how force transducer stiffness alters measured unbinding forces and kinetics of molecular complexes.* Biophys. J., 2008: p. biophysj.107.114454.
140. Izrailev, S., et al., *Molecular dynamics study of unbinding of the avidin-biotin complex.* Biophys. J., 1997. **72**(4): p. 1568-1581.
141. Paci, E., et al., *Forces and energetics of hapten-antibody dissociation: a biased molecular dynamics simulation study.* Journal of Molecular Biology, 2001. **314**(3): p. 589-605.
142. Curcio, R., A. Caflisch, and E. Paci, *Change of the unbinding mechanism upon a mutation: A molecular dynamics study of an antibody-hapten complex.* Protein Sci, 2005. **14**(10): p. 2499-2514.
143. Dastidar, S.G., D.P. Lane, and C.S. Verma, *Multiple Peptide Conformations Give Rise to Similar Binding Affinities: Molecular Simulations of p53-MDM2.* Journal of the American Chemical Society, 2008. **130**(41): p. 13514-13515.
144. Coureux, P.-D., et al., *Picometer-Scale Conformational Heterogeneity Separates Functional from Nonfunctional States of a Photoreceptor Protein.* Structure, 2008. **16**(6): p. 863-872.
145. Chilkoti, A. and P.S. Stayton, *Molecular origins of the slow streptavidin-biotin dissociation kinetics.* Journal of the American Chemical Society ; VOL. 117 ; ISSUE: 43 ; PBD: 1 Nov 1995, 1995: p. pp. 10622-10628 ; PL:.
146. Chu, V., et al., *Thermodynamic and structural consequences of flexible loop deletion by circular permutation in the streptavidin-biotin system.* Protein Sci, 1998. **7**(4): p. 848-859.
147. Freitag, S., et al., *A structural snapshot of an intermediate on the streptavidin-biotin dissociation pathway.* Proc Natl Acad Sci U S A, 1999. **96**(15): p. 8384-9.
148. Freitag, S., et al., *Structural studies of the streptavidin binding loop.* Protein Sci, 1997. **6**(6): p. 1157-1166.

149. Hyre, D.E., et al., *Early mechanistic events in biotin dissociation from streptavidin.* Nat Struct Biol, 2002. **9**(8): p. 582-5.
150. Rico, F. and V.T. Moy, *Energy landscape roughness of the streptavidin-biotin interaction.* J Mol Recognit, 2007. **20**(6): p. 495-501.
151. Troyer, J.M. and F.E. Cohen, *Protein conformational landscapes: Energy minimization and clustering of a long molecular dynamics trajectory.* Proteins: Structure, Function, and Genetics, 1995. **23**(1): p. 97-110.
152. Li, Y., *Bayesian Model Based Clustering Analysis: Application to a Molecular Dynamics Trajectory of the HIV-1 Integrase Catalytic Core.* J. Chem. Inf. Model., 2006. **46**(4): p. 1742-1750.
153. Laboulais, C., et al., *Hamming distance geometry of a protein conformational space: Application to the clustering of a 4-ns molecular dynamics trajectory of the HIV-1 integrase catalytic core.* Proteins: Structure, Function, and Genetics, 2002. **47**(2): p. 169-179.
154. Karpen, M.E., D.J. Tobias, and C.L. Brooks, 3rd, *Statistical clustering techniques for the analysis of long molecular dynamics trajectories: analysis of 2.2-ns trajectories of YPGDV.* Biochemistry, 1993. **32**(2): p. 412-20.
155. Gabarro-Arpa, J. and R. Revilla, *Clustering of a molecular dynamics trajectory with a Hamming distance.* Computers & Chemistry, 2000. **24**(6): p. 693-698.
156. Feher, M. and J.M. Schmidt, *Fuzzy Clustering as a Means of Selecting Representative Conformers and Molecular Alignments.* J. Chem. Inf. Comput. Sci., 2003. **43**(3): p. 810-818.
157. Brigo, A., et al., *Comparison of Multiple Molecular Dynamics Trajectories Calculated for the Drug-Resistant HIV-1 Integrase T66I/M154I Catalytic Domain.* Biophys. J., 2005. **88**(5): p. 3072-3082.
158. Gordon, H.L. and R.L. Somorjai, *Fuzzy cluster analysis of molecular dynamics trajectories.* Proteins: Structure, Function, and Genetics, 1992. **14**(2): p. 249-264.
159. Lei, H., et al., *Folding free-energy landscape of villin headpiece subdomain from molecular dynamics simulations.* Proceedings of the National Academy of Sciences, 2007. **104**(12): p. 4925-4930.
160. Weber, P.C., et al., *Structural origins of high-affinity biotin binding to streptavidin.* Science, 1989. **243**(4887): p. 85-88.
161. Lindqvist, Y. and G. Schneider, *Protein-biotin interactions.* Current Opinion in Structural Biology, 1996. **6**(6): p. 798-803.
162. Franz, C.M., et al., *Studying Integrin-Mediated Cell Adhesion at the Single-Molecule Level Using AFM Force Spectroscopy.* Sci. STKE, 2007. **2007**(406): p. pl5-.
163. Bryngelson, J.D., et al., *Funnels, pathways, and the energy landscape of protein folding: a synthesis.* Proteins, 1995. **21**(3): p. 167-95.
164. Honeycutt, J.D. and D. Thirumalai, *Metastability of the folded states of globular proteins.* Proceedings of the National Academy of Sciences of the United States of America, 1990. **87**(9): p. 3526-3529.
165. Devore, J.L., *Probability and Statistics for Engineering and the Sciences*. 6 ed. 2004: Brooks/Cole.
166. Aprikian, P., et al., *The Bacterial Fimbrial Tip Acts as a Mechanical Force Sensor.* PLoS Biol, 2011. **9**(5): p. e1000617.

167. Mai, B.K., M.H. Viet, and M.S. Li, *Top Leads for Swine Influenza A/H1N1 Virus Revealed by Steered Molecular Dynamics Approach.* Journal of Chemical Information and Modeling, 2010. **50**(12): p. 2236-2247.
168. Guzman, D.L., et al., *Computational and single-molecule force studies of a macro domain protein reveal a key molecular determinant for mechanical stability.* Proceedings of the National Academy of Sciences, 2010. **107**(5): p. 1989-1994.
169. Sheena, A., et al., *Elucidation of the Glucose Transport Pathway in Glucose Transporter 4 via Steered Molecular Dynamics Simulations.* PLoS ONE, 2011. **6**(10): p. e25747.
170. Xu, Y., et al., *Long route or shortcut? A molecular dynamics study of traffic of thiocholine within the active-site gorge of acetylcholinesterase.* Biophys J, 2010. **99**(12): p. 4003-11.
171. Le, L., et al., *Molecular Dynamics Simulations Suggest that Electrostatic Funnel Directs Binding of Tamiflu to Influenza N1 Neuraminidases.* PLoS Comput Biol, 2010. **6**(9): p. e1000939.
172. Liu, Y., et al., *Extension of a three-helix bundle domain of myosin VI and key role of calmodulins.* Biophys J, 2011. **100**(12): p. 2964-73.
173. Alexov, E.G. and M.R. Gunner, *Incorporating protein conformational flexibility into the calculation of pH-dependent protein properties.* Biophys J, 1997. **72**(5): p. 2075-93.
174. Georgescu, R.E., E.G. Alexov, and M.R. Gunner, *Combining Conformational Flexibility and Continuum Electrostatics for Calculating pKas in Proteins.* Biophys. J., 2002. **83**(4): p. 1731-1748.
175. Luo, B.H., et al., *Rationally designed integrin beta3 mutants stabilized in the high affinity conformation.* J Biol Chem, 2009. **284**(6): p. 3917-24.
176. Chen, J., et al., *Regulation of outside-in signaling and affinity by the beta2 I domain of integrin alphaLbeta2.* Proc Natl Acad Sci U S A, 2006. **103**(35): p. 13062-7.
177. Bajt, M.L. and J.C. Loftus, *Mutation of a ligand binding domain of beta 3 integrin. Integral role of oxygenated residues in alpha IIb beta 3 (GPIIb-IIIa) receptor function.* J Biol Chem, 1994. **269**(33): p. 20913-9.
178. Davies, M., et al., *Benchmarking pKa prediction.* BMC Biochemistry, 2006. **7**(1): p. 18.
179. Xiong, J.P., et al., *Crystal structure of the complete integrin alphaVbeta3 ectodomain plus an alpha/beta transmembrane fragment.* J Cell Biol, 2009. **186**(4): p. 589-600.
180. Katsumi, A., et al., *Integrin Activation and Matrix Binding Mediate Cellular Responses to Mechanical Stretch.* J. Biol. Chem., 2005. **280**(17): p. 16546-16549.
181. Kiosses, W.B., et al., *Rac recruits high-affinity integrin [alpha]v[beta]3 to lamellipodia in endothelial cell migration.* Nat Cell Biol, 2001. **3**(3): p. 316-320.
182. Schreiner, C.L., et al., *Isolation and characterization of Chinese hamster ovary cell variants deficient in the expression of fibronectin receptor.* J Cell Biol, 1989. **109**(6 Pt 1): p. 3157-67.
183. Sun, Z., et al., *Mechanical properties of the interaction between fibronectin and {alpha}5{beta}1-integrin on vascular smooth muscle cells studied using atomic force microscopy.* Am J Physiol Heart Circ Physiol, 2005. **289**(6): p. H2526-2535.
184. Kong, F., et al., *Demonstration of catch bonds between an integrin and its ligand.* The Journal of Cell Biology, 2009. **185**(7): p. 1275-1284.
185. Parsons, J.T., A.R. Horwitz, and M.A. Schwartz, *Cell adhesion: integrating cytoskeletal dynamics and cellular tension.* Nat Rev Mol Cell Biol, 2010. **11**(9): p. 633-643.

186. Bailly, M., et al., *Regulation of Protrusion Shape and Adhesion to the Substratum during Chemotactic Responses of Mammalian Carcinoma Cells.* Experimental Cell Research, 1998. **241**(2): p. 285-299.
187. Harms, B.D., et al., *Directional Persistence of EGF-Induced Cell Migration Is Associated with Stabilization of Lamellipodial Protrusions.* Biophysical Journal, 2005. **88**(2): p. 1479-1488.
188. Gupton, S.L. and C.M. Waterman-Storer, *Spatiotemporal Feedback between Actomyosin and Focal-Adhesion Systems Optimizes Rapid Cell Migration.* Cell, 2006. **125**(7): p. 1361-1374.
189. Bergman, J., et al., *Use of the pH-sensitive dye BCECF to study pH regulation in cultured human kidney proximal tubule cells.* Methods in Cell Science, 1991. **13**(3): p. 205-209.
190. Invitrogen, *BCECF*. 2006.
191. Thomas, J.A., et al., *Intracellular pH measurements in Ehrlich ascites tumor cells utilizing spectroscopic probes generated in situ.* Biochemistry, 1979. **18**(11): p. 2210-2218.
192. Steffan, J.J., et al., *Na+/H+ exchangers and RhoA regulate acidic extracellular pH-induced lysosome trafficking in prostate cancer cells.* Traffic, 2009. **10**(6): p. 737-53.
193. Steffan, J.J., et al., *HGF-induced invasion by prostate tumor cells requires anterograde lysosome trafficking and activity of Na+-H+ exchangers.* J Cell Sci, 2010. **123**(Pt 7): p. 1151-9.
194. Tominaga, T. and D.L. Barber, *Na-H exchange acts downstream of RhoA to regulate integrin-induced cell adhesion and spreading.* Mol Biol Cell, 1998. **9**(8): p. 2287-303.
195. Yang, X., et al., *Inhibition of Na+/H+ exchanger 1 by 5-(N-ethyl-N-isopropyl) amiloride reduces hypoxia-induced hepatocellular carcinoma invasion and motility.* Cancer Letters, 2010. **295**(2): p. 198-204.
196. Chen, M., et al., *Nckbeta adapter regulates actin polymerization in NIH 3T3 fibroblasts in response to platelet-derived growth factor bb.* Mol Cell Biol, 2000. **20**(21): p. 7867-80.
197. Srivastava, J., et al., *Structural model and functional significance of pH-dependent talin-actin binding for focal adhesion remodeling.* Proceedings of the National Academy of Sciences, 2008. **105**(38): p. 14436-14441.
198. Choi, C.K., et al., *Actin and [alpha]-actinin orchestrate the assembly and maturation of nascent adhesions in a myosin II motor-independent manner.* Nat Cell Biol, 2008. **10**(9): p. 1039-1050.
199. Ren, X.D., et al., *Focal adhesion kinase suppresses Rho activity to promote focal adhesion turnover.* Journal of Cell Science, 2000. **113**(20): p. 3673-3678.
200. Clark, E.A., et al., *Integrin-mediated Signals Regulated by Members of the Rho Family of GTPases.* The Journal of Cell Biology, 1998. **142**(2): p. 573-586.
201. Helfman, D.M., et al., *Caldesmon Inhibits Nonmuscle Cell Contractility and Interferes with the Formation of Focal Adhesions.* Molecular Biology of the Cell, 1999. **10**(10): p. 3097-3112.
202. Chrzanowska-Wodnicka, M. and K. Burridge, *Rho-stimulated contractility drives the formation of stress fibers and focal adhesions.* The Journal of Cell Biology, 1996. **133**(6): p. 1403-1415.

203. Kato, M. and M. Mrksich, *Using model substrates to study the dependence of focal adhesion formation on the affinity of integrin-ligand complexes.* Biochemistry, 2004. **43**(10): p. 2699-707.
204. Iwanaga, Y., D. Braun, and P. Fromherz, *No correlation of focal contacts and close adhesion by comparing GFP-vinculin and fluorescence interference of DiI.* European Biophysics Journal, 2001. **30**(1): p. 17-26.
205. Balaban, N.Q., et al., *Force and focal adhesion assembly: a close relationship studied using elastic micropatterned substrates.* Nat Cell Biol, 2001. **3**(5): p. 466-72.
206. Bhatt, A., et al., *Regulation of focal complex composition and disassembly by the calcium-dependent protease calpain.* Journal of Cell Science, 2002. **115**(17): p. 3415-3425.
207. Riveline, D., et al., *Focal Contacts as Mechanosensors.* The Journal of Cell Biology, 2001. **153**(6): p. 1175-1186.
208. Felgner, P.L., et al., *Lipofection: a highly efficient, lipid-mediated DNA-transfection procedure.* Proc Natl Acad Sci U S A, 1987. **84**(21): p. 7413-7.
209. Palmer, S.M., M.D. Schaller, and S.L. Campbell, *Vinculin Tail Conformation and Self-Association Is Independent of pH and H906 Protonationâ€* Biochemistry, 2008. **47**(47): p. 12467-12475.
210. Madri, J.A., B.M. Pratt, and J. Yannariello-Brown, *Matrix-driven cell size change modulates aortic endothelial cell proliferation and sheet migration.* Am J Pathol, 1988. **132**(1): p. 18-27.
211. Smith, A., et al., *A talin-dependent LFA-1 focal zone is formed by rapidly migrating T lymphocytes.* The Journal of Cell Biology, 2005. **170**(1): p. 141-151.
212. Dickinson, R.B. and R.T. Tranquillo, *Optimal Estimation of Cell Movement Indices from the Statistical Analysis of Cell Tracking Data.* AIChE Journal, 1993. **39**(12).
213. Ware, M.F., A. Wells, and D.A. Lauffenburger, *Epidermal growth factor alters fibroblast migration speed and directional persistence reciprocally and in a matrix-dependent manner.* Journal of Cell Science, 1998. **111**(16): p. 2423-2432.
214. DiMilla, P., et al., *Maximal migration of human smooth muscle cells on fibronectin and type IV collagen occurs at an intermediate attachment strength.* The Journal of Cell Biology, 1993. **122**(3): p. 729-737.
215. Palecek, S., et al., *Physical and biochemical regulation of integrin release during rear detachment of migrating cells.* J Cell Sci, 1998. **111**(7): p. 929-940.
216. Lee, S., et al., *Pericyte actomyosin-mediated contraction at the cell-material interface can modulate the microvascular niche.* J Phys Condens Matter, 2010. **22**(19): p. 194115.
217. Koide, A., et al., *Stabilization of a fibronectin type III domain by the removal of unfavorable electrostatic interactions on the protein surface.* Biochemistry, 2001. **40**(34): p. 10326-33.
218. Mallik, B., et al., *pH Dependence of Stability of the 10th Human Fibronectin Type III Domain: A Computational Study.* Biotechnology Progress, 2008. **24**(1): p. 48-55.
219. Zaman, M.H., et al., *Migration of tumor cells in 3D matrices is governed by matrix stiffness along with cell-matrix adhesion and proteolysis.* Proceedings of the National Academy of Sciences, 2006. **103**(29): p. 10889-10894.

220. Johnson, L.L., et al., *A Rationalization of the Acidic pH Dependence for Stromelysin-1 (Matrix Metalloproteinase-3) Catalysis and Inhibition.* Journal of Biological Chemistry, 2000. **275**(15): p. 11026-11033.
221. Fasciglione, G.F., et al., *pH- and Temperature-Dependence of Functional Modulation in Metalloproteinases. A Comparison between Neutrophil Collagenase and Gelatinases A and B.* Biophysical Journal, 2000. **79**(4): p. 2138-2149.
222. Zhao, X., et al., *pH dependency of mu-calpain and m-calpain activity assayed by casein zymography following traumatic brain injury in the rat.* Neurosci Lett, 1998. **247**(1): p. 53-7.
223. Franco, S.J. and A. Huttenlocher, *Regulating cell migration: calpains make the cut.* Journal of Cell Science, 2005. **118**(17): p. 3829-3838.
224. Rhoads, D.S. and J.L. Guan, *Analysis of directional cell migration on defined FN gradients: role of intracellular signaling molecules.* Exp Cell Res, 2007. **313**(18): p. 3859-67.
225. Smith, J.T., et al., *Measurement of Cell Migration on Surface-Bound Fibronectin Gradients.* Langmuir, 2004. **20**(19): p. 8279-8286.
226. Enaida, H., et al., *Effect of growth factors on expression of integrin subtypes in microvascular endothelial cells isolated from bovine retinas.* Fukushima J Med Sci, 1998. **44**(1): p. 43-52.
227. Klein, S., et al., *Integrin Regulation by Endogenous Expression of 18-kDa Fibroblast Growth Factor-2.* Journal of Biological Chemistry, 1996. **271**(37): p. 22583-22590.
228. Woods, D., et al., *Induction of β3-Integrin Gene Expression by Sustained Activation of the Ras-Regulated Raf-MEK-Extracellular Signal-Regulated Kinase Signaling Pathway.* Mol. Cell. Biol., 2001. **21**(9): p. 3192-3205.
229. Swietach, P., et al., *Modelling intracellular H+ ion diffusion.* Progress in Biophysics and Molecular Biology, 2003. **83**(2): p. 69-100.
230. Swietach, P., et al., *Experimental Generation and Computational Modeling of Intracellular pH Gradients in Cardiac Myocytes.* Biophysical Journal, 2005. **88**(4): p. 3018-3037.
231. al-Baldawi, N.F. and R.F. Abercrombie, *Cytoplasmic hydrogen ion diffusion coefficient.* Biophysical Journal, 1992. **61**(6): p. 1470-1479.
232. Lauffenburger, D., *Influence of external concentration fluctuations on leukocyte chemotactic orientation.* Cell Biochemistry and Biophysics, 1982. **4**(2): p. 177-209.
233. DeLisi, C. and F.W. Wiegel, *Effect of nonspecific forces and finite receptor number on rate constants of ligand--cell bound-receptor interactions.* Proceedings of the National Academy of Sciences, 1981. **78**(9): p. 5569-5572.
234. Maheshwari, G., et al., *Biophysical Integration of Effects of Epidermal Growth Factor and Fibronectin on Fibroblast Migration.* Biophysical Journal, 1999. **76**(5): p. 2814-2823.
235. Pruss, R.M. and H.R. Herschman, *Variants of 3T3 cells lacking mitogenic response to epidermal growth factor.* Proceedings of the National Academy of Sciences, 1977. **74**(9): p. 3918-3921.
236. Fukumura, D., et al., *Hypoxia and Acidosis Independently Up-Regulate Vascular Endothelial Growth Factor Transcription in Brain Tumors in Vivo.* Cancer Research, 2001. **61**(16): p. 6020-6024.

237. Xu, L., D. Fukumura, and R.K. Jain, *Acidic Extracellular pH Induces Vascular Endothelial Growth Factor (VEGF) in Human Glioblastoma Cells via ERK1/2 MAPK Signaling Pathway.* Journal of Biological Chemistry, 2002. **277**(13): p. 11368-11374.
238. Shi, Q., et al., *Regulation of vascular endothelial growth factor expression by acidosis in human cancer cells.* Oncogene, 2001. **20**(28): p. 3751-6.
239. Goerges, A.L. and M.A. Nugent, *Regulation of Vascular Endothelial Growth Factor Binding and Activity by Extracellular pH.* Journal of Biological Chemistry, 2003. **278**(21): p. 19518-19525.
240. Goerges, A.L. and M.A. Nugent, *pH Regulates Vascular Endothelial Growth Factor Binding to Fibronectin.* Journal of Biological Chemistry, 2004. **279**(3): p. 2307-2315.
241. Griffiths, L., et al., *The influence of oxygen tension and pH on the expression of platelet-derived endothelial cell growth factor/thymidine phosphorylase in human breast tumor cells grown in vitro and in vivo.* Cancer Res, 1997. **57**(4): p. 570-2.
242. Shi, Q., et al., *Constitutive and inducible interleukin 8 expression by hypoxia and acidosis renders human pancreatic cancer cells more tumorigenic and metastatic.* Clin Cancer Res, 1999. **5**(11): p. 3711-21.
243. D'Arcangelo, D., et al., *Acidosis Inhibits Endothelial Cell Apoptosis and Function and Induces Basic Fibroblast Growth Factor and Vascular Endothelial Growth Factor Expression.* Circulation Research, 2000. **86**(3): p. 312-318.
244. Sun, S., J. Wise, and M. Cho, *Human fibroblast migration in three-dimensional collagen gel in response to noninvasive electrical stimulus. I. Characterization of induced three-dimensional cell movement.* Tissue Eng, 2004. **10**(9-10): p. 1548-57.
245. Raeber, G.P., M.P. Lutolf, and J.A. Hubbell, *Molecularly Engineered PEG Hydrogels: A Novel Model System for Proteolytically Mediated Cell Migration.* Biophysical Journal, 2005. **89**(2): p. 1374-1388.
246. Zervantonakis, I., et al., *Concentration gradients in microfluidic 3D matrix cell culture systems.* International Journal of Micro-Nano Scale Transport, 2010. **1**(1): p. 27-36.
247. Paszek, M.J., et al., *Tensional homeostasis and the malignant phenotype.* Cancer Cell, 2005. **8**(3): p. 241-254.
248. Masuzaki, R., et al., *Assessing liver tumor stiffness by transient elastography.* Hepatology International, 2007. **1**(3): p. 394-397.
249. Freyman, T.M., et al., *Fibroblast contraction of a collagen-GAG matrix.* Biomaterials, 2001. **22**(21): p. 2883-2891.
250. Hinz, B. and G. Gabbiani, *Mechanisms of force generation and transmission by myofibroblasts.* Current Opinion in Biotechnology, 2003. **14**(5): p. 538-546.
251. Berendsen, H.J.C., D. van der Spoel, and R. van Drunen, *GROMACS: A message-passing parallel molecular dynamics implementation.* Computer Physics Communications, 1995. **91**(1-3): p. 43-56.
252. Lindahl, E., B. Hess, and D. van der Spoel, *GROMACS 3.0: a package for molecular simulation and trajectory analysis.* Journal of Molecular Modeling, 2001. **7**(8): p. 306-317.
253. Walton, E.B. and K.J. VanVliet, *Equilibration of experimentally determined protein structures for molecular dynamics simulation.* Physical Review E (Statistical, Nonlinear, and Soft Matter Physics), 2006. **74**(6): p. 061901.
254. Merkel, R., et al., *Energy landscapes of receptor-ligand bonds explored with dynamic force spectroscopy.* Nature, 1999. **397**(6714): p. 50-53.

255. Friddle, R.W., et al., *Near-Equilibrium Chemical Force Microscopy.* Journal of Physical Chemistry, 2008, accepted.
256. Schuttelkopf, A.W. and D.M.F. van Aalten, *PRODRG: a tool for high-throughput crystallography of protein-ligand complexes.* Acta Crystallographica Section D, 2004. **60**(8): p. 1355-1363.
257. Chernick, M.R., *Bootstrap Methods: A Practitioner's Guide (Wiley Series in Probability and Statistics)*. 1999: Wiley-Interscience.
258. Dunn, G.A., *Characterising a kinesis response: time averaged measures of cell speed and directional persistence.* Agents Actions Suppl, 1983. **12**: p. 14-33.
259. Yauch, R.L., et al., *Mutational Evidence for Control of Cell Adhesion Through Integrin Diffusion/Clustering, Independent of Ligand Binding.* The Journal of Experimental Medicine, 1997. **186**(8): p. 1347-1355.
260. Cressman, S., et al., *Binding and Uptake of RGD-Containing Ligands to Cellular αvβ3 Integrins.* International Journal of Peptide Research and Therapeutics, 2009. **15**(1): p. 49-59.
261. Canetta, E., et al., *Measuring cell viscoelastic properties using a force-spectrometer: Influence of protein-cytoplasm interactions.* Biorheology, 2005. **42**(5): p. 321-333.

Appendix A: Run files for MD simulations

GROMACS run parameter file for equilibration simulations (.mdp file format):

```
;
;     User spoel (236)
;     Wed Nov  3 17:12:44 1993
;     Input file
;
title               =  Yo
cpp                 =  /lib/cpp
constraints         =  all-bonds
integrator          =  md
dt                  =  0.002     ; ps !
nsteps              =  1500000   ; total 3 ns
comm_mode           =  Angular
nstcomm             =  1
comm_grps           =  Protein
nstxout             =  500
nstvout             =  1000
nstfout             =  0
nstlog              =  100
nstenergy           =  100
nstlist             =  10
ns_type             =  grid
coulombtype         =  PME
rlist               =  0.9
rcoulomb            =  0.9
rvdw                =  0.9
fourierspacing      =  0.12
pme_order           =  4
ewald_rtol          =  1e-5
; Berendsen temperature coupling is on in two groups
Tcoupl              =  berendsen
tc-grps             =  Protein  Other
tau_t               =  0.1 0.1
ref_t               =  300 300
; Energy monitoring
energygrps          =  Protein  SOL
; Isotropic pressure coupling is now on
Pcoupl              =  berendsen
Pcoupltype          = isotropic
tau_p               =  0.5
compressibility     =  4.5e-5
ref_p               =  1.0
; Generate velocites is off at 300 K.
gen_vel             =  no
gen_temp            =  300.0
gen_seed            =  174000
```

GROMACS run parameter file for steered MD simulations (.mdp file format):

```
;
;     User spoel (236)
;     Wed Nov  3 17:12:44 1993
;     Input file
;
title                =  Yo
cpp                  =  /lib/cpp
constraints          =  all-bonds
integrator           =  md
dt                   =  0.002     ; ps !
nsteps               =  500000    ; total 1 ns.
comm_mode            = Angular
comm_grps            = alpha beta
nstcomm              =  1
nstxout              =  500
nstvout              =  1000
nstfout              =  0
nstlog               =  100
nstenergy            =  100
nstlist              =  10
ns_type              =  grid
coulombtype          =  PME
rlist                =  0.9
rcoulomb             =  0.9
rvdw                 =  0.9
fourierspacing       =  0.12
pme_order            =  4
ewald_rtol           =  1e-5
; Berendsen temperature coupling is on in two groups
Tcoupl               =  berendsen
tc-grps               =  alpha beta_RGD other_RGD
tau_t                =  0.1 0.1
ref_t                =  300 300
; Energy monitoring
energygrps           =  Protein  SOL
; Isotropic pressure coupling is now on
Pcoupl               =  berendsen
Pcoupltype           = isotropic
tau_p                =  0.5
compressibility      =  4.5e-5
ref_p                =  1.0
; Generate velocites is off at 300 K.
gen_vel              =  no
gen_temp             =  300.0
gen_seed             =  173529
```

GROMACS pulling parameter file for steered MD simulations (.ppa file format). The normalized direction of pulling (afm_dir1) and the initial position of the free end of the spring relative to the reference_group (afm_init1) are determined by the initial distance between group_1 and the reference_group.

```
verbose = no
runtype = afm
group_1 = RGD
reference_group = alpha beta
reftype = com
pulldim = Y Y Y
afm_rate1 = 0.002
afm_k1 = 2492
afm_dir1 = 0.6580284924 0.1034578757 0.7458518426
afm_init1 = 3.70923 0.58318 4.20428
```

Appendix B: Integrin beta subunit sequence alignment

Sequence alignment for the first ~200 amino acids in the eight human integrin β subunits. The region containing ASPβ127 for β3 is highlighted.

```
Sequence Alignment - Integrins Beta
UniProt
CLUSTAL 2.1 multiple sequence alignment
SP|P18084|ITB5_HUMAN ------------------MPRAPAPLYACLLGLCALLPR-LAGLNICTSGS--------- 32
SP|P05106|ITB3_HUMAN ----------------MRARPRPRPLWATVLALGALAGVGVGGPNICTTRG--------- 35
SP|P18564|ITB6_HUMAN ------------------MGIELLCLFFLFLGRNDHVQG------GCALGG--------- 27
SP|P26010|ITB7_HUMAN -------------------MVAL-PMVLVLLLVLSRGESELDAKIPSTGDATEWRNPHLS 40
SP|P05107|ITB2_HUMAN -------------------MLGLRPPLLALVGLLSLG-------CVLSQECTKFK----- 29
SP|P05556|ITB1_HUMAN --------------------MNLQPIFWIGLISSVCC------VFAQTDENRCLKAN--- 31
SP|P26012|ITB8_HUMAN MCGSALAFFTAAFVCLQNDRRGPASFLWAAWVFSLVLGLGQGEDNRCASSN--------- 51
SP|P16144|ITB4_HUMAN -------------------MAGPRPSPWARLLLAALISVSLSGTLANRCKKAP------- 34

SP|P18084|ITB5_HUMAN -------ATSCEECLLIHPKCAWCSKEDFGSPR-SITSRCDLRANLVKNGCG-GEIESPA 83
SP|P05106|ITB3_HUMAN -------VSSCQQCLAVSPMCAWCSDEALPLG----SPRCDLKENLLKDNCAPESIEFPV 84
SP|P18564|ITB6_HUMAN -------AETCEDCLLIGPQCAWCAQENFTHPS-GVGERCDTPANLLAKGCQLNFIENPV 79
SP|P26010|ITB7_HUMAN MLGSCQPAPSCQKCILSHPSCAWCKQLNFTASGEAEARRCARREELLARGCPLEELEEPR 100
SP|P05107|ITB2_HUMAN -------VSSCRECIESGPGCTWCQKLNFTGPGDPDSIRCDTRPQLLMRGCAADDIMDPT 82
SP|P05556|ITB1_HUMAN -------AKSCGECIQAGPNCGWCTNSTFLQEGMPTSARCDDLEALKKKGCPPDDIENPR 84
SP|P26012|ITB8_HUMAN -------AASCARCLALGPECGWCVQEDFISGG-SRSERCDIVSNLISKGCSVDSIEYPS 103
SP|P16144|ITB4_HUMAN -------VKSCTECVRVDKDCAYCTDEMFRDRR------CNTQAELLAAGCQRESIVVME 81

SP|P18084|ITB5_HUMAN SSFHVLRSLPLS--SKGSGSAG--WDVIQMTPQEIAVNLRPGDKTTFQLQVRQVEDYPVD 139
SP|P05106|ITB3_HUMAN SEARVLEDRPLS--DKGSGDS---SQVTQVSPQRIALRLRPDDSKNFSIQVRQVEDYPVD 139
SP|P18564|ITB6_HUMAN SQVEILKNKPLS--VGRQKNS---SDIVQIAPQSLILKLRPGGAQTLQVHVRQTEDYPVD 134
SP|P26010|ITB7_HUMAN GQQEVLQDQPLSQGARGEGAT-------QLAPQRVRVTLRPGEPQQLQVRFLRAEGYPVD 153
SP|P05107|ITB2_HUMAN SLAETQEDH-------NGGQK-------QLSPQKVTLYLRPGQAAAFNVTFRRAKGYPID 128
SP|P05556|ITB1_HUMAN GSKDIKKNKNVTNRSKGTAEKLKPEDITQIQPQQLVLRLRSGEPQTFTLKFKRAEDYPID 144
SP|P26012|ITB8_HUMAN VHVIIPTENEIN---------------TQVTPGEVSIQLRPGAEANFMLKVHPLKKYPVD 148
SP|P16144|ITB4_HUMAN SSFQITEETQIDTTLRRS----------QMSPQGLRVRLRPGEERHFELEVFEPLESPVD 131

SP|P18084|ITB5_HUMAN LYYLMDLSLSMKDDLDNIRSLGTKLAEEMRKLTSNFRLGFGSFVDKDISPFSYTAP-RYQ 198
SP|P05106|ITB3_HUMAN IYYLMDLSYSMKDDLWSIQNLGTKLATQMRKLTSNLRIGFGAFVDKPVSPYMYISPPEAL 199
SP|P18564|ITB6_HUMAN LYYLMDLSASMDDDLNTIKELGSRLSKEMSKLTSNFRLGFGSFVEKPVSPFVKTTP-EEI 193
SP|P26010|ITB7_HUMAN LYYLMDLSYSMKDDLERVRQLGHALLVRLQEVTHSVRIGFGSFVDKTVLPFVSTVP-SKL 212
SP|P05107|ITB2_HUMAN LYYLMDLSYSMLDDLRNVKKLGGDLLRALNEITESGRIGFGSFVDKTVLPFVNTHP-DKL 187
SP|P05556|ITB1_HUMAN LYYLMDLSYSMKDDLENVKSLGTDLMNEMRRITSDFRIGFGSFVEKTVMPYISTTP-AKL 203
SP|P26012|ITB8_HUMAN LYYLVDVSASMHNNIEKLNSVGNDLSRKMAFFSRDFRLGFGSYVDKTVSPYISIHP-ERI 207
SP|P16144|ITB4_HUMAN LYILMDFSNSMSDDLDNLKKMGQNLARVLSQLTSDYTIGFGKFVDKVSVPQTDMRP-EKL 190
```